Electronic Structure and Electron Dynamics in Semiconductor Materials for New Photovoltaic Applications

Dissertation

zur Erlangung des akademischen Grades
doctor rerum naturalium
(Dr. rer. nat.)
im Fach Physik

vorgelegt der

Fakultät für Mathematik und Naturwissenschaften
Institut für Physik
Technische Universität Ilmenau

von

M. Sc. Philipp Sippel

Gutachter:

1. *Prof. Dr. Thomas Hannappel*
2. *Prof. Dr. Jure Demsar*
3. *Prof. Dr. Daniël Vanmaekelbergh*

Tag der Einreichung: *9. März 2015*
Tag der wissenschaftlichen Aussprache: *24. September 2015*

urn:nbn:de:gbv:ilm1-2015000378

Abstract

New photovoltaic concepts such as intermediate band solar cells or hot-carrier solar cells require long lifetimes of hot photoexcited carriers. Collection of their extra energy with respect to the band edges could then succeed. Under this aspect, the electronic structure and the electron relaxation in semiconductors were investigated focusing on the material's geometry and its surface. Both alter the electronic structure and thus can affect the electron-phonon interaction that is the main mechanism for carrier cooling. The role of the geometry was studied with time-resolved two-photon photoemission spectroscopy (tr-2PPE) on CdSe nanostructures, in particular 0D quantum dots and 2D quantum well nanoplatelets. For quantum dots it was shown that electron-phonon scattering via bulk states is not the dominant energy loss mechanism. Instead, the cooling rate depends notably on the surrounding capping or shell. Scattering via surface states is considered as an alternative relaxation pathway. In contrast, the nanoplatelets reveal fast relaxation rates, independent of thickness, ligands or a CdS shell. The corresponding energy loss rate is described with a model for LO phonon scattering in quantum wells. The effect of surface states on the relaxation of bulk electrons is studied exemplarily on III-V semiconductors, prepared by metal organic vapor phase epitaxy. Studies with 2PPE on GaP(100) reveal several surface states for two different surface reconstructions. Their corresponding energies can be used to explain prominent features in reflectance anisotropy spectra of the same surfaces. Tr-2PPE measurements on InP(100) were performed to analyze the electron scattering between 3D bulk states and a particular surface state (C2). The scattering rates were determined and the cooling of bulk electrons in the presence and absence of C2 was compared. All of the results indicate fast carrier relaxation. Therefore, a photovoltaic concept is presented that is based on intersubband transitions and that employs fast separation of the hot carriers to counteract the short lifetimes. This design was realized as a tandem solar cell, combining an InP pin-junction and a photovoltaic intersubband absorber of InGaAs/InAlAs/InAs quantum wells. Proof-of-principle for the operation of this concept is provided experimentally and the basic characteristics of the device are explained with an equivalent circuit design.

Zusammenfassung

Für neuartige Photovoltaikkonzepte wie die "Zwischenbandsolarzelle" oder die "Heiße-Ladungsträger-Solarzelle" werden lange Lebensdauern für heiße photogenerierte Ladungsträgern benötigt. Dies würde es erlauben, die zusätzliche Energie bezüglich der Bandkanten zu sammeln. Unter diesem Blickwinkel wurden die elektronische Struktur und die Elektronenrelaxation in Halbleitern untersucht, mit Schwerpunkt auf Geometrie und Oberfläche der Materialien. Beides beeinflusst die elektronische Struktur und kann somit Auswirkungen auf die Elektron-Phonon-Wechselwirkung haben, welche die Hauptursache für das Abkühlen der Ladungsträger in den meisten Materialien ist. Die Rolle der Geometrie wurde mittels zeitaufgelöster Zweiphotonen-Photoemissionsspektroskopie (tr-2PPE) an Hand von CdSe Nanostrukturen analysiert; im Speziellen 0D-Quantenpunkte und 2D-Nanoplättchen. Für Quantenpunkte wird gezeigt, dass Streuung über Volumenzustände nicht der dominante Energieverlustmechanismus ist. Stattdessen wird die Abkühlrate wesentlich durch die umgebenden Liganden und die Umhüllung bestimmt und es finden sich Hinweise auf Streumechanismen über Oberflächenzustände. An Nanoplättchen hingegen wird eine schnelle Relaxation beobachtet, unabhängig von Dicke, Liganden oder einer CdS Hülle. Die Energieverlustrate wird mit einem Modell für LO-Phononstreuung in Quantentrögen beschrieben. Die Bedeutung der Oberflächen für die Relaxation von Elektronen wird exemplarisch an III-V Halbleitern untersucht, welche mit metallorganischer Gasphasenepitaxie präpariert wurden. Studien mit 2PPE an GaP(100) offenbaren mehrere Oberflächenzustände an zwei verschiedenen Oberflächenrekonstruktionen. Anhand der zugehörigen Energien konnten markante Merkmale in Reflexions-Anisotropie-Spektren erklärt werden. Tr-2PPE Messungen an InP(100) wurden durchgeführt, um das Streuen von Elektronen zwischen 3D-Volumenzuständen und einem bestimmen Oberflächenzustand (C2) zu untersuchen. Die Streuraten wurden bestimmt und das Abkühlen von Volumenelektronen wurde für den Fall mit und ohne C2 untersucht und verglichen. All diese Resultate zeigen schnelle Ladungsträgerrelaxation. Ein photovoltaisches Konzept wird präsentiert, basierend auf Interssubbandübergängen, welche eine schnelle Trennung heißer Ladungsträger implementiert um die kurzen Lebenszeiten zu kompensieren. Dieses Design wurde in Form einer Tandemsolarzelle realisiert, in welcher ein InP pin-Übergang sowie ein photovoltaischer Intersubbandabsorber aus InGaAs/InAlAs/InAs Quantentrögen kombiniert sind. Das prinzipielle Funktionieren dieses Konzepts kann experimentell bestätigt und die grundsätzlichen Charakteristiken mit einem Ersatzschaltbild beschrieben werden.

Publications

Articles directly related to this work

1. P. Sippel, W. Albrecht, J.C. van der Bok, R.J.A. van Dijk-Moes, T. Hannappel, R. Eichberger, and D. Vanmaekelbergh, *Femtosecond Cooling of Hot Electrons in CdSe Quantum-Well Platelets*, Nano Lett. **15**, 2409 (2015).

2. P. Sippel, J.M. Szarko, T. Hannappel, R. Eichberger, *Ultrafast electron scattering from surface to bulk states at the InP(100) surface*, Phys. Rev. B **91**, 115312 (2015).

3. P. Sippel, S. Heitz, M. Elagin, M.P. Semtsiv, R. Eichberger, W.T. Masselink, T. Hannappel, K. Schwarzburg, *Concept and demonstration of an intermediate band tandem device for solar energy conversion*, Prog. Photovolt: Res. Appl.,DOI:10.1002/pip.2697 (2015).

4. M. Borgwardt, P. Sippel, R. Eichberger, M. P. Semtsiv, W. T. Masselink, and K. Schwarzburg, *Femtosecond excitation correlation photoluminescence in the presence of Shockley-Read-Hall recombination*, J. Appl. Phys. **117**, 215702 (2015)

5. P. Sippel, O. Supplie, M.M. May, R. Eichberger, and T. Hannappel, *Electronic structures of GaP(100) surface reconstructions probed with two-photon photoemission spectroscopy*, Phys. Rev. B **89**, 165312 (2014).

6. P. Sippel, K. Schwarzburg, M. Borgwardt, M. Elagin, S. Heitz, M.P. Semtsiv, W.T. Masselink, T. Hannappel, R. Eichberger, *Dynamics and two photon intersubband absorption of photovoltaic quantum structures*, Photovoltaic Specialist Conference (PVSC), IEEE 40th, 3254 (2014).

7. P. Sippel, W. Albrecht, D. Mitoraj, R. Eichberger, T. Hannappel, and D. Vanmaekelbergh, *Two-Photon Photoemission Study of Competing Auger and Surface-Mediated Relaxation of Hot Electrons in CdSe Quantum Dot Solids*, Nano Lett. **13**, 1655 (2013).

8. H. Döscher, O. Supplie, M.M. May, P. Sippel, C. Heine, A.G. Muñoz, R. Eichberger, H.-J. Lewerenz, and T. Hannappel, *Epitaxial III–V Films and Surfaces for Photoelectrocatalysis*, ChemPhysChem **13**, 2899 (2012).

Other articles

1. C. Strothkämper, A. Bartelt, P. Sippel, T. Hannappel, R. Schütz, and R. Eichberger, *Delayed Electron Transfer through Interface States in Hybrid ZnO/Organic-Dye Nanostructures*, J. Phys. Chem. C **117**, 17901 (2013).

Table of Contents

Abstract i

Kurzzusammenfassung iii

List of publications v

List of figures ix

Abbrevations and Symbols xi

1 Motivation and introduction 1

2 Theoretical background 5

2.1 Electronic states in semiconductors . . . 5

2.2 Confined electron states . . . 8

2.2.1 The planar infinite quantum well . . . 8

2.2.2 The spherical infinite quantum well . . . 11

2.3 Charge carrier dynamics in semiconductors . . . 14

2.3.1 Electron cooling in semiconductors . . . 15

2.3.2 Electron phonon scattering in quantum wells . . . 17

2.4 Principles of two-photon photoemission spectroscopy (2PPE) . . . 21

2.4.1 Single-beam 2PPE . . . 21

2.4.2 Time-resolved 2PPE . . . 24

2.4.3 Surface sensitivity of 2PPE . . . 25

3 Experimental 27

3.1 Laser system . . . 27

3.2 2PPE setup . . . 30

3.3 Reflectance anisotropy spectroscopy (RAS) . . . 33

4 Electron dynamics in nanostructures 35

4.1 Introduction to CdSe quantum dots and nanoplatelets . . . 35

4.1.1 Carrier dynamics and relevance for photovoltaics . . . 35

4.1.2 CdSe quantum dots and quantum dot solids . . . 36

4.1.3 CdSe nanoplatelets . . . 37

4.1.4 Influence of the ligand and the shell . . . 39

4.1.5 Sample preparation and transport to UHV . . . 41

4.2 Relaxation of hot electrons in CdSe quantum dots . . . 42

4.2.1 Sample characterization . . . 43

4.2.2 Calculation of the excitation densities . . . 43

4.2.3 Tr-2PPE measurements . . . 44

4.2.4 Discussion . . . 55

4.3 Hot electrons in CdSe nanoplatelets . . . 56

4.3.1 Sample characterization . . . 57

4.3.2 Calculation of the excitation densities . . . 58

4.3.3 Electron dynamics for different excitation energies . . . 59

4.3.4 Determination of the electron temperature . . . 62
4.3.5 Electron relaxation for different lattice temperature . . . 65
4.3.6 Comparison of different nanoplatelets . . . 68
4.3.7 Discussion . . . 69
4.4 Comparison of the electron dynamics in 0D and 2D CdSe nanostructures 71

5 Electronic structure and dynamics at III-V surfaces 73
5.1 Introduction to III-V semiconductor surfaces . . . 73
5.1.1 III-V semiconductors . . . 74
5.1.2 Electronic properties of InP and GaP . . . 74
5.1.3 Surface reconstructions of InP(100) and GaP(100) . . . 75
5.1.4 Sample preparation . . . 78
5.2 Electronic structures of GaP(100) surface reconstructions . . . 81
5.2.1 Characterization with RAS . . . 81
5.2.2 Band alignment . . . 83
5.2.3 Detection of surface states . . . 85
5.2.4 Energetic allocation of surface states . . . 88
5.2.5 Comparison with RAS . . . 94
5.2.6 Discussion . . . 95
5.3 Electron cooling at the InP(100) surface . . . 97
5.3.1 Single beam 2PPE . . . 98
5.3.2 Excitation high above the surface state C2 . . . 99
5.3.3 Energy Loss Rate . . . 101
5.3.4 Population and depopulation dynamics of C2 . . . 102
5.3.5 Discussion . . . 104
5.4 Summary of the results on III-V semiconductor surfaces . . . 107

6 Fast carrier separation with intersubband transitions 109
6.1 Introduction to photovoltaics with intersubband transitions . . . 109
6.1.1 The intermediate band solar cell . . . 110
6.1.2 Intersubband transitions and light management . . . 111
6.1.3 Quantum cascade photodetectors . . . 112
6.2 Tandem cell design with intersubband absorber . . . 114
6.2.1 Design . . . 114
6.2.2 Two-beam photocurrent measurements . . . 116
6.2.3 Limitations of this approach . . . 121
6.3 Discussion . . . 123

7 Conclusion 125

Appendices 127
A Tr-2PPE signal for reversed pump-probe order . . . 129
B Temperature dependent energy-loss-rate (ELR) . . . 130
C Background correction for tr-2PPE . . . 132

Bibliography 135

Acknowledgment 153

List of Figures

2.1 BRILLOUIN zone of the fcc lattice and band structure of InP. 6
2.2 DOS in the parabolic and non-parabolic approximation. 7
2.3 Electronic states in the infinite quantum well. 9
2.4 DOS for QWs of different thickness. 10
2.5 Size-dependent bandgap for CdSe QDs. 12
2.6 Electronic states and absorption spectrum for CdSe QDs. 13
2.7 Phonon dispersion for InP. 15
2.8 Energy-dependent polar mode scattering rates for electrons. 17
2.9 Possible scattering events in a QW. 18
2.10 LO phonon absorption and emission rates in a QW. 19
2.11 Formation of 2PPE spectra for initial, intermediate and final states. . . 22
2.12 Alignment of energy levels between sample and detector. 23
2.13 Schematic of time-resolved 2PPE. 25

3.1 Laser setup, including frequency conversion elements. 28
3.2 Exemplary auto- and crosscorrelation traces. 29
3.3 2PPE setup. 31

4.1 CdSe/CdS band alignment. 40
4.2 Mounting of the sample in the 2PPE setup. 41
4.3 Optical spectra of CdSe QDs in solution and on ITO. 43
4.4 TEM image of 4.2 nm sized CdSe QDs. 44
4.5 Temporal evolution of 2PPE spectra measured on CdSe QD solids for different cappings and excitation energies. 46
4.6 Transient occupation of the $1P_e$ level and rate model schemes. 49
4.7 Detailed fit of the transient occupation of the $1P_e$ level. 50
4.8 Transient occupation of the $1P_e$ level for different excitation energies. . 51
4.9 Transients at different kinetic energy in the vicinity of $1P_e$. 53
4.10 Model for the decay via an intermediate state in HDT-capped QDs. . . 54
4.11 Absorbance spectra and TEM images of nanoplatelets of different thicknesses with and without shell. 57
4.12 Transmittance spectra of CdSe nanoplatelets on ITO. 58
4.13 2PPE on CdSe(3 ML)/CdS core/shell NPs, varying $h\nu_{pump}$. 60
4.14 Total electron yield for CdSe(3 ML)/CdS core/shell NPs. 61
4.15 Cooling of the electron distribution, for $h\nu_{pump} = 2.60$ eV at CdSe(3 ML)/CdS core/shell nanoplatelets. 62
4.16 Evolution of the average electron energy and energy loss rates in CdSe nanoplatelets at different lattice temperatures. 66
4.17 Energy loss rates for CdSe NPs for variable thickness, capping, with and without CdS shell and compared to CdSe QDs. 68
4.18 Comparison of the electron relaxation in NPs and QDs. 71

5.1 Band structure of GaP. 75
5.2 Atomic structure of the III-rich surface reconstruction. 76
5.3 Band structure of the Ga-rich surface. 77
5.4 Atomic structure of the P-rich surface reconstruction. 78
5.5 UHV transfer system. 79
5.6 RAS of the Ga-rich and the P-rich surface reconstructions. 82
5.7 2PPE spectra for differently doped GaP(100) samples. 84
5.8 Band-bending-related spectral shift at the Ga-rich surface. 85
5.9 2PPE spectra of the Ga-rich surface, for different photon densities. . . 86
5.10 2PPE spectra before and after oxygen exposure. 87
5.11 Schematics of the surface state energies relative to the bulk band edges and the transitions that lead to peaks in the spectra. 88
5.12 2PPE spectra of the clean Ga-rich surface for different hν_{pump}. 89
5.13 2PPE spectra of the clean P-rich surface for different hν_{pump}. 90
5.14 Intermediate state energy for different peaks of the Ga-rich and P-rich surface in dependence of the excitation energy. 91
5.15 Polarization dependent 2PPE spectra of the Ga-rich surface. 93
5.16 Single-beam 2PPE at the InP(100) surface. 98
5.17 Tr-2PPE measurement at InP(100) for high excitation energy. 100
5.18 Mean kinetic energies and total electron yields of tr-2PPE spectra. . . . 101
5.19 Tr-2PPE for resonant C2 population. 103

6.1 Sketch of the intermediate band solar cell. 110
6.2 SEM pictures of the tandem solar cell sample. 112
6.3 Miniband alignment and photocurrent of a QCPD. 113
6.4 Principle of the proposed tandem cell. 115
6.5 Cell design and PIA layers. 116
6.6 Two-beam setup. 117
6.7 Measured and simulated photocurrent. 118
6.8 PIA minibands for applied bias voltage. 120

A.1 Signals for reversed pump probe order. 129

Abbrevations and symbols

1/2PPE	one/two-photon photoemission (spectroscopy)
a	lattice constant
BBO	β-barium borate
BZ	Brillouin zone
CB(M)	conduction band (minimum)
CV	capacitance-voltage (profiler)
DFT	density functional theory
DOS	density of states
Δt	time delay between *pump* and *probe*
E_F	*Fermi* level
E_g	band gap energy
E_{kin}	kinetic energy
E_{vac}	vacuum level
ED	electron distribution
ELR	energy loss rate
$\epsilon_{0/r}$	vacuum/relative permittivity
FWHM	full width at half maximum
fcc	face-centered cubic
Φ	work function
GSMBE	gas source molecular beam epitaxy
GVD	group velocity dispersion
h	Planck's constant
hν	photon energy
$\hbar$	$h/2\pi$
$\hbar\omega_{LO}$	LO phonon energy
HDT	1,6-hexanedithiol
hh	heavy hole (band)
HOPG	highly ordered pyrolytic graphite
IBSC	intermediate band solar cell
IST	intersubband transition
ITO	indium tin oxide
JDOS	joined density of states
$\mathbf{k}$	electron wavevector
LDA	local-density-approximation
LED	light-emitting diode
LEED	low-energy electron diffraction
lh	light hole (band)
LO	longitudinal optical
m_e	electron mass
m_{eff}	effective mass
MBE	molecular beam epitaxy
MCA	momentum conservation approximation

MCP	micro channel plate
MEG	multiple exciton generation
MOVPE	metal organic vapor phase epitaxy
NP	nanoplatelet
NOPA	non-collinear optical parametric amplifier
ODE	octadecene
OA	oleic acid
$\bar{P}$	mean laser intensity
PIA	photovoltaic intersubband absorber
PES	photoemission spectroscopy
PLE	photoluminescence excitation
PV	photovoltaics
$\mathbf{q}$	phonon wavevector
QCPD	quantum cascade photodetector
QD	quantum dot
QW	quantum well
QWIP	quantum well infrared photodetector
RAS	reflection anisotropy spectroscopy
ρ	density of states
SBZ	surface BRILLOUIN zone
SEM	scanning electron microscopy
SHG	second harmonic generation
SPV	surface photovoltage
STM	scanning tunnel microscopy
T_e	temperature of the electron distribution
T_{lat}	lattice temperature
TBP	tertiarybutylphosphine
TEM	transmission electron microscopy
TOF	time of flight
TOP	trioctylphosphine
tr-2PPE	time-resolved 2PPE
τ	time constant
U_{Bias}	bias voltage between sample and detector
UHV	ultra high vacuum
UPS	ultraviolet photoemission spectroscopy
UV	ultraviolet
VB(M)	valance band (maximum)
VIS	visible
WLC	white light continuum
XPS	X-ray photoemission spectroscopy

1 Motivation and introduction

The application of photovoltaic systems is one of the answers to the world's growing demands in energy without producing vast amounts of the greenhouse gas CO_2. The attractiveness of solar cells—in the eye of an investor—is determined mostly by their price and their capability to convert solar radiation into electrical power or, in other words, their solar energy conversion efficiency. For most of the solar cell concepts, which are in industrial production or currently under development, the latter is insurmountably determined by the SHOCKLEY-QUEISSER single-band-gap limit [1]. Besides thermodynamic considerations, the underlying detailed balance calculations also include the assumption that each photon with energy greater than the band gap creates exactly one electron-hole pair: photons with lower energy cannot be absorbed and all other photons lose their additional energy with respect to the band gap via phonon emission. The latter process is called cooling of the hot carriers, or carrier relaxation and is the major topic of this thesis.

Currently, only one concept is known to have reached efficiencies beyond this limit: the so-called multijunction solar cells or tandem cells that consist mainly of III-V compound semiconductors and that are already fabricated on an industrial scale: Cells with different band gaps are grown (or bonded) on top of each other and connected in series via tunnel junctions. The cell with the highest band gap is on top. Photons with lower energy than this band gap simply pass through and are absorbed in the second cell or pass on to the third cell with even lower band gap and so on. A new world record has been achieved just recently with a cell consisting of four subcells, reaching an efficiency of 46.5% with concentrated sun light corresponding to 324 suns [2, 3]. However, this approach is still very costly due to the sophisticated preparation methods and the involvement of rare materials like indium and gallium. Also, with rising number of junctions, the fine-tuning of the band gaps of the individual subcells becomes an increasingly difficult task. Hence, and of course also simply for scientific interest it is justified to push research on alternative concepts to overcome the SHOCKLEY-QUEISSER-limit.

Prominent approaches with this goal include the *intermediate band solar cell* [4], the *hot-carrier solar cell* [5] and designs based on multiple exciton generation [6–8]. All of these concepts involve the absorption of a broad spectrum of light in a single semiconductor section, without suffering the energy loss by carrier cooling. A sufficiently slow carrier relaxation is essential to allow for the collection of the carriers' excess energy by any means, depending on the particular concept. For conventional semiconductors, this is usually not fulfilled due to fast phonon emission, which is

the dominant electron cooling mechanism. This process critically depends on the electronic structure, which is typically determined by the crystal structure and the composition. Significant manipulation of the electronic structure can be achieved by nanostructuring these materials and confining the charge carriers in one, two or three dimensions. This in return modifies the electron-phonon interaction and in the most ideal case significantly reduces the energy loss rate of the hot carrier distribution [9, 10]. However, low-dimensional structures have unavoidably a much larger surface/bulk ratio than 3-dimensional concepts. A considerable fraction of the involved atoms are located directly at the interface, where the crystal lattice is truncated. This also effects the electronic structure and the arising surface/interface states must be considered for electron-phonon scattering and might influence and in the worst case accelerate the carrier cooling. Thus, careful investigation is required to disentangle the contributions of geometry and surface on the charge carrier relaxation and to identify materials that are appropriate candidates for the above-mentioned concepts. This thesis is designated to investigate the electronic structure and the dynamics of hot electrons in low-dimensional semiconductors and at semiconductor surfaces and to discuss the impact on photovoltaic concepts that require long hot-carrier lifetimes. This is done mainly by time-resolved measurements on different material systems.

Following the introduction, Chapter 2 provides the theoretic framework for this thesis and an overview of the related physics. Also, the concepts and models are presented that are compared to the experimental data in parts of the thesis.

In Chapter 3, the experimental methods are described, which were applied. Namely, these are time-resolved two-photon photoemission spectroscopy (tr-2PPE), that was implemented for the study of hot-electron dynamics and the investigation of the electronic structure, and reflectance anisotropy spectroscopy as an indirect method that is also sensitive to the surface electronic structure.

Chapters 4,5 and 6 contain the results obtained in this thesis. Each chapter concentrates on a different material system, which is presented and described in the first section of the particular chapter:

In Chapter 4, studies with tr-2PPE on the electron dynamics of CdSe nanostructures are presented, in particular, 0D quantum dots and 2D quantum well nanoplatelets. These samples were prepared via wet-chemical synthesis with different thicknesses and surface terminations. The differences between the two geometries are analyzed and the influences of different organic and inorganic cappings are investigated. This allows to analyze also surface-related electron relaxation pathways. The samples were manufactured and provided by the *Debye Institute for Nanomaterials*

Science at the *University of Utrecht*.

The effect of the surface electronic structure on the electron cooling is covered more specifically in Chapter 5. Here, (tr-)2PPE measurements on GaP(100) and InP(100) surfaces are presented, prepared by metal-organic vapor phase epitaxy (MOVPE). An ultra-high-vacuum shuttle system allowed for the investigation of well-defined and contamination-free surface reconstructions. Studies on the electronic structures of different atomic reconstructions of the GaP(100) surface are presented. The results are compared to measurements with reflectance anisotropy spectroscopy — a method that is also highly sensitive to surface states. This is followed by time-resolved measurements on a particular InP(100) surface reconstruction. Here, the scattering of electrons between 2D and 3D surfaces is investigated directly. By quenching the surface states with oxygen, carrier relaxation in the presence and absence of a specific surface state is studied. These materials were grown directly at the *Helmholtz Zentrum Berlin*.

The last part of this thesis is formed by Chapter 6 and complements the preceding investigations with an applied study. A concept is presented that shows how intersubband transitions might be employed to harvest infrared sunlight, even in the presence of fast hot-electron relaxation. This approach has obvious analogies to the intermediate band solar cell but implements a mechanism for fast separation of the hot carriers. The operation of the concept is demonstrated with photocurrent measurements on an actual structure, consisting of an InP pin-junction and a series of InGaAs/InAlAs/AlAs quantum wells. The corresponding samples were provided by the *FeT* group of the *Humboldt University Berlin*. Finally, the results are summarized in Chapter 7 and an outlook for further research is provided.

2 Theoretical background

The results obtained experimentally in this thesis are regularly compared to simulated data. This chapter shall give a quick introduction on the most important theoretical concepts that will play a role in these calculations or that will be helpful to understand the observed phenomena. At first, a brief description on the electronic structure of infinite bulk semiconductors is provided. This is followed by an explanation of the electronic structures in 2D quantum wells and 0D quantum dots. Secondly, an overview of carrier dynamics in semiconductors is presented, with a focus on the interaction of electrons with polar optical phonons — specifically in quantum wells. Finally, the main mechanisms of 2PPE are explained, as this method was used to obtain a large quantity of the results, presented in this thesis.

2.1 Electronic states in semiconductors

For a single electron in a periodic potential the SCHRÖDINGER equation is given by [11]

$$H\Psi(\mathbf{r}) = \left(-\frac{\hbar^2}{2m}\nabla^2 + V(\mathbf{r})\right)\Psi(\mathbf{r}) = E\Psi(\mathbf{r}). \tag{2.1}$$

Here, H is the single particle HAMILTONian, m the electron mass, $\Psi(\mathbf{r})$ the single particle wave function and E the corresponding energy eigenvalue. $V(\mathbf{r})$ is the periodic potential which is invariant to translation and thus fulfills

$$V(\mathbf{r}) = V(\mathbf{r} + \mathbf{R}) \tag{2.2}$$

for each lattice vector $\mathbf{R}$. The solution for Eqs. 2.1 and 2.2 is the BLOCH function

$$\Psi_{n,\mathbf{k}}(\mathbf{r}) = \frac{1}{\sqrt{N}} e^{i\mathbf{k}\mathbf{r}} u_{n,\mathbf{k}}(\mathbf{r}). \tag{2.3}$$

The function $u_{n,\mathbf{k}}(\mathbf{r})$ has the periodicity of the lattice and fulfills

$$u_{n,\mathbf{k}}(\mathbf{r}) = u_{n,\mathbf{k}}(\mathbf{r} + \mathbf{R}). \tag{2.4}$$

Hereby, N is the number of unit cells, n the band index and $\mathbf{k}$ the wave vector. The bands are related to the original orbitals of the electrons and the energy eigenvalues $E_n(\mathbf{k})$, that correspond to the wave functions in Eq. 2.3, form the electronic structure of the material. Semiconductors are characterized by certain energy gaps, where

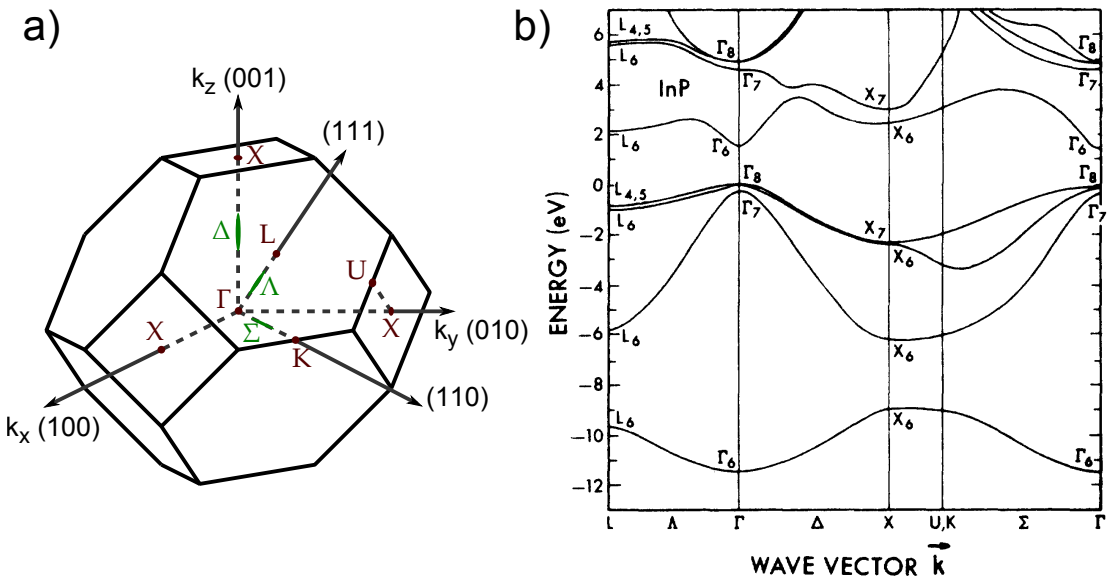

Figure 2.1: (a) BRILLOUIN zone of the face-centered cubic (fcc) lattice with the points of high symmetry being indicated. (b) Band structure of InP calculated with the pseudopotential method (Reprinted with permission from. [12]. © (1976) American Physical Society.)

no solutions $E_n(\mathbf{k})$ exist and by the FERMI-level lying inside this band gap. The states below the band gap form the valence band and are almost completely occupied in thermodynamic equilibrium. Analog, the conduction band (CB) is formed by states above the band gap that are almost completely unoccupied. Optical transitions between VB and CB lead to the generation of charge carriers and form the basis of classical photovoltaics.

The electronic structure of a semiconductor is complex and can be calculated with a variety of methods. An example of a band structure is shown in Fig. 2.1 for the semiconductor InP together with the shape of the BRILLOUIN-zone for the face centered cubic (fcc) lattice. For small $\mathbf{k}$, $E_n(\mathbf{k})$ can usually be described analytically. This is very handy, as most optical and electronic semiconductor properties can be explained with the shape of the bands near the BRILLOUIN (BZ) center (the Γ-point), where the VB (CB) has a maximum (minimum). Here, the CB electrons depend quadratically on $\mathbf{k}$, similar to the case of free electrons and

$$E_{CB}(\mathbf{k}) \approx E_{CB}(0) + \frac{\hbar^2 k^2}{2m_{eff}}. \tag{2.5}$$

m_{eff} is the effective mass of the electrons and describes the curvature of the bands. At the conduction band minimum (CBM) the resulting density of states (DOS) per

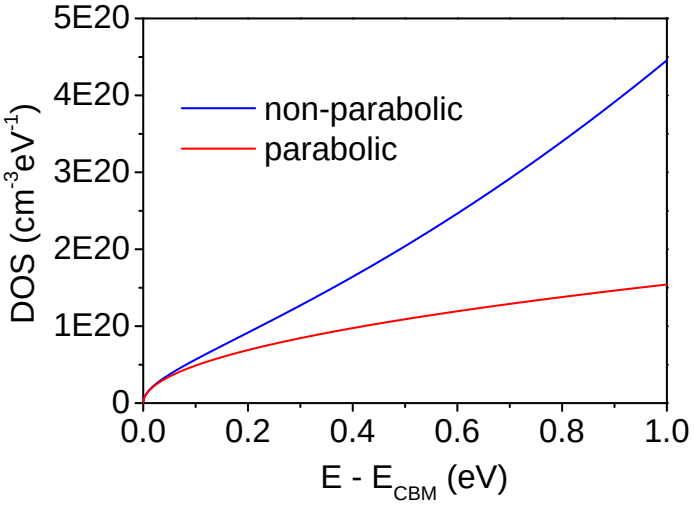

Figure 2.2: DOS of Γ-point conduction band electrons for InP with $m_{eff} = 0.08\, m_e$ and a bandgap of $E_g = 1.34\,\mathrm{eV}$ in the parabolic and non-parabolic approximation.

volume unit is

$$\rho_{3D}(E) := \frac{dN}{dE} = \frac{1}{2\pi^2}\left(\frac{2m_{eff}}{\hbar^2}\right)^{3/2} E^{1/2} \tag{2.6}$$

and plotted in Fig 2.2 versus the electron energy. For larger $\mathbf{k}$, however, the energy dispersion becomes strongly non-parabolic and can be approximated with [13]

$$\frac{\hbar^2 k^2}{2m_{eff}} =: \gamma(\mathbf{k}) \approx E(\mathbf{k})\left(1 + \alpha E(\mathbf{k}) + \beta E^2(\mathbf{k})\right), \tag{2.7}$$

where α and β can be related to the bandgap. This expression leads to a significant higher DOS for electrons with high excess energy as shown in Fig. 2.2.

For the three valence bands, isotropy needs to be taken into account as well. More sophisticated **kp** perturbation theory involving eight bands results in

$$E_{hh/lh}(\mathbf{k}) = -Ak^2 \mp \sqrt{B^2k^4 + |C|^2\left(k_x^2k_y^2 + k_y^2k_z^2 + k_z^2k_x^2\right)} \tag{2.8}$$

for the dispersion of the light and heavy hole bands at the Brillouin zone center, with A,B and C being related to the Luttinger parameters that are tabulated for many semiconductors.

2.2 Confined electron states

Finite structures or heterostructures can be described with the SCHRÖDINGER equation in the presence of an external potential $U(\mathbf{r})$:

$$[H_0 + U(\mathbf{r})]\,\Psi(\mathbf{r}) = E\Psi(\mathbf{r}) \tag{2.9}$$

where H_0 is the HAMILTONian of the unperturbed lattice. Assuming parabolic bands and only a small perturbation that changes slowly compared to the lattice constant, one can separate the wave function into

$$\Psi(\mathbf{r}) \approx u_{n,0}(\mathbf{r})F_c(\mathbf{r}), \tag{2.10}$$

where $u_{n,0}(\mathbf{r})$ is the cell-periodic part of the BLOCH function and $F_c(\mathbf{r})$ is referred to as *envelope function* of the wave function. Accordingly [14],

$$\left[-\frac{\hbar^2}{2m_{eff}}\nabla^2 + E_c(\mathbf{r})\right] F_c(\mathbf{r}) = EF_c(\mathbf{r}). \tag{2.11}$$

Here, $E_c(\mathbf{r}) := E_c + U(\mathbf{r})$ can be understood as the local band edge energy, well known from thousands of figures that show the alignment of bands for all sorts of semiconductors, plotted vs the growth direction.

For semiconductor structures of small dimensions or semiconductor heterostructures, Eq. 2.11 needs to be solved with the appropriate boundary conditions. For potential well structures like quantum wells (QWs) or quantum dots (QDs), this leads to electron states that are localized in at least one dimension and to a splitting of the energetic levels, similar to molecular or atomic states. In the following this will be demonstrated for 2- and 0-dimensional structures with infinite barriers.

2.2.1 The planar infinite quantum well

Consider

$$U(\mathbf{r}) = U(z) = \begin{cases} 0, & \text{for } 0 \le z \le L \\ \infty, & \text{else} \end{cases} \tag{2.12}$$

for the external potential $U(\mathbf{r})$ in Eq. 2.11. This scenario is sketched in Fig. 2.3. The problem can be separated into three independent parts, one for each spatial direction [14]. Regarding the translation invariance in the x- and y-directions, the envelope function can be written as $F(\mathbf{r}) = e^{ik_x x}e^{ik_y y}\chi(z)$. For $z < 0$ and $z > L$ it is clear that $\chi(z) = 0$, as here $U = \infty$. For $0 \le z \le L$ Eq. 2.11 transforms to

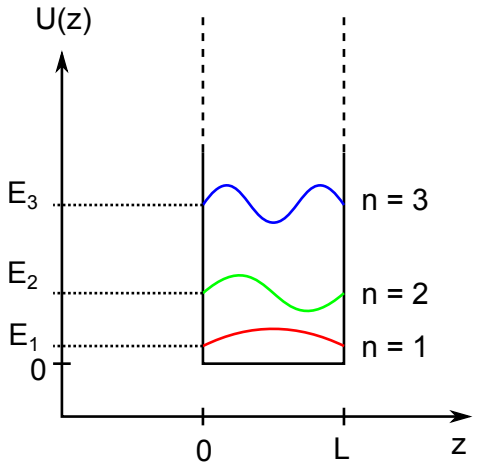

Figure 2.3: External potential $U(z)$ for the infinite quantum well. The wave functions of the three energetically lowest confined states are represented by the colored curves.

$$\left[-\frac{\hbar^2}{2m_{eff}}\frac{\partial^2}{\partial z^2}+\frac{\hbar^2 k_{\parallel}^2}{2m_{eff}}\right]\chi(z)=(E-E_c)\,\chi(z), \tag{2.13}$$

where $k_{\parallel}^2 := k_x^2 + k_y^2$ has been introduced. This is a well known quantum mechanical problem with the solution

$$\chi(z) = A\sin(k_z z) + B\cos(k_z z)\,. \tag{2.14}$$

The boundary conditions require $\chi(z)$ to be continuous and due to the symmetry of Eq. 2.12 it follows that $\chi(0) = \chi(L) = 0$ and thus $B = 0$ and

$$k_z = \frac{\pi n}{L} \tag{2.15}$$

with n being an integer. Inserting Eqs. 2.14 and 2.15 in Eq. 2.13 then results in

$$E = E_c + \frac{\hbar^2 k_{\parallel}^2}{2m_{eff}} + \underbrace{\frac{\hbar^2\pi^2 n^2}{2m_{eff}L^2}}_{:=E_n}\,. \tag{2.16}$$

Hereby, E_n is the energy of the confined states with a characteristic $\frac{n^2}{L^2}$ dependency, showing that the confinement effect increases with decreasing structure size and vanishes for macroscopic dimensions. Normalization of the wave-function yields [15]

$$\chi_n = \sqrt{\frac{2}{L}}\sin\left(\frac{\pi n z}{L}\right), \tag{2.17}$$

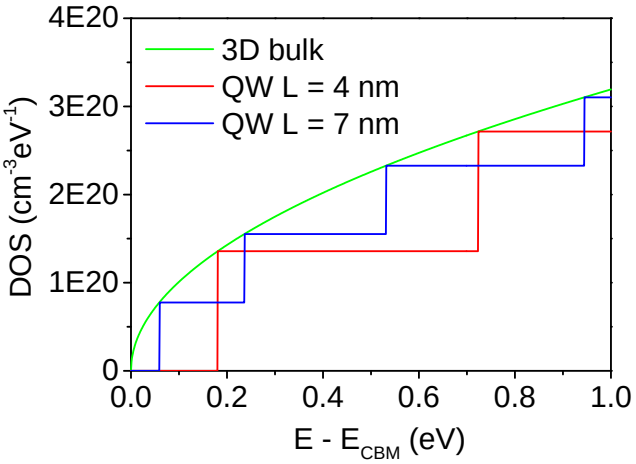

Figure 2.4: DOS for CdSe quantum wells ($m_{eff} = 0.13\, m_e$, $E_g = 1.74\,\text{eV}$, Ref. [16]) of different sizes, compared to the bulk case.

which is shown in Fig. 2.3. This approach suffices to describe a variety of features observed in QWs on a qualitative basis. For more quantitative results it is especially necessary to take into account that the barrier hight is always finite. This generally leads to a penetration of the wave-functions of the confined states into the barriers. Also the confinement energy significantly decreases; an effect that becomes more distinct with decreasing well width. For higher subbands, also non-parabolicity becomes important and the confinement energy is typically overestimated when applying the parabolic approximation.

Density of states and selection rules

The DOS can be calculated from Eq. 2.16 andasd

$$\rho_{2D}(E) = \frac{1}{2\pi}\left(\frac{2m_{eff}}{\hbar^2}\right)\sum_i \Theta\left(E - E_i\right), \tag{2.18}$$

where the sum is over all energy levels according to Eq. 2.16. Thus, for the 2D case $\rho(E)$ is a step-like function as shown in Fig. 2.4, where it is compared to the 3D case.

Three kinds of optical transitions are distinguished for quantum wells: (i) Interband transitions between conduction band and valence band states. (ii) Intersubband transions (IST) between two bands belonging to either the conduction or the valence band. (iii) Intraband transitions between two states of the same band. For interband transitions, evaluation of the dipole matrix element with the wave functions in Eqs. 2.10 and 2.17 yields $\Delta n = 0$; *i.e.* the quantum indices of the involved conduction band (CB)- and valence band (VB) state must be the same. Furthermore, $\mathbf{k}_{\|}$

must be conserved. A correct treatment of ISTs is not possible within the approximations made for Eq. 2.10 [17]. For the infinite quantum, a more fundamental approach shows that transitions are only possible between subbands of opposite symmetry with a maximum transition probability for neighboring subbands [17, 18]. Another very important result is that transitions can only occur if the electric field, associated with the radiation, has non-zero components perpendicular to the interfaces [17]. This has dramatic consequences for the design of devices and experiments that involve ISTs. For efficient absorption, ways have to be found to couple light into the structure that has non-zero POYNTING vector components parallel to the interface plane.

2.2.2 The spherical infinite quantum well

The electronic states of a spherical quantum dot can be deduced in a similar manner as for the planar quantum well. In this case the external potential is given by

$$U(\mathbf{r}) = U(r) = \begin{cases} 0, & \text{for } r < R \\ \infty, & \text{else} \end{cases} \tag{2.19}$$

with R being the radius of the quantum dot. The solutions of equation Eq. 2.11 in spherical coordinates are [19]

$$F_{n,l,m}(\mathbf{r}) = \sqrt{\frac{2}{R}} \frac{j_l\left(k_{n,l} r\right)}{j_{l+1}\left(k_{n,l} R\right)} Y_{l,m}\left(\Theta, \Phi\right). \tag{2.20}$$

with $Y_{l,m}\left(\Theta, \Phi\right)$ being the spherical harmonics and j_l the spherical BESSEL function of the first kind and order l. The n-th root of j_l is denoted as $\kappa_{n,l}$ and $k_{n,l} := \kappa_{n,l}/R$. The quantum numbers are restricted to

$$n = 1, 2, 3... \tag{2.21}$$
$$l = 0, 1, 2... \quad (\mathrm{S}, \mathrm{P}, \mathrm{D}, ...) \tag{2.22}$$
$$m = 0, \pm 1, \pm 2, ..., \pm l. \tag{2.23}$$

The corresponding energy eigenvalues are

$$E_{n,l} = E_c + \frac{\hbar^2 k_{n,l}^2}{2 m_{eff}} = E_c + \frac{\hbar^2}{2 m_{eff}} \left(\frac{\kappa_{n,l}}{R}\right)^2, \tag{2.24}$$

showing a similar size dependence ($1/R^2$) as for the planar quantum well (cf. Eq. 2.16).

Results of this model for wurtzite CdSe quantum dots are compared in Fig. 2.5 to photoluminescence excitation (PLE) measurements of NORRIS and BAWENDI [20].

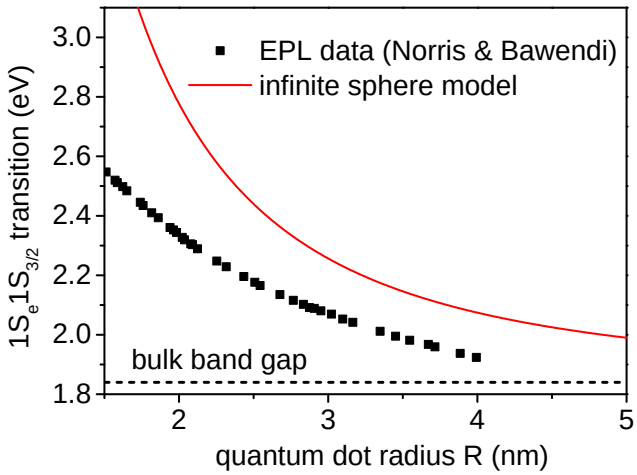

Figure 2.5: Lowest transition energy for CdSe quantum dots in dependence of the QD radius according to Eq. 2.24, with independently confined electrons and holes. Also PLE data from NORRIS and BAWENDI [20] at $T = 10\,\mathrm{K}$ is shown.

Here, the lowest optical transitions are shown.[1] While the size dependence is well reflected by the model, the confinement energy is overestimated, which is mostly related to the assumption of infinite barriers and the missing COULOMB interaction.

Density of states, selection rules, notation

The DOS can be deduced directly from Eq. 2.24 without further calculation and just depends on the number of confined levels. For one single dot, the DOS offers two spin-degenerate states at each level and if plotted versus the energy would be a series of δ-functions [15]. Calculation of the dipole matrix elements with the wave functions in Eq. 2.20 allows to depict the selection rules for optical transitions. This yields that transitions are only allowed for $\Delta n = 0$ and $\Delta l = 0$.

This description of electronic states holds quite well for conduction band electrons. However, for the valence band the situation is more complex due to its six-fold degeneracy at $\mathbf{k} = 0$, which is lifted by spin orbit coupling. This is comparable to the bulk case, where spin orbit coupling leads to the evolution of the light hole-, the heavy hole- and the split-off band. In particular, one needs to consider the coupling of the quantum number l related to the envelope function, the electron spin s and the angular momentum L related to the cell-periodic BLOCH part of the wave function $u_{\mathbf{k}}(\mathbf{r})$. Thus, the "good" quantum number F corresponding to $\mathbf{F} = \mathbf{l} + \mathbf{L} + \mathbf{s}$ and its projection F_z are introduced and used to distinguish the valence band states. The

[1] This means from the "heavy hole" valence band maximum (VBM) to the conduction band minimum (CBM) state 1S$_e$. The parameters are taken from Ref. [20] at 10 K and are: $E_g = 1.84\,\mathrm{eV}$, $m_{eff}^{el} = 0.11\,m_e$ and $m_{eff}^{hh} = 1.14\,m_e$.

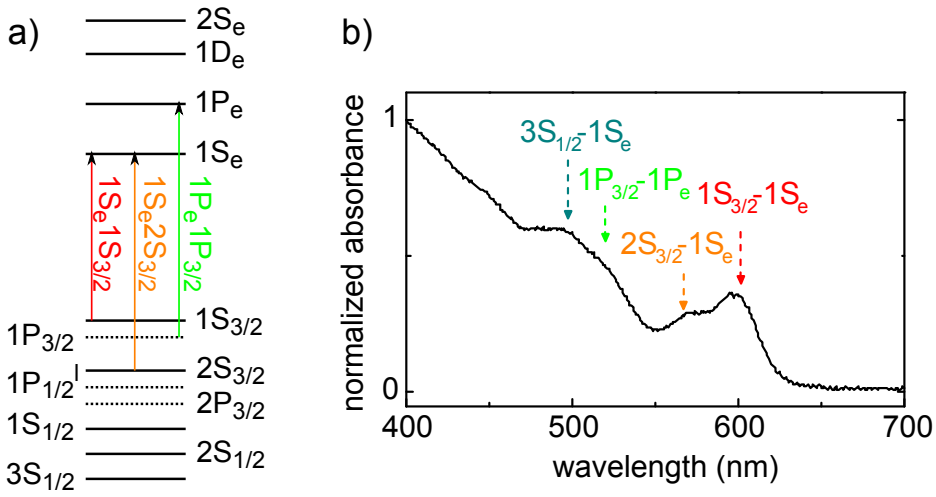

Figure 2.6: (a) Schematic of the conduction and valence band states in a quantum dot. Dashed lines are P hole states. The three energetically lowest allowed optical interband transitions are indicated. (b) Absorption spectrum of a CdSe QD with $R = 2.1\,\mathrm{nm}$. Prominent features have been assigned to certain transitions, according to Ekimov [21].

common notation of a quantum dot state then is "nl_{F_z}" and the highest lying valence band state accordingly is $1S_{3/2}$ [22]. The evolving electron and hole states and the three lowest allowed optical transitions are schematically shown in Fig. 2.6, together with the absorption spectrum of CdSe quantum dots with $R = 2.1\,\mathrm{nm}$.

This treatment of the hole states still neglects features such as a coupling of the S and D bands but here it shall server to explain the principle evolution of different valence band states and the origin of the hole state notation. These mixing effects also soften the strict selection rules for optical dipole transitions, mentioned above. A comprehensive description can be found *e.g.* in Ref. [20]. Also, the Coulomb interaction between electron and hole was completely neglected here. However, the the Coulomb interaction scales with $1/R$ and the confinement effect with $1/R^2$ (cf. Eq. 2.24). For sufficiently small sizes, typically below the exciton Bohr radius ($\approx 6\,\mathrm{nm}$ for CdSe [21]), one speaks of the *strong confinement regime* [23]. Here electron and hole wave functions can be treated in first approximation independently as *particles-in-a-sphere*. For the quantum dots investigated in this thesis, this is always fulfilled.

2.3 Charge carrier dynamics in semiconductors

If a semiconductor is illuminated with a laser pulse of sufficient photon energy ($h\nu \geq E_g$), charge carriers are generated and the thermodynamic equilibrium is disturbed. Accordingly, several stages of relaxation take place until the system returns to equilibrium. The carrier relaxation, happening on different timescales, has been classified into four temporally overlapping regimes by SHAH [24]:

a) Coherent regime ($< 200\,\mathrm{fs}$) Directly after photoexcitation there is a well-defined phase relationship between the wave function of the exciting light and the created excitations, which can be of real or virtual kind. This coherence can lead to multi phonon and interference effects, and is destroyed on a femtosecond timescale by scattering events that randomize the phase of the generated charge carriers, a process that is know as *dephasing*.

b) Non-thermal regime ($< 2\,\mathrm{ps}$) The initially generated carrier distributions (electrons and holes) are usually non-thermal, *i.e.* cannot be characterized by a temperature. Instead their distributions reflect the shape of the pump pulse and the involved bands. However, due to carrier-carrier scattering the non-thermal distributions become hot thermalized distributions, within a few hundred femtoseconds or faster. [25–27]

c) Hot-carrier regime($\approx 1-100\,\mathrm{ps}$) The temperature of such a thermalized carrier distribution is usually higher than the lattice temperature, provided that the exciting photons supply enough excess energy. Thus, the excited carriers emit phonons until the temperatures of carriers and lattice equilibrate. The energy of optical phonons is typically much larger than the energy of acoustic phonons. For polar semiconductors in particular, emission of longitudinal optical phonons via the FRÖHLICH interaction [28] is the dominant energy loss mechanism. During this regime also the LO phonon distribution increases temporally and the resulting "hot" phonons decelerate further cooling [29]. This effect is most pronounced for high carrier densities.

d) Isothermal regime($> 100\,\mathrm{ps}$) After equilibration of phonons, electrons and holes, *i.e.* after all distributions can be described with the same temperature, there is still an excess of electrons and holes compared to the thermodynamic equilibrium. These excess carriers recombine either radiatively or non-radiatively until the semiconductor is returned to thermodynamic equilibrium.

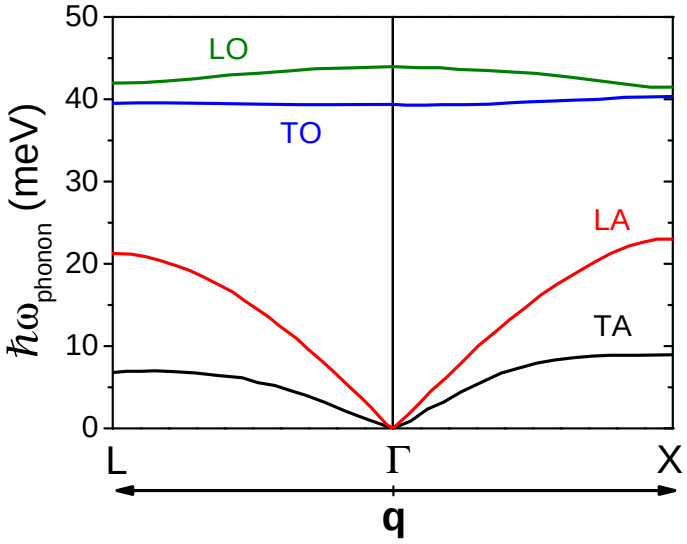

Figure 2.7: Calculated dispersion of phonons in InP. Data taken from Ref. [30].

2.3.1 Electron cooling in semiconductors

In this section, the fundamental concept of electron-phonon scattering is presented. Fig. 2.7 shows the phonon dispersion for InP (density functional theory (DFT) calculations from Ref. [30]). For low phonon wave vectors $\mathbf{q}$, *i.e.* near Γ, the energy of the acoustic phonons is much lower than the optical phonon energy. Thus, scattering with acoustical phonons is approximately elastic and most of the electron energy is lost via optical phonons. The focus hereby is on the interaction with longitudinal optical (LO) phonons, first described by FRÖHLICH [28], which is the dominant mechanism for energy transfer from hot electrons to the lattice.

The rate of electron-phonon scattering is well described with first order time-dependent perturbation theory

$$W = \frac{2\pi}{\hbar} \int |\langle f|H_{ep}|i\rangle|^2 \, \delta\left(E_f - E_i\right) dS_f, \tag{2.25}$$

also know as FERMI*'s Golden Rule*. Here, H_{ep} is the time-dependent perturbation of the one-electron SCHRÖDINGER equation, $|i\rangle$ and $|f\rangle$ are the initial and final states and the integral is performed over all final states S_f. The matrix element for an allowed process is given by

$$|\langle f|H_{ep}|i\rangle|^2 = \frac{\hbar}{2NM'} \frac{C_{\mathbf{q}}^2 I^2\left(\mathbf{k}, \mathbf{k}'\right)}{\omega_{\mathbf{q}}} \left(n\left(\omega_{\mathbf{q}}\right) + 1/2 \mp 1/2\right) \tag{2.26}$$

with $\mathbf{q}$ being the wave vector of the scattered phonon, ω_q the corresponding frequency,

M' the appropriate mass of the oscillator, which is the effective mass $\bar{M}$ of the unit cell for polar mode scattering, and N the number of unit cells of the periodic crystal. $n(\omega_{\mathbf{q}})$ is the phonon occupation of the mode $\mathbf{q}$ and in thermal equilibrium described by the BOSE-EINSTEIN distribution function

$$n(\omega_{\mathbf{q}}) = \frac{1}{e^{\frac{\hbar\omega}{k_B T_{lat}}} - 1}, \tag{2.27}$$

where T_{lat} is the lattice temperature. The minus sign in Eq. 2.26 is taken for absorption and the plus sign for emission of a phonon. $I(\mathbf{k}, \mathbf{k}')$ is the overlap integral of the wave functions of initial and final states over the unit cell and for spheric, non-parabolic bands one obtains $I(\mathbf{k}, \mathbf{k}') = 1$. $C_{\mathbf{q}}^2$ is the coupling parameter, which for polar mode scattering is

$$C_{\mathbf{q}}^2 = \left(\frac{ee^*}{V_0\epsilon_0}\right)^2 \frac{q^2}{\left(q^2 + q_0^2\right)^2}. \tag{2.28}$$

Hereby, V_0 is the unit cell volume, q_0 the reciprocal DEBYE screening length and e^* the effective charge in the atoms which can be expressed as

$$e^{*2} = \epsilon_0 \bar{M} \omega_{LO}^2 V_0 \epsilon_p^{-1} \tag{2.29}$$

in first approximation [31], with

$$\frac{1}{\epsilon_p} := \frac{1}{\epsilon_r(\infty)} - \frac{1}{\epsilon_r(0)} \tag{2.30}$$

and the static and high-frequency permittivitites $\epsilon_r(0)$ and $\epsilon_r(\infty)$.

Integration of Eq. 2.25 with Eq. 2.26 and Eq. 2.28, under careful treatment of the integration boundaries, finally yields

$$W(\mathbf{k}) = \frac{e^2\hbar\omega_{LO}}{2\pi\hbar^2\epsilon_p}\sqrt{\frac{m_{eff}}{2E(k)}}\left[n(\omega_{LO})\sinh^{-1}\left(\frac{E(k)}{\hbar\omega_{LO}}\right)^{1/2} + \right.$$
$$\left. + \left(n(\omega_{LO}) + 1\right)\sinh^{-1}\left(\frac{E(k)}{\hbar\omega_{LO}} - 1\right)^{1/2}\right], \tag{2.31}$$

whereby screening has been neglected. The first term in the brackets represents phonon absorption events and is consequently linearly dependent on the phonon occupation number. The second term denotes phonon emission. The part which is linear in respect to $n(\omega_{LO})$ belongs to stimulated phonon emission events, while the remaining term corresponds to spontaneous phonon emission. Scattering rates for InP, using Eq. 2.31 are plotted in Fig. 2.8, separately for phonon absorption and emission. Note

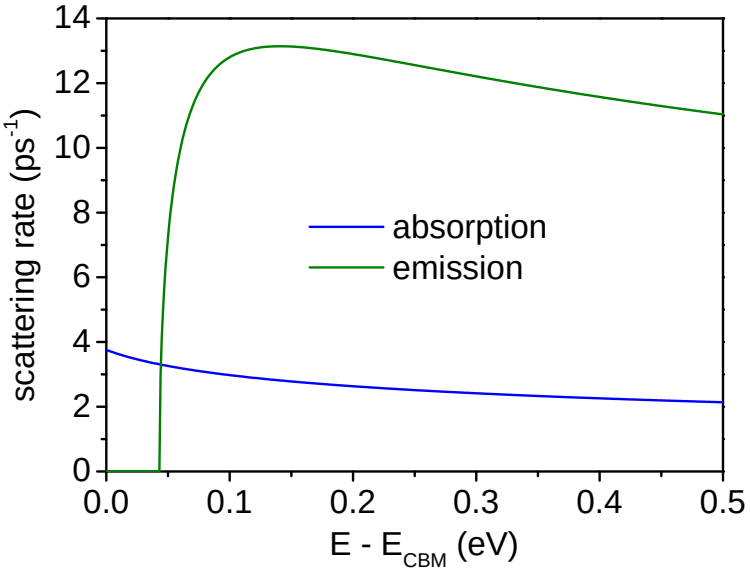

Figure 2.8: Polar mode scattering rates for electrons in dependence of their excess energy, according to Eq. 2.31, using InP parameters from the LANDOLT-BÖRNSTEIN database [32] ($m_{eff} = 0.08\, m_e$; $\hbar\omega_{LO} = 43\,\text{meV}$; $T_l = 300\,\text{K}$; $\epsilon_r\,(\infty) = 9.61\,\epsilon_0$; $\epsilon_r\,(0) = 12.56\,\epsilon_0$; ϵ_0 being the vacuum permittivity).

that this treatment does not take into account the non-parabolicity of the bands, which slightly increases the rates for higher energies [33].

2.3.2 Electron phonon scattering in quantum wells

The following section follows the approach of RIDLEY and RIDDOCH, presented in Refs. [34, 35]. Polar optical mode scattering in semiconductor quantum wells exhibits some remarkable differences to bulk systems. On the one hand, the electron wave functions are considerably different in 2D due to the discretization along the z-direction as shown in Sec. 2.2.1. On the other hand, also the phonon distribution is subject to quantization effects and the spacial distribution of the wave functions must be considered. In general one distinguishes between (i) guided modes in the well or the barrier, (ii) interface modes and (iii) penetrating modes, common to barrier and well [36]. As a first approximation only the quantization of the electron wave functions is regarded, while the phonon distribution is assumed bulk-like, *i.e.* a single band of phonon energy $\hbar\omega_{LO}$. In this case and with the electron wave functions in Eq. 2.17, the matrix element in Eq. 2.25 for polar mode scattering is

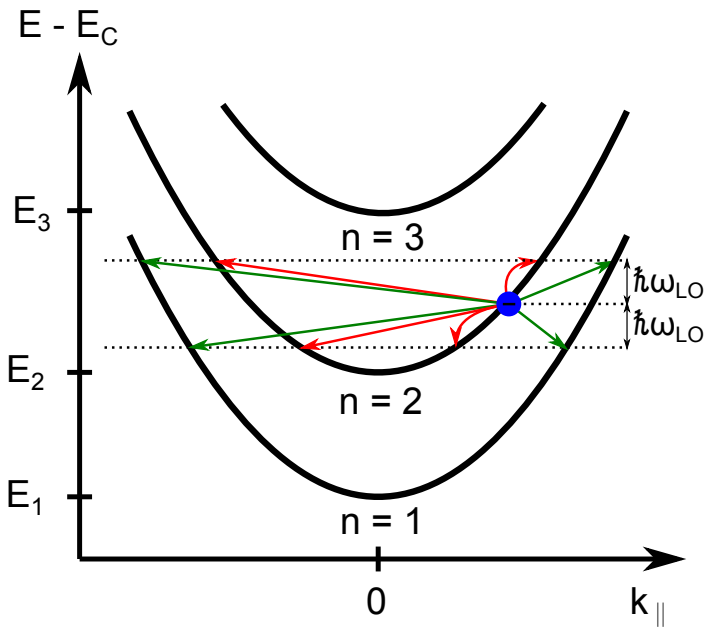

Figure 2.9: Possible final states for an electron that can be reached by absorbing or emitting a single LO phonon. The green arrows correspond to intersubband scattering processes and the red arrows to intraband scattering.

$$|\langle \mathbf{K}'|H_{ep}|\mathbf{K}\rangle|^2 = \frac{e^2\hbar\omega_{LO}}{2\epsilon_p\Omega}\frac{Q^2}{\left(Q^2+q_0^2\right)^2}\delta_{\mathbf{k}',\mathbf{k}\pm\mathbf{q}} \times \\ \times |G(q_z)|^2 \left(n(\omega_{LO}) + 1/2 \mp 1/2\right). \tag{2.32}$$

$\mathbf{K}$ and $\mathbf{K}'$ denote the 3D wave vectors of the electron states before and after the scattering event, respectively. $\mathbf{k}$ and $\mathbf{k}'$ are the corresponding components in the (x, y) plane. Also the 3D phonon wave vector $\mathbf{Q}$ is expressed by an in-plane component $\mathbf{q}$ and q_z. Ω is the phonon cavity volume. All interference effects are contained in

$$G(q_z) = \frac{2}{L}\int_0^L e^{iq_z z}\sin(k_z' z)\sin(k_z z)\,dz. \tag{2.33}$$

One distinguishes between intraband scattering, where the initial and final electron state belongs to the same subband, and intersubband scattering with initial and final electron states belonging to different subbands. The latter process is typically between one and two magnitudes weaker than intraband scattering. This is related to the overlap of the wave functions of the participating states that for intra-subband scattering is always complete but for intersubband scattering is often only partial [15]. Figure 2.9 shows the possible final states for an electron that can be reached by absorbing or emitting a single LO phonon.

Evaluation of Eq. 2.25 with Eq. 2.32 gives the scattering rate between the sub-

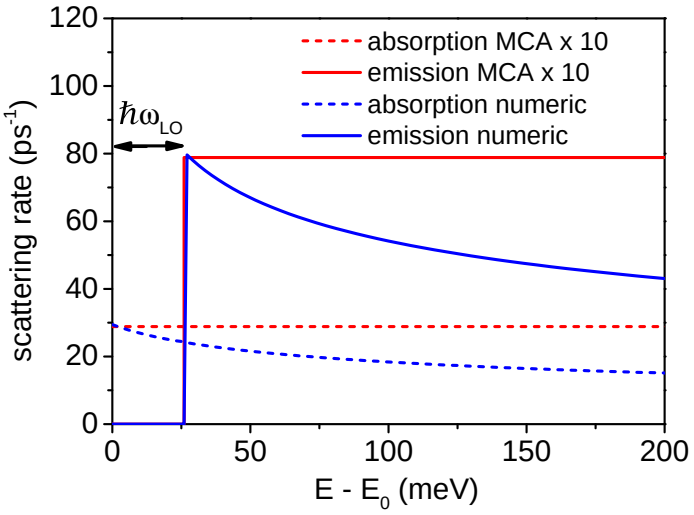

Figure 2.10: Rates for absorption (dashed) and emission (solid) of LO phonons via polar mode intraband scattering in the lowest subband of a CdSe quantum well. The red lines show the MCA results of Eq. 2.36 and the blue lines represent numerical solutions of Eqs. 2.34 and 5.6. The parameters are [16]: $\epsilon_r(\infty) = 6.3\,\epsilon_0$; $\epsilon_r(0) = 9.3\,\epsilon_0$; $m_{eff} = 0.13\,m_e$; $L = 1.5\,\mathrm{nm}$; $\hbar\omega_{LO} = 26\,\mathrm{meV}$; $T_l = 300\,\mathrm{K}$.

bands n and m:

$$W_{nm}(\mathbf{k}) = \frac{e^2\omega_{LO}L}{8\pi\epsilon_p}\left(n(\omega_{LO}) + \tfrac{1}{2} \mp \tfrac{1}{2}\right) \times$$
$$\times \int_0^\infty \int_0^{2\pi} F_{nm}(q)\delta_{\mathbf{k}',\mathbf{k}\pm\mathbf{q}}\delta\left(E_{\mathbf{K}'} - E_{\mathbf{K}} \mp \hbar\omega_{LO}\right) q\,dq\,d\theta \tag{2.34}$$

with the angle θ between $\mathbf{q}$ and $\mathbf{k}$ and

$$\begin{aligned} F_{nm}(q) = &\left\{(1+\delta_{n,m}) \,/\, \left[(m-n)^2\pi^2 + q^2L^2\right] + \right. \\ &\left. + 1/\left[(m+n)^2\pi^2 + q^2L^2\right]\right\}(1-\epsilon) \\ \epsilon = &qL\left(1 \pm e^{-qL}\right) 32\pi^4 m^2 n^2 \left(\left[(m-n)^2\pi^2 + q^2L^2\right] \times \right. \\ &\times \left[(m+n)^2\pi^2 + q^2L^2\right]\left\{(1+\delta_{n,m}) \times \right. \\ &\left.\left. \times \left[(m+n)^2\pi^2 + q^2L^2\right] + \left[(m-n)^2\pi^2 + q^2L^2\right]\right\}\right)^{-1} \end{aligned} \tag{2.35}$$

The upper sign is used when n is odd and m is even or *vice versa*, while the lower sign is used if both expressions are odd or even. This term accounts for the interference effects. Neglecting those and putting $\epsilon = 0$ yields the bulk-like momentum conservation approximation (MCA). Under these circumstances Eq. 2.34 can be evaluated analytically. For intra-subband scattering in the lowest sub-band ($n = m = 1$)

and for $E_0 \ll \hbar\omega_{LO}/4$, this results in

$$W_{\mathbf{K}} \approx \frac{e^2}{2\epsilon_p \hbar L} \left(n(\omega_{LO}) + \tfrac{1}{2} \mp \tfrac{1}{2} \right). \tag{2.36}$$

This term is energy independent, despite of the sudden onset of phonon emission for $E_{\mathbf{K}} = \hbar\omega_{LO}$, as for lower electron energies there would be no final electron states available after phonon emission. However, the MCA is valid only for $k_0 L \geq 4$, where $k_0 = (2m_{eff}\omega_{LO}/\hbar)$ and thus does not hold for very narrow wells. This can be seen in Fig. 2.10, where the scattering rates obtained with the MCA diverge from the numerical results by a factor of ≈ 10.

2.4 Principles of two-photon photoemission spectroscopy

Photoemission spectroscopy (PES) is a common method to study core energy levels and the electronic structure of valance electrons in samples, ranging from metals, over semiconductor to liquid systems: the binding energy of electrons is determined by using photons to promote them above the vacuum level E_{vac} via the photoelectric effect. Thus, they can escape the sample and a detector can be used to measure their kinetic energy that is related to their initial energy. Two-photon photoemission spectroscopy (2PPE) is a particular type of PES. In contrast to the commonly used ultraviolet PES (UPS) and X-ray PES (XPS), 2PPE typically employs photon energies below the ionization energy of the sample. Consequently, the absorption of two or more photons is required for an electron to exceed the vacuum level E_{vac} of the sample. Absorption of the first photon leads to the occupation of originally unoccupied states — *e.g.* conduction band states of a semiconductor — that would be invisible to UPS and XPS. Introducing a variable time delay between both absorption steps (*e.g.* in the form of time-delayed laser pulses) allows furthermore to measure the dynamics of photoexcited electrons. Comprehensive overviews of the basics and applications of 2PPE can be found in Refs. [37, 38]. In our work, laser pulses with durations below 50 fs were employed to achieve the photon densities, required for the two-photon processes. The experiments conducted here can be divided in two principal categories: The non-time-resolved mode (single-beam 2PPE) is used to study the electronic structure of the material, involving occupied and unoccupied states. In the time-resolved mode (tr-2PPE), two pulsed beams with a variable time delay are employed in a pump probe manner to study the dynamics of photoexcited electrons.

2.4.1 Single-beam 2PPE

In this mode only a single pulsed beam with a photon energy of $3.8\,\mathrm{eV} \leq h\nu \leq 5.2\,\mathrm{eV}$ is employed and the signal arises due to electrons that have absorbed two photons within the duration of one pulse. The resulting kinetic energy spectrum contains information of occupied but also of unoccupied states, which is a major benefit compared to PES. This is also the main challenge of the method as the features in the kinetic energy spectra need to be disentangled carefully. All transitions involve an initial state E_{in} (a state, occupied in thermal equilibrium) and a final state E_{fin}, (an unoccupied state above the vacuum level). To reach the final state an electron in the initial state absorbs two photons. This can occur stepwise via an intermediate state E_{im}, *i.e.* a state below the vacuum level that was unoccupied in thermal equilibrium, but also directly via coherent two-photon-absorption [39], involving virtual intermediate states

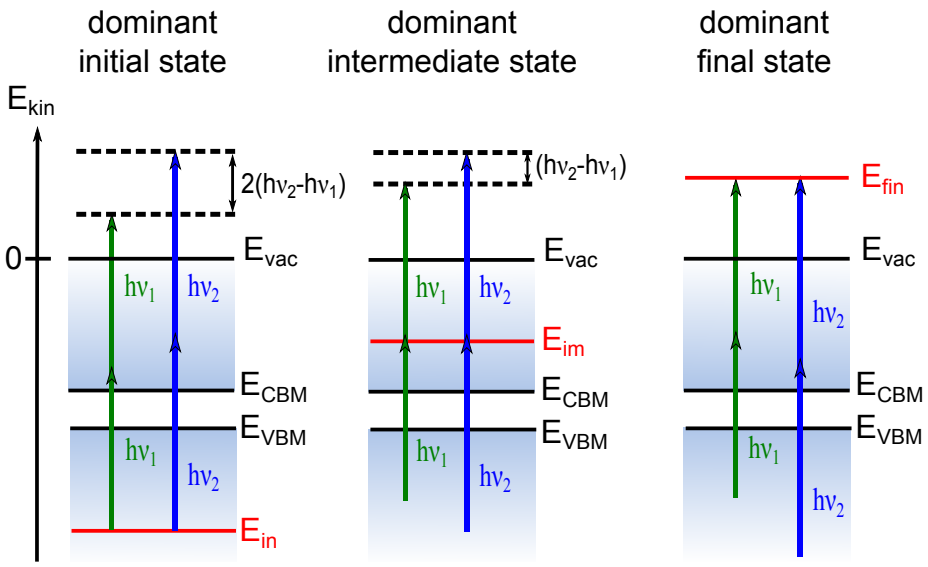

Figure 2.11: Formation of 2PPE spectra for dominant initial, intermediate and final states. The green and blue arrows show the result for two experiments with different photon energy ($h\nu_1 < h\nu_2$) and the effect on the kinetic energy of the photoemitted electrons.

inside the band gap [40–42]. The corresponding 2PPE spectrum contains information of the joint density of states (JDOS) of initial, intermediate and final states, as well as of the corresponding transition matrix elements (see *e.g.* Ref. [43]). The energies of all involved states are separated by the photon energy of the laser beam (assuming that no relaxation takes place between the absorption of the two photons) and

$$E_{kin} = E_{fin} = E_{im} + h\nu = E_{in} + 2h\nu. \tag{2.37}$$

Hereby, E_{kin} denotes the kinetic energy of the photoemitted electrons with respect to the vacuum level of the sample and $h\nu$ is the applied photon energy. In many cases, a certain peak that evolves in a 2PPE spectrum can be related to one specific state. Especially states without dispersion orthogonal to the surface $\left(\frac{dE}{dk_\perp} = 0\right)$, such as surface states, can by identified by measuring the kinetic energy of a certain peak in dependence of the photon energy.[2] This is shown in Fig. 2.11 for the cases of dominant initial, intermediate and final states. It is a major task in single-beam 2PPE experiments to vary the photon energy and identify the dominant states by the

[2]For bulk bands the interband transitions shift typically nonlinearly with the photon energy, due to the complex shape of the bands. Surface states, however, have 2D bands. As only electrons, emitted normal to the surface are measured, these electrons must thus stem from the BZ center and the peaks in the kinetic spectra shift linearly with the photon energy.

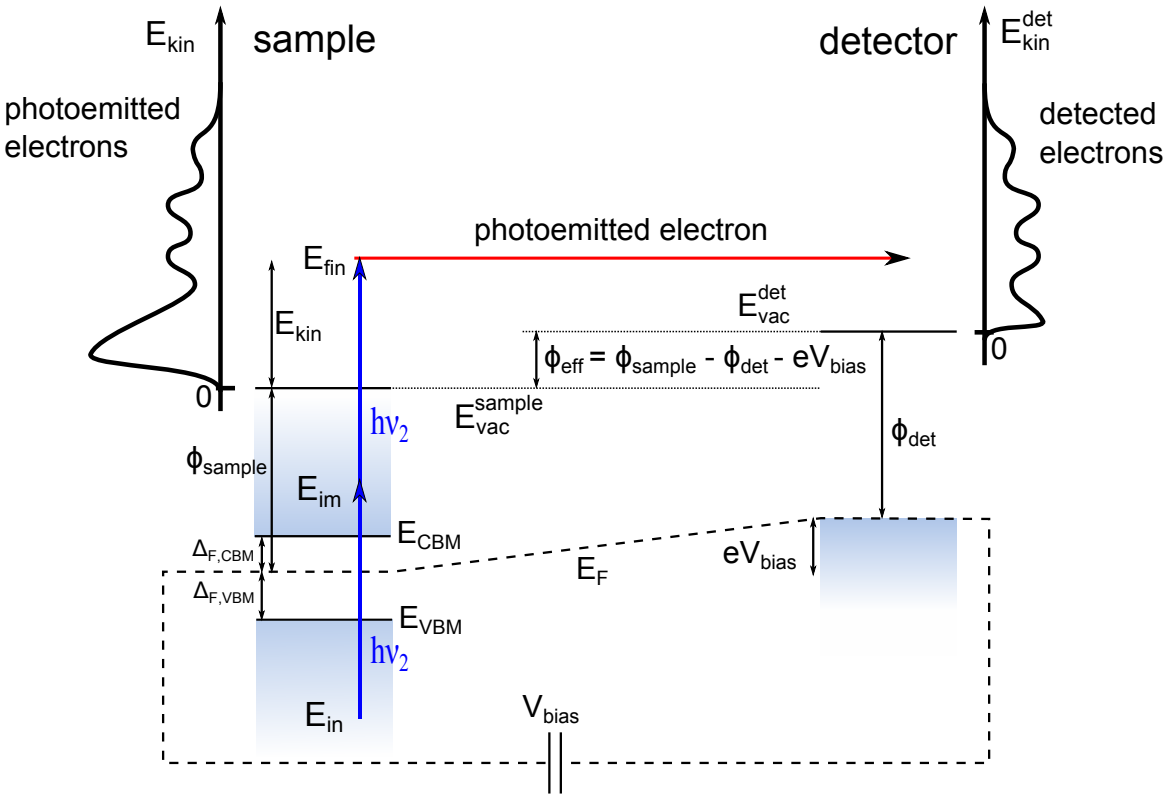

Figure 2.12: Relation between the energies of photoemitted and detected electrons and illustration of the different energy levels and work functions of the sample and the detector.

shift of the peaks in kinetic energy, according to Eq. 2.37.

Furthermore, these states are to be allocated energetically with respect to a fixed energy level of the sample. In Eq. 2.37 this level would be the vacuum level of the sample and in typical PES experiments, usually a "binding energy" is defined with respect to the FERMI level E_F. For semiconductors this is often problematic, since E_F and E_{vac} can vary with respect to the band edges and depend *e.g.* on the doping of the material and the surface termination. If the bulk properties are known, the valence band and conduction band edges E_{VBM} and E_{CBM} are suited better as a reference to compare spectra of related samples. In this case the position of an initial state with respect to the VBM is

$$(E_{in} - E_{VBM}) = E_{kin} - 2\mathrm{h}\nu + \Phi_{sample} + \Delta_{F,VBM}. \tag{2.38}$$

Here, $\Phi_{sample} := E_{vac} - E_F$ is the work function of the sample and $\Delta_{F,VBM} := E_F - E_{VBM}$. These quantities have all been summarized on the left hand side in Fig. 2.12. Analogue, the position of an intermediate state with respect to the CBM

can be determined from the kinetic energy by

$$(E_{im} - E_{CBM}) = E_{kin} - \mathrm{h}\nu + \Phi_{sample} - \Delta_{F,CBM} \tag{2.39}$$

with $\Delta_{F,CBM} := E_{CBM} - E_F$. The expressions $\Delta_{F,CBM}$ and $\Delta_{F,VBM}$ are defined by the doping and the band alignment at the surface and need to be determined separately.

So far, the kinetic energy refers to the vacuum level of the sample. However, the electron detector measures the kinetic energy of the electrons after passing through the difference in electrostatic potential between sample and detector as shown in Fig. 2.12. The relation between the energies of photoemitted and detected electrons is

$$\begin{aligned} E_{kin}^{det} &= E_{kin} + \Phi_{eff} \\ \Phi_{eff} &:= \Phi_{sample} - \Phi_{det} - \mathrm{e}V_{bias}. \end{aligned} \tag{2.40}$$

Here, Φ_{det} is the work function of the detector and V_{bias} is the bias voltage that is applied to detector. A positive V_{bias} is used in order to detect electrons with low kinetic energy, that would otherwise not reach the detector. A negative V_{bias} is employed to repulse a large signal at low kinetic energies, that often occurs from secondary electrons, *i.e.* electrons that have lost parts of their kinetic energy by inelastic scattering. Throughout this work, the kinetic energy always refers to the vacuum level of the specific sample and was calculated according to Eq. 2.40. The electron detection will be discussed in more detail in Sec. 3.2.

2.4.2 Time-resolved 2PPE

For time-resolved 2PPE measurements two pulsed beams are employed an a pump probe like experiment as shown schematically in Fig. 2.13. One of the beams is passed over an electronically controlled delay stage of variable length to generate an adjustable time delay between both pulse trains. The beam with the pulse arriving first at the sample is used to photoexcite charge carriers to intermediate states and therefore also referred to as the pump beam or the pump pulse or simply the *pump*. The photon energy that is chosen depends on the aim of the particular measurement. The other beam that arrives second at the sample promotes the photoexcited electrons above the vacuum level, allowing to measure their kinetic energy and thus determine their intermediate state energy according to Eq. 2.39. This is the so called probe beam or *probe* and the photon energy used here is typically around $\mathrm{h}\nu_{probe} = 4.5\,\mathrm{eV}$. The electron distribution generated by the pump immediately begins to strive for thermal equilibrium and the kinetic energy spectrum thus strongly depends on the time delay between pump and probe. Recording spectra for different pump probe delays accordingly allows to measure the temporal evolution of the photoexcited electron

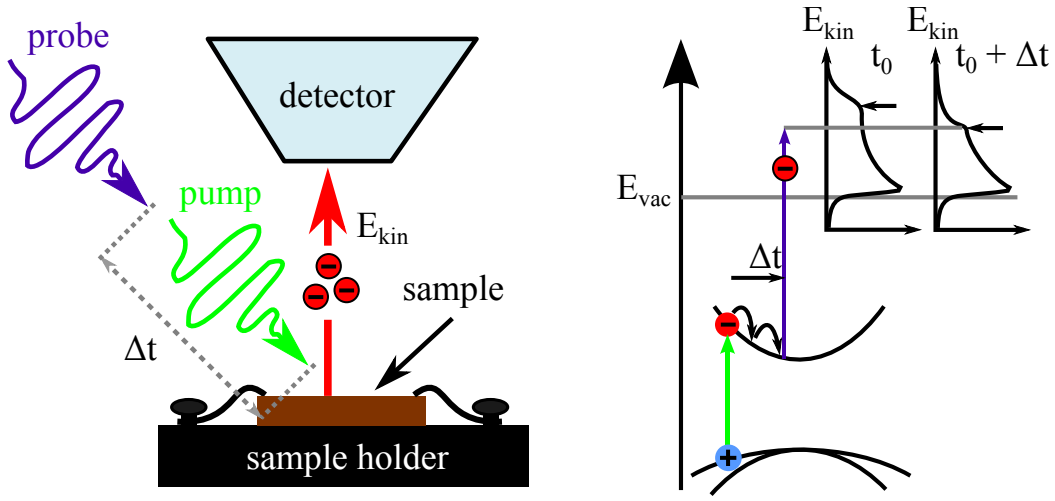

Figure 2.13: Schematic of time-resolved 2PPE. left: View of the sample, with the incoming beams. right: Cooling electrons and transformation of the tr-2PPE spectra for different Δt.

distribution.

2.4.3 Surface sensitivity of 2PPE

The surface sensitivity of 2PPE is determined, on the one hand, by the inelastic mean free electron path. This is the average path that an electron that was photoexcited above the vacuum level can travel, before being scattered inelastically. Such a scattering event leads usually to an energy loss of the electrons. These scattered electrons are known as secondary electrons and form a large background signal, that is most pronounced at low kinetic energies and present in almost every measurement conducted here. For kinetic energies $> 10\,\mathrm{eV}$ the inelastic mean free electron has been investigated for a variety of materials and at $10\,\mathrm{eV}$ it is approximately $1-10\,\mathrm{nm}$ [44]. However, at lower kinetic energies, as experienced here, almost no data is available in literature and this property must be treated with care. Typically, 2PPE groups assume a surface sensitivity of a "few nanometers" [45, 46].

On the other hand, the surface sensitivity is influenced by the absorption length of the employed photons. The probe beam typically has a higher photon energy than the pump beam and thus also a smaller absorption length. For $h\nu_{probe} = 4.5\,\mathrm{eV}$, *e.g.* InP has an absorption length of $\approx 10\,\mathrm{nm}$ [47]. If the absorption length is similar for the pump beam also diffusion needs to be considered. Depending on the mobility of the sample the photoinduced electron density at the surface can drop by 50% easily within hundreds of femtoseconds.

3 Experimental

This chapter shall provide a description of the most important measurement techniques used in thesis. The predominantly applied method is two-photon photoemission spectroscopy and at first the interconnected laser system that provides the pulses for these measurements is explained. Hereby, the focus is on the devices that are used to generate the different wavelength ranges required for (tr)-2PPE. This is followed by a description of the actual measurement setup including the ultra-high-vacuum environment and the electron detection. Finally reflectance anisotropy spectroscopy is explained. This technique was used as a complementary method to study the surface electronic structure of GaP(100) surfaces.

3.1 Laser system

A regenerative amplified laser system manufactured by *Coherent* is used to generate the required fundamental laser pulses. The whole setup, including frequency conversion elements and prism compressors is sketched in Fig. 3.1. A *Mira* Ti:Sapphire oscillator, pumped with a *Verdi5* continuous wave (cw) laser, generates pulses with a repetition rate of 76 MHz, a central wavelength of ≈ 800 nm and pulse energies of 13 nJ. A grating-based compressor/expander unit is used to extend the duration of these laser pulses to ensure a damage-free amplification in a *RegA9050* regenerative amplifier that is pumped with a *Verdi12* laser. Here, single laser pulses from the oscillator are coupled into a cavity with another Ti:Sapphire crystal and after several round trips released with an amplified pulse energy of $\approx 10\,\mu$J at a repetition rate of 150 kHz. These pulse are passed again through the compressor/expander unit, this time to be compressed for the subsequent non-linear processes, and finally have a pulse energy of $\approx 6.7\,\mu$J and a half width of ≈ 50 fs.

The actual 2PPE experiments require wavelengths in the optical range (VIS) for pumping of the semiconductor samples but also ultraviolet (UV) light to photoemit electrons. Therefore, it is necessary to convert the fundamental wavelength of 800 nm. In a first stage, this is done with two home-made non-collinear optical parametric amplifiers (NOPA), operating simultaneously [48] as shown in Fig. 3.1. Approximately 90% of the beam is passed into NOPA 1. Here ≈ 100 mW are split off and focused into a 3 mm sapphire plate, generating a white light continuum (WLC), ranging from

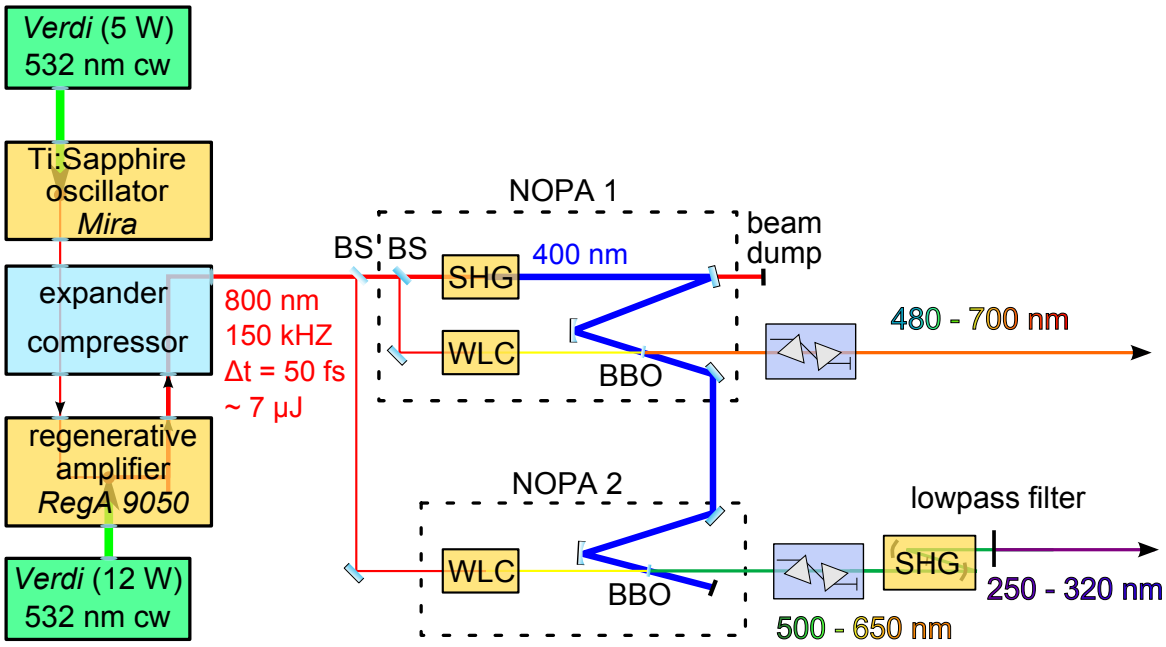

Figure 3.1: Laser setup, including frequency conversion elements and prism compressors. BS denote beam splitters. Beam path lengths as shown are arbitrary.

$\approx 460 - 1000\,\mathrm{nm}$.[1] The main part of the beam, instead is focused into a β-barium borate (BBO) crystal for second harmonic generation (SHG). This results in a 400 nm beam of $\approx 100\,\mathrm{mW}$ power. Now, a certain spectral part of the WLC is amplified via the actual parametric amplification process [42]. This done by focusing both beams into another another 2 mm thick BBO crystal and ensuring spatial and temporal overlap of the pulses. If the angle of the birefringent crystal is adjusted appropriately, phase matching between both beams is achieved and energy is transferred from the 400 nm beam to the WLC.

As the WLC has a large negative chirp, only a specific wavelength interval can overlap temporally with the 400 nm pulse. Also, phase matching can only be achieved for a certain wavelength range. By tilting the crystal angle and varying the time delay between the 400 nm beam and the WLC, the amplified wavelength region can be tuned over a range from 480 nm to 700 nm with a resulting pulse energy from 100 nJ to 330 nJ, depending on the selected peak wavelength. It should also be noted that the WLC and the 400 nm beam are overlapped non-collinearly. That way, not only the phase velocity- but also the group velocity vector components in the WLC propagation direction are matched for both beams. This greatly reduces the temporal walk-off and allows to use thick crystals. The benefits are a very efficient amplification

[1] This is achieved via the non-linear optical *Kerr* effect and is known as self-phase modulation and described *e.g.* in Ref. [42].

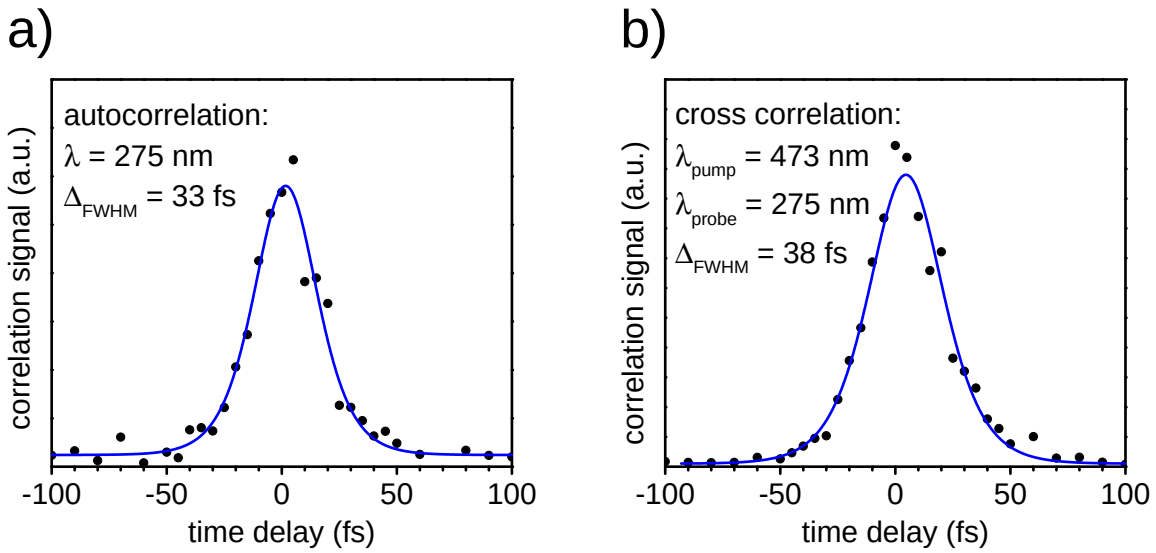

Figure 3.2: (a) Autocorrelation of $\lambda = 275\,\mathrm{nm}$ pulses. (b) Crosscorrelation of $\lambda = 275\,\mathrm{nm}$ pulses and $\lambda = 473\,\mathrm{nm}$ pulses. Both curves have been fitted with a sech^2 profile. The deduced pulse widths are $\Delta_{275\,\mathrm{nm}} = 21\,\mathrm{fs}$ and $\Delta_{473\,\mathrm{nm}} = 29\,\mathrm{fs}$.

process and broad ($> 30\,\mathrm{nm}$) output spectra. Thus, very short laser pulses can be achieved by subsequent pulse compression.

To generate the UV light for the probe beam, usually the output of NOPA 2 is passed through another SHG which is build with a $75\,\mu\mathrm{m}$ thick BBO and concave mirrors instead of lenses to minimize the *chirp* generated due to group velocity dispersion (GVD). The fundamental is separated with an appropriate shortpass filter and the resulting UV pulses have a center wavelength between 250 and 320 nm and pulse energies of ≈ 2 to $\approx 7\,\mathrm{nJ}$. For experiments requiring high photon energies ($> 4.8\,\mathrm{eV}$), instead the output of NOPA 1 is frequency doubled.

To minimize the duration of the laser pulses, the output beams of both NOPAs are passed through two separate prism compressor lines. Hereby, the "red" fraction of the pulse spectrum is passed through the thicker part of the prism and travels an effective longer optical path, compared to the "blue" fraction of the spectrum. This compensates or precompensates the positive *chirp* that accumulates when the beam passes several optical elements since here, due to the GVD, the "blue" part of the spectrum is slower than the "red" part. The achieved pulse durations are directly checked and optimized within the 2PPE setup by exploiting coherent two-photon-photoemission on a Cu(111) single crystal [39]. This crystal is prepared beforehand by several sputtering and heating cycles in the according chamber of the UHV setup (see Fig. 3.3). Exemplary crosscorrelation and autocorrelation traces are shown in Fig. 3.2 and have been fitted with a "sech^2" profile, which is typical for ultra-short

pulses from mode-locked lasers. The pulse durations are derived by dividing the experimental full width at half maximum (FWHM) by a factor of ≈ 1.54, resulting in a duration of 21 fs and 29 fs for the UV, respectively, the VIS pulse. The pulse shapes vary between the experiments and depend highly on the wavelength and the state of the whole setup and sometimes GAUSS profiles have been found to describe the traces better.

3.2 2PPE setup

Beam management

As explained in Sec. 2.4, the 2PPE experiments are conducted in different modes. This requires switchable beam paths as depicted in Fig. 3.3. The frequency doubled output of NOPA 2 (the UV beam) is split after the SHG. One part forms the probe beam and is passed through a delay stage, that can be electronically controlled with a resolution of $\approx 1\,\mu$m, respectively, ≈ 5 fs. Thus, a time delay between pump and probe pulse can be achieved. The maximum time delay of ≈ 70 ps is limited by the travel range of the stage, which is ≈ 10 mm. The other part of the UV beam travels a path of equal length and acts as pump beam for measurements with high excitation energy. To ensure that the GVD of both beams can be precompensated simultaneously, a quartz plate (chirper) is inserted in the probe beam path that has the same thickness as the beam splitter. For the tr-2PPE measurements with VIS excitation, the beam from NOPA 1 is used as pump instead of the second UV beam. For the single-beam experiments both pump beams are blocked.

All utilized beams are eventually focused with a concave mirror onto the sample inside the vacuum chamber. The angle of incidence is typically 45°. However, by tilting the sample with respect to the spectrometer a certain angle resolution can be achieved as shown in Fig. 3.3. All beams are p-polarized when hitting the sample, unless an additional $\lambda/2$ wave plate is employed.

Ultra high vacuum chambers

The 2PPE experiments must be performed in ultra high vacuum (UHV) in order to detect the photoemitted electrons. This enables furthermore to investigate contamination-free samples *e.g.* grown via MOVPE (see also Sec. 5.1.4). The UHV system, consisting of multiple chambers, is shown in Fig. 3.3 on the right hand side. The samples were inserted first into an interim chamber either via a special UHV shuttle or a transfer rod attached to a small container that could also be evacuated or filled with nitrogen, to avoid air-exposure of the samples. The interim chamber was evacuated afterwards,

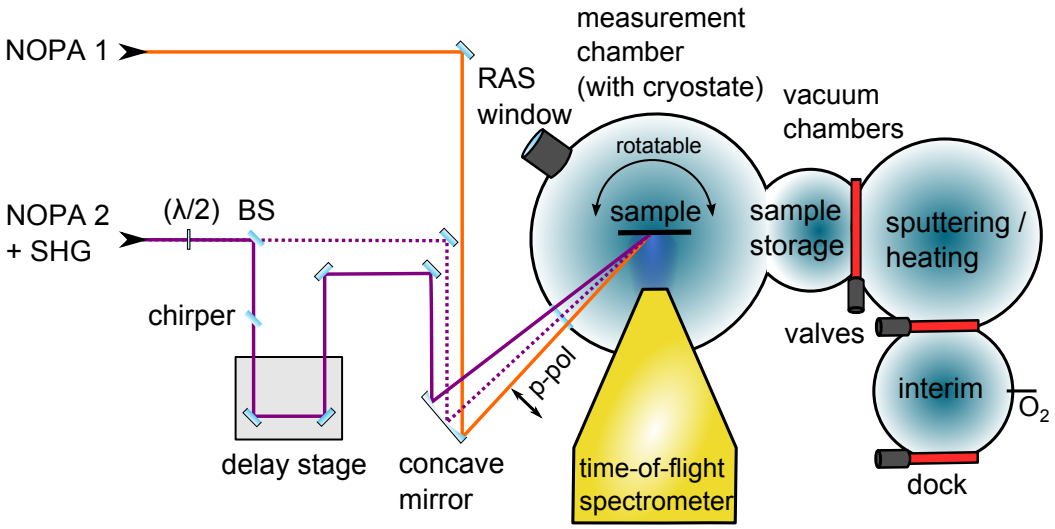

Figure 3.3: 2PPE setup, showing the last part of the laser paths and the vacuum chambers with the time-of-flight spectrometer. The dashed violet- and the orange paths are the optional pump beams.

allowing to transfer the samples to the main chambers. Via a valve, also gases could be introduced and the samples could *e.g.* be exposed to oxygen to quench their surface states. In the actual measurement chamber, the sample was locked in a cryostat that could be filled with helium for low-temperature measurements. This chamber contained also a storage for up to four samples and a low-strain window for RAS measurements under similar conditions. The base pressure of the main chambers was typically around $\approx 5 \times 10^{10}$mbar.

Electron detection

The kinetic energy of the photoemitted electrons is determined from the electrons' time-of-flight (TOF) *i.e.* the time between the laser pulse hitting the sample (*start* event) and the electrons arriving at the detector (*stop* events). The TOF spectrometer was built in this institute and has a length of 313 mm between entrance aperture and the cathode, which leads to an acceptance angle of $\pm 7.3°$. Drift-tube and cathode grid are covered with carbon to ensure a homogeneous potential inside the TOF spectrometer. Behind the cathode is a set of two multi-channel plates (MCP), twisted by an angle 90° with respect to each other, followed by a planar anode. The total potential difference between anode and cathode is 2.8 kV. At the anode, the electron cascade is collected and afterwards coupled out electrically with a capacitor [49]. Thus, for each detected electron a measurable electrical pulse is generated that can be inserted in the appropriate counting device. A bias potential could be applied to the spectrometer, which is electronically isolated from the vacuum chamber to

accelerate or decelerate photoemitted electrons (see Sec. 2.4).

The electronic signals from the TOF spectrometer form the *stop* and are recorded by a multiscaler card of the *FAST ComTec* company with a time signature with respect to the corresponding *start* event.[2] The card allows to record events with a time resolution of 250 ps and also multiple *stop* events per *start* event. Thus, it is not necessary to reduce the *stop* event rate artificially in order to prevent the suppression of low energetic electrons. The typical count rate in the conducted experiments was below 10 kHz. The *start* event signal stems from a photodiode that picked up a small fraction of light from the laser.

The conversion of flight time to kinetic energy is conducted in first approximation by neglecting the acceleration or deceleration that happens between the sample surface and the TOF aperture. Instead it is assumed that the electron has reached its final drift velocity immediately after the photoemission process. Then

$$E_{kin}^{det} = \frac{m_e}{2} v^2 \tag{3.1}$$

$$v = \frac{s}{t_{drift}} \tag{3.2}$$

with the electron velocity v and the distance s between sample and cathode. Hereby, s includes not only the drift tube length but also the distance between aperture and sample which is usually 3 mm in the conducted experiments. The total drift time t_{drift} depends on the difference between *start* and *stop* events Δt and

$$t_{drift} = \Delta t - t_0. \tag{3.3}$$

t_0 is an offset due to the different electrical and optical paths of the *start* and *stop* signals. Determination of t_0 is done via UV light, scattered to the MCPs. This leads to a signal, which basically represents simultaneous incidence of the pulse on the sample and detection of the photons ($t_{drift} \approx 0$).

Determination of the kinetic energy of the photoemitted electrons with respect to the sample vacuum level (cf. Sec. 2.4) is done under consideration of Eq. 2.40

$$E_{kin} = \frac{m_e}{2} \left(\frac{s}{\Delta t - t_0} \right)^2 - \Phi_{eff}. \tag{3.4}$$

To account for the acceleration/deceleration between sample and TOF aperture for $\Phi_{eff} \neq 0$, numerical calculations are necessary. The difference compared to the "constant velocity approximation" is small for low applied bias voltages. However, for

[2] Beforehand they are passed through a preamplifier and are subject to pulse shaping with a constant fraction discriminator.

all experiments performed in this work this has been considered. A more detailed treatment of this topic can be found *e.g.* in Refs. [50–52]. The influence of the acceleration/deceleration can also be used to determine the work function of the detector, if the sample work function is known. This was done here, with a Cu(111) sample, which is known to have a work function of $\Phi = 4.85\,\mathrm{eV}$ [53], resulting in $\Phi_{det} = 4.5\,\mathrm{eV}$, in agreement with previous measurements [49].

Energy resolution

The energy resolution of 2PPE experiments is subject to several different influences. First there is the resolution of the detector. For the actual setup the secondary electron edge of a Cu(111) crystal could be resolved with a resolution of $\approx 50\,\mathrm{meV}$. As this signal is independent of the photoexciting laser pulses, we correlate this directly with the detector resolution. Second, the electrons are photoexcited and -emitted directly by the laser pulses that have a spectral width of $\approx 100\,\mathrm{meV}$ and cannot be substantially further compressed, since otherwise the time-resolution reduces due to the FOURIER limit. Convolution of the pulse widths with the detector resolution results in an overall resolution of $\approx 150\,\mathrm{meV}$ which is in fact, the narrowest line width that could be observed for two-photon absorption from an occupied surface state at the Cu(111) surface with the current setup.

3.3 Reflectance anisotropy spectroscopy (RAS)

Reflectance anisotropy spectroscopy is an optical method. A broad visible polarized spectrum from a xenon lamp falls under (almost) normal incidence onto a sample and the reflected light is measured and analyzed. The rather simple setup described *e.g.* in Ref. [54] is one aspect that makes RAS very favorable for the damage-free *in-situ* characterization of epitaxial growth processes *e.g.* via MOVPE [55–57]. The second main aspect is that the RAS signal correlates with the anisotropy of a surface and a high anisotropy typically indicates a well-reconstructed surface. This approach especially applies for crystals that have a cubic lattice and thus no bulk anisotropy. RAS is very sensitive to optical dipole transitions at the surface. Therefore, it can also be employed as an indirect method to determine the surface electronic structure, which is the most interesting point for this thesis. The RAS signal is defined as

$$\frac{\Delta r}{r} = 2\frac{r_x - r_y}{r_x + r_y} \tag{3.5}$$

with $r_{x,y}$ being two orthogonal components of the complex reflectivity (known, from the FRESNEL equations) that are parallel to the surface plane. An actual assignation

of features in RA spectra to surface-state related transition is not straightforward. This can be shown with a very simplified model that assumes that the surface is a thin finite layer that is sandwiched between a semifinite crystal and the vacuum. Details of this approach are described *e.g.* in Ref. [54]. Then

$$\frac{\Delta r}{r} = \frac{4\pi i d}{\lambda} \frac{\Delta \epsilon_s}{\epsilon_b - 1}, \tag{3.6}$$

where λ is the wavelength of the light, d the thickness of the surface layer, ϵ_b the dielectric function of the bulk and $\Delta\epsilon_s := \epsilon_s^x - \epsilon_s^y$ the difference between the surface dielectric-function components in the x and y directions. This shows that the signal arises by a complicated interplay between the complex dielectric functions of the bulk and the surface. The RAS signal itself is also a complex quantity and in this thesis always the real part is analyzed. Peaks in RA spectra, thus do not necessarily coincide exactly with the transition energies. A common approach to employ RAS for the investigation of surface states therefore uses DFT theory to calculate the surface electronic structure and the corresponding dielectric function. The results are used to simulate the RA spectra, which are then compared to experimental data [58, 59].

4 Electron dynamics in nanostructures

In this chapter the dynamics of hot carriers in CdSe nanostructures are investigated to determine the influence of the sample geometry on the electron relaxation. At first, an introduction to CdSe quantum dots and nanoplatelets is given, which are the material systems that were studied. The main characteristics are presented and the preparation of the samples is described. This is followed by studies with tr-2PPE on the carrier dynamics in CdSe quantum dots with a focus on the effect of hole-scavenging ligands on the electron relaxation. In the next section, measurements on CdSe nanoplatelets are presented, investigating the underlying mechanism of electron relaxation in these novel materials. Finally, the results for quantum dots and nanoplatelets are compared. Parts of this chapter have been reprinted in part, with permission from Nano Lett. 13, 1655 [60],

4.1 Introduction to CdSe quantum dots and nanoplatelets

Nanostructured semiconductors can be prepared with a variety of methods and in plenty different shapes. Amongst those, spherical quantum dots are probably the most prominent type. Since the variety of different possible shapes and sizes leads to confinement in either 1, 2 or 3 dimensions, these materials are perfect model systems to study the influence of the geometry of low-dimensional nanostructures on the relaxation of hot carriers. In the upcoming sections, the focus lies on 0-dimensional CdSe QDs and 2-dimensional nanoplatelets (NPs), which both have been prepared via chemical synthesis in solution. Furthermore, wet-chemical synthesis allows for growing a CdS shell around the colloids and/or to vary the surrounding capping molecules. Thus the properties of the surface/interface can be manipulated in different ways to study its effect on the charge carrier dynamics.

4.1.1 Carrier dynamics and relevance for photovoltaics

Due to the changeability of the band gap by simple size variation, semiconductor quantum dots are promising candidates for photovoltaics. Another consequence of the confinement are the large energy spacings at the bottom of the CB, which exceed typical phonon energies, creating a theoretical phonon bottleneck [9]. Such slowed

down relaxation dynamics can be exploited in third generation PV, based on hot electrons as intermediate band solar cells [4] and hot-carrier cells [62]. Measurements on the carrier dynamics revealed that the relaxation is fast, nevertheless. This was ascribed to an AUGER-like process, where the electron relaxes to the CBM by donating its excess energy to the hole [63–65], followed by much faster relaxation of the hole via the dense spectrum of VB states. For quantum wells and thus nanoplatelets, the DOS is continuous so that in principle relaxation via phonons is always possible. However, electrons in higher lying subbands need to scatter to lower subbands via phonons in order to reach the CBM. Transitions between subbands with large energy spacing require phonons with high wave vectors. As the wave function overlap between states of different subbands in only partial (cf. Sec. 2.3) and the FRÖHLICH scattering probability goes with $1/q^2$ (cf. Eq. 2.28), higher lifetimes in the upper subbands might be possible. Attention in terms of PV was also received by QDs, due to high probability of multiple exciton generation (MEG). This was first observed for PbSe quantum dots in 2004 [66], but later also for QDs of other compositions, including CdSe [67]. In a solar cell, MEG could lead to quantum efficiencies beyond 100%, allowing to exceed the SHOCKELY-QUEISSER-limit.

4.1.2 CdSe quantum dots and quantum dot solids

Wet chemical production in solution allows to achieve high-quality QDs in an easy and cheap way compared to expensive and elaborate epitaxial methods. That way, QD dispersions with diameters ranging from ≈ 2 to 20 nm can be obtained [21, 68] with a standard deviation of $< 5\%$ for the size distribution [69]. CdSe QDs can be fabricated with a zinc blende and wurtzite phase that have comparable electronic and optical properties and size dependence [70]. This is explained with the similarity in bulk electronic properties for both phases (*e.g.* band gap ≈ 1.74 eV [16]). The measurements, conducted in this thesis have all been performed on QDs of the wurtzite phase. These are well established and extensive previous studies supply a fundamental framework for the complex experiments conducted here. Aside from optical and electronic properties that can be controlled via the QD size, as described in Sec. 2.2.2, also the possibility to form QD solids is one of the main motivations to push further research in this field. A QD solid is basically a periodic lattice, formed of QDs that are aligned in a regular 3-dimensional pattern. For small distances between neighboring QDs, minibands form from the confined states and significantly enhance the transport properties of the meta-material [68]. This opens the door to a variety of different optoelectronic applications, including light emitting diodes (LEDs) and solar cells [68, 71]. For the latter, different approaches have been suggested like QD sensitized solar cells or hybrid solar cells in conjunction with polymers but also conventional pn-junction

cells, consisting of stacked p- and n-type QD solids [72].

Quantum dot synthesis

All quantum dots and nanoplatelets investigated in this thesis were prepared by the *Condensed Matter and Interfaces* group of the *Debye Institute for Nanomaterials Science* at the *University of Utrecht*. The wet-chemical synthesis of CdSe QDs was based on the hot-injection method developed by Murray *et al.* [73]. For the specific QDs in this thesis the modifications of Peng *et al.* [74] and Mello Donegá *et al.* [75] were implemented. The synthesis took place under nitrogen atmosphere in a glove box. In the first step the two precursors are prepared. For the cadmium precursor, 0.64 g of cadmium acetate, 3.68 g of oleic acid and 25.92 g of octadecene (ODE) are mixed and heated under vacuum until the water in the ODE and the acetate evaporated and cadmium oleate is formed. The concentration of the cadmium oleate was 0.075 M. For the Se precursor, 1.417 g of selenium and 7.5 g of trioctylphosphine (TOP) were mixed.

Afterwards 11.9 g of ODE were added to dilute the mixture to 0.74 M. 5.2 g of the Se precursor, 1.11 g of trioctylphosphine-oxide and 3.2 g of octadecylamine were mixed in a flask and heated up to 300° C. The heating mantle was removed and 4.9 g of the Cd precursor were injected, followed by rapid nucleation. During the injection the temperature of the reaction mixture dropped and was raised again to the growth temperature of 280° C. Subsequently, growth was allowed for several minutes until the desired QD size was achieved. By adding a mixture of hexane and methanol the CdSe QDs with their ligand oleic acid (OA) were seperated from the organic rest and afterwards washed with acetone and put into a centrifuge for several minutes. The precipitated QDs were dissolved in toluene.

4.1.3 CdSe nanoplatelets

CdSe nanoplatelets are two-dimensional crystals with thicknesses of only a few monolayers, leading to confined electronic states. For this material, these objects, also known as nanoribbon, nanosheets or nanodisks have been first reported in 2006 by Joo *et al.* [76] in the wurtzite crystal phase and by Ithurria *et al.* in 2008 in the zinc blende crystal phase [77]. For this thesis, all experiments were conducted on zinc blende NPs, which therefore are treated exclusively in the following paragraphs. Here, the top and bottom facets are perpendicular to the [100]-direction [78–80] with lateral dimensions up to 700 nm [81].

Eye-catching — in contrast to the well-established quantum wells grown with molecular beam epitaxy (MBE) and MOVPE — is the extreme thinness of the platelets, down to two monolayers [82] and the corresponding confinement energies

of more than 1 eV [83]. Hereby, one monolayer refers to one layer of Cd atoms and one layer of Se atoms. Recent investigations have shown, however, that both sides of the platelet are terminated with a Cd layer [84]. Consequently 2 monolayers can be more realistically interpreted as 2 1/2 ML and so on. This has lead to some confusion in determining the thickness in different publications [82–84]. Here it was decided to assign nanoplatelets with a first absorption peak at ≈ 4.64 eV to a thickness of 3 ML, according to Ref. [82] (although 3 1/2 ML would probably be more correct).

Another remarkable property of the CdSe nanoplatelets is the good thickness control [77] and atomically flat preparation that has been verified with photoluminescence on NP ensembles, showing extremely narrow linewidths (≈ 40 meV at 300 K) that are comparable to the emission of single NPs [85]. In these studies also radiative life times < 300 ps at 20 K were measured with associated quantum yields of 50% at RT, up to almost 100% at cryogenic temperatures, for NPs mantled with an appropriate shell [86]. These properties make NPs interesting for opto-electronic devices like narrow emission LEDs [87] and lasing applications [88–90].

Nanoplatelet synthesis

The nanoplatelets synthesis was conducted under similar condition as the quantum dot preparation. The recipe for the CdSe (3 ML) platelets (absorption peak at 464 nm) is based on a paper by Ithurria *et al.* [80]. 240 mg cadmium acetate, 286 μL OA and 15 mL ODE were mixed in a threeneck flask and degassed for 1 hour at 80° C. Then after heating the mixture to 170° C under nitrogen flow, 150 μL of TOPSe at 1 M were injected. The reaction was stopped after 45 min and 10 mL of methanol and 30 mL of butanol were added. Afterwards the solution was centrifugated at 3000 rpm for 5 min and after removal of the supernatant dispersed in 30 mL hexane. For the preparation of 5 ML thick platelets (absorption peak at 550 nm), 170 mg $Cd(myr)_2$, 15 mg Se and 15 mL ODE were mixed in a threeneck flask and degassed for 1 hour. Under nitrogen flow the mixture was heated to 240° C and 1.5 mL of 0.1 M SeODE were injected. After 10 s, 80 mg of cadmium acetate were added and after another minute the reaction was stopped and the temperature reduced to room temperature by adding 14 mL hexane. Subsequently, 1 mL of OA was added to the mixture. Afterwards the solution was centrifuged at 5000 rpm to separate the NPs emitting at 550 nm from thinner NPs and QDs.

The CdS shells were grown around the platelets by the layer-by-layer method described by Mahler *et al.* [91]. At first, 1.2 mL of nanoplatelet solution were mixed with 1.2 mL hexane and 50 μL of bis-trimethylsilylated TMS_2S in a vial and stirred for 60 min. Afterwards the solution was washed with 1.5 mL ethanol and centrifugated at 3000 rpm. The supernatant was removed and 5 mL of hexane and 20 mg of the Cd precursor $Cd(OAc)_2(H_2O)_2$ were added and the solution was sonicated for 10 min.

3 mL of ethanol were added to the mixture and after another centrifugation step the solution was dispersed in hexane.

4.1.4 Influence of the ligand and the shell

Ligands

Ligands play a significant role in the colloidal stability of the nanoparticles. Furthermore, the ligands passivate dangling bonds, which are known to otherwise cause midgap states, that are *e.g.* responsible to the blinking phenomena, observed in NPs [84]. For the platelet growth they play an even more crucial rule as they couple to Cd bonds at the (100) surfaces [84] and thus prevent further growth in these directions, thus leading to lateral growth of the CdSe seeds [80] and the formation of 2D objects. For QDs the passivation is required to achieve high fluorescence yields, as Cd dangling bonds act as electron traps [92] and the Se dangling bonds tend to trap the photogenerated holes [93]. Oleic acid (OA) is the surrounding ligand of the QDs and NPs after our synthesis but can be exchanged with other ligands *e.g.* 1,6-hexanedithiol (HDT). Both ligands attach to the cadmium ions as they are positively charged and the oxygen and the sulfur from the oleic acid and the HDT, respectively, are negatively charged. HDT and thiols in general have been shown to act as hole scavengers since the redox potential lies above the VBM [94, 95]. This will be important, when electron relaxation mechanisms are discussed that involve the hole. According to transmission electron microscopy (TEM) studies [92], the spacing between neighboring QDs is $\approx 1.8 \pm 0.2$ nm for (washed) OA capping. For HDT cappings similar studies on PbSe quantum dots revealed a ligand length of ≈ 0.95 nm [96]. In the latter study it was also shown that the mobility of electrons and holes drops exponentially with increasing ligand length, so that the HDT capped samples are expected to have higher mobilities.

CdS shell

CdSe QDs as well as NPs can be mantled with a CdS shell, thus forming a heterostructure. Especially for QDs this has been investigated in great detail, previously. In contrast to organic ligands that cover either the anionic or cationic bonds at the surface, a CdS shell also allows to passivate the Se dangling bond states of the core surface and thus to remove the corresponding hole traps, leading to significant enhancement of the quantum yield [97]. The exact band alignment between CdSe and CdS is ambiguous in literature and seems to depend on the sample geometry as well as on the growth technique and can be either type I or type II [97–100]. However, there is general agreement that for QDs most of the band offset can be ascribed to the

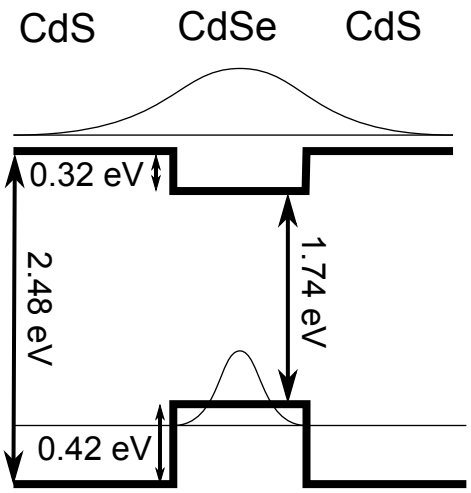

Figure 4.1: Schematic of the band alignment for a CdSe/CdS core/shell QD according to Wei *et al.* [100]. Schematics of the wavefunctions of the highest occupied and lowest unoccupied states are shown.

valence band and the hole wavefunctions are thus confined to the CdSe core, while the electron is delocalized over the CdSe core and the CdS shell. An exemplary sketch of the band alignment is shown in Fig. 4.1. The electron delocalization in any case is related to the strong confinement energy of the electron, which typically exceeds the offset difference. In fact, Peng *et al.* calculated that this description holds for a CBM offset from 0.3 eV (type I) to −0.3 eV (type II) for a dot diameter of 3.7 nm and shells as thick as 1.7 nm [97].

Nanoplatelet core/shell structures were first realized by Mahler *et al.* in 2012 and are still a topic of heavy research [91]. In CdSe/CdS core/shell nanoplatelets, features similar to core/shell QDs have been observed like a red shift of the absorption peaks [91] and a suppression of hole trapping [101]. However, the latter effect is probably less pronounced than for QDs, since both of the large facets are terminated with Cd atoms and Se dangling bonds are thus unlikely. Furthermore, for NPs, the growth of a CdS shell also increases the broadening of the photoluminescence peak, which was related to stronger exciton-phonon coupling in the shell [86] and might thus also have an influence on the dynamics of hot electrons.

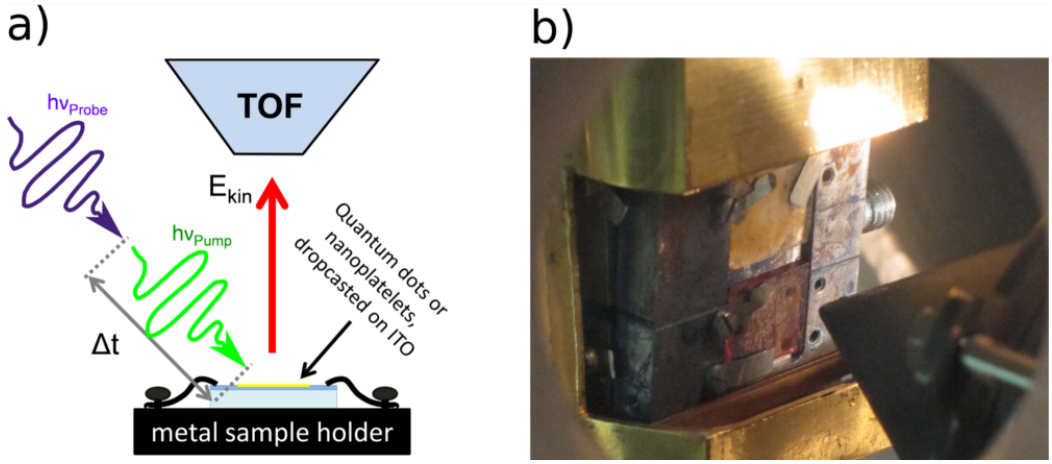

Figure 4.2: (a)Schematic of the sample, mounted on the sample carrier in the 2PPE setup. (b) Two mounted samples in the tr-2PPE setup in front of the TOF-tube.

4.1.5 Sample preparation and transport to UHV

Colloids (either QDs or NPs) with the same ligand as in the solution, namely oleic acid, were brought onto an indium tin oxide (ITO) layer on glass or on highly ordered pyrolytic graphite (HOPG) by either dropcasting or dipcoating. Our results, have shown that no charging occurs at room temperature for both substrates and only for rare cases at low temperatures for ITO. For practical (and financial) reasons, therefore most of the experiments were conducted with ITO substrate. The ligand exchange from oleic acid to HDT was done via dipcoating. Firstly, the substrate was dipped into the colloid solution for 30 s or 1 min, depending on the specimen, and then allowed to dry for several seconds. In the second step the substrate was dipped into the ligand solution, 0.1 M HDT in methanol, for 30 s or 1 min and dried again. Subsequently, for 10 s the substrate was dipped into methanol. This cycle was repeated 20 to 60 times depending on the specimen. These steps were also conducted by the *Utrecht group* within glovebox environment, to prevent oxygenation of the colloids. The substrates with the colloids were sealed in glass vials and brought to the *Helmholtz Zentrum Berlin* and put into another glovebox. Here the samples were unpacked and mounted on steel or molybdenum sample carriers with metal clamps that were positioned on bare ITO spots to ensure electronic contact. The sample carrier was then locked into a nitrogen-filled container that could be transported and attached to the 2PPE UHV chamber. That way it could be ensured that the samples have never been exposed to air during the whole preparation cycle (cf. Sec. 5.1.4). A schematic of the sample carrier including the sample inside the tr-2PPE setup is shown in Fig. 4.2.

4.2 Relaxation of hot electrons in CdSe quantum dots

The decay electrons from the $1P_e$ state to the $1S_e$ state in colloidal CdSe QDs was mostly studied by transient absorption spectroscopy [94, 102, 103] in which the occupation of the $1S_e$ and $1P_e$ states was monitored. For CdSe QDs it was generally observed that the $1P_e \rightarrow 1S_e$ decay, over an energy gap of one to three hundred meV, happens with a time constant in the sub-ps range. This is unexpectedly fast concerning the phonon-bottleneck model that has been proposed for nanometer-sized quantum dots, thus questioning our physical understanding of strongly confined quantum dots [9]. Why the so-called *phonon bottleneck* is not active in preserving hot carriers in QDs with strong confinement has been an issue of extensive research in the last years. Several decay mechanisms that circumvent the phonon bottleneck have been proposed: the two most prominent ones are an AUGER-type energy donation of the hot electron to the valence hole, which afterwards decays back via a denser spectrum of hole states [63–65], or a surface-mediated electron decay via energy transfer to the capping molecules [104]. It was recently shown with CdSe quantum dots that the lifetime of the $1P_e$ state can be enhanced by more than two orders of magnitude by a core-multi-shell architecture [10]. This was rationalized by the fact that in such systems the exciton wave function shows less overlap with the capping or surface states.

Most of the studies have been performed on dispersions of non-interacting QDs. It is, however, of considerable interest to study the fate of hot electrons in a quantum dot solid with an architecture that resembles that in a QD solar cell as close as possible. We have prepared thin films of QDs by drop casting of QD suspensions on a conducting substrate. The decay of the hot $1P_e$ electrons in such a system was measured with tr-2PPE with the pump tuned to resonantly excite hot ($1P_e$, $1P_{3/2}$) excitons in the QD solid. The emitted electrons are replaced by carrier injection from the electric contact, hence mimicking the photocurrent flow in an illuminated solar cell. Only very recently tr-2PPE has been used in the field of quantum dots as a method to study multi-exciton generation on PbSe nanocrystals [105]. Excitons with very high excess energy (several times the band gap) were generated and the subsequent relaxation of the electrons was studied. The dynamics of electrons present in the $1P_e$ and $1S_e$ states could, however, not be resolved. Here, by selectively exciting the $1P_{3/2}1P_e$ dipole transition, we show the feasibility of 2PPE for the study of hot electrons photogenerated in the $1P_e$ state in a QD solid. The energetics and $1P_e \rightarrow 1S_e$ relaxation dynamics were studied in two types of QD solids: systems consisting of oleic acid and 1,6-hexanedithiol capped 4.2 nm sized CdSe QDs, respectively.

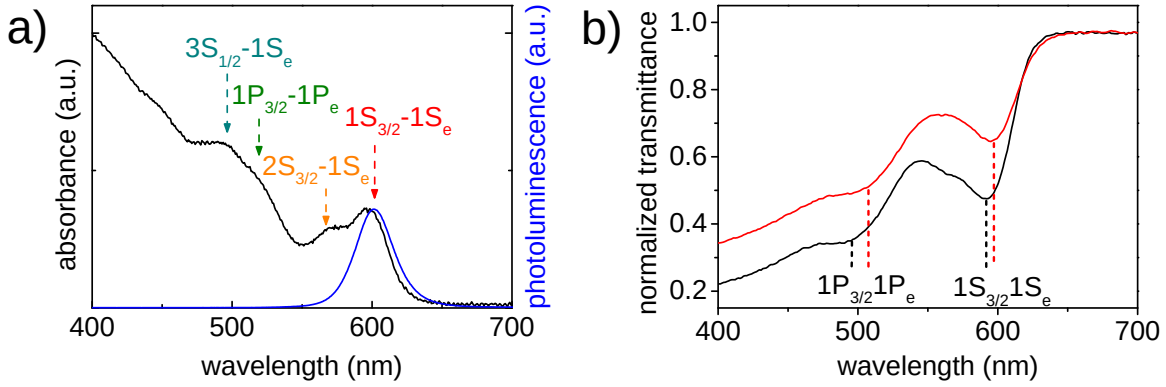

Figure 4.3: (a) Absorption and emission spectra of the CdSe quantum dots in suspension. Interband transitions are labeled following the common nomenclature [21]; (b) Optical transmittance of the CdSe QD solids on an ITO substrate, the black line is for the QDs capped with oleic acid, the red line for the QDs capped with hexanedithiol. The slightly red-shifted optical absorption of HDT-capped QDs indicates successful ligand exchange.

4.2.1 Sample characterization

Absorption and emission measurements are shown in Fig. 4.3(a). The assignment of the transitions to the peaks was done, following Ekimov *et al.* [21] and is explained in more detail in Sec. 2.2.2. These measurements verify the quality of the samples with a size dispersion of 5%, which can also be seen in a TEM image of the investigated QDs that is shown in Fig. 4.4. The absorbance spectrum in Figure 4.3(a) has been measured on QDs in solution and reveals the good quality of the QD solution. Here, also the peaks belonging to different transitions can be clearly distinguished (cf. Fig. 2.6). This yields the appropriate pump energy in the 2PPE measurements that is required to address the $1P_{3/2}1P_e$ and $1S_{3/2}1S_e$ optical transitions. In order to assure an equally good quality for the QD arrays on a substrate, transmittance measurements were conducted that are shown in Fig. 4.3(b). The $1S_{3/2}1S_e$ dip is slightly red-shifted for the HDT-capped QDs in respect to the oleic acid capped QD arrays. This is in agreement with previous reports and most probably related to an extension of the exciton wave function into the ligand [106, 107] and indicates that the ligand exchange was successful [108].

4.2.2 Calculation of the excitation densities

To determine the excitation density, it is necessarily to determine the absorption cross section of the QDs. UV-VIS measurements of 3.7 nm diameter CdSe QDs in solution yield an absorption cross section of $1.3 \times 10^{-15}\,\mathrm{cm}^2$ for the first absorption

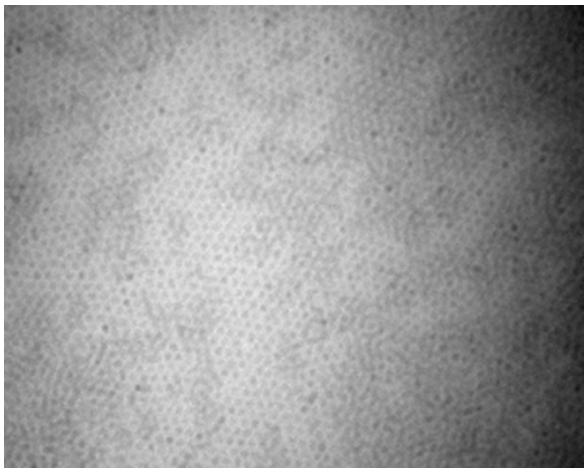

Figure 4.4: TEM image of 4.2 nm sized CdSe QDs in solution.

peak. This is in good agreement with literature values, where cross sections of $< 4 \times 10^{-15}\,\mathrm{cm}^2$ were determined for QDs with a diameter between 2.3 nm and 4.8 nm for wavelengths $> 470\,\mathrm{nm}$ [109]. For a photon flux of $5 \times 10^{13}\,\mathrm{cm}^{-2}$ per pulse, typical for our measurements, this results in excitation density of 0.065 excitons per QD for our data, respectively < 0.2 excitons per QD for the conservative estimation based on the literature data [109]. According to the POISSON distribution this means that less than 10% of the photoexcited QDs will have more than one exciton, so it can be guaranteed that most of the signal stems from QDs with one single exciton.

4.2.3 Tr-2PPE measurements

Figure 4.5(a) shows 2PPE results recorded at 4.2 nm CdSe QDs capped with oleic acid pumped with a photon energy, which is tuned to address the$1P_{3/2}1P_e$ transition. In the transmission spectra shown in Fig. 4.3(b) the dips related to the $1P_{3/2}1P_e$ and $3S_{1/2}1S_e$ cannot be distinguished, thus impeding to selectively address only the $1P_{3/2}1P_e$ transition. To be sure to excite $1P_e$ electrons we tune the peak photon energy of the $\approx 20\,\mathrm{nm}$ broad excitation pulse to the maximum of the broad structure around $\lambda \approx 500\,\mathrm{nm}$, which is due to both transitions. Hence, besides quantum dots with an electron in $1P_e$ state, there will be also quantum dots with an electron in $1S_e$ directly after excitation.

The 2PPE spectra have been recorded at specific time delays between the pump and probe pulse, hence they represent the relaxation dynamics of the electrons that were pumped into the $1P_e$ state. The probe photon energy for these measurements was tuned to $h\nu_{probe} = 4.59\,\mathrm{eV}$. A background correction was done by subtracting a spectrum at negative time delays, with the probe pulse arriving $\approx 10\,\mathrm{ps}$ before the

pump pulse, since in this case no photoinduced signal is expected. This is necessary as the probe beam itself causes a background when it pumps and probes within its own pulse duration, thus exciting higher states in the dot and ligand. This procedure is explained in detail in Appendix C. The big sharp peak at low energies around 0.3 eV is the secondary electron peak stemming from electrons that are inelastically scattered on their way to the surface and subsequently have lost most of their excess energy and barely succeed in leaving the sample. A clear feature can be seen at around 1.75 eV indicating the intensity decrease of the electrons with highest kinetic energy for increasing pulse time delays. Since the kinetic energy of the electrons coming from different states is resolved in the 2PPE spectra a clear distinction can be made between electrons originating from the $1S_e$ and $1P_e$ state: the electrons with the highest kinetic energy can only stem from the $1P_e$ electronic state since the pump energy is adjusted to match the $1P_{3/2}1P_e$ transition and energetically higher lying electron states cannot be reached with the used photon energy.

The temporal and energetic behavior of these $1P_e$ electrons can be distinctly accentuated by subtracting the contribution of any long-living electrons. The latter consists of the $1S_e$ electrons excited directly by the pump pulse, and of already relaxed $1P_e$ electrons. This is done by subtracting the signal that remains for pump-probe time delays longer than 30 ps. Figure 4.5(b) shows the resulting spectra obtained from the data of Fig. 4.5(a). The peak at 1.7 eV stems from electrons emitted from the $1P_e$ states. This peak has a FWHM of ≈ 0.4 eV originating both from the limited resolution of the apparatus and the absolute position of the $1P_e$ states in the sample. Firstly, we have an energy resolution of > 0.15 eV of the 2PPE setup itself (cf. Sec. 3.2). Secondly, partially due to a distribution in size and strong confinement, and partially due to inhomogeneous charging, the absolute energy of the $1P_e$ state in the sample may vary over about hundred meV. Thirdly, electron tunneling spectroscopy in an STM has shown that there is a strong intrinsic broadening of the electron states due to electron-phonon coupling [110]. Finally, we should also consider that — in contrast to a single crystalline sample [111] — QD solids have a rough surface, possibly also with variations of the surface potential that may alter the kinetic energy of the emitted electrons.

The intensity of the $1P_e$ electrons drops significantly with increasing time delays and after 0.6 ps only a small fraction is left that is completely gone after 10 ps. In comparison, for QD solids with HDT-capped CdSe quantum dots, the $1P_e$ peak still shows a significant intensity after 0.6 ps indicating a longer decay time compared to oleic acid capped samples. As a reference experiment, the pump pulse center energy was adjusted to the $1S_{3/2}1S_e$ transition of the HDT capped QDs (Fig. 4.5(d)), which

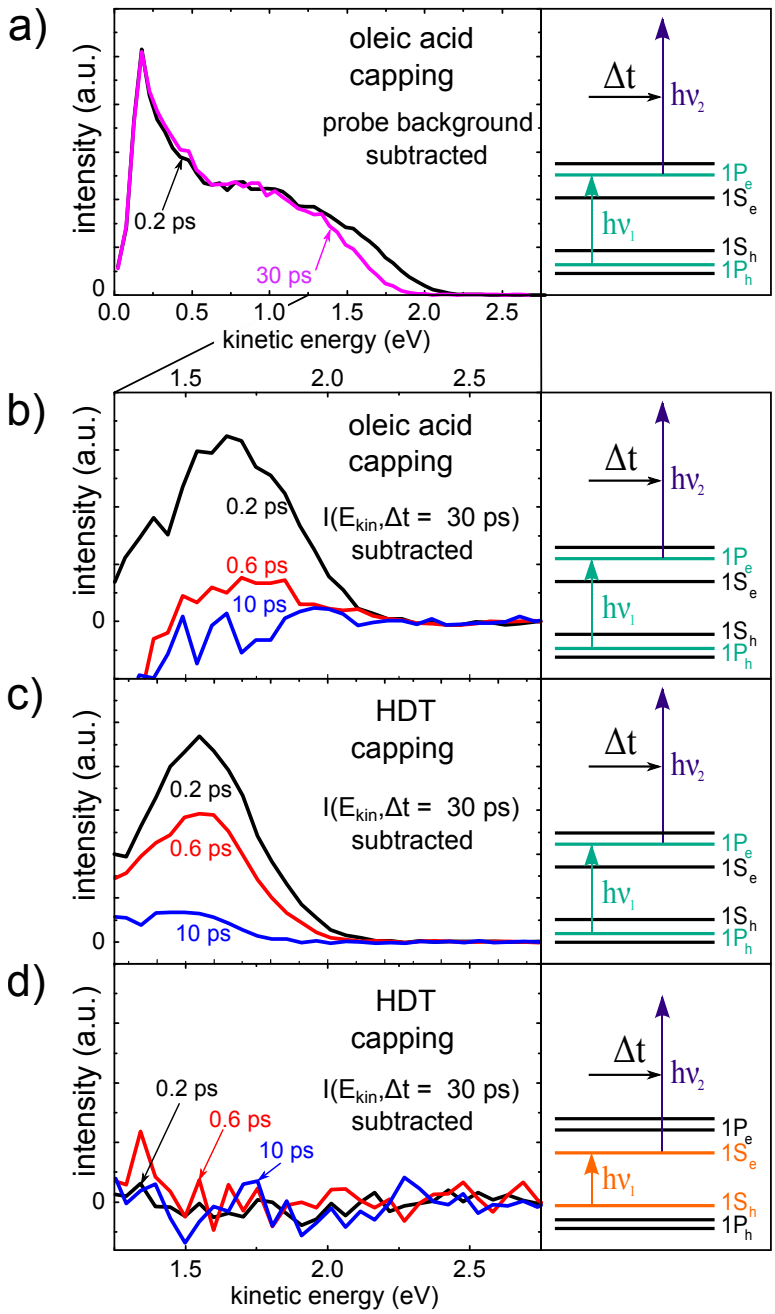

Figure 4.5: Temporal evolution of 2PPE spectra. (a) and (b) show the results for a solid with OA-capped quantum dots for $1P_{3/2}1P_e$ excitation: (a) as measured, (b) after subtraction of the long lived contribution. (c) and (d) represent the results obtained with a solid of HDT-capped QDs: (c) for $1P_{3/2}1P_e$ excitation (d) reference experiment with $1S_{3/2}1S_e$ excitation (in both cases the long-lived contribution has been subtracted). The excitation pathways are visualized on the right hand side.

should leave the $1P_e$ states unpopulated.[1] It is clear that then no change in signal is

[1] Another reference experiment with excitation energies below the band gap resulted in no photoinduced signal at all, as expected.

measured in the energy range between 1 and 2 eV in the entire time window. Hence, this proves that the time-dependent intensities in Figs. 4.5(b) and (c) can be safely attributed to the $1P_e$ electrons. It should also be noticed, that the kinetic energy of the $1S_e$ electrons cannot be identified since a $1S_e$ peak (expected 0.3 eV below the $1P_e$ signal [112]) is not visible in the spectra. Instead, a rather broad and time-independent shoulder is observed in the region between the secondary electron peak and the $1P_e$ peak. We attribute the broad structure to secondary electrons stemming from $1S_e$ electrons that have lost a part of their energy by inelastic scattering before leaving the sample. The QDs with their surrounding ligands are complex systems and charges or dipoles on the surface can alter the kinetic energy of the photoemitted electrons. For the measurements with $1P_{3/2}1P_e$ excitation also secondary electrons stemming from $1P_e$ are expected to overlap energetically with the signal from $1S_e$ electrons. Since $1P_e$ electrons would provide a signal that decreases in time and the $1S_e$ electrons a signal that rises approximately with the same time constant, it can be understood that the broad feature arising from inelastic scattered electrons of both states does not show a clear time-dependence in the measurement window of the apparatus up to 40 ps. The visibility of feeding of electrons into the $1S_e$ state is further hindered since it is overlapped with the background signal belonging to $1S_e$ electrons directly excited by the pump pulse by the $3S_{1/2}1S_e$ transition. In addition, the "backward process" occurring at lower kinetic energy regions around $\Delta t = 0$ fs in which the roles of the laser pulses are exchanged masks the signal in the $1S_e$ energy range in the first ≈ 200 fs. This is explained in detail in Appendix A. Since the probe pulse is in the UV range, it excites states with high excess energy and the pump pulse "probes" these states. This can be seen as the reverse process of *normal* 2PPE and thus a corresponding decay is observed at negative time delays. However, this process also influences the first ≈ 200 fs of positive time delay as there is still a temporal overlap of pump and probe pulses leading to a very high excitation intensity compared to the rest of the signal.

Energetic differences between oleic acid and HDT capped QDs can be addressed via the work function. A good estimate for the work function can be obtained from the position of the secondary electron edge in the kinetic energy spectra. It was observed that the oleic acid-capped QD solids show a work function that varied between 3.2 eV and 3.5 eV when the laser spot was scanned over a given sample, or when different QD solids were measured. In contrast, the samples consisting of HDT-capped QDs all have a constant work function of 3.5 eV. The work function is sensitive to surface dipoles and charges. Other groups also observed that exchanging ligands shifts the energy levels relative to the vacuum level and also the vacuum level itself [113, 114]. This was attributed to a dipole creation between the ligand anchor group and the surface of the QD. We believe that the variation of the work function with oleic acid-capped

QDs can be attributed to a residual charging by photogeneration and photoemission. Due to the photoemission of electrons the sample becomes locally positively charged, and could remain so if the valence band holes are not sufficiently rapidly replenished by carrier injection from the back-contact and transport to charged QDs. Due to the long oleic acid molecules around the QDs, the tunneling barriers between the QDs in the sample are considerable, and transport may not be fast enough. In contrast, HDT is a much shorter molecule and by improved carrier transport, the empty states in the valence band are sufficiently fast refilled [68, 115].

It is convenient to compare the $1P_e$ and $1S_e$ energy levels that were deduced above with intermediate state energy considerations that were explained in Sec. 2.4 and that will be applied more explicitly for the GaP(100) surfaces in Sec. 5.2. Hereby, we consider that for a sample with a work function of 3.5 eV, and a probe photon energy of 4.56 eV we find that $1P_e$ is located at $E_{kin} = 1.75\,\text{eV}$.[2] The state $1S_e$, that in principle is identical with the CBM, lies $\approx 300\,\text{meV}$ lower and thus at $E_{kin} = 1.45\,\text{eV}$. Inserting these values in Eq. 2.39 finally yields that the FERMI-level is located $\approx 0.4\,\text{eV}$ below the CBM. For CdSe quantum dots the FERMI level is typically determined by deep hole trap states like unsaturated Se dangling bonds or Cd - S bonds related to HDT [92, 93] and is thus a reference for the average number of trap states per QD.

To evaluate the temporal evolution of the electrons in the $1P_e$ state, the mean intensity of photoemitted electrons at kinetic energies corresponding to the $1P_e$ peak (compare Figs. 4.5(b) and (c)) is averaged over 0.2 eV and plotted for different pulse time delays. The resulting transient populations of $1P_e$ is shown in Fig. 4.6(a) for oleic acid and HDT capped samples.[3] The OA-capped sample shows a much faster decay than the HDT capped one; the curve can be fitted with a monoexponential decay and a constant offset for positive pump-probe delays. The contribution of photoelectrons emitted due to reversed pump probe order are taken into account with an exponential curve that decays with negative time delays. Figure 4.7(a) shows the resulting fit with the individual contributions. The durations of the laser pulses are implemented by GAUSSian generation terms for the pump and convoluted with the probe pulse profile.

We ascribe the fast decay with a time constant of $\tau = 220 \pm 20\,\text{fs}$ to an AUGER-like process, where the electron relaxes to $1S_e$ by transferring its excess energy to the hole. This process is visualized in Fig. 4.6(b). Similar time constants observed by transient absorption spectroscopy were also ascribed to an AUGER-like relaxation [103, 116]. The offset stays constant for at least 40 ps, which is the measurement limit of the used setup. It is also present at the HDT capped sample but not visible after

[2] Note that for measurement in Fig. 4.5(c) a workfunction of $\Phi = 3.3\,\text{eV}$ was assumed, thus the shift by 0.2 eV. This however does not affect the results.

[3] To minimize contributions other than $1P_e$ electrons, the shown transients represent only the intensity of photoemitted electrons from the high energy edge of the $1P_e$-related signal.

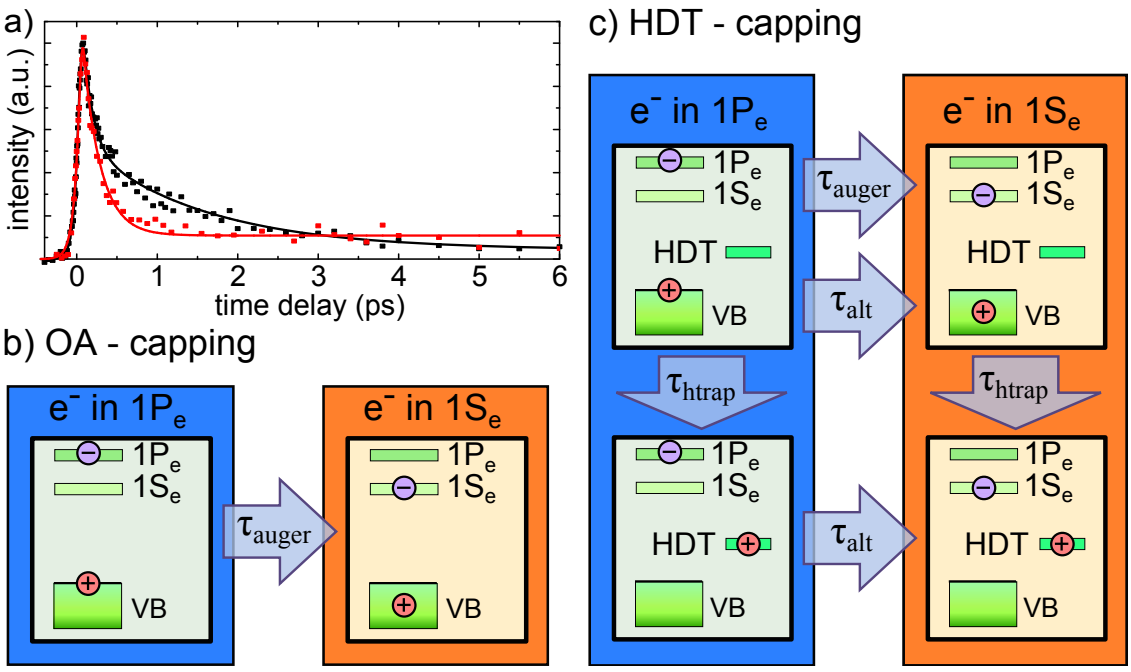

Figure 4.6: (a) Transient occupation of the $1P_e$ level in OA (red) and HDT capped (black) samples. Symbols represent the 2PPE data; solid lines are fits based on the models shown in (b) and (c), respectively. (b) Scheme of a rate model for the AUGER-type relaxation process in OA capped samples. (c) Scheme of a rate model for the relaxation process in HDT capped samples involving the AUGER-type process, hole trapping and an alternative relaxation mechanism in which the valence hole is not involved. VB marks the valence band, which for simplicity is here drawn as continuum.

normalization of the transients, since the actual signal is much bigger than for the OA capped samples.[4] The bigger signal for HDT capped samples probably stems from the better refilling of photoemitted electrons through the back contact. Although, in principle, injection of hot electrons into the electrode can form an alternative decay path parallel to the $1P_e$-to-$1S_e$ relaxation [117], it can be neglected here since the nanocrystalline film is about 50−100 nm in thickness and hot electron transfer between the nanocrystals is much slower than the measured decay. Thus, substrate effects are not seen in the conducted 2PPE measurements.

As stated above, the dips related to the $1P_{3/2}1P_e$ and $3S_{1/2}1S_e$ transitions cannot

[4] The offset might be related to charging effects during the measurement that slightly influence the background signal. On the other hand a comparable offset has already been observed in transient absorption measurements of pyridine-capped [94] and ZnS-capped [65] CdSe QDs and has been associated with the formation of charge transfer complexes in the former or high energetic long living states, populated by nonlinear photon absorption in the latter case, respectively.

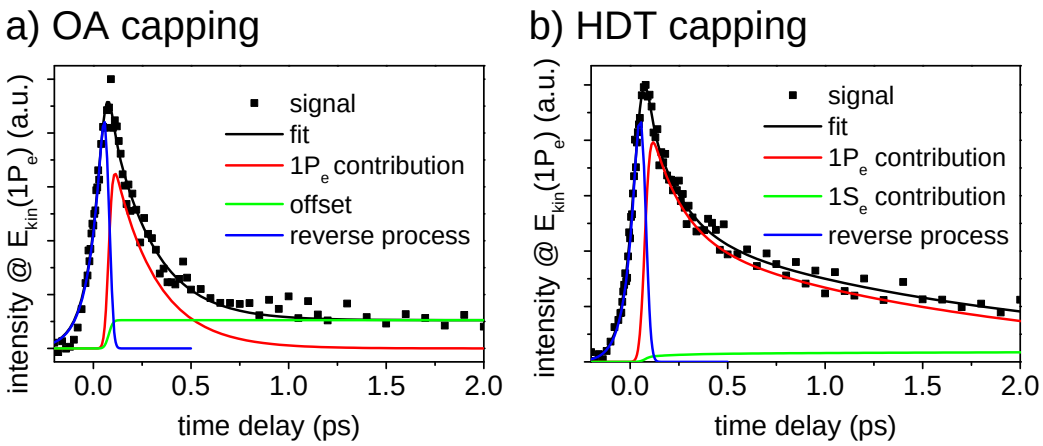

Figure 4.7: (a) Transient occupation of the $1P_e$ level in OA (a) and HDT-capped (b) samples. The fit for the OA-capped samples contains the model shown in Fig. 4.6(b) with an additional contribution from the backwards process and a constant offset. For the HDT-capped samples the fit implements the model shown in Fig. 4.6(c) and given with Eqs. 4.1 and includes also a contribution of $1S_e$ and the backwards process.

be distinguished in the transmission spectra shown in Fig. 4.3(b). We thus performed measurements with different pump photon energies to find out if the excitation of the $1P_e$ level depends critically on the matching of pump photon energy and the $1P_{3/2}1P_e$ transition energy. Transients of the $1P_e$ level for different $h\nu_{pump}$ are shown in Fig. 4.8 with very similar shapes, indicating a population of the level for all three cases. As the QD absorption line and the pump pulse have a spectral width of $\approx 150\,\text{meV}$ ($\approx 30\,\text{nm}$ at this photon energy) there is always an overlap between the $1P_{3/2}1P_e$ absorption line and the pump spectrum, which explains the similar signals. Also a slight off-resonant excitation would only lead to a larger portion of QDs with direct excitation of the $1S_e$ level and thus to a larger background signal. To excite the next higher lying electron state $1D_e$, photon energies $\geq 3\,\text{eV}$ would be required [118].

The $1P_e$ electron decay curve of the HDT capped sample shows a more complex decay, involving much slower components on a ps timescale. This forms a strong indication that the AUGER process is suppressed. We argue that this suppression is due to trapping of the hole in a localized state in the band gap. This is in line with studies by WUISTER *et al.* [95] who showed by photoluminescence measurements that the hole can be trapped by thiol ligand states located inside the band gap. Transient absorption studies for CdSe nanocrystals by different groups showed that the lifetime of $1P_e$-electrons is considerably increased into the ps time scale after hole capture, similar to our findings [65, 104]. In fact, this decay is still much faster than one would expect in terms of the phonon bottleneck [9] and points to the existence of an alternative relaxation mechanism. Previous works have proposed that this non-

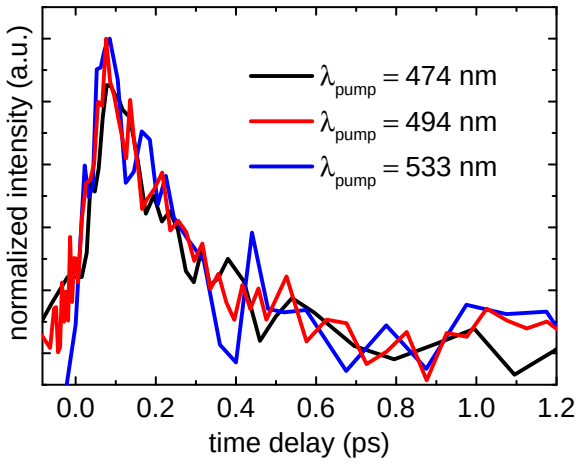

Figure 4.8: Transient occupation of the $1P_e$ level at OA-capped QDs for different excitation energies, as indicated in the legend.

AUGER process is mediated by surface states or capping molecules [10].

We have used a generalized kinetic scheme (Fig. 4.6(c)) that accounts for the AUGER pathway and the alternative relaxation pathway in case trapping of the hole occurs. Directly after photoexcitation (top left in the scheme), the electron is in the $1P_e$ state, while the hole is in $1P_{3/2}$. Due to the smaller energy spacings between the valence band states, the hole relaxes extremely fast [64]. Then, two competing processes take place; the electron can relax to $1S_e$ by the AUGER-like process with a time constant τ_{AUGER}, or the hole can be trapped by the HDT ligand states with a time constant τ_{htrap}, impeding the AUGER-like process. In this state of the system (bottom left in the scheme), relaxation of the electron to $1S_e$ is still possible via the alternative relaxation pathway (time constant τ_{alt}) mediated by the surface or the capping molecules. The dynamics are thus described by the following system of coupled rate equations:

$$\begin{aligned}
\frac{dn_{VB}^{1P_e}}{dt} &= -\frac{n_{VB}^{1P_e}}{\tau_{\text{AUGER}}} - \frac{n_{VB}^{1P_e}}{\tau_{htrap}} + G_{1P_e}(t) \\
\frac{dn_{trap}^{1P_e}}{dt} &= \frac{n_{VB}^{1P_e}}{\tau_{htrap}} - \frac{n_{trap}^{1P_e}}{\tau_{alt}} \\
\frac{dn_{VB}^{1S_e}}{dt} &= \frac{n_{VB}^{1P_e}}{\tau_{\text{AUGER}}} - \frac{n_{VB}^{1S_e}}{\tau_{htrap}} + G_{1S_e}(t) \\
\frac{dn_{trap}^{1S_e}}{dt} &= \frac{n_{VB}^{1S_e}}{\tau_{htrap}} + \frac{n_{trap}^{1P_e}}{\tau_{alt}}.
\end{aligned} \tag{4.1}$$

Hereby n denotes the fraction of photoexcited QDs in a particular state with the electron position denoted by the upper- and the hole position denoted by the lower

index. $G_{1P_e}(t)$ and $G_{1S_e}(t)$ are the generation terms for a direct filling of the $1P_e$ and $1S_e$ levels, respectively. The fit shown in Fig. 4.7(b) is performed according to this model and consists of a contribution of the $1P_e$ electrons, a small influence of the $1S_e$ electrons and a decay for negative time-delays due to reversed pump-probe order. Pulse widths are integrated in the same manner as described above for the OA-capped dots. The best agreement between model and data is found with $\tau_{\text{AUGER}} = 290 \pm 20\,\text{fs}$, $\tau_{htrap} = 360 \pm 20\,\text{fs}$ and $\tau_{alt} = 1.7 \pm 0.2\,\text{ps}$. The AUGER time constant is slightly larger than for the oleic acid capped sample. The trapping time of 350 fs is comparable with transient absorption measurements of KLIMOV *et al.* providing a hole trapping time constant of about 400 fs for pyridine-capped samples [65]. The competition of hole trapping and AUGER process has been simulated very recently with more sophisticated methods [119]. The simulated QDs were much smaller and thus the time constants were much longer, but the resulting relative magnitudes of the timescales were found in good agreement with the data, measured here. Accordingly, for efficient deceleration of the electron cooling, the hole trapping/extractions needs to be significantly faster than the AUGER-process [119].

The mechanism behind hot electron relaxation in CdSe quantum dots in the state with a trapped hole (bottom left in Fig. 4.6c) is still a matter of discussion. We note that all previous results on that matter rely on transient absorption measurements that monitor the populations of $1S_e$ and $1P_e$ states, but in contrast to 2PPE are unable to detect electrons in states between the $1P_e$ and $1S_e$ state in a direct way. The time constant of $\tau_{alt} = 1.7\,\text{ps}$, which remains after hole trapping, must be ascribed to a relaxation mechanism that does not involve the hole. Pathways that have been proposed are via energy transfer to vibrational states of the capping molecules or via surface/interface/ligand related states which are energetically located between $1S_e$ and $1P_e$ [120, 121]. 2PPE is sensitive for electrons in surface [122–124] and molecular adsorbate states [125, 126]. Therefore, we performed a detailed analysis of the dynamic behavior in the energy range just below the $1P_e$ signal. In Fig. 4.9 transients are shown which correspond to different regions in the kinetic energy spectrum shown in Fig. 4.5(b) and (c) for OA and HDT capped samples, respectively. For both cappings, the curves look very similar in the first few hundred femtoseconds when monitored for different energy windows.[5] While the transients for the OA capped sample remain similar throughout the whole time scale, the slow component of the decay curve for HDT-capped QDs shows a strong dependence on the particular kinetic energy window. Only at 0.2 eV above $E_{kin}(1P_e)$ we observe a time constant of

[5] The transients are shown only for $\Delta t > 200\,\text{fs}$, as for smaller time delays the "backwards process" described above starts to introduce artifacts. The remaining signal for $\Delta t = 30\,\text{ps}$ was subtracted as shown in Fig. 4.5(c) and the resulting curves were normalized by dividing by their particular value at $\Delta t = 350\,\text{fs}$.

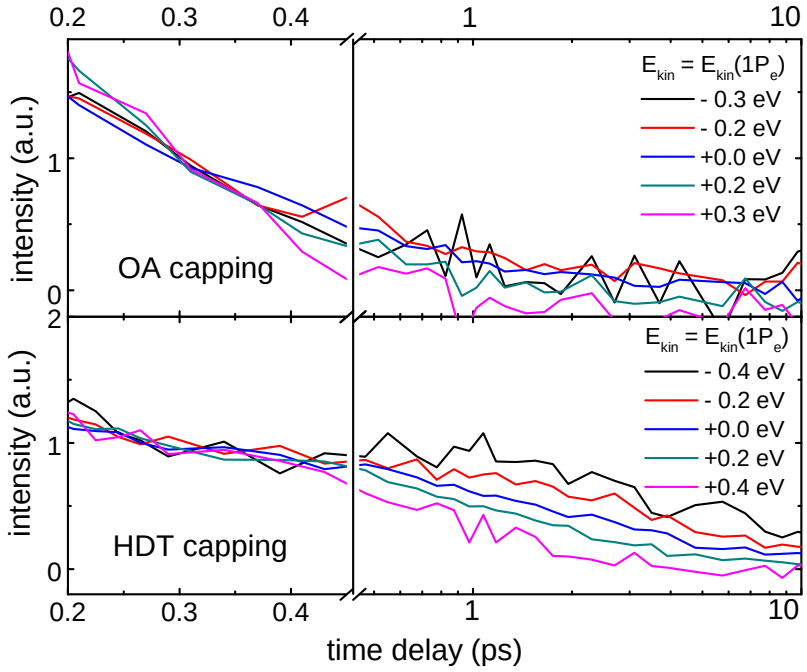

Figure 4.9: Transients at different kinetic energy in the vicinity of $1P_e$ for oleic acid and HDT-capped samples.

$\tau_{alt} = 1.7\,\text{ps}$ reported above. At 0.4 eV above the maximum of the $1P_e$ peak, where the signal is already very small, we see a decay of $\tau_{alt} \approx 1\,\text{ps}$. The transients at lower kinetic energies, however, show a slower and more complex decay in the first few picoseconds, all ending in a slow mono-exponential tail with a time constant of around 5 ps. These results point to a stepwise relaxation involving additional states between $1P_e$ and $1S_e$. We attribute the slow tail of 5 ps to electrons that transiently populate states between $1S_e$ and $1P_e$.

In order to support this interpretation we compare our experimental data to calculations based on a rate equation model shown in Fig. 4.10(a) that accounts for electron trapping of the $1P_e$ state and subsequent further relaxation to $1S_e$. As time constants we use $\tau_{1P_e \to interm} = 1\,\text{ps}$ for the relaxation from $1P_e$ to the intermediate state and $\tau_{interm \to 1S_e} = 5\,\text{ps}$ for the relaxation from the intermediate state to $1S_e$. These are the time constants obtained by fitting the decay of the transient 0.4 eV above $E_{kin}\,(1P_e)$ and by a single-exponential approximation for the slow tail of the transients at lower energy, respectively. The simulated transient populations of $1P_e$, the intermediate state and $1S_e$ in Fig. 4.10(b) are $p_{1P_e}\,(\Delta t)$, $p_{interm}\,(\Delta t)$ and $p_{1S_e}\,(\Delta t)$, respectively. The calculated energy dependent 2PPE signal is finally a linear combination of all

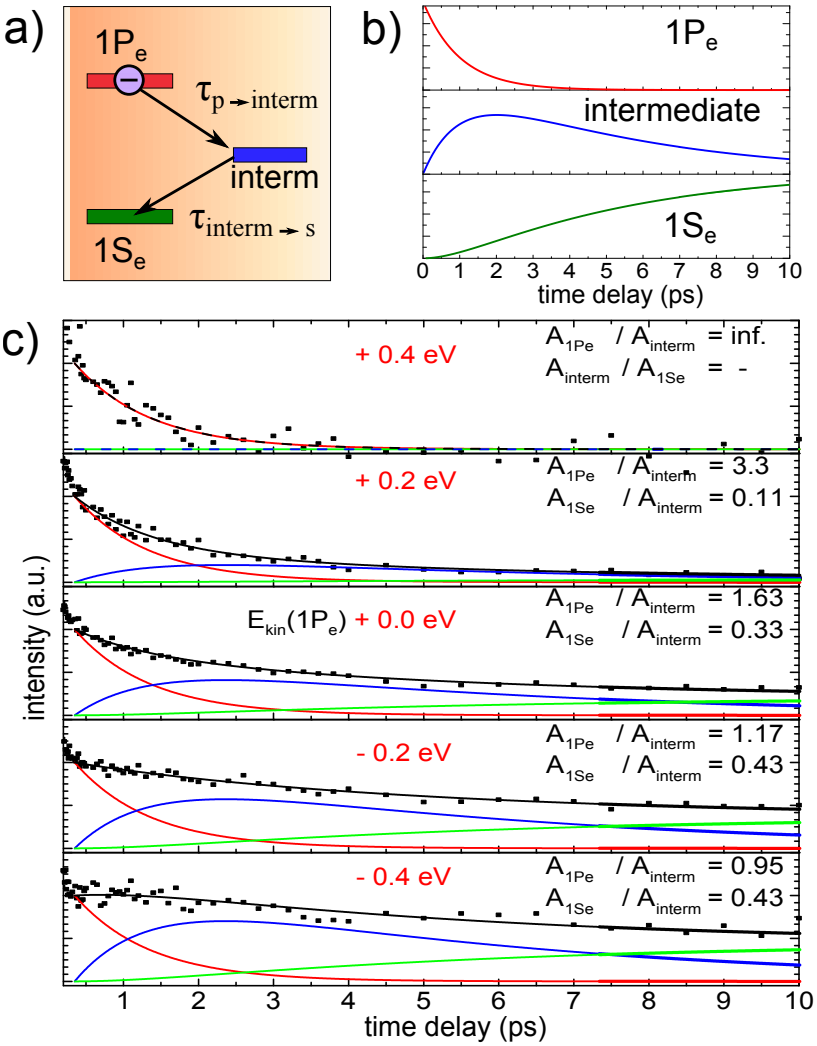

Figure 4.10: (a) Simple rate model, describing the decay from $1P_e$ to $1S_e$ via an intermediate state. (b) Occupation of $1P_e$, intermediate state and $1S_e$, according to the model with $\tau_{1P_e \to interm} = 1\,\text{ps}$ and $\tau_{interm \to 1S_e} = 5\,\text{ps}$. (c) 2PPE-transients of the HDT capped samples at different E_{kin} near the $1P_e$ peak signal. Black squares represent the experimental data; the black lines are simulated curves, based on the model described in the text. The red, blue and green lines show the individual contributions of $1P_e$, intermediate and $1S_e$ state, respectively.

three contributions

$$\begin{aligned} I\left(E_{kin}, \Delta t\right) &= A_{1P_e}(E_{kin}) \times p_{1P_e}\left(\Delta t\right) + A_{interm}(E_{kin}) \times p_{interm}\left(\Delta t\right) + \\ &+ A_{1S_e}(E_{kin}) \times p_{1S_e}\left(\Delta t\right), \end{aligned} \tag{4.2}$$

with the energy dependent coefficients $A_{1P_e}(E_{kin})$, $A_{interm}(E_{kin})$ and $A_{1S_e}(E_{kin})$. As can be seen in Fig. 4.10(c), we achieve good agreement between the calculated curves

and the measured data, by using a set of values for these coefficients which reflects the expected energy dependence: a dominant contribution of $1P_e$ state electrons for the transients at the high energetic side and a growing contribution of intermediate and $1S_e$ state electrons towards lower energies. It has to be noted, that the constant offset at long delay times related to directly photoexcited $1S_e$ electrons has to be treated as an additional parameter and is also varied to get the best agreement between the simulated and the experimental curves. Furthermore the onset of the simulated curves is set to 350 fs, since this model describes only the dynamics after hole capture and does not take into account the fast components due to the AUGER-process.

4.2.4 Discussion

Our results support the idea that the slow relaxation process, which becomes prominent when the AUGER process is blocked, constitutes electron relaxation via intermediate states. The assumption of one discrete intermediate state between $1P_e$ and $1S_e$ is probably far too simple. However, it can be argued that a model involving multiple intermediate states or even a continuum of states will provide similar results, meaning a fast relaxation at high kinetic energies and a slower and more complex behavior at lower kinetic energies due to increasing importance of lower lying electron states [45]. A possible mechanism of electron relaxation via intermediate states in quantum dots has been investigated theoretically [120, 121]. Potential candidates for these intermediate states could be the Cd dangling bonds that lie close or within the conduction band [92, 93, 127]. Intermediate state related relaxation has been proposed as an explanation for slow electron relaxation observed in transient absorption measurements at CdSe nanocrystals with hole-trapping capping molecules [104]. However, infrared spectra indicated resonant vibrational ligand states and the authors of the study assigned this as the alternative relaxation path [104]. It was also shown that an appropriate core / multi-shell structure can be used to extend the lifetime of electrons in $1P_e$ up to > 1 ns [10]. The multi-shell architecture needs to ensure that the electron is separated from the hole, that the surface has no electron traps and that the hole is separated from the ligands [10].

4.3 Hot electrons in CdSe nanoplatelets

The measurements, presented in the previous section, show that the hot electron relaxation in 0-dimensional quantum dots is highly determined by the surface or the surrounding ligands, which is in agreement with studies performed with transient absorption and time-resolved photoluminescence spectroscopy [10, 128] and terahertz spectroscopy [64]. The predicted phonon bottleneck [62] thus only becomes important if the alternative relaxation pathways are successfully "deactivated" [10]. In this section we take our research to the next dimension and investigate the relaxation of hot carriers in CdSe quantum well nanoplatelets. These materials constitute a good model system to further the understanding of the opto-electronic properties of 2D semiconductors [84, 85, 129–132], as the electronic structure is expected to be comparable to conventional epitaxially grown III-V quantum wells. The interchangeability of the surrounding ligands, as well as the possibility to grow shells, allows for an intense study of the influence of the interface properties on the electron dynamics. Furthermore, the lateral size of the platelets, down to less than $100 \times 100\,\mathrm{nm}^2$, makes it possible to study dynamics for low excitation densities, down to a single exciton per platelet.

The cooling of hot carriers in NPs has been studied recently by Pelton *et al.* by means of optical spectroscopy with approximately 5 ps time resolution [133]. Only measurements at high excitation intensities, resulting in about 100 electron hole pairs per platelet, were shown; the cooling taking place in the 10 ps time regime. For lower excitation densities no charge carrier relaxation could be resolved in these measurements. This time scale agrees with previous results obtained with other quantum well systems and even bulk CdSe [29, 134]. In view of electron-phonon scattering, which occurs on a femtosecond time scale [24, 29, 135], this cooling is rather slow and has been attributed to the heating of the optical phonon distribution; the high density of hot carriers generate a high density of LO phonons (not in thermal equilibrium with the lattice), which are either reabsorbed by the electrons, diffuse away, or slowly decay to phonons of lower energy [135–137]. However, for low excitation densities and on the early times scales the hot phonon effect will be less pronounced and much faster cooling is expected for the hot carriers. In principle, the mechanism of cooling by phonon emission in bulk semiconductors also holds for 2D quantum wells [134, 138–141] (see also Sec. 2.3.2), but interface reactions can also play a role here. To separate quantum well and surface related mechanisms, a variety of tr-2PPE measurements is performed in this section. In particular, this includes experiments for variable excitation energies and lattice temperatures. Furthermore, samples with different thickness and different cappings are studied.

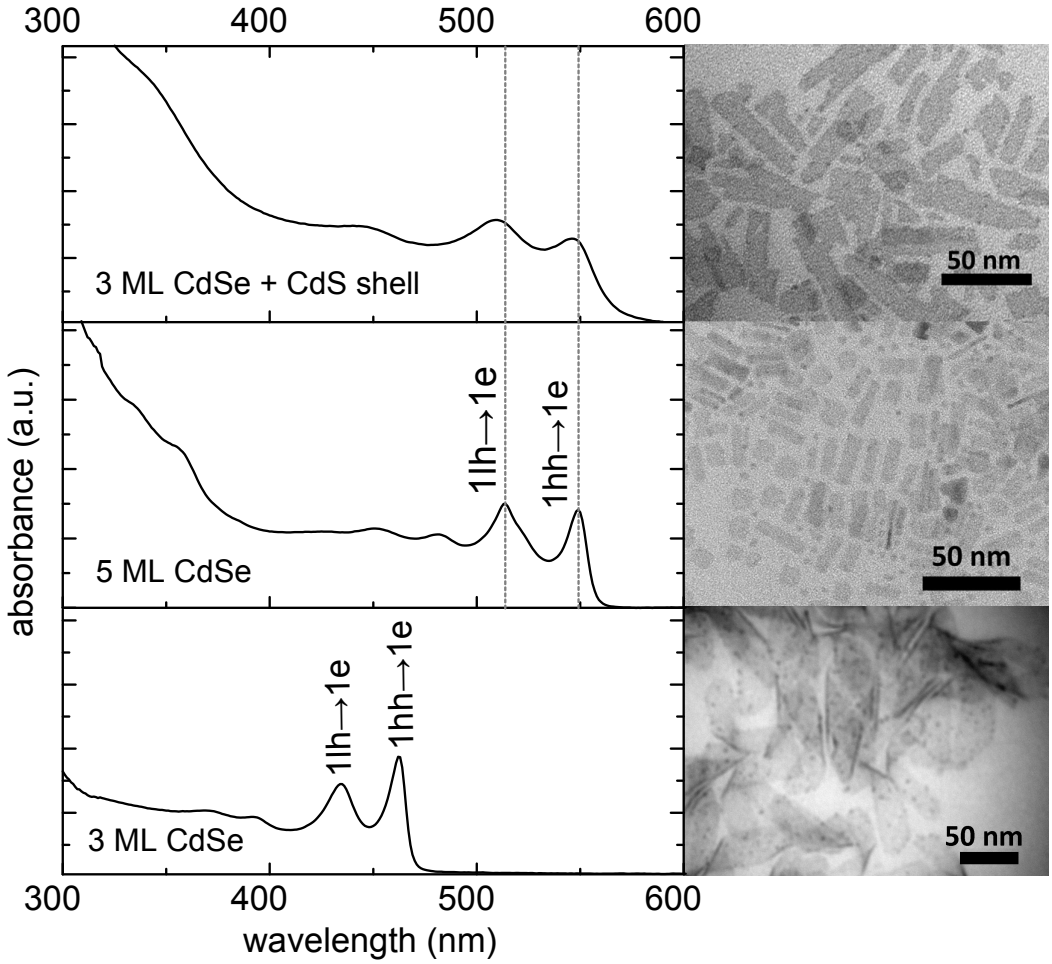

Figure 4.11: Absorbance spectra and TEM images of nanoplatelets of different thickness with and without shell. The transitions corresponding to the two energetically lowest peaks have been indicated.

4.3.1 Sample characterization

In Fig. 4.11, we present typical absorbance spectra[6] and TEM pictures of nanoplatelets with different sizes and with and without shell. The platelets are nearly flat 2D systems with lateral dimensions of about $(5-20)\times(20-70)\,\mathrm{nm}^2$. The first absorption and emission peak is situated at $\approx 550\,\mathrm{nm}$ (2.25 eV), for CdSe(5 ML) platelets and CdSe(3 ML)/CdS core/shell platelets. For the thinner CdSe(3 ML) NPs the first absorption/emission peak is located at $\approx 460\,\mathrm{nm}$ (2.68 eV) as shown on the left hand side of Fig 4.11. The wider bandgap is directly related to stronger confinement energy. The samples which are used for the 2PPE measurements were prepared in the same way as described for the QDs. Figure 4.12 shows transmittance spectra of the platelets

[6] An exponential background has been removed from the spectra, which is most probably related to light scattering at the samples.

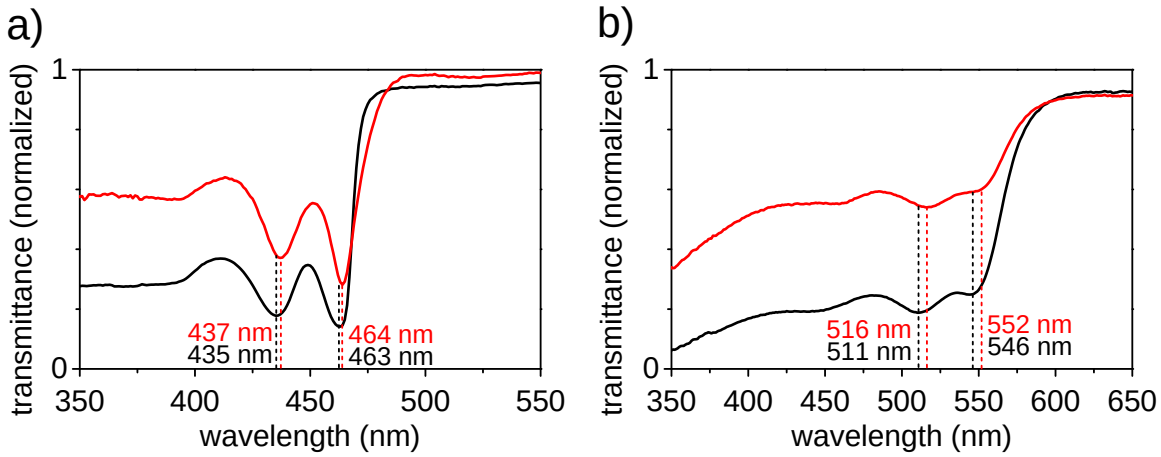

Figure 4.12: Transmittance spectra of (a) CdSe(3 ML) NPs and (b) CdSe(3 ML)/CdS core/shell NPs on ITO with oleic acid (black) and HDT (red) capping.

on ITO substrates. No shift of the exciton peaks is found for the OA capped samples, compared to the absorbance spectra shown in Fig. 4.11. This indicates that the interaction between neighboring platelets and between platelets and the ITO is low and has no significant influence on the electronic levels of the platelets. Exchange of the oleic acid for HDT leads to a slight red shift, similar to the observations for quantum dots (cf. Sec. 4.2). This implies that the ligand exchange was successful.

4.3.2 Calculation of the excitation densities

The time-resolved 2PPE measurements were conducted with different pump photon energies: either in the visible ($460 - 600\,\mathrm{nm}$ *i.e.* $\mathrm{h}\nu_{pump} = 2.0 - 2.7\,\mathrm{eV}$) or in the UV ($274\,\mathrm{nm}$ *i.e.* $\mathrm{h}\nu_{pump} = 4.52\,\mathrm{eV}$). For our experiments with visible excitation, the photon flux per pulse was below $5 \times 10^{13}\,\mathrm{cm}^{-2}$. For pumping in the UV, the photon flux was even lower, i.e. $7.5 \times 10^{11}\,\mathrm{cm}^{-2}$ at $\mathrm{h}\nu_{pump} = 4.52\,\mathrm{eV}$. We estimated the excited carrier density per nanoplatelet, based on absorption cross sections determined for CdSe nanoplatelets by other groups [88, 133]. The sizes of the platelets are different in our study than in the literature. However, if any light coupling effects are neglected, the absorption cross section should only depend on the amount of CdSe material. Therefore the absorption coefficient for the NP CdSe material was calculated by dividing the absorption cross section by the platelet volume. Comparison of the results from different groups [88, 133] gives an average absorption coefficient of $\alpha_{np} = (1.4 \pm 0.4) \times 10^5\,\mathrm{cm}^{-1}$, for a wavelength of 400 nm. This is close to the bulk value $\alpha_{bulk}(400\,\mathrm{nm}) = 1.5 \times 10^5\,\mathrm{cm}^{-1}$ [142], showing that our approach is legitimate as a first approximation. For excitation energies in the visible spectrum, the dependency of the absorption cross section on the excitation wavelength is taken into account by

scaling up/down according to the transmission spectrum of the nanoplatelet sample (cf. Fig. 4.11). For excitation with $h\nu_{pump} = 4.52\,eV$ we scale according to the bulk absorption spectrum [142], where $\alpha_{bulk}(4.52\,eV) = 8 \times 10^5\,cm^{-1}$, since no data is available for nanoplatelets in this wavelength range. The resulting excitation densities are ≈ 5 electrons per platelet for pumping in the visible, and ≈ 1 electron per platelet for $h\nu_{pump} = 4.52\,eV$.

4.3.3 Electron dynamics for different excitation energies

The measured kinetic energy spectrum reflects the energy distribution of the photogenerated electrons within the semiconductor.[7] Recording spectra for different time delays between the pump and probe pulses allows to measure the temporal evolution of the electron distribution after photoexcitation. Figure 4.13(b) shows the kinetic energy of the emitted electrons as a function of the time delay between pump and probe for $h\nu_{pump} = 2.30\,eV$ (540 nm), $h\nu_{pump} = 2.60\,eV$ (478 nm), and $h\nu_{pump} = 4.52\,eV$ (274 nm). These experiments were conducted on CdSe(3 ML)/CdS core/shell NPs as these are the most stable samples.[8] An illustration of the corresponding excitation schemes is shown in Fig. 4.13(a). The band structure is a crude sketch and the curvature of the bands is just a simple guess. However, the sequence of the bands at the Brillouin zone center follows the calculations by Benchamekh *et al.* [84], but neglects the split off bands.

With $h\nu_{pump} = 2.30\,eV$ (first peak of the absorption spectrum) electrons are excited to the bottom of the conduction band (scheme (i) in Fig. 4.13(a)). The green plots show the corresponding kinetic energy of electrons that are photoemitted from the CBM, convoluted with the energy resolution of the setup, which is approximately 0.2 eV, and serve as a reference. Deconvolution yields that the bottom of the CB is situated approximately 3.55 eV below the vacuum level of the sample as discussed further below. The blue and purple curves represent the 2PPE results with $h\nu_{pump} = 2.60\,eV$ and $h\nu_{pump} = 4.52\,eV$, respectively, (schemes (ii) and (iii) in Fig. 4.13(a)), leading to hot electrons with an initial maximum excess energy of 0.35 eV and 2.27 eV above the CBM, respectively. The average excess energy of the photoexcited electrons, however, is considerably lower due to the dispersion of the heavy hole valence band and transitions from lower lying valence bands.[9] Spectral features related to transitions from the different hole-bands could not be resolved since the spectral resolution is

[7] For more details, see Sec. 2.4.

[8] As will be shown later, no substantial differences in the electron dynamics were measured for NPs of different thickness and with or without shell.

[9] Especially for the measurement with $h\nu_{pump} = 4.52\,eV$ it needs to be taken into account that transitions from the highest VBs to the lowest CB are in principle forbidden in terms of dipole selection rules near the BZ center (see Sec. 2.2.1).

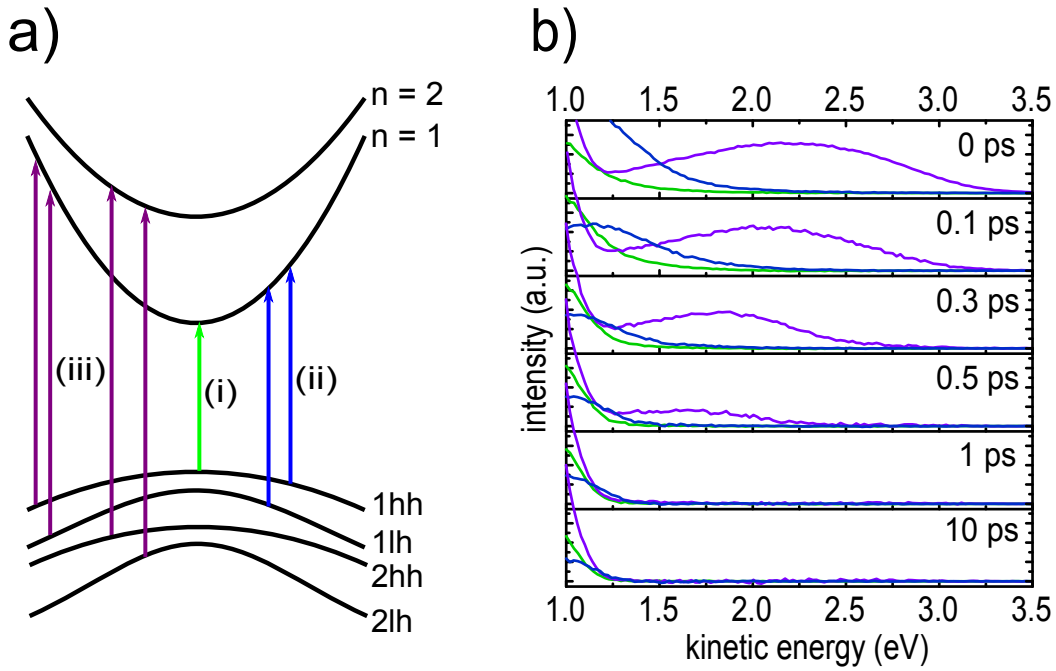

Figure 4.13: Different excitation schemes (a) and the resulting 2PPE spectra (b) of CdSe(3 ML)/CdS core/shell nanoplatelets, for different $h\nu_{pump}$ as a function of time delay between pump (2.30 eV, 2.60 eV, 4.52 eV) and probe (4.52 eV). Green (i): $h\nu_{pump} = 2.30\,eV$ corresponding to the lowest energy transition (1hh→1e cf. Fig. 4.11), leading to almost cool electrons at the bottom of the conduction band. Blue (ii): $h\nu_{pump} = 2.60\,eV$, leading to hot electrons with a maximum excess energy of 0.35 eV. Purple (iii): $h\nu_{pump} = 4.52\,eV$, leading to hot electrons with a maximum excess energy of 2.27 eV.

limited to approximately 0.2 eV, as discussed in Sec. 3.2. The signal at the low kinetic energy edge ($E_{kin} < 1.1\,eV$) contains large amounts of secondary electrons *e.g.* electrons that have lost parts of their kinetic energy by inelastic scattering processes and must be treated with care. This is especially pronounced for excitation with $h\nu_{pump} = 4.52\,eV$. As expected, these two different pump energies result in very different electron distributions at short time delays. Overall, the distributions change fast in the < 0.5 ps time domain and more slowly on later times; at $\Delta t = 1$ ps, the electrons have nearly completely cooled down to the CBM, in accordance to 2PPE measurements of the electron dynamics at 3D semiconductor interfaces (cf. Ref. [111] and Sec. 5.3).

A notable feature that we observe is that the total electron yield (shown exemplarily in Fig. 4.14 for the measurement with $h\nu_{pump} = 4.52\,eV$) decreases with time delay. This effect is most pronounced for high excitation energies. Different scenarios could explain this behavior: (i) Diffusion of the electrons away from the surface. However, for an equivalent drop of signal, electron mobilities larger than $\mu_e = 100\,cm^2Vs^{-1}$

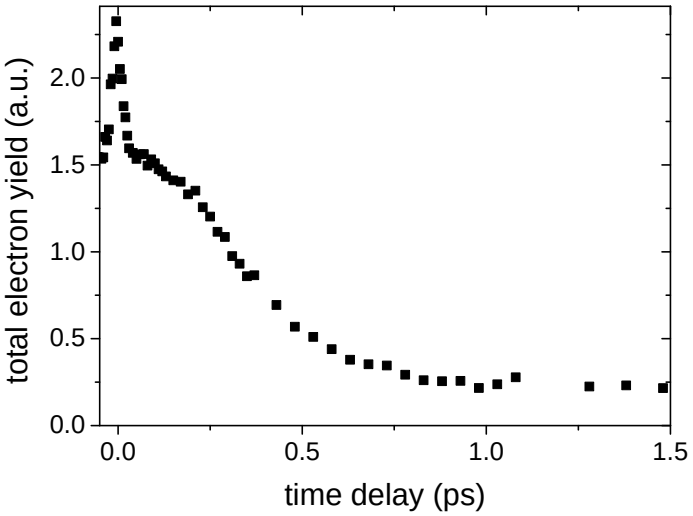

Figure 4.14: Total electron yield measured for CdSe(3 ML)/CdS core/shell nanoplatelets with $h\nu_{pump} = 4.52\,eV$. Only electrons with $E_{kin} > 1\,eV$ were considered to minimize the influence of secondary electrons and 1PPE. Selection of a different cutoff results mostly in a variation of the offset.

would be required, which is very unlikely for the OA capped platelet solids. Also substantial differences for OA and HDT capped samples are to be expected, but not measured. (ii) Fast recombination. This mechanism is also unlikely, since recombination is usually much slower. It would be expected also for excitation to the band edges ($h\nu_{pump} = 2.30\,eV$), which is not the case. (iii) Electrons scatter into states where they have a lower probability to be photoemitted because of the dipole selection rules. This might lead to an overestimation of the average electron energy, especially for high energetic electrons and can also effect the deduced carrier cooling rates. However, according to Ref. [143] this should rather lead to an underestimation of the electron cooling rate, which is in contradiction to our observations. So the exact reason for the drop of signal remains speculative. In any case it prevents the comparison of transients for specific kinetic energy ranges as done for the quantum dots, since effects of electron cooling and electron "vanishing" will intermix. To circumvent this, all of the following analysis aims on separating the loss of electron yield from the shape change of the electron distribution (ED), either by fitting or by calculating the average energy of the ED. This approach is also appropriate, since for the NPs it can be clearly seen that the electron distributions shift towards low kinetic energy in contrast to the measurements at the quantum dots, where rather a decrease of a signal at certain energies was seen. This already indicates electron cooling via a continuous density of states.

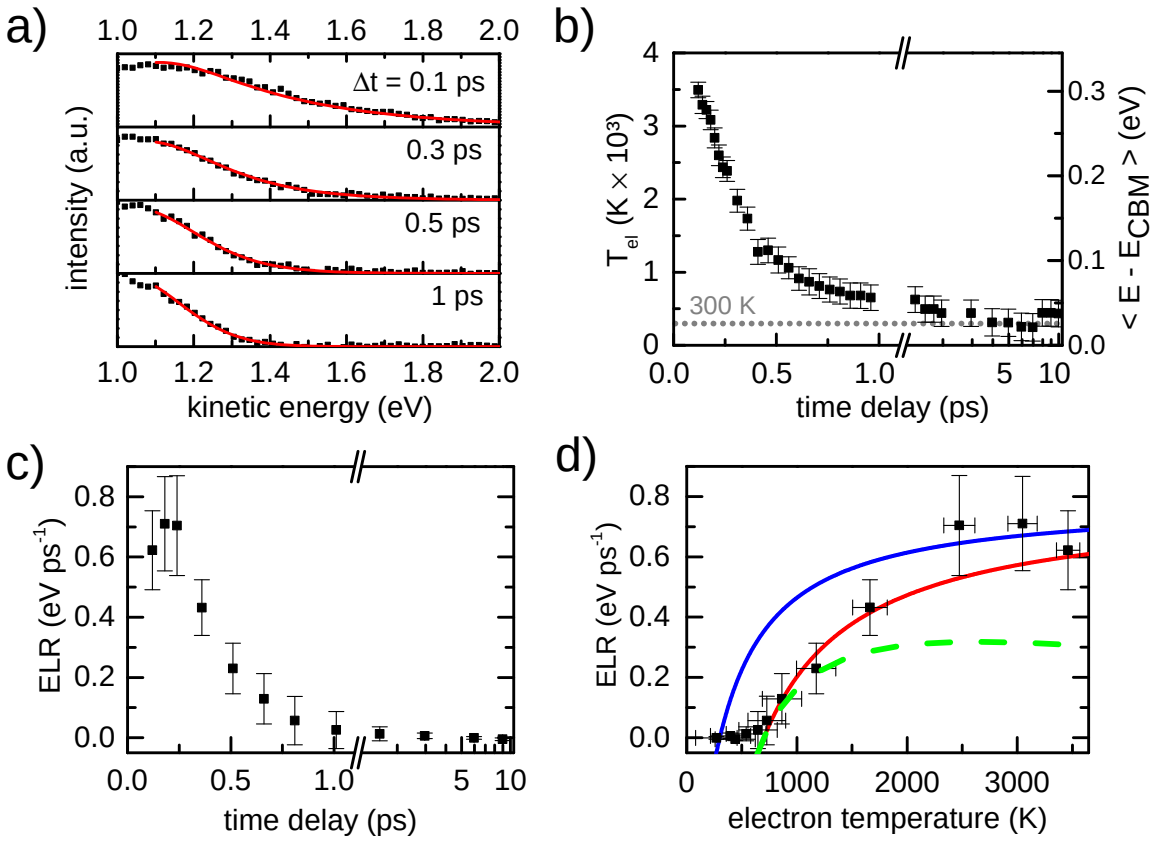

Figure 4.15: Cooling of the electron distribution, for $h\nu_{pump} = 2.60\,\text{eV}$ at CdSe(3 ML)/CdS core/shell NPs.
(a) Kinetic energy spectra for different Δt (black symbols) with fits of the high kinetic energy tails based on a stepwise DOS and the FERMI-DIRAC statistic (red lines).
(b) Resulting electron temperature as function of Δt, obtained from the fits in (a) (left) and the corresponding average electron energy with respect to the CBM (right).
(c) Average ELR per electron as a function of Δt, obtained by calculating the derivation of the average energy curve in (b).
(d) ELR as function of electron temperature (black squares); from (b) and (c). Result of Eq. 4.4 for $\tau = 33\,\text{fs}$ with $T_{lat} = 700\,\text{K}$ (red solid line) and $T_{lat} = 300\,\text{K}$ (blue solid line). For $T_{lat} = 700\,\text{K}$, also numeric results according to Refs. [34, 35] are shown (green dashed line).

4.3.4 Determination of the electron temperature

We now focus in detail on the cooling of electrons pumped with $h\nu_{pump} = 2.60\,\text{eV}$, *i.e.* that have a maximum excess energy of 0.35 eV; Fig. 4.15(a) shows the kinetic energy distribution of the CdSe (3 ML)/CdS core/shell sample, with normalized intensity. The ED of the hot electron gas (consisting of ≈ 5 electrons per platelet on average) can be described by an electron temperature T_e, which is a result of equilibration

in an electron gas by very fast electron-electron scattering[10] that happens typically within less than 100 fs [25–27]. This electron temperature was extracted by fitting the high energy tail of the kinetic energy spectra with the product of the FERMI-DIRAC distribution function and the step-like DOS of a quantum well with infinite barriers,[11] 1.5 nm thickness and an effective mass [16] of $m_{eff} = 0.13\,m_e$.[12] Since the band alignment and doping of the NPs is not clear, $\Delta_{F,CBM}$ is not known (cf. Sec. 2.4). We therefore include the position of the CBM as a fitting parameter. For $\Delta t > 150$ fs we obtained clear fitting results with $E_{kin}^{CBM} = 0.97$ eV. Using the considerations shown in Sec. 2.4 we depict that the CBM is located ≈ 3.55 eV below the vacuum level. With a work function of ≈ 3.6 eV, measured via the secondary electron cutoff, this suggests that the FERMI-level is very close to the conduction band minimum and the sample therefore is rather n-type. For $\Delta t < 150$ fs, there is a small but considerable deviation between the experimental data and our fit (see Fig. 4.15(a)); spectrum at $\Delta t = 0.1$ ps), compared to the almost perfect fit for larger time delays. This might indicate that the electron distribution has not developed to a state of equilibrium within this time interval. However, it could also be related to our DOS approximation that becomes arguable for higher electron energies that play a role at early time delays.

The electron temperature extracted this way is plotted in Fig. 4.15(b) for $\Delta t > 150$ fs as a function of the time delay between pump and probe. We see that T_e drops from 3500 K at $\Delta t = 150$ fs to about 650 K within 1 ps, followed by a significantly slower relaxation on the picosecond time scale. For an accurate determination of the electron temperature, it is necessary to take into account, that the energy resolution of the setup is rather coarse compared to the width of an ED at low electron temperatures, which *e.g.* is only $\Delta_{ED} \approx k_B T_e \approx 0.026$ eV for $T_e = 300$ K. In the fit this was included by convolution with a corresponding Gaussian, and with $\Delta_{res}^{FWHM} = 0.12$ eV the electron temperature asymptotically approaches ≈ 300 K for long pump probe delays. We note that the energy resolution is subject to an unavoidable uncertainty due to several broadening influences. From our considerations on the electron resolution, shown in Sec. 3.2 it can be more or less excluded that the energy resolution is much better than 0.12 eV. Assuming a larger broadening on the other hand results in carrier temperatures below the lattice temperature, which violates the second law of thermodynamics. We therefore conclude that the electron temperature might be slightly underestimated.

Now, we translate this electron temperature into the average electron energy with

[10] See also Sec. 2.3.

[11] See again Sec. 2.2.1 and especially Fig. 2.4 for this approximation.

[12] The quasi-FERMI-level μ_e of the carrier distribution is adjusted automatically for each temperature so that the electron number $n = \int f(E, \mu_e)\rho_{2D}(E)dE$ agrees with the excitation density per platelet, calculated as shown above.

respect to the CBM, given by

$$\langle E - E_{CBM} \rangle = k_B T_e \tag{4.3}$$

for a 2D DOS, based on the infinite quantum well when approximating the FERMI-DIRAC statistics with a MAXWELL-BOLTZMANN distribution.[13] The average energy with respect to the CBM is shown on the right hand ordinate in Fig. 4.15(b), with the error bars representing the statistic error due to the finite electron count rate. $T_e = 3500\,\mathrm{K}$ corresponds to an average energy of $\approx 0.3\,\mathrm{eV}$, while the maximum excess energy that could be reached in this experiment is $0.35\,\mathrm{eV}$, given by the difference between the pump photon energy and the band gap. The fact that we observe a lower value is presumably caused by optical transitions from the lower lying light hole band and by a small part of the excess photon energy used to excite holes, as shown schematically in Fig. 4.13(a). By calculating the derivation of the average energy, we can now deduce the time dependent ELR per electron as shown in Fig. 4.15(c).[14]

Combining the data in Fig. 4.15(b) and (c) yields the ELR as a function of the electron temperature. This is shown in Fig. 4.15(d), revealing a strong dependence of the ELR on the electron temperature. In this temperature regime, the transfer of energy from a hot electron gas to the lattice in polar semiconductors is dominated by the emission of LO phonons. For quantum wells with infinite barriers, RIDLEY has approached this case theoretically [34, 35], assuming a bulk-like LO phonon band with a constant phonon energy $\hbar\omega_{LO}$. This has been shown in detail in Sec. 2.3.2. For the lowest sub-band, the phonon emission and absorption rate τ^{-1} can be approximated as constant if $Lq_{max} \geq 4$, where q_{max} is the maximum momentum of the emitted/absorbed phonon and L the thickness of the quantum well [34]. However, only electrons with $E - E_{CBM} \geq \hbar\omega_{LO}$ can emit phonons, as otherwise there are no states available for the scattered electrons. Based on this, the average ELR per electron was calculated as a function of electron temperature, resulting in

$$\left\langle -\frac{dE}{dt} \right\rangle = \frac{\hbar\omega_{LO}}{\tau} \exp\left(-\frac{\hbar\omega_{LO}}{k_B T_e}\right) \frac{\exp\left(\frac{\hbar\omega_{LO}}{k_B T_{lat}}\right) - \exp\left(\frac{\hbar\omega_{LO}}{k_B T_e}\right)}{\exp\left(\frac{\hbar\omega_{LO}}{k_B T_{lat}}\right) - 1}, \tag{4.4}$$

where T_{lat} is the lattice temperature. The derivation of this equation and the involved

[13] The mean average energy is $\langle E - E_{CBM} \rangle = \frac{\int E f(E,\mu_e)\rho_{2D}(E)dE - E_{CBM}}{\int f(E,\mu_e)\rho_{2D}(E)dE}$. With $\rho_{2D} = \rho_0 \Theta(E - E_{CBM})$ for the first subband (cf. Eq. 2.18) and $f(E,\mu_e) = e^{\frac{\mu_e}{k_B T_e}} e^{\frac{-E}{k_B T_e}}$ Eq. 4.3 directly follows.

[14] As the data point scattering of the raw data leads to extremely noisy signals when calculating the derivation, the amount of data points has been reduced beforehand, making the data more smooth.

approximations are shown in detail in Appendix B. For $T_{lat} \to 0$ the fraction on the right hand side approaches unity and Eq. 4.4 becomes a relation, well-known from textbooks [24] and also valid for bulk semiconductors. The blue line in Fig. 4.15(d) shows the result of Eq. 4.4 for $\tau = 33\,\mathrm{fs}$, $T_{lat} = 293\,\mathrm{K}$ and $\hbar\omega_{LO} = 26\,\mathrm{meV}$ which is the LO phonon energy for CdSe [16]. For $T_e > 2000\,\mathrm{K}$ this agrees with the measured data, but for $T_e < 2000\,\mathrm{K}$ the measured ELR is lower than the calculated curve and furthermore drops drastically at $T_e \approx 700\,\mathrm{K}$. This indicates that the cooling via LO phonon emission is suppressed, either for electron temperatures $< 700\,\mathrm{K}$ in general or after a certain amount of energy has been transferred to the lattice *e.g.* due to the buildup of a hot phonon distribution that slows down further cooling. Interestingly this value is close to the initial temperature of $\approx 650 - 900\,\mathrm{K}$ that Pelton *et al.* measured for platelets of 4 and 5 ML thickness, with $h\nu_{pump} = 3\,\mathrm{eV}$. However, they could not resolve the early very fast relaxation that occurs on the sub-ps timescale. This might indicate that the observed 700 K pose some sort of threshold after which the relaxation continues with a slower speed.

We also plotted the result of Eq. 4.4 for the same parameters as above, but $T_{lat} = 700\,\mathrm{K}$ (red line in Fig. 4.15(d)), thus simulating the case of hot LO phonons. For $T_e < 2000\,\mathrm{K}$, the agreement is quite good, indicating that the formation of a hot phonon distribution might be a valid explanation for the decelerated carrier cooling. These simulations are based on the assumption that the electron-phonon scattering time is constant. However, in our case the wells are pretty thin and $Lq_{max} \geq 4$ is not fulfilled. Consequently, the electron-phonon scattering rates will be energy dependent as shown in Fig. 2.10. We therefore calculated the ELR also numerically, according to Riddoch and Ridley [35], choosing CdSe parameters from standard compendia with $T_{lat} = 700\,\mathrm{K}$.[15] This is shown as green dashed line in Fig. 4.15(d) and also agrees with the measured data for $T_e < 1500\,\mathrm{K}$. For, higher electron temperatures the ELRs are strongly underestimated. We remark that the parameters, used here, apply for bulk CdSe but might be significantly different for thin nanoplatelets with CdS shell. For high excitation energies, especially the approximation of infinite barriers needs to be treated with care [144]. In that respect the agreement is quite impressive, regarding that the calculations are based on just four material parameters (ϵ_∞,ϵ_s,m_{eff},$\hbar\omega_{LO}$).

4.3.5 Electron relaxation for different lattice temperature

Now, we discuss the effect of the lattice temperature on the electron cooling dynamics by comparing tr-2PPE measurements at room temperature to those at 25 K (Fig. 4.16). We show results obtained with CdSe (3 ML) platelets (absorption peak at 2.67 eV), for a pump photon energy of 4.52 eV. At this photon energy, electrons

[15] $\epsilon_\infty = 6.3$; $\epsilon_s = 9.3$; $m_{eff} = 0.13\,m_e$ [16].

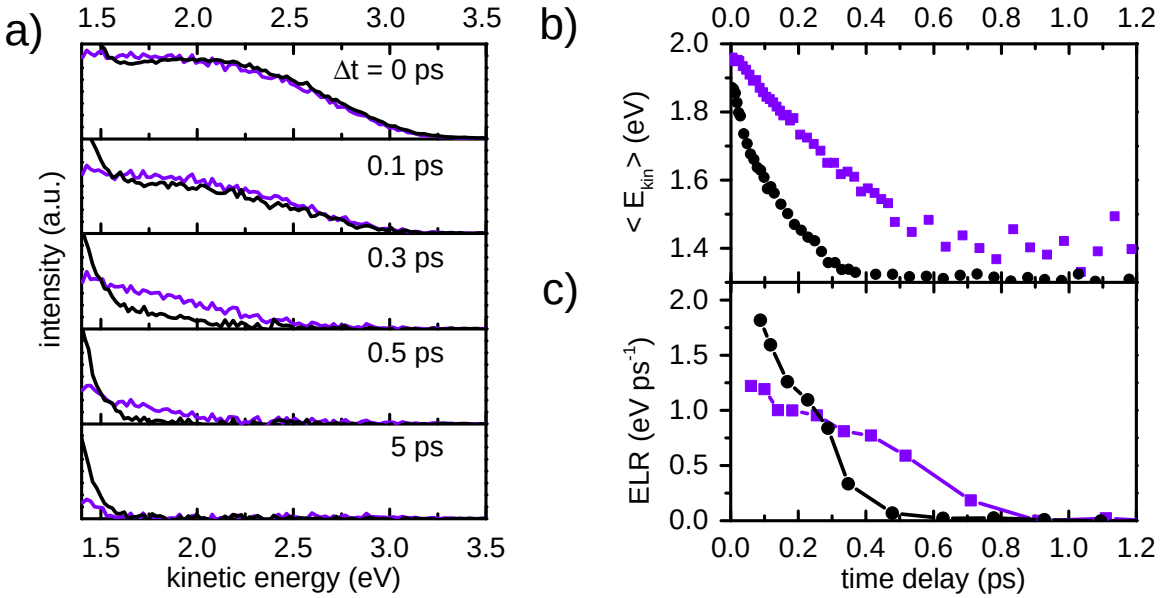

Figure 4.16: Average electron energy and ELR in CdSe (3 ML) nanoplatelets at $T_{lat} = 293\,\mathrm{K}$ (purple) and $T_{lat} = 25\,\mathrm{K}$ (black) for $h\nu_{pump} = 4.52\,\mathrm{eV}$.
(a) Kinetic energy spectra for different pump probe delays.
(b) Average kinetic energy, obtained from (a) as function of time delay. To minimize the influence of secondary electrons, electrons with $E_{kin} < 1.2\,\mathrm{eV}$ were neglected.
(c) Resulting ELRs, obtained by calculating the derivations of the curves in (b).

with high excess energy are created, allowing us to monitor the relaxation process over a wider energy range and at excitation densities of ≈ 1 exciton per nanoplatelet. In Fig. 4.16(a), the kinetic energy distribution is presented for different pump-probe delays. For single electrons the electron temperature is not a proper quantity. Instead, we calculate the average kinetic energy of the photoemitted electrons, given by

$$\langle E_{kin} \rangle = \frac{\sum E_{kin,i} n_i}{\sum n_i} \tag{4.5}$$

where n_i is the number of photoemitted electrons with $E_{kin,i}$. The resulting curves are shown in Fig. 4.16(b). To reduce the influence of secondary electrons, that have a high count rate at low kinetic energies, electrons with $E_{kin} < 1.2\,\mathrm{eV}$ were neglected. For a MAXWELL-BOLTZMANN distribution and a constant 2D DOS, this just leads to a constant offset of the average kinetic energy and

$$\langle E_{kin} \rangle = \langle E - E_{CBM} \rangle + C \tag{4.6}$$

where C is a constant that contains this offset, the photon energy and the vacuum level of the sample. By derivation of $\langle E_{kin} \rangle$, C drops and again the time dependent

average ELR is obtained, which is shown in Fig. 4.16(c) for both temperatures. Error bars would be of comparable size as in Fig. 4.15 but are omitted here and in the following for the sake of clarity.

It is clearly seen that in the first 0.3 ps, where most of the relaxation occurs, the ELR for the measurement at $T_{lat} = 25\,\mathrm{K}$ is significantly higher than for the measurement at room temperature. At low temperatures, less phonons are thermally activated and consequently less phonons are absorbed by the electrons, leading to a faster relaxation. It should be kept in mind that lowering the lattice temperature not only freezes phonon modes but also can influence the electronic properties of the material. According to Tessier *et al.*, the band gap should increase by approximately 0.05 eV [86], when cooling NPs of similar size down to 25 K. Thus, at 25 K lattice temperature the electrons will have slightly less excess energy which in turn should lead to a slower relaxation, in contrast to the faster relaxation that was measured.

The drastic increase in ELR cannot be explained with the model in Eq. 4.4 as for single electrons the assumption of a thermalized electron distribution does not hold anymore. The measured ELR reaches $\approx 1.8\,\mathrm{eVps^{-1}}$ for $T_{lat} = 25\,\mathrm{K}$ and the corresponding phonon emission rates are thus $> \frac{1.8\,\mathrm{eVps^{-1}}}{26\,\mathrm{meV}} \approx 1/15\,\mathrm{fs^{-1}}$ which is significantly faster than the values we found in the measurements, shown in Fig. 4.15. This indicates the importance of alternative decay pathways such as the emission of TO phonons and LO phonon emission via deformation potential scattering that become dominant for high excess energy. Polar optical mode scattering on the other hand decreases due to the electrostatic nature of the interaction as high q values are required for the scattering events [145] (see also Eq. 2.28). Furthermore, intersubband scattering between the $n = 1$ and the $n = 2$ energy levels would have to be considered for a precise theoretical description at such high excess energies. However, a deceleration of the carrier cooling for high energetic electrons in upper subbands as expected for quantum well structures (cf. Sec. 2.3.2) was not even observed for room temperature.

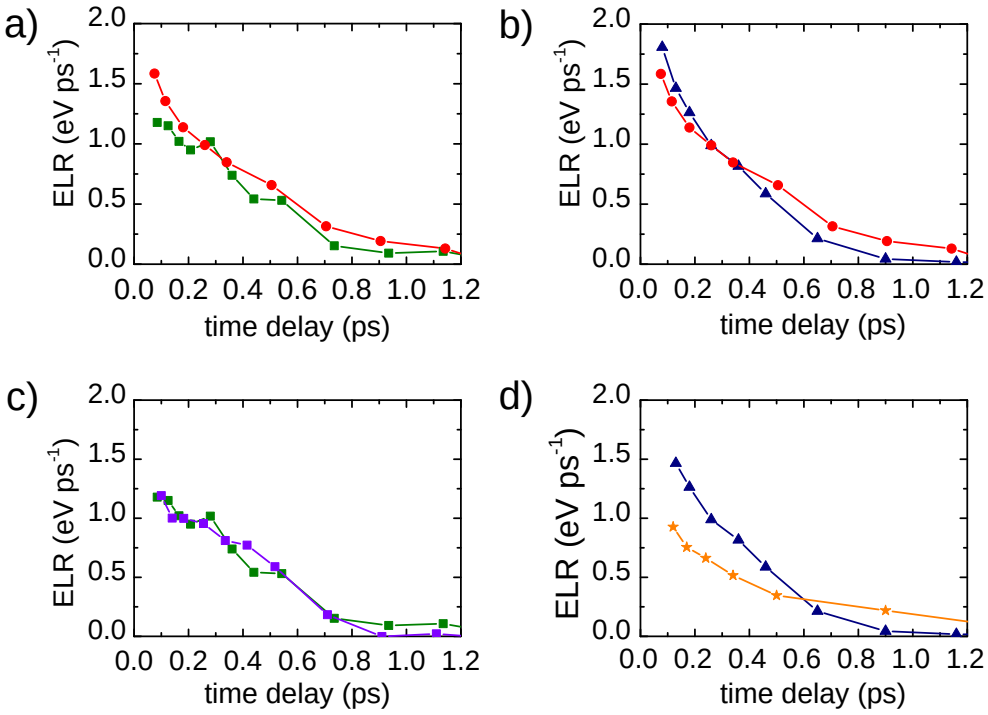

Figure 4.17: Comparison of the ELRs as a function of time delay. The measurements were performed at room temperature with $h\nu_{pump} = 4.52\,eV$.
(a) CdSe(3 ML)/CdS core/shell platelets (red) compared with CdSe(3 ML) platelets (green), both capped with OA.
(b) CdSe(3 ML)/CdS core/shell platelets (red curve) compared with CdSe(5 ML) platelets (blue), both capped with OA.
(c) CdSe(3 ML) platelets with OA capping (green) compared with identical platelets, capped with HDT (purple).
(d) 3.5 nm diameter CdSe QDs with HDT ligands, preventing AUGER relaxation via the VB holes (orange), compared to CdSe(5 ML) platelets with OA capping (blue).

4.3.6 Comparison of different nanoplatelets

In order to investigate the effect of the thickness of the quantum-well platelets and the surface chemistry on the electron energy loss mechanism(s), we performed measurements on different samples; the results are summarized in Fig. 4.17. All measurements were performed with a pump photon energy of $h\nu_{pump} = 4.52\,eV$ and the shown ELRs were deduced in the same fashion as for the measurements with different lattice temperatures. Figure 4.17(a) shows the ELRs for CdSe(3 ML) samples, with and without CdS shell. Overall, we find a strikingly similar ELR in nearly the entire time window, except for the first 200 fs. We note that the first absorption feature of the core/shell system is considerably red-shifted with respect to the core-only platelets. To avoid the thickness-related discrepancies, we also compare results for CdSe(5 ML) platelets

with the CdSe(3 ML)/CdS core/shell platelets in Fig. 4.16(b). As shown in Fig. 4.11, both these samples have their first absorption resonance at nearly the same energy, which means that also the initial excess kinetic energy of the photoexcited electrons should be similar. In this case, the ELR is nearly identical for the entire time span in which cooling takes place. The results presented in Fig. 4.17(a) and (b) (and several repetitions of these experiments with other samples) show that the ELR in the CdSe platelets does not change by the presence of a CdS shell around the platelets. In Fig. 4.17(c) we investigate whether the trapping of valence band holes at the surface has any effect on the electron cooling. We compared bare CdSe(3 ML) platelets with OA capping with the same platelets, capped with HDT that has shown to act as hole trap [95]. As demonstrated in the previous section, for quantum dots this ligand exchange has a heavy impact on the electron dynamics and prevents energy donation from the electron to the hole.[16] It is obvious from Fig. 4.17(c) that in the case of platelets we find no difference in the ELR between the samples, which indicates that AUGER-type electron cooling is not important in the case of 2D platelets. This mechanism seems to be unable to compete with direct electron decay via the conduction band by LO-phonon emission. In Fig. 4.17(d), we compare the ELR of CdSe(5 ML) nanoplatelets with that of CdSe quantum dots of 3.5 nm diameter with their lowest optical transition (2.18 eV) being nearly identical to that of the nanoplatelets (2.25 eV). HDT was used as capping for the QDs, to suppress the AUGER-type cooling pathway, as demonstrated in Sec. 4.2. Our results show that the ELR for the platelets is significantly higher and hence, cooling via the continuous 2D conduction band is much faster than in QDs. This effect is even more pronounced, when comparing our results on nanoplatelets with CdSe QDs with HDT, when the second lowest electron level $1P_e$ is photoexcited resonantly [103, 116].

4.3.7 Discussion

These results show that in CdSe platelets of $3-5$ ML thickness hot electrons lose most of their excess kinetic energy in the first picosecond after excitation. The ensuing further cooling is markedly slower and the minimum of the CB is reached within 10 ps. The energy loss rate, thereby, strongly depends on the average energy or temperature of the electron gas in the platelets. The results show no measurable dependence on the platelets thickness and the surface layer around the platelets, whether it is a different ligand or a thin layer of CdS. The nature of our measurement does not

[16] As we expect that the surface chemistry of the facets of the platelets is very similar to that of nanocrystals, we anticipate that holes are trapped at the surface of thiol-capped platelets as well. An indication for that is presented in Ref. [91], where it was reported that the photoluminescence quantum yield drops to half the value if the platelets are recapped with thiols.

allow to evaluate minor changes in relaxation rate *e.g.* due to different DOS in the lowest subband [34, 146] or due to a change in the dielectric constant by variation of the capping. Nevertheless, if the major decay mechanisms were surface-related our experiments should show significant variations in the measured ELRs as found for the CdSe quantum dots. It is therefore concluded that surface-related decay mechanisms play a secondary role and instead fast phonon-assisted cooling within the platelets is the dominant decay mechanism. Also no evidence for AUGER-type electron-to-hole energy donation was found in experiments, where the oleic acid capping was replaced with HDT. Instead the ELR does not change notably, indicating that electron-phonon scattering via the FRÖHLICH-interaction happens on a significantly faster time scale.

All the above results imply that the electron cooling along the 2D bands of the nanoplatelets by emission of LO phonons is the main cooling mechanism. For the state directly after photoexcitation, the dependence of the ELR on the electron temperature can be described well with a simplified model for polar-mode scattering in 2D systems. Good agreement is found with a scattering rate of $\tau = 33\,\mathrm{fs}$, which is close to the 15 fs calculated for FRÖHLICH interaction in 2D systems, using basic assumptions[17] and standard CdSe parameters [16]. However, this model cannot describe a drastic breakdown in ELR that we measure for $T_e < 700\,\mathrm{K}$. This might be explained by a strong reduction of the LO phonon emission rate for electrons with $T_e < 700\,\mathrm{K}$. A different explanation is the build-up of a distribution of hot LO phonons during the cooling process: by reabsorption of these hot phonons the cooling is considerably slowed down. When approximating this hot phonon distribution with a lattice temperature of $T_{lat} = 700\,\mathrm{K}$, good quantitative agreement is found between model and data in this electron temperature range. Slow decay attributed to the hot phonon bottleneck is commonly reported for experiments with 2D and 3D CdSe; the ELR then mostly reflects the lifetime of the optical phonons that is estimated to be $6 - 9\,\mathrm{ps}$ [135]. In this respect, VENGURLEKAR *et al.* reported that the cooling rates in bulk CdSe at cryogenic temperatures [135] depended strongly on the excitation intensity; the ELRs being more than an order of magnitude lower than measured in our experiments. Also the measurements of PELTON *et al.* on CdSe nanoplatelets [133] exhibit a decay constant of several tens of picoseconds for the electron cooling from 700 K to room temperature, hence, much slower than observed here. The difference must be caused by the excitation intensities resulting in > 100 excitons/platelet in Ref. [133], while here the excitation density leads to ≈ 5 excitons/platelet and the ELR reduction due to hot phonons increases with increasing excitation density [135].

[17] According to SHAH [24] the characteristic rate for polar optical phonon scattering in 2D semiconductors is $\frac{e^2\sqrt{2m_{eff}\hbar\omega_{LO}}}{8\hbar^2}\left(\frac{1}{\epsilon_r(\infty)} - \frac{1}{\epsilon_r(0)}\right)$.

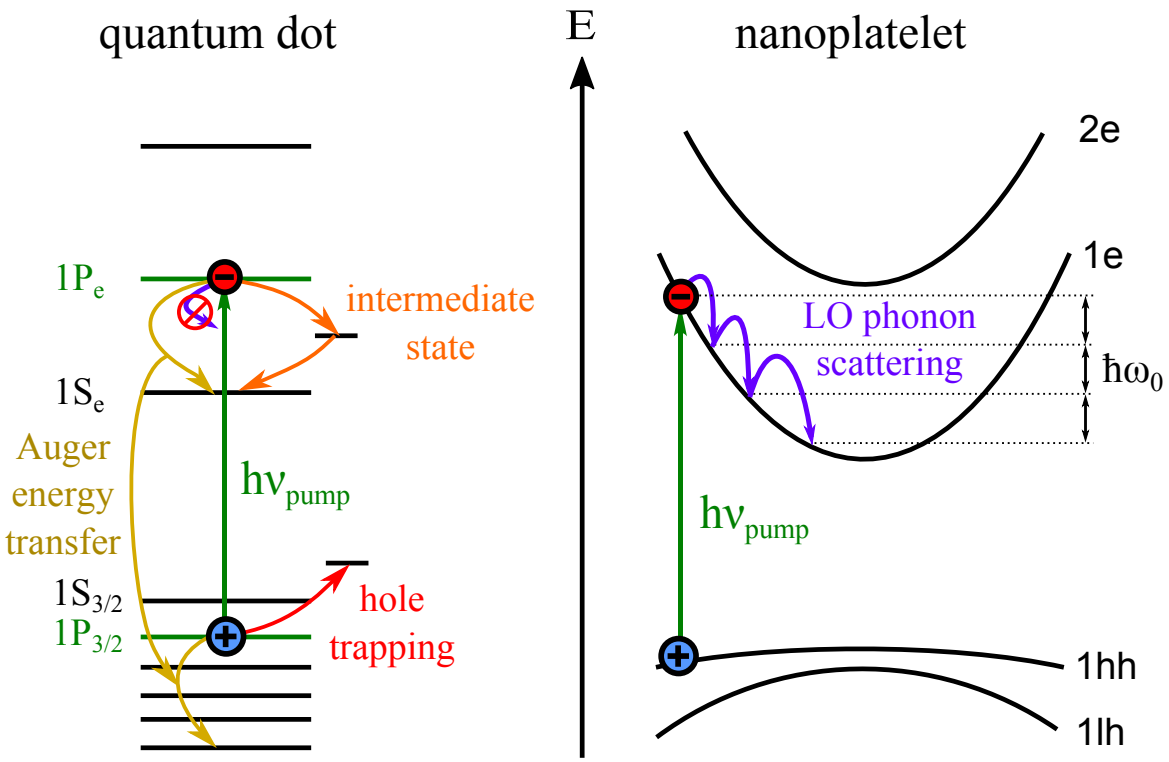

Figure 4.18: Comparison of the electron relaxation in quantum dots (left) and nanoplatelets (right). In nanoplatelets, electrons can reach the CBM by the emission of single LO phonons (purple arrows). In QDs this mechanism is not possible since the energetic distance between the electronic levels is larger than the LO phonon energy. Instead, the electron reaches the CBM *e.g* by AUGER-like energy transfer to the hole (yellow arrows) or via scattering with intermediate states (orange arrows) or other not fully-eluded mechanisms. The AUGER-like mechanism can be suppressed via hole trapping (red arrow).

4.4 Comparison of the electron dynamics in 0D and 2D CdSe nanostructures

The dynamics of hot electrons in CdSe nanoplatelets and quantum dots show fundamentally different characteristics. The main findings are summarized in Fig. 4.18. In CdSe QDs which are capped with oleic acid the electrons relax to the CBM with a time constant of < 300 fs. Exchanging the oleic acid for hole scavenging HDT substantially reduced the velocity of the electron relaxation. This can be explained with an AUGER-mechanism that is suppressed if the hole is removed from the quantum dot. The competition of AUGER-relaxation and hole trapping was described with a rate model and has just recently been verified by a theoretics group, revealing excellent agreement with the measured data [119]. In the absence of the hole, the relaxation is

significantly slowed down. Evidence was found that the relaxation takes place via intermediate states between the lowest conduction band states. These states are likely to be associated with the interface or the ligands in agreement with other studies, having shown that the choice of shells and ligands allows to extend the hot carrier lifetime up to 1 ns [10, 104]. This shows the principle existence of a phonon bottleneck and the possibility to suppress phonon emission for discrete energy levels.

This is in sharp contrast to the observations on 2D CdSe nanoplatelets. Here the cooling happens on similar time scales as in bulk semiconductors and for low excess energies most of the relaxation is finished within 500 fs. No considerable dependence on the thickness and the nature of the surface is observed — be it a CdS capping or the hole-scavenging ligand HDT. This demonstrates that AUGER-like energy transfer to the hole or relaxation via ligand or surface states has no considerable contribution to the electron relaxation. Instead evidence for electron cooling via LO phonon emission — as shown on the right hand side of Fig. 4.18 — is found in various form:
(i) The energy-dependent dynamics can be described with a simplified model for LO phonon scattering.
(ii) The rate of electron cooling increases for lower lattice temperatures, indicating less absorption of LO phonons by the electrons.
(iii) The cooling slows down after ≈ 1 ps and happens on a time scale of tens of picoseconds. This is even more pronounced for higher excitation densities [133] and indicates the reabsorption of hot LO phonons, that were emitted by the cooling electrons.

In conclusion, the results show that hot electron relaxation in nanostructures is determined by the geometry as well as the interface properties. In view of PV concepts based on hot carriers, the results favor quantum-dot-based designs due to the slower relaxation. However, the surface and the capping have a pronounced influence on the carrier lifetimes in these systems and the underlying mechanisms are still discussed controversial [63, 104, 118]. Surface-related dynamics in these and comparable systems are mostly investigated by comparing results from differently prepared samples. The actual processes often remain vague and with most experimental methods, bulk and surface contributions are difficult to discriminate. In the next part of the thesis, well-defined III-V semiconductor surfaces are investigated with (tr)-2PPE. These surfaces are prepared with epitaxial methods and have been subject to an in-depth characterization. Thus, they serve as excellent model systems to study the energetics of interface/surface states and their influence on the dynamics of hot conduction band electrons.

5 Electronic structure and dynamics at III-V semiconductor surfaces

In this chapter 2PPE is employed to study the energetics and electron dynamics at III-V semiconductor surfaces. At first an introduction to III-V semiconductor surfaces—in particular of GaP(100) and InP(100)—is given. The atomic and electronic structures are described and the growth and preparation of the investigated samples is explained. In the next section, studies on the electronic structure of two different surface reconstructions of GaP(100) are presented, combining 2PPE and RAS. This is followed by a time-resolved investigation of the scattering between bulk- and surface states at the In-rich InP(100) surface reconstruction. Finally, these results are summarized. Parts of this chapter have been reprinted in part, with permission from Phys. Rev. B 89, 165312 [147],

5.1 Introduction to III-V semiconductor surfaces

Most electronic and optical properties of semiconductors are well described with the electronic structure of the bulk material (cf. Sec. 2.1). However, if photoexcited charge carriers are put into play, as in every solar cell, the interface or surface properties become very important. Most famous or infamous is probably the recombination of minority carriers via mid-gap surface states that limits the life times of many photovoltaic devices [149, 150] and poses highest requirements on the preparation and passivation of these surfaces. In a similar way, electronic states that are isoenergetic with the conduction band (commonly also referred to as surface resonances) might influence electron cooling. These effects will become even more important for nanostructured material with a considerable fraction of the atoms allocated at the surface or interface. Evidence for this was found *e.g.* in the previous chapter for CdSe QDs. Here, fast electron relaxation via intermediate states was observed, which are most likely associated with the interface or the ligands. An appropriate material for the study of surface properties are III-V semiconductor surfaces that can be prepared via MOVPE with very high quality. This and the considerable basis of previous studies makes them ideal model systems for the investigation of the electronic structure and the dynamics of electrons at the surface.

5.1.1 III-V semiconductors

III-V semiconductors are essential components of electronic and opto-electronic devices like—but by far not limited to—lasers, light-emitting diodes (LEDs) and solar cells. The ability to alloy different binary materials to ternary or quaternary compounds offers a large flexibility to tune the physical properties to fulfill the particular demands. Advanced epitaxial methods such as MOVPE or MBE, allow for a high surface and interface quality and can be used to grow layered structures in a large variety of configurations, including quantum wells on a single nanometer scale. However, fundamental limits are still posed by the accumulation of strain in lattice-mismatched heterostructures that beyond the critical thickness leads to strain relaxation and the accompanied formation of defects.

The typically employed components are indium, gallium and aluminum for the group III elements and arsenic, phosphorus, antimony and nitrogen for the group V elements. Most of the compounds crystallize in the zinc blende crystal structure that consists of two fcc sub-lattices of group III, respectively, group V atoms, that are shifted with respect to each other by $\{a/4, a/4, a/4\}$. Here a is the lattice constant, which for room temperature is 5.45 Å for GaP, and 5.87 Å for InP [151]. The (binary) nitrogen containing compounds are no less important but play a peculiar role and will not be considered in this work, since, under normal circumstances, they crystallize in the hexagonal wurtzite structure and thus can have fundamentally different properties.

5.1.2 Electronic properties of InP and GaP

The zinc blende structure for III-V semiconductors is formed by covalent as well as ionic tetrahedrally oriented binding. The ionic part is caused by electron transfer from the group III to the group V atoms. The covalent character is determined particularly by s^1p^3 hybridization of the s^2p^1 and s^2p^3 orbitals from the group III, respectively, group V atoms and the resulting band structure near the center of the BRILLOUIN-zone is determined by these hybrid states. Calculated band structures of InP and GaP are shown in Fig. 2.1, respectively, Fig. 5.1. At Γ the six p orbitals form the three upper valence bands (heavy hole (hh), light hole (lh) and split-off (so); see Sec. 2.1) as well as the second lowest conduction bands, while the lowest conduction band originates from the two atomic s-orbitals [152, 153]. These bands are twofold degenerate due to the electron spin. The valence band maximum for III-V semiconductors is at the Γ point and there are three different local CBMs: one at Γ, which is also the global minimum for InP, one at L and one near X, the latter two being four- and threefold, respectively, since they occur multiple times inside the BZ as can be seen in Fig. 2.1. For GaP the global CBM is at $\mathbf{k} = \{0.95, 0, 0\}\,\frac{2\pi}{a}$ [151], making it an indirect semiconductor with a band gap of $E_g = 2.26\,\text{eV}$ at room temperature [154]. The band shape near the

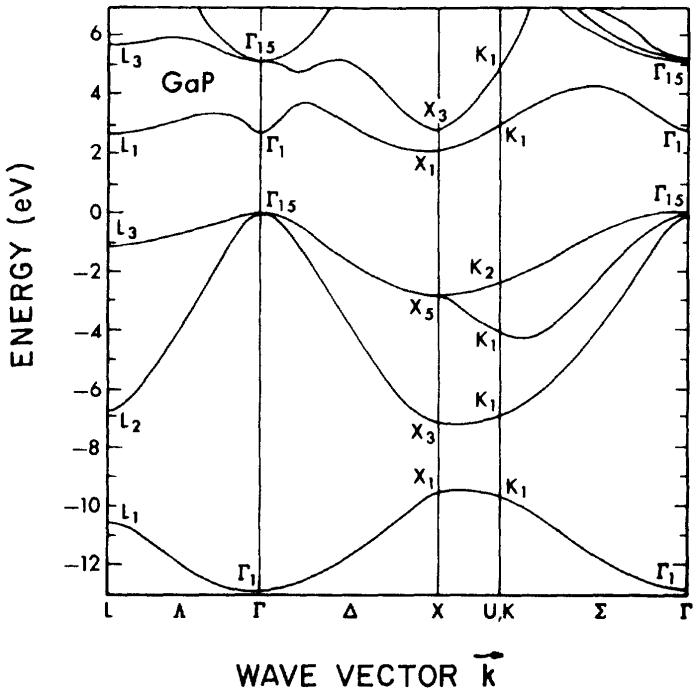

Figure 5.1: Band structure of gallium phosphide, calculated with the pseudopotential method (Reprinted with permission from [12] © (1976) American Physical Society.).

minimum can be described with [155]

$$E(\mathbf{k}) = \frac{\hbar^2 k_{\parallel}^2}{2m_l^*} + \frac{\hbar^2 k_{\perp}^2}{2m_t^*} - \sqrt{(\Delta/2)^2 + \Delta_0 \frac{\hbar^2 k^2}{2m_1^*}}, \tag{5.1}$$

where m_l^* and m_t^* are the longitudinal and transversal effective electron masses and Δ_0, Δ and m_1^* are specific band parameters. The lowest direct interband transition for GaP is at Γ with $E_g^{dir} = 2.74\,\mathrm{eV}$ at room temperature. For InP this transition is equivalent to the band gap, which at room temperature is $E_g = 1.34\,\mathrm{eV}$ [32].

5.1.3 Surface reconstructions of InP(100) and GaP(100)

If a zinc blende crystal is cut perpendicular to the [100] direction, then the uppermost layer at the cutting plane contains only atoms of one of the two components. Thus, one distinguishes between group-III (In,Ga) or group-V (P)-rich surfaces, which can be achieved under different preparation conditions. However, the termination of the bulk structure is accompanied with the breaking of covalent bonds. As these dangling bonds are energetically not favorable, the surface components reconstruct in order to minimize the associated energy [156]. The surface reconstructions that

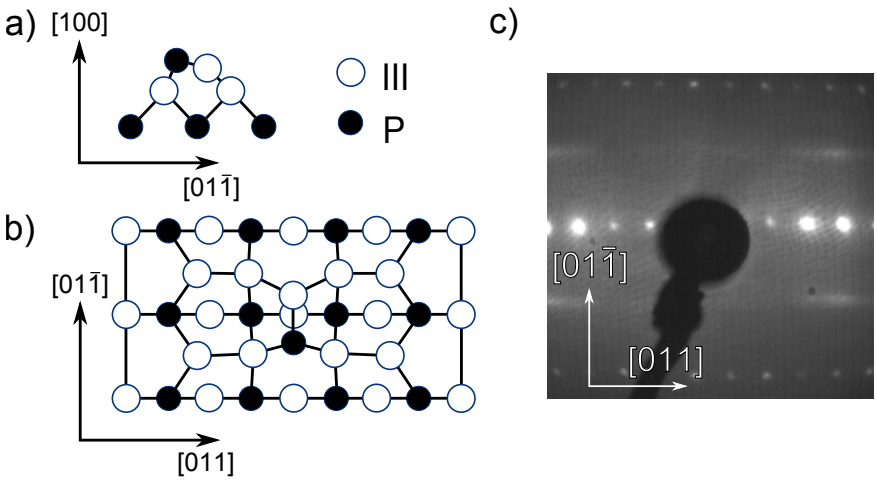

Figure 5.2: Atomic structure of the III-rich (2×4) *mixed-dimer* surface reconstruction, according to FRISCH *et al.* [163]. (a) side view, (b) top view and (c) LEED picture of the Ga-rich GaP surface, recorded with 90 eV electron energy.

can be prepared for GaP(100) with MOVPE include the Ga-rich (2×4) *mixed-dimer* surface reconstruction [157, 158] and the P-rich $(2 \times 2)/c(4 \times 2)$ surface reconstruction. Both surface reconstructions have also been successfully prepared and identified for InP(100) [159–161]. For simplicity these reconstructions will be referred to as *Ga/In/III-rich* and *P-rich* surfaces, respectively.

The III-rich *mixed-dimer* (100) surface reconstruction

Different surface reconstructions have been discussed for the III-rich (2×4) (100)-surfaces of InP [162] and GaP [163], one of them the *mixed-dimer*-reconstruction, which according to calculations is the ground state of the III-rich surfaces [163]. The unit cell is characterized by mixed dimers, consisting each of a group-III- and a phosphorous atom, on top of a layer of group III-atoms as shown in Fig. 5.2(a,b). The according low-energy electron diffraction (LEED) pattern (Fig. 5.2(c)) clearly indicates that the surface is (2×4)-reconstructed. For InP, the LEED pattern looks similar [164]. Further evidence that the prepared surfaces reconstructions are identical with the one in Fig. 5.2(a,b) was obtained with scanning tunnel microscopy (STM) measurements [158, 164, 165].

For InP, the electron structure has already been investigated in great detail. Theoretical DFT calculations with GW approximation have been performed by SCHMIDT *et al.* to determine the localization, the energies and the dispersion of several surface state bands [58, 162]. The results have been compared to experimental reflection anisotropy spectroscopy (RAS) data and reasonable agreement was found [58, 162]. The lowest lying conduction band states are labeled C1 and C2 and correspond to

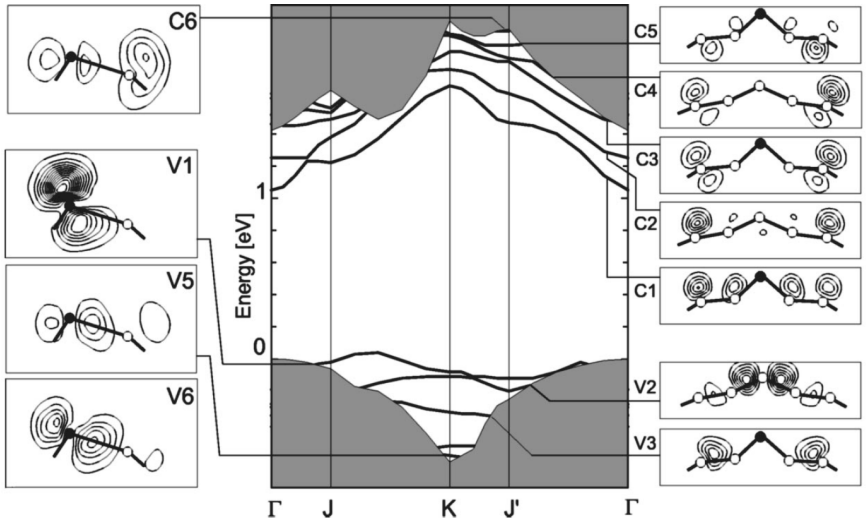

Figure 5.3: Surface band structure of the Ga-rich surface, calculated by SCHMIDT *et al.* with DFT-LDA theory [167]. The shaded regions correspond to the projected bulk band structure and the underestimated band gaps are an artifact of this approach. The squared wave functions are shown in panels on the left and right hand side with a contour spacing of 10^{-3} bohr^{-3}(Reprinted with permission from [167] © (2000) American Vacuum Society).

In dangling bonds. The highest lying valence band states are V1, related to bonds between first and second layer cations, and V2, corresponding to the dangling bond of the *mixed-dimer* P atom. [58]. The states V1, C1 and C2 could also be identified by TÖBEN *et al.* with single-beam 2PPE. Accordingly, V1 is located 0.1 eV below the VBM and C1 and C1 lie 0.25 eV, respectively, 0.85 eV above the CBM [124].

Similar calculations were done for the Ga-rich GaP(100) surface [166] and can explain most or the prominent features in experimental RA spectra. According to these calculations, the highest occupied surface state V1 lies slightly above the VBM and is associated with the dangling bond of the *mixed-dimer* P atom (as V2 for InP). V2, corresponding to the bonds between first and second layer cations (as V1 before), is located slightly below the VBM [166]. The lowest unoccupied states C1 and C2 are again related to Ga dangling bonds and located in the upper part of the band gap. Unfortunately, there are no values reported for GaP. The surface band structure calculated by SCHMIDT *et al.* is shown in Fig. 5.3 but only contains qualitative information as the bulk bandgap is drastically underestimated. The surface band shapes are similar to InP with the conduction bands having their minima near the SBZ center. Experimental data on surface states of GaP(100) surfaces are available for other surface reconstructions [168] but not for this particular surface reconstruction.

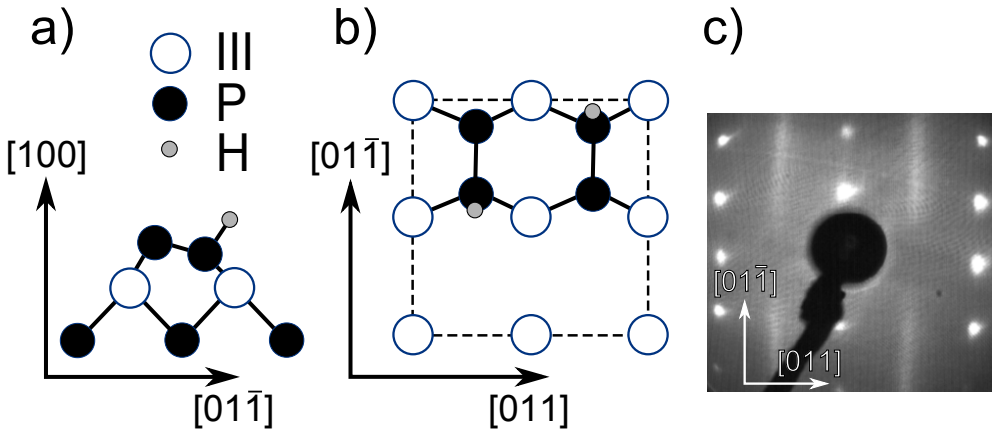

Figure 5.4: Atomic structure of the P-rich $(2 \times 2)\,/c\,(4 \times 2)$ surface reconstruction, according to Hahn *et al.* [59]. (a) side view, (b) top view and (c) LEED picture of the P-rich GaP surface, recorded with 90 eV electron energy.

The P-rich $(2 \times 2)\,/c\,(4 \times 2)$ (100) surface reconstruction

The P-rich $(2 \times 2)\,/c\,(4 \times 2)$ surface reconstruction—often also referred to as (2×1) / (2×2) reconstruction—can only be grown in a hydrogen containing ambient [158, 161, 169, 170] since it is capped by hydrogen atoms that attach to the uppermost layer of phosphorous atoms [59]. For the samples prepared here this requirement is fulfilled by the carrier gas H_2 that is used for the MOVPE process. A LEED image of the P-rich surface is shown in Fig. 5.4(c), exhibiting a (2×1) pattern with half-order streaks in the $[01\bar{1}]$ direction. A schematic of the surface unit cell, which accounts for the (2×1) pattern is shown in Fig. 5.4(a,b). Phase shifts between rows of such unit cells lead to $c\,(4 \times 2)$ reconstructed domains [171].

DFT calculations of the electron structure of the P-rich GaP surface have been performed by Hahn *et al.* and the resulting surface band structure is found in Ref. [59]. Particularly interesting for the evolution of RA spectra is the surface state V1 in the vicinity of the VBM, stemming from the lone pair of the *unbuckled* top phosphorous atom. There is also a series of conduction band surface states that are related to bonds of the top phosphorous atoms with each other and the second layer atoms but also extend to the third and forth atomic layers [59]. Unfortunately, no actual energetic positions have been reported for this surface.

5.1.4 Sample preparation

The samples were prepared with MOVPE. In this technique, one or more metal-organic precursors are mixed with a carrier gas (typically hydrogen) at pressures between 50 mbar and 950 mbar. The carrier gas is directed over the hot substrate

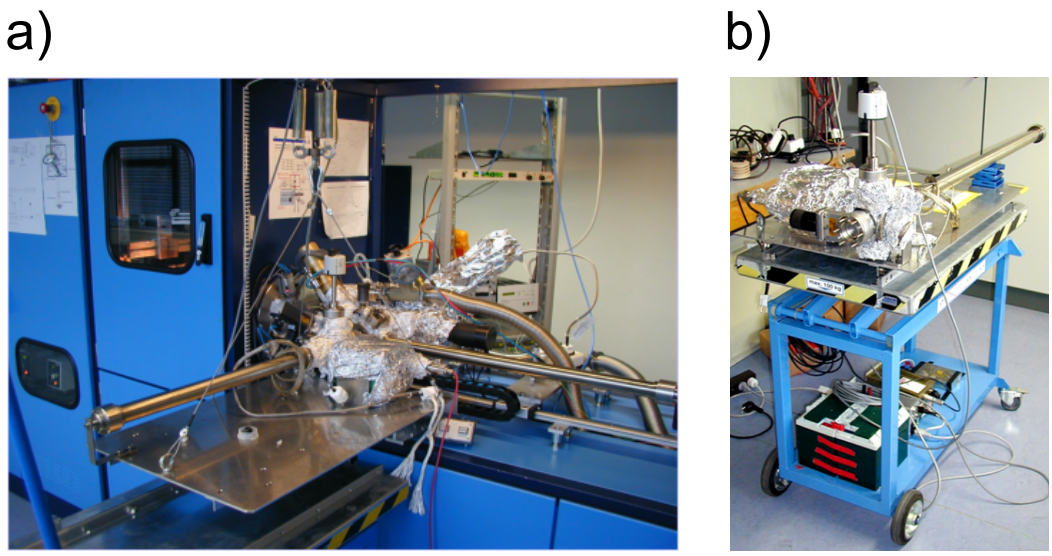

Figure 5.5: UHV shuttle system. (a) Attached to the MOVPE reactor. (b) Free standing.

surface leading to the decomposition of the precursors and the deposition of the corresponding inorganic components at the crystal lattice of the sample. For this study, a modified [172] commercial MOVPE reactor (*Aixtron AIX 200*) was employed. The substrate is clamped to a molybdenum sample carrier that is fitted into a graphite suscepter during the process, which is heated by illumination with infrared lamps.

UHV transfer

A UHV chamber was attached directly to the reactor exit and could be switched from nitrogen ambient to UHV within seconds after a fresh-prepared sample was fetched there from the reactor with a manipulator. This allowed for contamination-free surfaces as has been shown with several surface science techniques such as XPS, UPS, LEED, STM and FOURIER-transform infrared spectroscopy [158, 170, 173, 174]. As these experiments, as well as the 2PPE measurements are conducted in separate UHV chambers, a custom-designed UHV shuttle system [172] with a base pressure of $< 4 \times 10^{-10}$ mbar was used to transfer the samples directly to these setups, without leaving the UHV. Pictures of this transfer system are shown in Fig. 5.5.

A *LayTec EpiRAS* RA spectrometer was mounted above the MOVPE reactor and aimed directly onto the sample inside. Thus, the growth process could be monitored and controlled *in situ*, as the RA spectra of well-defined surfaces are well known due to elaborate benchmarking experiments [56, 175, 176]. A second RA spectrometer of the same model could be mounted to the UHV chamber where the 2PPE measurements were conducted, thus allowing us to measure under identical conditions (see Chap. 3).

Growth and surface preparation

Gallium phosphide The investigated GaP samples were grown on $\approx 2 \times 1\,\mathrm{cm}^2$ pieces of GaP(100) wafers, purchased from the *ComSeCore* company. Mostly, sulfur-doped wafers were used with a background doping of $n = 7.8 \times 10^{17}\,\mathrm{cm}^{-3}$. For dedicated p-type samples as a reference, zinc-doped wafers were used, with a doping of $p = 5 \times 10^{17}\,\mathrm{cm}^{-3}$. For all GaP samples, GaP buffer layers of about 600 nm thickness were grown on the wafer to ensure flat doping profiles near the surface. The growth was conducted with tertiarybutylphosphine (TBP) and triethylgallium as precursors without additional doping components for the samples on n-type substrates. For the films, grown on p-type substrates, diethylzinc was used to achieve a doping of $p = 5 \times 10^{17}\,\mathrm{cm}^{-3}$, as determined with a capacitance–voltage (CV) profiler. The nominally undoped films had a background doping of $p < 5 \times 10^{15}\,\mathrm{cm}^{-3}$. However, the CV method was not very accurate at such low doping, so that additional investigations were necessary, as will be discussed in the next section.

For deoxidation, the samples were annealed at 650° C with constant TBP flow to stabilize the surface, while the actual homoepitaxial film growth was conducted at 620° C. To achieve a P-rich surface reconstruction, the sample was cooled down afterwards with TBP stabilization and annealed at 420° C without TBP. For the preparation of Ga-rich surfaces, samples were subsequently annealed for 5 minutes at 700° C without any precursor supply. Given temperatures were measured with a thermocouple placed inside the susceptor. During all steps, RAS was used to control the surface preparation *in situ*. Detailed descriptions of the preparation steps have been reported elsewhere [55, 158, 172, 175].

Indium phosphide The InP samples were grown on sulfur-doped InP(100) substrates ($n = 2 \times 10^{18}\,\mathrm{cm}^{-3}$). After a deoxidation step, where the sample was annealed at 600° C with constant TBP flow for about 8 min, an InP film of about 600 nm thickness was grown with the precursors TBP and trimethylindium at 580° C. The absence of additional doping components resulted in a background doping of $n = 5 \times 10^{15}\,\mathrm{cm}^{-3}$ [124]. Cooling down the sample afterwards under absence of TBP flow resulted in a sample with the In-rich surface reconstruction as verified *in situ* with RAS.

5.2 Electronic structures of GaP(100) surface reconstructions

While the morphologies of GaP(100) surfaces have been studied in great detail [158, 163, 164], the electronic structures have mostly been an issue for theoretical treatment [59, 166, 177] and little experimental data is available [168, 169]. However, GaP increasingly receives attention as absorber material for hydrogen generation by photoelectrolysis [178], notably because of its wide band gap in comparison to other III-V semiconductors. This approach might be even more promising, when diluting GaP with nitrogen, leading to the formation of a direct band gap [179–181]. The effect of oxygen and water adsorption on the electronic structure of GaP(100) surfaces was recently calculated [182, 183] and for water absorption also investigated experimentally [184]. Here, two-photon photoemission spectroscopy (2PPE) with femtosecond laser pulses is used to study the electronic structure of the well-defined and well-established [158, 176] Ga-rich (2×4) and P-rich $(2 \times 2)/c(4 \times 2)$ surface reconstructions of GaP(100). By comparing two different surface reconstructions, surface- and bulk-related features can be clearly distinguished and the differences between the surface electronic structures can be discriminated. Besides measuring clean surfaces immediately after the preparation, the same samples were also studied after controlled exposure to oxygen. This enables the identification of dangling-bond states and the study of the effect of adsorbed oxygen on the surface electronic structure, allowing a comparison to recent theoretical calculations [182]. Also RAS, an optical method that is highly sensitive to surface state transitions [54, 58], was employed under identical experimental conditions as the 2PPE experiments. The results of both methods are compared.

5.2.1 Characterization with RAS

RA spectra of the P- and Ga-rich surface reconstructions, before and after O_2 exposure are shown in Fig. 5.6. The principles of this method were described in Sec. 3.3. Features in the RA spectra can be associated with electronic transitions [54] that are either directly related to surface states or involve surface-modified bulk states [185]. The RA spectra of the samples investigated here show excellent qualitative agreement with previous MOVPE-grown samples [172, 186–188], insuring well-defined and reproducible surfaces available to the 2PPE experiments. The Ga-rich surface is very sensitive to background pressure even in UHV, so that surface state-related features start to decrease continually after preparation. The RAS signal of the Ga-rich surface, shown in Fig. 5.6, was measured after the 2PPE experiments. This results in surface state-related peaks with an unavoidable lower amplitude, compared to measurements

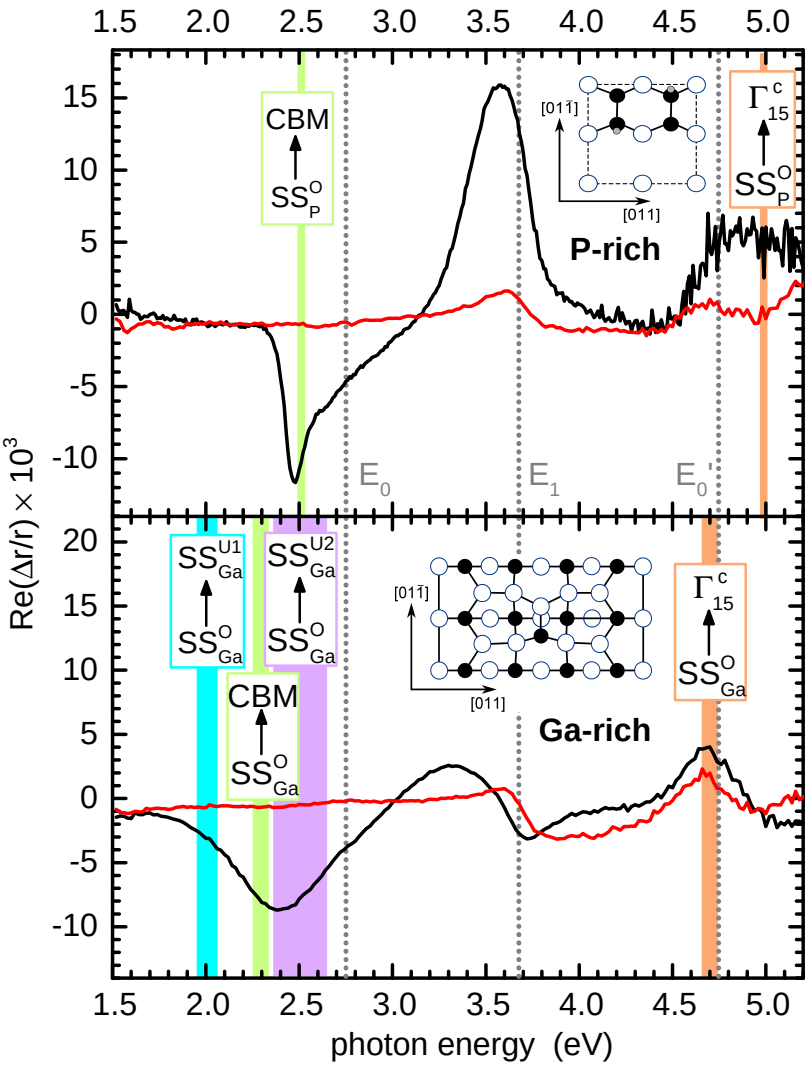

Figure 5.6: RA spectra of the Ga-rich and the P-rich surface reconstruction, clean (black) and after O_2-exposure (red). The insets show the atomic models of the Ga- and the P-rich surface reconstructions according to FRISCH *et al.* [163] and HAHN *et al.* [59], respectively. Dashed lines indicate critical point transitions and vertical bars indicate energy differences between occupied and unoccupied surface states, as well as between occupied surface states and selected bulk states, as identified with 2PPE.

shown in former publications that were performed directly after preparation [55]. To ensure that no spectral shifts occurred, RA spectra were also recorded in between 2PPE measurements.

DFT calculations with local density approximation (LDA) by SCHMIDT *et al.* [166] and HAHN *et al.* [59], revealed that the features up to $h\nu \approx 3.7\,eV$ are completely related to surface state transitions for both surfaces. We see clearly that these features vanish after O_2 exposure for both surface reconstructions, which indicates the entire

quenching of surface states. For energies $h\nu \geq 3.7\,eV$ we also noticed a drop in amplitude and a change in shape, but no complete disappearance of the signal. This also agrees with the calculations [59, 166] that predicted a signal in this energy region, which is related to surface-modified bulk transitions located at atomic layers below the surface [58] and thus likely unaffected by oxygen exposure. For the Ga-rich surface, the peak at ca. 4.7 eV, in particular, was assigned to an anisotropic modification of the E_0' bulk transition [166]. The change of the broad feature between 3.5 and 4.5 eV at the Ga-rich surface and its slight shift towards higher energies could be due to the formation of Ga-O-Ga or Ga-O-P bonds [182, 184], but is not discussed here.

5.2.2 Band alignment

To allocate surface states, appearing in the 2PPE spectra energetically with respect to the bulk bands, it is necessary to know the position of the FERMI level relative to the bulk bands at the surface. The procedure for this was illustrated in Sec. 2.4. Here, this was not trivial, since we deliberately did not dope the samples to ensure a surface quality as high as possible. With CV measurements we found $n < 10^{15}\,cm^{-3}$ for the background doping level that is determined by impurities, introduced during growth or diffusing from the sulfur-doped substrate. However, at such low doping concentrations the uncertainty of the CV-method is too high for our purpose.

We therefore grew a reference sample with a well-defined p-doping of $p = 5 \times 10^{17}\,cm^{-3}$, using diethylzinc as doping precursor. In this case, the position of the FERMI level E_F is well defined and was calculated to be 0.2 eV above the VBM by solving

$$p = \int_{-\infty}^{\infty} \rho_{GaP}(E) \times f\,(E, E_F)\,dE \tag{5.2}$$

numerically for E_F. Here, $f\,(E, E_F)$ is the FERMI distribution at $T = 300\,K$ and $\rho_{GaP}(E)$ the density of states of the band edges, derived using the effective mass approximation shown in Sec. 2.1 and literature parameters [32]. Due to the different doping levels, the 2PPE kinetic energy spectra of the differently doped samples appear shifted with respect to each other by ΔE_{kin} since in Eq. 2.39 the term $\Delta_{F,CBM}$ depends on the doping. For two differently doped samples thus

$$\Delta_{F,CBM}^{undoped} = E_g - \Delta_{F,VBM}^{p-type} - \Delta\Phi - \Delta E_{kin} \tag{5.3}$$

This allowed us to allocate the position of the FERMI level in a 2PPE spectrum of the undoped samples, simply by shifting it in energy until it matches the spectrum of the p-type sample. Spectra of the p-type and an undoped sample are shown in Fig. 5.7. The p-type sample had a P-rich surface reconstruction, while the surface

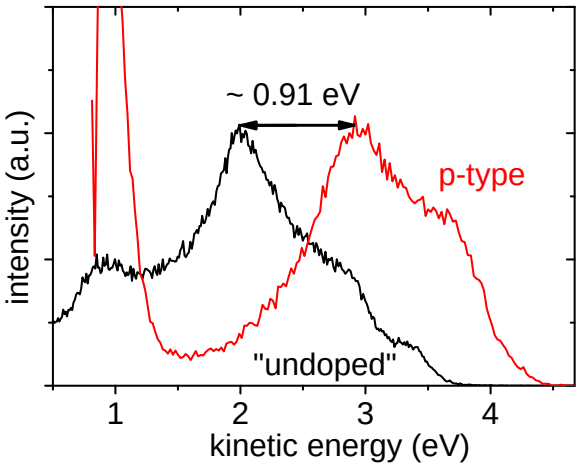

Figure 5.7: 2PPE spectra of a p-doped sample (P-rich) and an undoped sample (Ga-rich).

reconstruction of the undoped sample was Ga-rich in this case. However, as the band-alignment remained unaffected by the particular reconstruction throughout all our measurements, this posed no problem. The measured shift was $\Delta E_{kin} = 0.91\,\text{eV}$ and the work functions were $\Phi = 4.7\,\text{eV}$ for the p-type sample and $\Phi = 4.0\,\text{eV}$ for the undoped samples.

Putting these values and a band gap spacing [154] of 2.26 eV, into Eq. 5.3 yields that the FERMI level of the undoped sample is located *ca.* 0.45 eV below the level of the conduction band minimum E_{CBM}. In turn, based on calculations of the density of states and with Eq. 5.1 for the CBM, Eq. 5.2 (with n for p) returns a background doping concentration of $n \approx 10^{14}\,\text{cm}^{-3}$, in agreement with the C-V-profiling measurements.

Surface photovoltage

We noted that the spectrum of the undoped sample shifts to lower kinetic energies with higher laser intensities, following a logarithmic dependence that is typical for photovoltage. This can be seen in Fig. 5.8, where the high energy edge of the spectrum is shown for the Ga-rich surface for different beam powers P, after normalization and curve smoothing. The effect is most pronounced when measuring with laser intensities $< 20\,\mu\text{W}$. We explain this by an upward surface band bending at the undoped samples, which is compensated for by increasing light intensities through surface photovoltage (SPV) [189–192]. As seen in the inset of Fig. 5.8, the shift can be fitted with SHOCKLEY's diode-equation,

$$V(P) = nk_B T_{latt} \ln\left((P - P_{min})\frac{B}{I_S} + 1\right) + V_0 \tag{5.4}$$

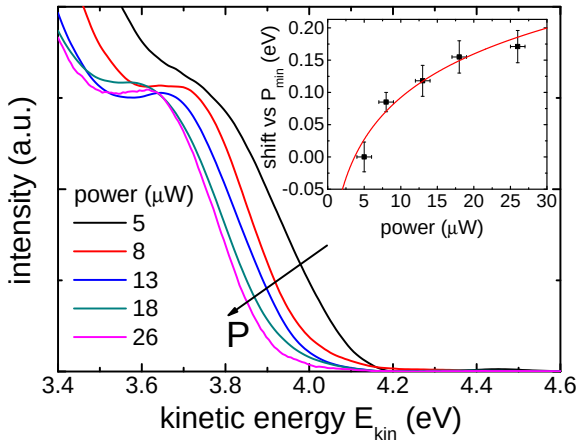

Figure 5.8: High energy edge of the spectrum of the Ga-rich surface for different beam powers P, after normalization and curve smoothing. The inset shows the shift relative to the spectrum recorded with $P = 5\,\mu$W (black squares) and a fit according to SHOCKLEY's diode-equation.

underlining the photovoltaic nature of the effect. Here, n is the ideality factor, I_S the saturation current, B a factor that accounts for the conversion of laser power into current and V_0 the photovoltage induced by P_{min}. Unambiguous fitting is not possible as the parameters require heavy extrapolation. Nevertheless, it can be deduced that a photovoltage $V_0 > 0.2\,$eV is already present for $P_{min} = 5\,\mu$W, indicating a band bending of more than 0.4 eV under dark conditions. For the p-type sample, we assume flat-band conditions, as no such shift could be observed here.

The comparison between spectra of p-type and undoped samples could not be performed for each single measurement. In order to have comparable conditions, we kept the laser intensity considerably high for all measurements. A nonuniform compensation of the band bending due to changes in SPV for different measurements would introduce an error in the energy scaling. We estimate the resulting tolerance in determining the FERMI level position to $\Delta\,(E_{CBM} - E_F) \approx 0.15\,$eV, limited by the uncertainty of the doping concentration at the p-type sample and possible variations of the SPV. This results in an overall accuracy of $\Delta E \approx 0.21\,$eV for allocating a 2PPE signal energetically with respect to the bulk bands. Here also the broadening due to the spectral width of the laser pulse and the resolution for the kinetic energy contribute (cf. Sec. 3.2).

5.2.3 Detection of surface states

To guarantee that the detected electrons belong to two-photon processes and do not involve more or less photons, it is convenient to perform measurements that depend

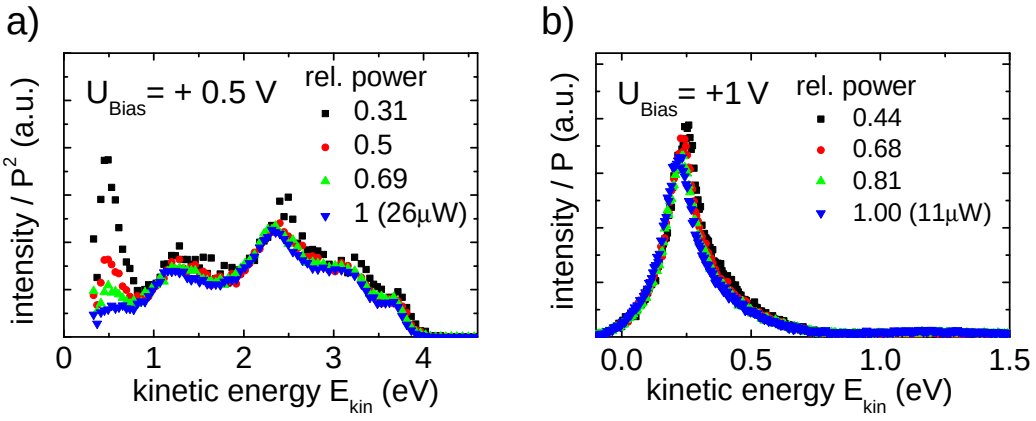

Figure 5.9: 2PPE spectra of the Ga-rich GaP(100) surface, recorded with different laser beam power and thus different photon densities. (a) Recorded with $V_{bias} = 0.5\,\mathrm{V}$ and divided by the square of the laser beam power. (b) Recorded with $V_{bias} = 1\,\mathrm{V}$ and divided by the laser beam power.

on the photon density of the exciting pulses. The easiest way to do this, is by simple variation of the laser beam power. The relationship between power and count rate then gives unambiguous information of the order of the underlying process. This can be seen in Fig. 5.9, for the Ga-rich surface and two different bias voltages.

For $V_{bias} = 0.5\,\mathrm{V}$ most of the low energetic electrons are suppressed and cannot reach the detector as explained in Sec. 2.4. The spectra have been divided by P^2 and match over a wide energetic range, which shows that the corresponding electrons are all photoemitted by absorbing two photons, each. For $V_{bias} = 1\,\mathrm{V}$ on the other hand, the spectra are totally dominated by low energetic electrons which dwarf the high energetic part. Here, the spectra have been scaled linearly with the laser power, resulting in good agreement. This shows that these electrons are photoemitted by absorbing only one photon, each (1PPE). The corresponding states must be located inside the bandgap and might relate to Ga-clusters at the surface [50], which could accumulate due to the high preparation temperatures. For the P-rich surface all signal could be related to 2PPE signals, without any 1PPE contribution. However, a high signal at low energies depends on the spot of the sample that is measured and, as seen later, increases strongly by oxygen exposure. Thus, here also a relation to defects or coverage with adatoms seems likely.

Discrimination between bulk- and surface-related features was achieved by measuring kinetic energy spectra of both the Ga-rich and the P-rich GaP(100) surface reconstructions before and after O_2 exposure. Dangling-bond surface states are quenched completely when the surface is exposed to O_2, as has been reported for other semiconductors [193–195], and as is also indicated by the RAS measurements (cf. Fig. 5.6).

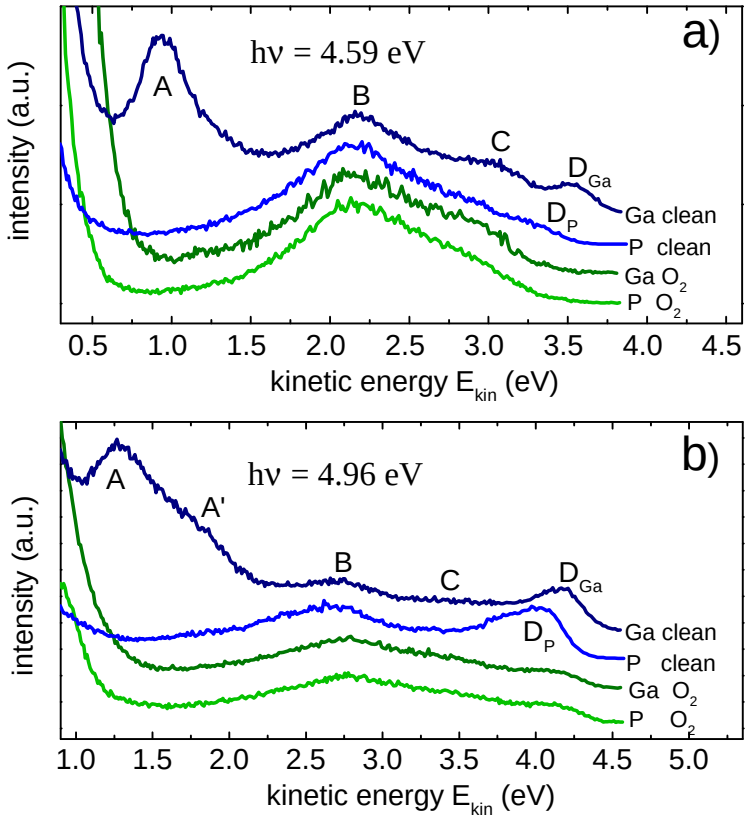

Figure 5.10: Spectra of both surface reconstructions, indicated here with *Ga* and *P*, respectively, before and after oxygen exposure. The excitation energies were (a) hν = 4.59 eV and (b) hν = 4.96 eV. The spectra are normalized to the peak **B** and shifted with respect to the y-axis for better visibility.

2PPE spectra, recorded with a photon energy of hν = 4.59 eV, are compared in Fig. 5.10(a). The prominent peak at $E_{kin} \approx 2.2$ eV, that is clearly visible in all measurements and that remains unaffected after O_2 exposure, was used as a reference for normalization. Apart from the secondary electron edge, up to four prominent features can be distinguished. One peak at $E_{kin} \approx 1$ eV, labeled **A**, could only be observed at the Ga-rich surface unexposed to O_2 and is consequently attributed to a surface state of this particular surface. Two peaks, labeled **B** and **C**, at $E_{kin} \approx 2.2$ eV and $E_{kin} \approx 3$ eV, respectively, remained clearly visible prior to and after O_2 surface treatment and are therefore assigned to bulk transitions. At the high energy edge, before O_2 exposure, the Ga-rich surface shows a peak at $E_{kin} \approx 3.6$ eV, referred to as $\mathbf{D_{Ga}}$, whereas the P-rich surface shows a shoulder at $E_{kin} \approx 3.3$ eV, labeled $\mathbf{D_P}$. Since both surface reconstructions show a significantly different behavior in this energy region, $\mathbf{D_P}$ and $\mathbf{D_{Ga}}$ can be clearly assigned to surface-related states of each particular surface reconstruction.

5.2.4 Energetic allocation of surface states

In the following, we intend to allocate the observed surface states energetically within the band diagram of GaP that is shown in a simplified form in the middle of Fig. 5.11 for **k**-values between Γ and X, where **k** is orthogonal to the surface. In this figure

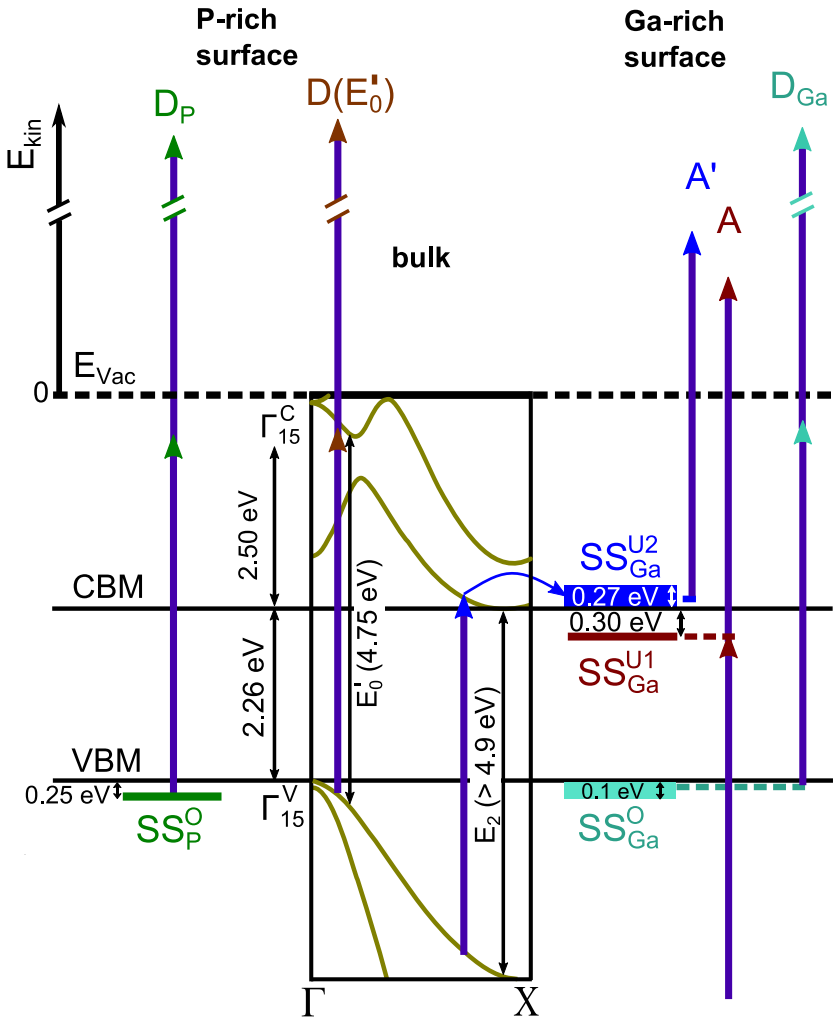

Figure 5.11: Schematics of the surface state energies relative to the bulk band edges on the left hand side for the P-rich surface and on the right hand side for the Ga-rich surface. Vertical arrows correspond to photons of $h\nu \approx 4.86\,\mathrm{eV}$ and indicate transitions that lead to peaks in the spectra. The bars labeled $SS^{U/O}_{Ga/P}$ denote unoccupied/occupied surface states at the Ga-, respectively, P-rich surface according to the indices. The bulk band structure in the middle, sketched according to Ref. [196], illustrates the bulk transitions, discussed in the text. The curved arrow indicates a scattering process. Peaks **B** and **C** have been left out, since their origin could not be allocated unambiguously.

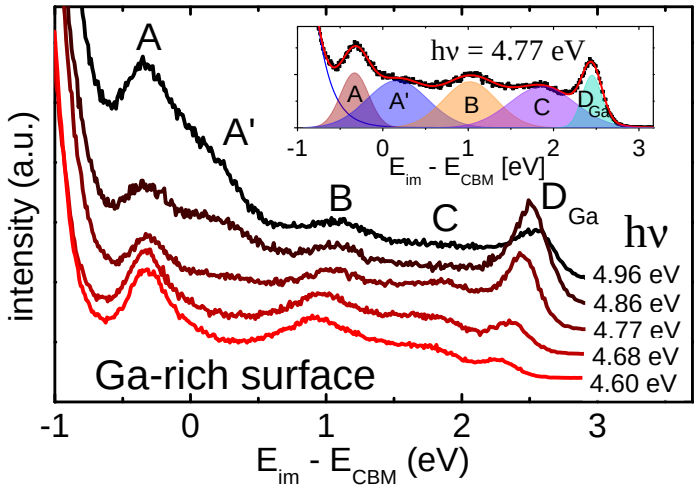

Figure 5.12: 2PPE spectra of the clean Ga-rich surface for different excitation energies. The energy scale represents the intermediate state energy with respect to the CBM. The inset shows the multiple gauss fit with a monoexponential background, which was used to determine the positions of the peaks, exemplarily for the spectrum recorded with $h\nu = 4.77\,\mathrm{eV}$.

we also summarize the surface state positions and the formation of the corresponding peaks in the 2PPE kinetic energy spectra. For detailed information on the band structure of GaP see *e.g.* Refs. [12, 151, 154] and Fig. 2.1(b). We can calculate the intermediate state energy E_{im} from the applied photon energy and measured kinetic energy as described in Sec. 2.4. In Fig. 5.11 this is schematically shown as the position where the arrowhead depicting the first photon meets the origin of the second arrow that figuratively lifts the second photon above the vacuum level. Here, as reference energy we preferably use E_{CBM} instead of the vacuum level E_{Vac}, which is used as reference for the kinetic energy.

In Fig. 5.12, spectra for different photon energies at the Ga-rich surface are shown. The energy scale reflects the intermediate state energy with respect to the CBM according to Eq. 2.39. A shoulder next to **A** appears for excitation energies $h\nu \geq 4.77\,\mathrm{eV}$ and is labeled **A′**. Comparing spectra of both surface reconstructions before and after oxygen exposure in Fig. 5.10(b) for $h\nu = 4.96\,\mathrm{eV}$ reveals that **A′** also appears only at the clean Ga-rich surface, indicating a relation to surface states. The same procedure was applied for the clean P-rich surface as shown in Fig. 5.13.

Figure 5.14 displays the intermediate state energy of all peaks from Figs. 5.12 and 5.13 for both surfaces, plotted versus the excitation energy. The positions of the peaks were determined using a fit with multiple GAUSSians and a monoexponential background for the secondary electron edge, as shown exemplarily in the inset of Fig. 5.12. Error bars, representing the uncertainty in fitting the spectra, would be

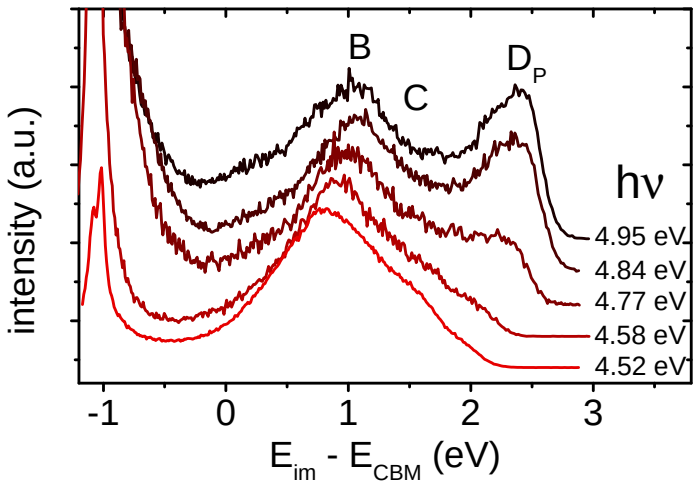

Figure 5.13: 2PPE spectra of the clean P-rich surface for different excitation energies. The energy scale represents the intermediate state energy with respect to the CBM.

smaller than the size of the symbols. The uncertainty due to the band alignment as discussed in Sec. 5.2.2 is not included, as it would lead to an identical shift of all values.

Surface state bands are two-dimensional and do not show any dispersion orthogonal to the surface. The dispersion parallel to the surface can be disregarded here as only electrons are detected that are photoemitted normal to the surface. Thus, unoccupied surface states can be clearly identified as peaks which stay at the same intermediate state energy when the photon energy is varied [123] (this is best understood when comparing with Fig. 2.11). For an occupied surface state, on the other hand, a peak in the 2PPE spectrum arises due to coherent two-photon-absorption. The energy of the corresponding virtual intermediate state then depends linearly on the excitation energy [123] with a slope of $\frac{dE_{im}}{d(h\nu)} = 1$.

Peak A: The slope values of the surface state-related peaks were extracted using linear regression and are shown in Fig. 5.14, next to the fitting curves. We found $\frac{dE_{im}}{d(h\nu)} \approx 0$ for **A**, indicating that this peak corresponds to an unoccupied surface state that is transiently populated within the laser pulse duration in the 2PPE experiment. This state is energetically allocated in the bulk band gap, ca. 0.3 eV below the CBM and will be referred to as SS^{U1}_{Ga} in the following. The lower index denotes the surface and the upper surface refers to nature of the state (occupied/unoccupied) and numbers the surface state.

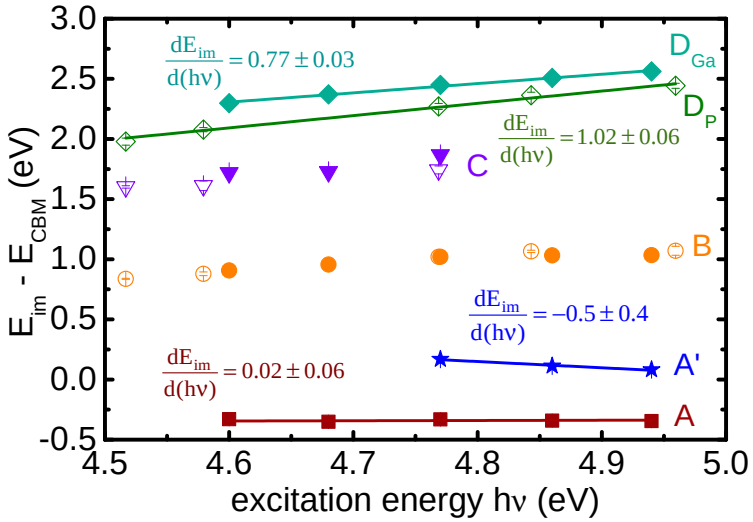

Figure 5.14: Intermediate state energy with respect to the CBM for different peaks of the Ga-rich (filled symbols) and P-rich (open symbols) surface in dependence of the excitation energy. The energy scale is calculated according to Eq. 2.39. Values for **A′** and **C** are only plotted for excitation energies, where unambiguous extraction of the peak position was possible.

Peak A′: To facilitate the comprehension of the following analysis, it is advised to have a close look at Fig. 5.11 where the results and parts of the band structure have been illustrated graphically. Our finding of $\frac{dE_{im}}{d(h\nu)} < 0$ for **A′** cannot be explained by pure surface state transitions, which means that bulk states with dispersion normal to the surface are involved. The only unoccupied bulk states in the corresponding intermediate state energy range (80 to 270 meV above the CBM) are in the vicinity of the high symmetrical X point of the BRILLOUIN zone. Reported values [151] for the direct transition E_2 from X_5^v to X_1^c in this energy region range from 4.9 to 5.3 eV. This is clearly energetically above the here observed threshold energy of $h\nu \approx 4.77$ eV for the appearance of **A′**. However, transitions along the $\Gamma \rightarrow X$ direction close to the X valley are possible at lower photon energies since the distance between valence and conduction band narrows when moving from X towards Γ (cf. Fig. 5.11). When using higher photon energies, the bulk transition shifts closer to X in reciprocal space and energetically lower states are populated, which explains the measured $\frac{dE_{im}}{d(h\nu)} < 0$ for **A′**. As **A′** could not be observed after O_2 exposure or at the P-rich surface, we assume that electrons in bulk states close to the CBM are not directly visible in the 2PPE spectra. This can be explained by the absence of final states which are allowed in terms of dipole selection rules. Photoemission from surface states on the other hand can be strongly enhanced due to different selection rules (this will be demonstrated explicitly in the following section for InP(100)). We attribute the appearance of **A′** at

the clean Ga-rich surface to extremely fast scattering into isoenergetic surface states with a high photoemission probability. These states are called SS_{Ga}^{U2} in the following (cf. Fig. 5.11).

Peaks $\mathbf{D_P}$ and $\mathbf{D_{Ga}}$: For the surface state-related peak $\mathbf{D_P}$, we find $\frac{dE_{im}}{d(h\nu)} = 1.02 \pm 0.06$. We thus relate $\mathbf{D_P}$ to an occupied surface state at the P-rich surface that lies approximately 0.25 eV below the VBM and will be labeled SS_P^O. The energetic position of the initial state is derived as in Eq. 2.38. For the Ga-rich surface, the dispersion of $\mathbf{D_{Ga}}$ exhibits $\frac{dE_{im}}{d(h\nu)} = 0.77 \pm 0.03$ eV, which is untypical for peaks related to non-dispersing states and thus indicates the involvement of bulk states. The corresponding occupied surface states are to be allocated 0.0 eV to 0.1 eV below the VBM and will be labeled SS_{Ga}^O.

We noticed a shoulder at $E_{kin} = 4.2$ eV in the spectra of the O_2-exposed samples, recorded with a photon energy of $h\nu = 4.96$ eV (cf. Fig. 5.10). Since this shoulder occurs at both surface reconstructions and is independent of oxygen exposure, we attribute it to a bulk transition. Variation of the excitation energy at the O_2-exposed mixed-dimer surface reveals that this shoulder appears only for $h\nu \geq 4.76$ eV (cf. Fig. 5.10). This threshold energy for the proposed corresponding bulk transition is in very good agreement with the transition energy $E_0' \approx 4.75$ eV [154] between the VBM (Γ_{15}^v) and Γ_{15}^c. The states at Γ_{15}^c are expected [154] to lie about 2.5 eV above the CBM (see also Fig. 5.11), which also agrees with the 2.4 to 2.6 eV measured here.

Peaks B and C: The bulk intermediate states, which contribute to **B** and **C**, are located in a range of 0.84 to 1.07 eV and 1.60 to 1.87 eV respectively above the CBM. An unambiguous assignment to certain points of the Brillouin-zone was not possible, as a large variety of transitions is possible at the photon energies that have been employed.

Polarization-dependent measurements

The geometric anisotropy of both GaP(100) surface reconstructions suggests that the corresponding surface-state-related dipole transitions are optically anisotropic, too. We investigated the polarization dependence of surface related transitions explicitly by recording 2PPE spectra of the Ga-rich surface with laser beams of different polarization but constant intensity and $h\nu = 4.86$ eV. The results are shown in Fig. 5.15(a). For p-polarized light, one component of the electric field vector is parallel to the $[01\bar{1}]$ crystal axis and lying in the surface plane of the sample. The influence of the other field component that is perpendicular to the surface was found to be negligible by varying the angle of incidence. For s-polarized light, the whole field vector is parallel

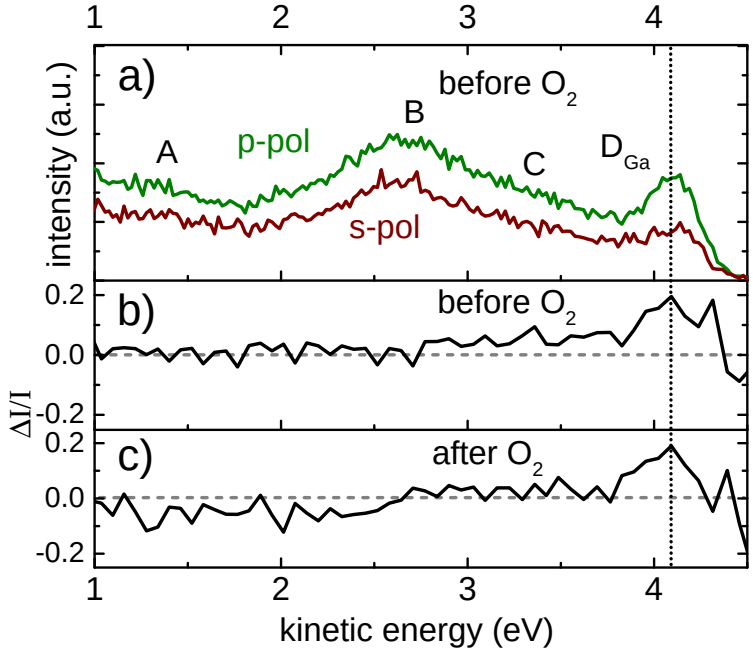

Figure 5.15: (a) 2PPE spectra of the Ga-rich surface recorded with a photon energy of $h\nu = 4.86\,eV$ with p and s polarized laser light of same intensity, respectively, before oxygen exposure of the sample. (b) Anisotropy of the signal based on the assumption that peak **B** is isotropic for the sample before oxygen exposure and (c) after oxygen exposure. The vertical dashed line marks the position of $\mathbf{D_{Ga}}$.

to [011] and thus also lies in the surface plane.[1]

The spectrum with p-polarized light shows generally a higher photoelectron yield, which can be mostly ascribed to the higher reflection of s-polarized light under an incidence angle of 45°. However, the difference in intensity is not as pronounced as expected by applying the FRESNEL equations, probably because most of the 2PPE signal stems directly from the surface where the FRESNEL theory is not sufficient to describe the intensities correctly. Both spectra therefore need to be normalized to an isotropic feature. In the following, peak **B** is chosen as an isotropic reference, since all our measurements indicate that it is purely bulk related. Based on this assumption, we evaluate the polarization-dependent measurements by defining

$$\frac{\Delta I}{I} = \frac{I_{p-pol} - I_{s-pol}}{I_{p-pol} + I_{s-pol}} \tag{5.5}$$

[1] A drop in intensity for the surface state-related peaks, as compared to the spectra in Fig. 5.12, is attributed to the fact that these measurements have not been conducted immediately after preparation. Thus, parts of the highly sensitive surface states might have been already quenched, as discussed in Sec. 5.2.1.

as the anisotropy of the signal, being 1 (−1) for a signal only appearing with p-polarized (s-polarized) light and zero for an isotropic signal. In Fig. 5.15(b), we see that the signal is isotropic over the whole energetic range, except for a significant increase centered at around 4.1 eV, which agrees with the position of the peak $\mathbf{D_{Ga}}$. This anisotropy of $\mathbf{D_{Ga}}$ hints to the existence of at least one polarization-dependent transition involved in the evolution of this peak that was above assigned to both occupied surface state SS^{O}_{Ga} and the bulk transition E_0' between Γ^{v}_{15} and Γ^{c}_{15} (cf. Fig 5.11).

To distinguish, whether the anisotropy stems from the bulk or the surface state component of $\mathbf{D_{Ga}}$ or both, we repeated the polarization-dependent 2PPE measurement after quenching the surface state contribution with oxygen, so that

$$\left.\frac{\Delta I}{I}\right|_{clean} = \frac{I^{bulk}_{p-pol} + I^{SS}_{p-pol} - I^{bulk}_{s-pol} - I^{SS}_{s-pol}}{I^{bulk}_{p-pol} + I^{SS}_{p-pol} + I^{bulk}_{s-pol} + I^{SS}_{s-pol}} \tag{5.6}$$

$$\left.\frac{\Delta I}{I}\right|_{O_2} = \frac{I^{bulk}_{p-pol} - I^{bulk}_{s-pol}}{I^{bulk}_{p-pol} + I^{bulk}_{s-pol}}. \tag{5.7}$$

Here I^{bulk} and I^{SS} are the bulk and surface state contributions to $\mathbf{D_{Ga}}$, respectively.

It follows, that for a polarization-independent surface state contribution ($I^{SS}_{p-pol} = I^{SS}_{s-pol}$), a significantly stronger anisotropy is expected for the O_2-exposed sample. However, such a change in anisotropy could not be observed, as seen in Fig. 5.15(c), while the amplitude of $\mathbf{D_{Ga}}$ drops considerably after O_2 exposure, as discussed earlier. Thus, both contributions are anisotropic: the E_0' bulk contribution and the surface state contribution to $\mathbf{D_{Ga}}$, involving SS^{O}_{Ga}, with a higher transition probability for light that is polarized parallel to the Ga-P top dimers. Our finding of $\frac{dE_{im}}{d(h\nu)} < 1$ for this peak (cf. Fig. 5.14) suggests also the existence of a possible direct transition between SS^{O}_{Ga} and the bulk states Γ^{c}_{15} leading to a signal that overlaps in the 2PPE spectra with the E_0' bulk contribution.

5.2.5 Comparison with RAS

The measured polarization dependence of the peak $\mathbf{D_{Ga}}$ for a photon energy of $h\nu = 4.86$ eV should also have an effect on the RA spectra in the corresponding energy range. In fact, at $h\nu \approx 4.7$ eV there is a prominent feature (cf. Fig. 5.6) for both surfaces that was previously found to result from a surface-induced optical anisotropy of the E_0' bulk transition, by comparing experimental RAS data with DFT based simulations [58]. This is in line with the observed bulk contribution to the peak $\mathbf{D_{Ga}}$ in the 2PPE spectra, which we also associate with the transition E_0', and that is also polarization dependent. A possible transition between SS^{O}_{Ga} and the bulk states

Γ_{15}^{c} would be energetically close to the E_0' transition. The RAS peak at the Ga-rich surface reconstruction shows a significant drop in intensity after O_2 exposure (cf. Fig. 5.6), in agreement with the observed quenching of the SS_{Ga}^{O} surface states in the 2PPE measurements. This indicates that also the RAS peak has certain surface-state related contributions that might be associated with the occupied surface state SS_{Ga}^{O}.

The good agreement between RAS and 2PPE for this transition at high energies justifies a direct comparison of both methods also for other features, which are observed in both methods. The energetic differences between the occupied and unoccupied surface states, as well as between the occupied surface states and the CBM, have been indicated with vertical bars in Fig. 5.6. Transitions between these states will appear in the corresponding RA spectra, if they are allowed in terms of dipole selection rules and anisotropic.[2] We see that the observed spacings in the surface electronic structure suitably explain the different shapes of the RAS curves for the Ga- and the P-rich surface reconstructions.

5.2.6 Discussion

The results are compared to theoretical calculations found in literature.[3] Schmidt *et al.* [166] and Hahn *et al.* [59] performed DFT-LDA calculations for the Ga-rich and P-rich surface reconstructions that are investigated here, and used their results to simulate RA spectra. Diagrams of the calculated surface electronic structures can be found in Refs. [59, 166] and Fig. 5.3.[4]

The finding of an occupied surface state SS_{Ga}^{O}, 0.0 to 0.1 eV below the VBM at the Ga-rich surface agrees well with an occupied surface state V1 (related to the phosphorus dangling bond) that was calculated to be located slightly above the VBM [166]. The unoccupied surface state SS_{Ga}^{U1}, 0.3 eV below the CBM, is in accordance with a predicted series of unoccupied states C1-C5 in the upper part of the bulk band gap [166] (related to dangling bonds of second layer cations). The appearance of the

[2] As explained in Sec. 3.3 RAS peaks are not necessarily centered exactly at the energy of the corresponding transitions, since the RA signal arises due to a complex interplay between the surface and bulk dielectric function.

[3] It is important to keep in mind that the surface states that were probed with 2PPE (cf. Fig. 5.11) are solely located in the center of the surface Brillouin zone ($\bar{\Gamma}$), as only electrons are detected that are photoemitted normal to the surface.

[4] An underestimation of the calculated band gaps was treated by employing the GW-approximation for the Ga-rich surface [166], while for the P-rich surface reconstruction Hahn *et al.* indicate that the self-energy was approximated by a rigid shift in energy [59]. Since perfect agreement of the experimental and calculated RA spectra could not be achieved, the accuracy of the corresponding calculated surface state energies might be limited. However, since the main features of the experimental RA spectra could be simply reproduced, we expect the calculated values to suffice for a qualitative comparison.

peak **A′**, which is specific for the Ga-rich surface and associated with SS_{Ga}^{U2} slightly above the CBM, might also be related to C1-C5. Disappearance of the unoccupied surface state peaks after O_2 exposure also agrees well with calculations of Wood *et al.* for the Ga-rich surface, where a strong quenching of near CBM surface states was predicted [182] for chemisorption of O_2. However, an enhancement of occupied surface states close to the VBM that was predicted by WOOD *et al.*, is in contradiction to the quenching of the occupied surface states observed here.

For the P-rich reconstruction, the surface state SS_P^O, 0.25 eV below the VBM, can be identified as a lone-pair state of the lower phosphorus atom that has also been calculated in the vicinity of the VBM [59]. For this surface reconstruction, no unoccupied surface were observed at all with 2PPE. This coincides with the fact that at this surface no cation dangling bonds are predicted [59]. The calculated surface states all belong to bonds of the cations with each other and the wavefunctions are rather restricted to layers below the actual surface. The prominent peak in the RA spectra at low energies corresponds very good with the energetic difference between SS_P^O and the CBM. According to HAHN *et al.* this peak was associated with transitions between V1 and the unoccupied states C1,C2,C3 [59]. This indicates that these stares lie close to the bulk CBM or even intermix with the bulk conduction band states. Transitions between surface states and bulk states have been observed in 2PPE experiments by other groups [197] and also described theoretically [198]. The exact nature of the bulk states near the surface and how much intermixing with the surface states occurs, however, will remain speculative without further calculations.

5.3 Electron cooling at the InP(100) surface

InP is a model system for studying electron cooling in compound semiconductors, as well as an essential material component of high-performance opto-electronic devices [2, 199]. Time-resolved optical methods such as photoluminescence or transient absorption spectroscopy have been applied extensively to investigate the fundamental physical aspects of bulk carrier dynamics [26, 27, 200, 201]. These methods are sensitive mostly to the bulk and consequently there is still little data available regarding the actual charge carrier dynamics at semiconductor surfaces. While tr-2PPE is an appropriate method to study electron dynamics at semiconductor surfaces [48, 202], most studies focused on the underlying bulk electron dynamics [189, 203–206] and surface state related studies are almost exclusively to be found for silicon [202, 207].

An exception are the experiments by Töben *et al.* on the electronic properties and electron dynamics of well-defined InP(100) surfaces [111, 124, 208], *i.e.* the P-rich and the In-rich (2×4) surface reconstructions, the latter having also been used as a functionalized part of applications such as in water splitting devices [199, 209]. An in-depth description of the In-rich mixed-dimer surface that is investigated here was shown in Sec. 5.1.3. The locations of the surface states detected by Töben *et al.* for the In-rich surface [124] are shown in the inset of Fig. 5.16(a). The electron dynamics of C1 have already been investigated with tr-2PPE and theoretical *ab initio* calculations [111, 208]. A time constant of 35 fs was depicted for the scattering from bulk states to C1. However, the depopulation dynamics, *i.e.* the scattering of electrons from the low-energetic surface state C1 to energetically adjacent bulk states could not be resolved because of the superimposed high energy tail of the photoexcited bulk electron distribution. The measurements thus reflected the cooling of the hot carrier distribution with a rate constant of $(1/7)\,\mathrm{ps}^{-1}$ instead of the depopulation of C1 [208].

Here, the same surface reconstruction of InP(100) is studied but with a focus on the surface state C2, which is associated with dangling bonds of the second layer of In atoms [58, 162] and lies considerably higher in the CB. This reduces the influence of the photoexcited bulk electron distribution that is centered at lower energies, thus allowing to discriminate the depopulation dynamics of C2 from the cooling of the bulk electrons. Two different excitation schemes with respect to the applied laser pump energy were applied. Accordingly, C2 was either populated indirectly by relaxing bulk electrons that were photoexcited high into the conduction band, or directly by resonant optical excitation. Hence, scattering processes from surface to bulk states as well as the scattering from bulk to surface states could be investigated in separate experiments. Both experiments were conducted before and after exposing the sample to oxygen and thus quenching C2 completely, as done in the previous section for GaP.

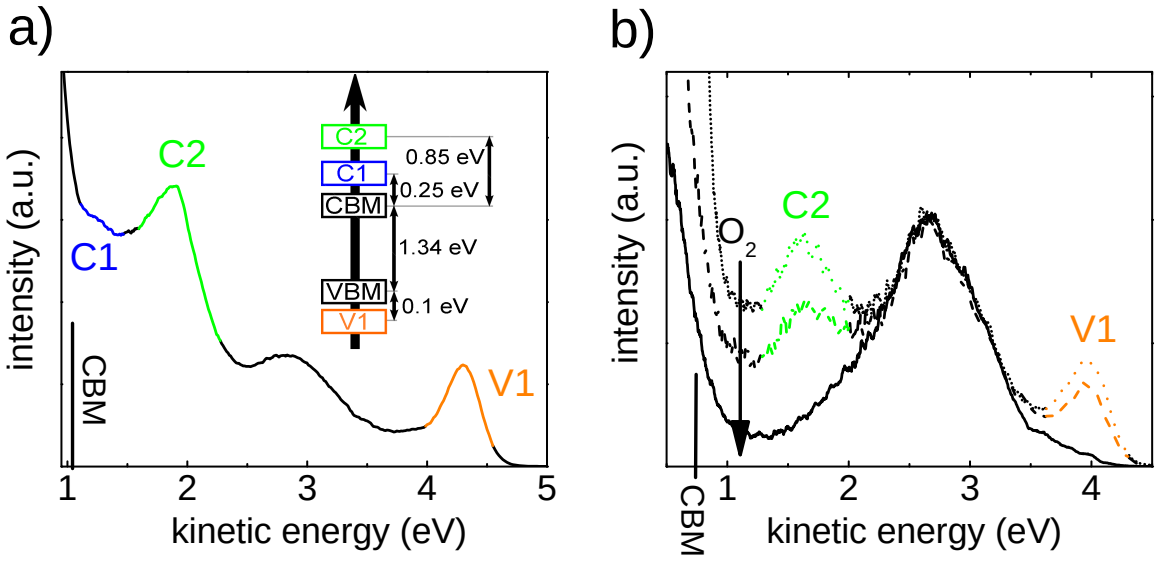

Figure 5.16: Assignment of surface states to peaks in 2PPE spectra. (a) Single-beam 2PPE spectrum with $h\nu = 4.82\,eV$. Peaks associated with the surface states C1, C2 and V1 have been highlighted. (b) 2PPE spectrum for $h\nu = 4.55\,eV$, after different stages of O_2 exposure. From top to bottom: no O_2, $0.3 \times 10^3\,mbar\,sec$, $1.5 \times 10^3\,mbar\,sec$. Inset: Energetic position of the surface states, identified with 2PPE in Ref. [124].

5.3.1 Single beam 2PPE

Figure 5.16(a) shows the kinetic energy spectrum of the In-rich (2×4) InP(100) surface reconstruction that was measured by illuminating the sample with only one pulsed UV beam ($h\nu = 4.82\,eV$). This follows the approach used in the previous section to visualize the surface electronic structure. Most interesting for this study are the peaks labeled V1, C1 and C2 that have been related to surface states of this specific surface reconstruction in previous experiments [124] and calculations [58, 162]. We illustrated the energetic positions of these surface states with respect to the bulk band edges in the inset of Fig. 5.16(a). V1 was attributed to two-photon absorption from an occupied state 0.1 eV below the VBM, leading to the photoemission of electrons in the high kinetic energy range. The peaks of C1 and C2 correspond to unoccupied surface states 0.25 eV and 0.85 eV above the CBM, respectively. In particular we used the prominent peak C2 as a reference to allocate the CBM in our spectra, according to Töben *et al.* [124], exactly 0.85 eV below C2. The broad peak with a maximum at $E_{kin} \approx 2.8\,eV$ originates from intermediate bulk states, populated via interband transitions [124]. The results show striking similarities with the analogue spectra of the Ga-rich GaP(100) surface, shown *e.g.* in Fig. 5.12. V1 has similarities to SS^{O}_{Ga} ($\mathbf{D_{Ga}}$) and the bulk structure corresponds to peaks **B** and **C**. Differences originate

from the unequal electron structures. The states C1 and C2 also have their equivalents in SS_{Ga}^{U1} (**A**) and SS_{Ga}^{U2} (**A′**). However, for InP the higher lying state C2 is more dominant, while for GaP the lowing lying state SS_{Ga}^{U1} was more pronounced. Direct association of these states would be very speculative and is not done here.

The photon energy of $h\nu = 4.82\,eV$ was applied to get an overview of the different surface states. However, we found that a lower photon energy of $h\nu = 4.55\,eV$ is better suited for time-resolved measurements which aim at the surface dynamics specifically of C2. Most importantly, this reduces the influence of the broad background, caused by 1PPE, which would otherwise overlap energetically with the signal originating from C2. A corresponding kinetic energy spectrum with $h\nu = 4.55\,eV$ is shown in Fig. 5.16(b). Here, the C2 peak remains clearly visible at $E_{kin} \approx 1.6\,eV$ but C1 has disappeared and V1 shows a smaller amplitude compared to the spectrum with $h\nu = 4.82\,eV$. Exposing the sample to oxygen again leads to the complete disappearance of all surface state related features, similar to the results on GaP(100) in the previous section and reported in other studies [195].This can be seen in Fig. 5.16(b), where also measurements are shown that were recorded after different stages of O_2 exposure and normalized to the amplitude of the bulk peak that is not affected.

5.3.2 Excitation high above C2

To study the filling of C2 by electrons that relax from high energetic bulk states, we performed time-resolved 2PPE experiments. In this first particular measurement the pump beam has the same photon energy as the probe beam ($h\nu = 4.55\,eV$) to fill states high above the CBM. The contour plot in Fig. 5.17(a) displays the electron count rate vs kinetic energy and time delay for the clean surface. A static background of photoelectrons that are emitted by the individual beams has been removed as described in Appendix C.

For a time delay of $\Delta t = 0$, i.e. when both pulses overlap on the sample at the same time, the kinetic energy spectrum resembles the spectrum that is obtained when only a single laser beam is used (cf.Fig. 5.16(b)). The most pronounced signals are the prominent bulk peak centered at $E_{kin} = 2.57\,eV$ and the C2 peak at $E_{kin} \approx 1.60\,eV$. The contour plot shows how the pump-induced electron distribution relaxes to lower energies and towards the CBM at $E_{kin} \approx 0.75\,eV$ by transferring excess energy to the atomic lattice. The bulk peak maximum shifts to lower energies most rapidly and after $\approx 200\,fs$ we see a drastic increase of the photoelectron yield centered at C2 that attains its maximal value at $\Delta t \approx 580\,fs$. We interpret this as electrons that scatter from bulk states to C2 due to phonon emission or absorption.

To verify this, the experiment was repeated after quenching the surface states with oxygen. In Fig. 5.17(b) we compare spectra for different time delays between the

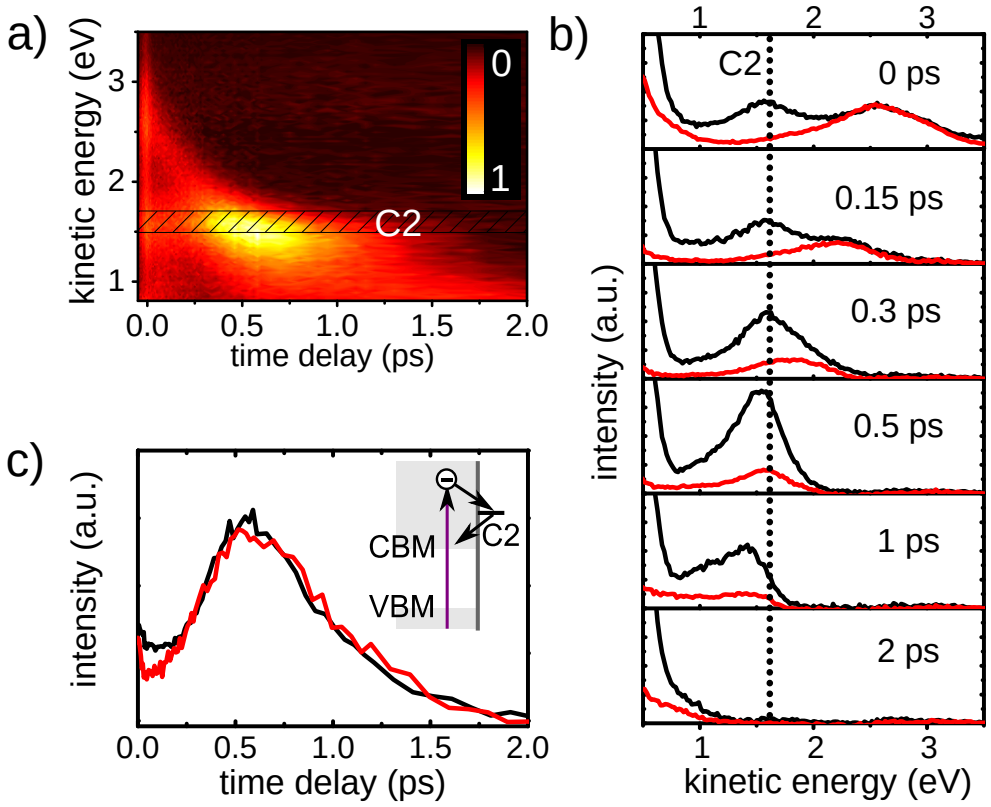

Figure 5.17: Tr-2PPE measurement with $h\nu_{pump} = h\nu_{probe} = 4.55\,eV$. (a) Contour plot of the unexposed surface, with the kinetic energy corresponding to C2 indicated with a striped bar. The color represents the normalized count rate. (b) Spectra for different pump probe delays for the unexposed (black) and the O_2-exposed surface (red). (c) Normalized transients before (black) and after (red) oxygen exposure for the energy level of C2, indicated in (b) with a dotted line.

pump and probe pulses before (black) and after (red) oxygen exposure. The cooling of the bulk electron distribution looks similar for both cases within the first 200 fs. However, the measurement recorded after O_2 exposure lacks the prominent 2PPE signal enhancement at the C2 energy level. Instead, the electron distribution continues to relax towards the CBM at $E_{kin} \approx 0.75\,eV$ with a total electron yield that is rather constant, compared to the drastic increase, which is observed for the sample before O_2 exposure. This can be seen in Fig. 5.18(a), where the integral measured number of electrons is plotted against the pump probe delay. A rise of the signal is clearly present before oxygen exposure but absent afterwards, which reinforces our argument of an enhanced photoemission from C2. Hereby, only electrons with $E_{kin} > 0.7\,eV$ were taken into account to avoid the influence of 1PPE and secondary electrons. While the strong signal enhancement is well represented in the total electron yield, this quantity must be treated with care since it is also subject to effects like electron diffusion into

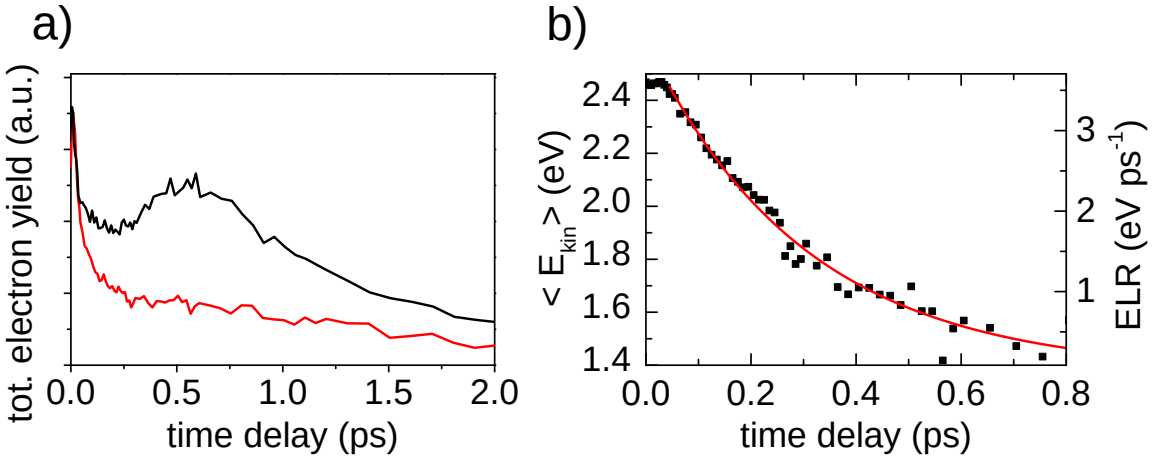

Figure 5.18: (a) Total electron yield of the tr-2PPE spectra recorded with $h\nu_{pump} = h\nu_{probe} = 4.55\,eV$ as a function of time delay before (black) and after (red) O_2 exposure. (b) Mean kinetic energy of the tr-2PPE spectra recorded at the O_2-exposed surface. The line shows a monoexponential fit used to determine the average energy loss rate per electron, indicated on the right hand y-axis.

the bulk as well as electron scattering into side valley states, which are invisible to 2PPE, when only measuring electrons photoemitted normal to the surface.

5.3.3 Energy Loss Rate

The absence of a comparable C2 signal for the O_2-exposed surface allows us to analyze the cooling of the bulk distribution in more detail. In Fig. 5.18(b) we plotted the average energy of the electron distribution vs time delay. Only electrons with $E_{kin} > 1\,eV$ were considered here, to avoid the influence of 1PPE and secondary electrons. This value is somehow arbitrary, however, variation by $\pm 0.2\,eV$ has an effect of less then 10% on the results in the shown time window. The curve was fitted monoexponentially to calculate the corresponding time dependent ELR, which is given by the derivation of the mean kinetic energy and shown on the right-hand y-axis of the plot. The effects mentioned above, that can manipulate the total electron yield, play an even more important role here [143]. As can be seen in Fig. 5.18(a) (red line) the total electron yield stays very constant in the time window of Fig. 5.18(b). Also as can be seen in Fig. 5.17(b) for $\Delta t = 0.5\,ps$, both spectra have their maximum at the same energy. This indicates that the measured ED at least approximates the real ED at the surface. We find an initial relaxation speed of $\approx 3.5\,eV\,ps^{-1}$ that drops rapidly as the electron distribution approaches the CBM. This decrease of ELR, when the electron distribution approaches the CBM, is typically attributed to the accumulation of electrons at the bottom of the conduction band. Electrons cannot emit optical

phonons if they have less excess energy than the optical phonon energy, due to the lack of available electronic states as described in Sec. 2.3 and Ref. [24]. Extraction of the electron temperature and modeling of the temperature-dependent ELR, as in Sec. 4.3 for CdSe nanoplatelets, was not done here. This is due to the fact, that for high excess energies, the bandstructure is strongly non-parabolic and also the L and X sidevalleys become involved. An appropriate simulation would require to account for this and also for scattering mechanisms such as TO-phonon scattering and intervalley scattering that do not play a role near the BZ center.

5.3.4 Population and depopulation dynamics of C2

In order to analyze the population and depopulation dynamics of C2, we compare transients of the corresponding kinetic energy range before and after O_2 exposure in Fig. 5.17(c). The curves were normalized to their maximum value. For early times the signal from the clean surface is slightly larger due to an initial population of C2. However, for longer time delays both curves are almost identical and resemble the total electron yield curve for the sample before O_2 exposure (black line in Fig. 5.18(a)). This indicates that the cooling rate of the electron distribution does not notably change on this time scale by the presence of C2 but is instead determined by the relaxation of the bulk electron distribution. The scattering in and out of the surface states presumably happens on a much faster time scale but cannot be distinguished in this measurement as the electron distribution has already considerably broadened temporally and energetically before reaching the energy level of C2.

Therefore, we performed experiments with a pump photon energy of $h\nu_{pump} = 2.33\,eV$ aiming on a direct population of the surface state C2 without prior electron relaxation. For this photon energy, an optical transition to C2 from occupied surface states in the vicinity of the VBM was predicted in DFT calculations by Schmidt *et al.*, in agreement with RAS measurements of the In-rich InP(100) surface [159]. A contour plot of the corresponding tr-2PPE measurement is shown in Fig. 5.19(a). The energy range of C2 that was measured before, in the experiments with $h\nu_{pump} = 4.55\,eV$ (cf. Fig. 5.16(b)), is indicated with a striped bar and clearly overlaps with the photoexcited electron distribution, as expected for an initial resonant population of C2. However, the center of the peak is below C2. We relate this to bulk electrons, photoexcited via interband transitions. Since the heavy hole band at the Brillouin zone center is rather flat compared to the conduction band [151], the electrons take most of the excess energy. Thus, electronic bulk states near C2 are populated, which could also lead to population of C2 through scattering processes.

To clarify this, we once again distinguished between bulk and surface state related signals by comparing measurements before and after oxygen exposure of the sample.

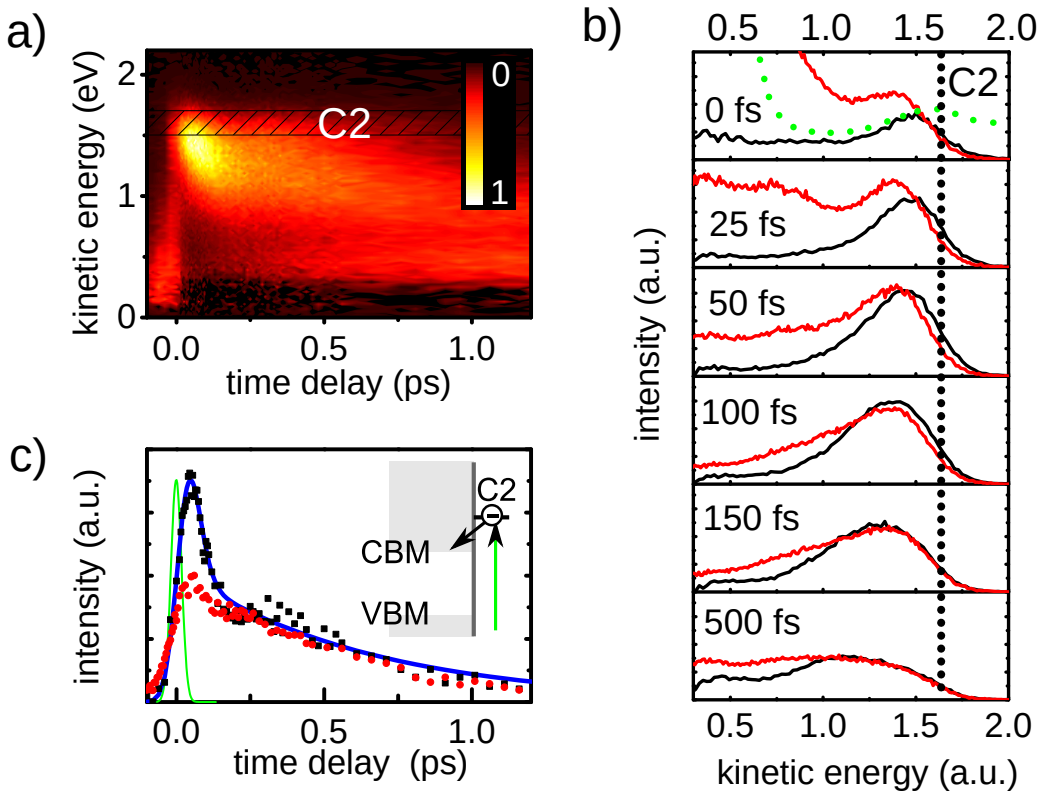

Figure 5.19: Tr-2PPE measurement with $h\nu_{pump} = 2.33\,eV$ and $h\nu_{probe} = 4.55\,eV$. (a) Contour plot before O_2 exposure. C2-indication and color as in Fig. 5.17(a). (b) Spectra for different Δt before (black) and after O_2 exposure (red). The green dotted line is the spectrum, generated by illuminating with the probe only (cf. Fig. 5.16(b)). (c) Transient signal for the energy level of C2, indicated in (b) with a black dotted line, before (black squares) and after (red spheres) O_2 exposure. The green line shows the time resolution and the blue line the fit described in the text.

Corresponding spectra for different pump probe delays before (black) and after (red) O_2 exposure are presented in Fig. 5.19(b). After appropriate normalization they look identical for $\Delta t > 150\,fs$ and $E_{kin} > 1\,eV$. As the signal in this range is unaffected by O_2 exposure we conclude that it stems completely from bulk electrons. The differences for $E_{kin} < 1\,eV$ are difficult to entangle as O_2 exposure also leads to a significant change in the generation rate of secondary electrons and 1PPE. For $\Delta t < 150\,fs$, however, there are remarkable differences between both measurements. The maximum of the electron distribution that forms immediately after excitation is centered 0.1 eV (clean surface) respectively 0.2 eV (O_2-exposed surface) below the level of C2. We attribute the higher initial peak energy for the clean surface to a resonant population of C2. In Fig. 5.19(c) we compare transients before and after O_2 exposure for the electrons in the vicinity of C2 with $1.65\,eV < E_{kin} < 1.75\,eV$, where the differences

are most pronounced. While the rise time of the signal in both cases reflects the time resolution of the setup, we see clearly different decay behaviors before and after oxygen exposure.

The transient of the O_2-exposed sample decays with a time constant of $\tau_{slow} \approx 600\,\text{fs}$. The clean surface on the other hand shows a rapid decay during the first 150 fs and only for longer time delays, the curve of the clean surface follows the one measured for the O_2 exposure. We fit this data with a simple biexponential model to take into account the slow bulk signal. We used the length of the pump pulse ($\Delta_{fwhm} \approx 33\,\text{fs}$) as rise time and convoluted the modeled data with a GAUSSian curve corresponding to the probe pulse ($\Delta_{fwhm} \approx 27\,\text{fs}$). The result is plotted in Fig. 5.19(c) as a blue line, giving a time constant of $\tau_{fast} = 20\,\text{fs}$ for the rapid decay. As this decay only occurs at the clean surface, we attribute the 20 fs time constant to the depopulation of the surface state C2. The signal increases again slightly in the range $200\,\text{fs} < \Delta t < 300\,\text{fs}$—a feature that was found to be more prominent in measurements with lower pump photon energies and that has been related in previous measurements to electrons returning from the X valley to the Γ valley by intervalley scattering [208].

5.3.5 Discussion

For the tr-2PPE measurements with about 2 eV excess energy, shown in Fig. 5.17, we observe a prominent signal enhancement at the C2 energy level after $\approx 200\,\text{fs}$ for the clean surface. This is clearly identified as the population of C2 by electrons that relax from higher energetic bulk states. Since the transients from this energy level look very similar for the clean and the O_2 exposed surface, we conclude that the presence of the surface states does not significantly influence the electron cooling. The photoexcited electron distribution ranges several nanometers into the bulk due to the finite absorption coefficient [210] while the surface state extends only about 0.5 nm into the bulk following DFT calculations [58]. Thus, only a small percentage of the photoexcited electrons actually populate the surface states. Consequently, most of the energy loss processes occur inside the bulk and the ELR is not affected by O_2 exposure of the surface and quenching of the surface state C2.

The drastic increase in amplitude for $\Delta t > 300\,\text{fs}$, that we see in the tr-2PPE signal when the electron distribution reaches C2, relates to a higher probability of electrons in the surface state to be photoemitted and subsequently detected than for electrons in the bulk [211]. This is not unexpected, since most bulk electrons at this energy level populate the four L valleys due to a DOS which is approximately one magnitude higher than for the Γ valley, considering the effective electron masses at the valley minima [151]. As the L-valleys lie along the [111]-directions in **k**-space, the

corresponding photoemitted electrons have a non-zero transversal momentum and are thus not detected with our setup (cf. Chapter 3).

In the experiments with a pump photon energy of $h\nu_{pump} = 2.33\,eV$, shown in Fig. 5.19, C2 is populated directly by optical excitation. The rapid drop of the initial amplitude with a time constant of $\tau_{fast} = 20\,fs$ in the transient of the C2 energy level (cf. Fig. 5.19(c)) does not appear in the measurement after O_2 exposure of the sample. This strongly indicates that τ_{fast} corresponds to C2-to-bulk scattering, since we found out that electrons in C2 have a higher probability of being photoemitted than electrons in the bulk (cf. Fig. 5.17(b)). Bulk-to-C2 scattering would thus lead to a rising signal instead, as found for the monochromatic measurements (cf. Fig. 5.17) and reported by TÖBEN *et al.* in their experiments that focused on the dynamics of C1 [111, 208].

With a time constant of $\tau_{fast} = 20\,fs$, C2-to-bulk scattering happens on a similar time scale as bulk-to-C1 scattering, determined in previous experiments, where a time constant of $\tau = 35\,fs$ was measured [111]. To compare the C2 to bulk scattering with bulk-to-bulk scattering at the same energy level, we estimate the bulk phonon emission time constant in the energy region of C2 from Fig. 5.18. Between 300 fs and 800 fs, when the electron distribution passes the energy level of C2, we find an ELR per electron of 0.25 to $1.5\,eV\,ps^{-1}$. One can assume that the phonon emission rate is much larger than the phonon absorption rate at this excess energy and that the cooling happens mainly via the generation of optical phonons, having energies of about 40 meV. This assumption is a typical approach for electron-phonon scattering processes near the CBM [31] and results in an average optical phonon emission time between $1/160 fs^{-1}$ and $1/27 fs^{-1}$ in this energy range, which is slower than the measured $\tau_{fast} = 20\,fs$. Comparing the bulk scattering times with the results found for CdSe nanoplatelets (cf. sec. 4.3), we observe that the phonon emission rates happen on a similar time scale ($\approx 17 fs$ for the NPs and $\approx 12 fs$ for InP at the maximal employed excess energy). Similar bulk values were also observed for GaAs where SCHMUTTENMAER *et al.* found lifetimes of $< 50\,fs$ for electrons $\approx 2\,eV$ above the CBM [189]. For silicon also lifetimes $< 50\,fs$ were reported [207].

It is necessary to take into account that the depopulation of the surface state is not restricted to the emission of optical phonons but can also happen via acoustic phonons and absorption processes. Acoustic phonons have a smaller energy than optical phonons and thus play a minor role in the cooling of the electron distribution near the BZ center [31]. Nevertheless, they may become important for the depopulation of C2 and can explain the short life time of electrons in C2, together with the other mechanisms discussed before

Our measurements show that scattering from surface to bulk states can be extremely efficient and similarly as fast as electron-phonon scattering between bulk

states, in particular for electrons with high excess energy where the bulk DOS is also high. Therefore the presence of surface states at the InP(100) surface is unlikely to slow down electron cooling. An accelerating effect is also not expected when most electrons are located in the bulk. However, in nanostructured devices a major share of the atoms forms the surface/interface and hence surface states must be taken into account and considered as equally relevant for electron-phonon scattering events as bulk states. This will be especially important, when trying to minimize the bulk scattering rates *e.g.* with semiconductor quantum dots.

5.4 Summary of the results on III-V semiconductor surfaces

Our results on GaP(100) surfaces demonstrate the discrepancies between the electronic structures of the bulk and the surface. For both investigated surfaces, occupied surface states were detected in the vicinity of the VBM. Their energies complement theoretical calculations that describe dangling-bond-, respectively, lone-pair-states at the top P atoms. The Ga-rich surface reconstruction exhibits unoccupied states in the vicinity of the CBM, which presumably originate from the cation atoms of the second layer of the surface. All of these surface states are quenched when the respective surface is exposed to oxygen. Furthermore, a correlation was found between features in the RA spectra, and the energy spacings between states at the surface, which were detected with 2PPE. Future 2PPE studies might be conducted with a second beam of a different photon energy. Thus, optical surface state transitions that were indicated in RA spectra can be selectively photoexcited to allocate the energetic positions of the corresponding surface states.

The time-resolved measurements on the In-rich InP(100) surface show that the scattering from surface to bulk states happens on a time-scale of $\approx 20\,\mathrm{fs}$ and is of comparable magnitude as scattering from bulk to surface states at the same surface reconstruction [111]. This shows that for materials with suppressed relaxation via bulk states — as observed in the measurements on CdSe QDs — scattering between bulk and interface states can be a very efficient alternative electron cooling mechanism. However, for InP the influence of the surface on bulk electron cooling seems to be negligible as seen from the tr-2PPE measurements with high-excitation energy. This indicates that the surface-mediated relaxation cannot compete with the bulk processes, in agreement with our tr-2PPE measurements on CdSe nanoplatelets, in the previous chapter. Here, we also found that the relaxation is very fast and can be described with a simple model for "2D-bulk" LO phonon scattering.

In conclusion, our results show that surface-mediated scattering processes happen within tens of femtoseconds but still cannot compete with efficient bulk LO-phonon scattering as observed in 2D and 3D compound semiconductors. However, if the bulk scattering processes can be slowed down, *e.g.* by separating the electronic states by more than the LO-phonon energy, the surface mediated scattering becomes important and careful preparation of the surface is required to achieve high hot-electron life times [10]. This is very important for concepts such as hot-carrier solar cells and intermediate band solar cells. Materials are required with efficient suppression of bulk and surface-mediated carrier relaxation at the same time. This has not yet been realized satisfactory. An alternative solution of this problem could be achieved by

accelerated charge carrier separation. That way, energy loss by carrier relaxation could be circumvented. In the following and last part of this thesis the latter road is taken and a design is presented that employs intersubband absorption in quantum wells to promote electrons to higher lying subbands. A stepwise alignment of the electronic states is engineered to achieve fast transport of these electrons towards the n-contact, thus avoiding the loss of energy by premature relaxation to the conduction band minimum.

6 Fast carrier separation with intersubband transitions

In the previous chapters, the fast carrier relaxation was studied that is present in most materials and that is disadvantageous for any photovoltaic concept that relies on hot carriers. To harvest this energy nevertheless, approaches are required that employ an even faster collection of the hot-carriers' extra energy. In this chapter, a concept is presented that follows this idea. At first an introduction on photovoltaics with intersubband transitions is presented, including a brief description of the intermediate band solar cell design. Afterwards, a novel and related concept is shown that combines intersubband transitions with fast separation of the hot carriers. Measurements on an actual device were conducted — providing proof-of-principle — and are compared to simulations. Finally the prospects and limitations of this approach are discussed. Parts of this chapter have been reprinted in part, with permission from Prog. Photovolt: Res. Appl., DOI:10.1002/pip.2697 [212],

6.1 Introduction to photovoltaics with intersubband transitions

Nanostructering semiconductors and thus confining the charge carriers in one, two or three dimensions leads to the evolution of discrete states (cf. Secs. 2.2.1 and 2.2.2). The transitions between the confined states in the CB or the VB are called intersubband transitions (ISTs) and follow certain selection rules. The splitting energies are determined by the thickness and the offsets between the barrier- and well material and typically correspond to infrared light. Hence, the implementation of ISTs is a fundamental idea [4] to exploit photons of the sun with lower energy than the bandgap. Parallel to the ISTs there are the interband transitions between VB and CB available and therefore theoretical concepts were developed to exploit both and thus absorb a broad share of the solar spectrum. The most prominent concept regarding this is the so-called intermediate band solar cell [4].

Carriers, photoexcited via ISTs are basically hot carriers and thus can cool down to the band edges. Similar to non-radiative recombination in classic solar cells this means the complete loss of the energy that was gained via the IST. Thus, slow carrier cooling in combination with fast extraction of the hot carriers is required for successful implementation in a solar cell. In the previous sections, it was demonstrated that

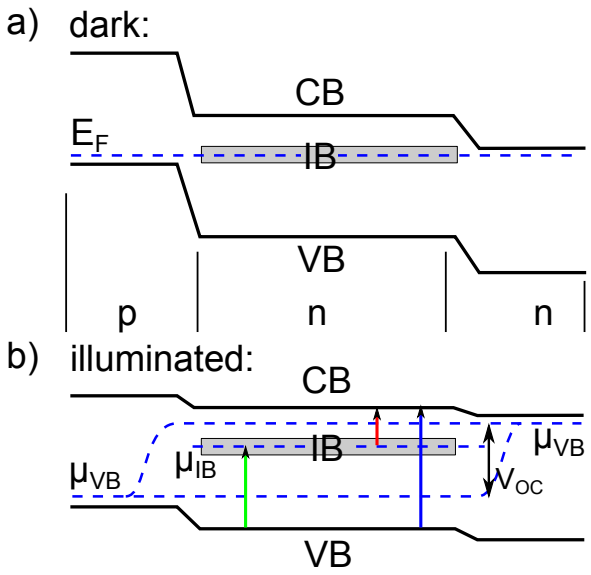

Figure 6.1: Sketch of the intermediate band solar cell according to Ref. [213] (a) in darkness and (b) under illumination. The y-axis represents energy and the x-axis the growth direction (cf. the envelope function approach in Sec. 2.2).

the carrier cooling is very fast and difficult to decelerate. Consequently, fast hot-carrier extraction is necessary. This is difficult with the classic IBSC design as will be shown in the following. Here, a related concept is presented that aims on combining intersubband transitions with interband transitions and fast charge carrier separation. This is done — again on basis of III-V semiconductors (see overview in Sec. 5.1.1) — with an InP pin-(p-type - intrinsic - n-type) junction and a complex stack of InGaAs/InAlAs/AlAs quantum wells to tailor the alignment of electronic states.

6.1.1 The intermediate band solar cell

In the IBSC, a section with three different energy bands is embedded between a p- and an n-type section. This is sketched in Fig. 6.1. The middle band is called intermediate band (IB) and for optimal performance should be filled by 50% with electrons, meaning that the FERMI-level is exactly in the middle of the intermediate band under dark conditions [4]. Photons can then be absorbed by optical transitions between all three bands: VB $\rightarrow$ IB, IB $\rightarrow$ CB and VB $\rightarrow$ CB. Here and in the following we will always assume that the IB is closer to the VB and that the absorber region is thus n-type. Under illumination all three bands have individual quasi-FERMI-levels and only electrons in the CB can be transported towards the n-contact so that the V_{OC} of the cell is the difference between the quasi FERMI-levels of the VB and the CB. As the bands are flat in the absorber section, there is no strong gradient in electro-chemical potential that would drive the carriers to the p-, respectively n-type sections of the

cell. Since this region is also highly doped, as explained above, non-radiative recombination for the minority carriers is very likely to become problematic. However, under ideal conditions, including maximal concentration, LUQUE and MARTÍ calculated a theoretical maximum efficiency [4] of 63%, which exceeds the theoretical efficiency of a two-terminal tandem solar cell [214] which is $\approx 55\%$, for the same assumptions.

The concepts to realize an IBSC include different approaches, *e.g.* the utilization of IBs consisting of defect states in highly mismatched II-VI and III-V alloys [215]. The discretization of states in QWs and QDs is also very promising. Most focus has yet been put on QDs, due to their potentially high hot-electron lifetimes (as discussed in Chapter 4). The principal operation of such cells has already been demonstrated [216, 217] and research groups are currently working to improve the efficiencies [218, 219]. Quantum wells are not advantaged in terms of hot carrier lifetimes [215], as shown also for the nanoplatelets in Chapter 4, but proof-of-principle has also been reported [220]. On the other hand they have the big advantage that they can be grown epitaxially with huge variety in composition, thickness and even strain-compensated. This enables more sophisticated layouts that could compensate for the fast carrier relaxation.

6.1.2 Intersubband transitions and light management

Intersubband transitions in quantum wells are only allowed in terms of dipole selection rules for light with a POYNTING vector perpendicular to the quantum well planes [221] (see also Sec. 2.2.1). Strategies to couple light in the samples that fulfill this requirement include illumination of the samples under the BREWSTER angle and prism-like geometries [222]. However, these approaches are better suited for spectroscopic investigations than for photovoltaic application, due to their low efficiency and complex geometries. A different solution is the application of a lattice on top of the sample to deflect the incoming light away from the direction normal to the surface, thus allowing for ISTs. For the tandem sample that will be addressed in the following section, a grating was applied lithographically to the surface. Pictures of the sample, obtained with scanning electron microscopy (SEM), are shown in Fig. 6.2. Gold was sputtered on the surface with chrome as adhesive layer and afterwards removed with a lift-off process from the areas with the photoresist. The mesh width of the resulting Au diffraction grating was $4\,\mu$m and the incoming light in the near infrared is thus refracted, resulting in non-zero POYNTING vector components that are perpendicular to the quantum well planes. Thus, the absorption of IR light under normal incidence is possible. The gold grid also served as front contact, while for the back contact the substrate was connected to a chip carrier via indium soldering.

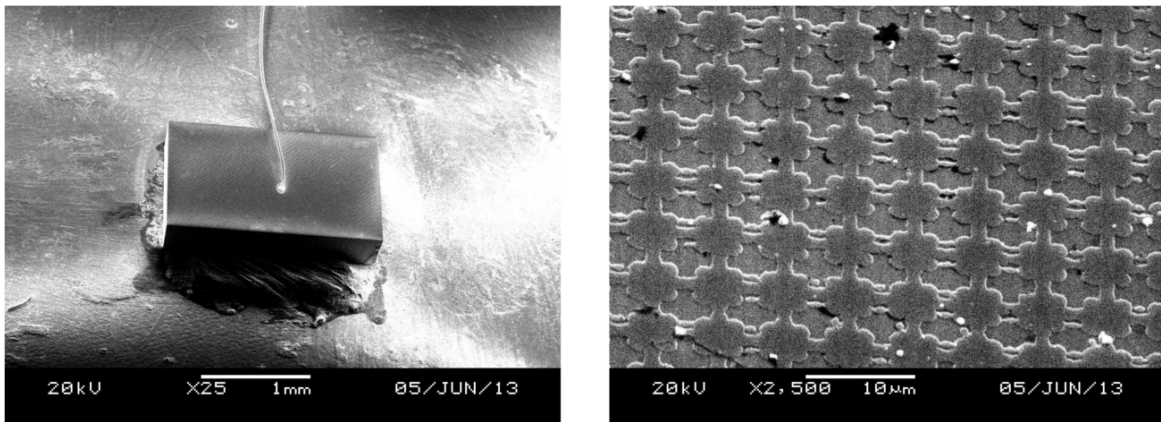

Figure 6.2: SEM pictures of the tandem solar cell sample and the Au lattice on its top surface.

6.1.3 Quantum cascade photodetectors

Quantum cascade photo detectors (QCPDs) utilize the ISTs that arise by electron confinement in quantum wells [223–226] to absorb and detect photons in the infrared part of the electromagnetic spectrum. Similar to quantum well infrared photodetectors [227] (QWIPs), the photoexcited electrons are delivered to an external circuit to generate current. While in QWIPs an external forward bias is necessary to separate the photoexcited electrons and holes, QCPDs allow for the operation without bias [223]. This is achieved by growing an asymmetric stack of quantum wells with different thicknesses so that the corresponding subband states form an energy staircase. If the step size matches the optical phonon energy, scattering between the steps becomes faster than the relaxation to the ground state and electrons travel towards the direction of the energetically lowest step [223]. For an efficient carrier extraction, the scattering processes between different states of one miniband need to be faster than the relaxation towards the CBM, similar to quantum cascade lasers [228]. The term miniband hereby refers to the confined states that extend over several QWs for small barriers and that due to the coupling form again narrow energy bands.

Due to their absorption in the infrared range, QCPDs have already been proposed for thermo-photovoltaic applications [225]. A sample that contains a QCPD embedded in a n-type structure was grown and processed by the *FeT* group of the *Humboldt University Berlin*. For "real" QCPDs, such a structure is typically repeated multiple times, to achieve higher signal-to-noise ratio. As here only a single QCPD iteration is used, the term “cascade” seems inappropriate and we will refer to it as “photovoltaic intersubband absorber” (PIA). The band alignment is shown in Fig. 6.3(a). This sample was designed to achieve a broadband absorption, as desired for PV applications and is based on an earlier layout [229]. The second lowest miniband states (moduli

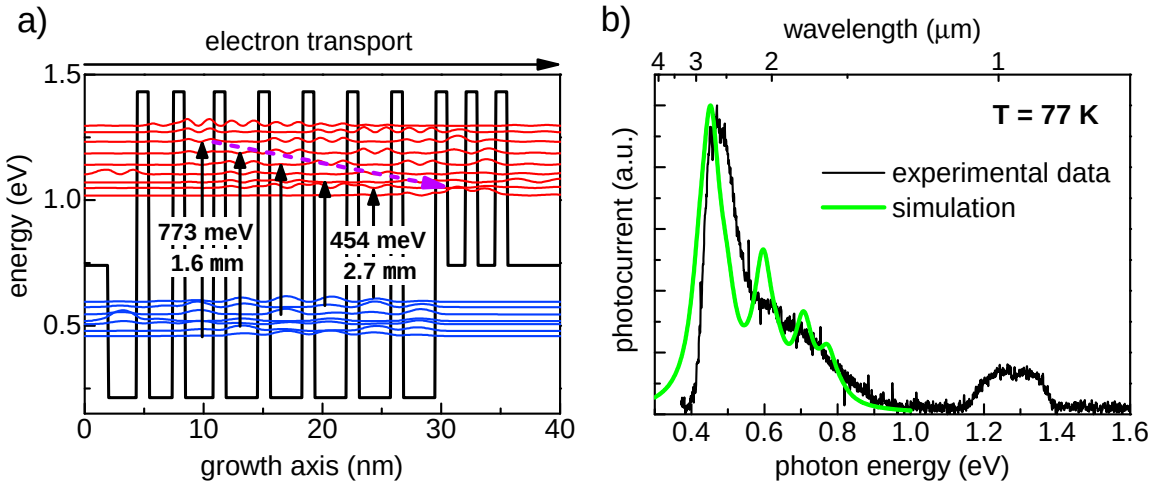

Figure 6.3: (a) Miniband alignment and photocurrent of a QCPD in full-n-type structure (cf. Fig. 6.5(a)). The wave functions represent solutions of the SCHRÖDINGER equation, calculated via the approach described in Ref. [15]. (b) Spectral photocurrent response of the same sample and simulated curve. Measured and calculated by the *HU* group.

squared wavefunctions shown in red) form a staircase down to the lowest state that is clearly localized at the right hand side of the structure. Thus electrons photoexcited via ISTs are transported towards this direction, following the purple arrow. This sample allows to measure the spectral photocurrent response for a given quantum well configuration. This is shown in Fig. 6.3(b), together with the simulated spectra based on the dipole matrix elements between the wave functions. Good qualitative agreement is found between measurements and simulation, indicating that the structure is capable of infrared-light absorption and charge carrier separation without an external bias. The charge carrier separation process for exactly this structure was also studied in a theoretical group of the *Technical University Berlin* by MILDE *et al.* Via an analysis of the competing electron scattering mechanisms, it could be shown that the electrons in higher minibands are driven towards the "right hand side" of the structure [**milde_light_2014**].

6.2 Tandem cell design with intersubband absorber

An advanced strategy was proposed by YIN and PAIELLA in form of a theoretical concept of a novel thermo-photovoltaic tandem cell [226]. Here, a PIA and a pn-junction are operating in series with the PIA located inside the n-type section of the pn-structure. Thus, similar to conventional multijunction tandem solar cells, photons in a wide energy range can be absorbed with reduced thermalization and transmission losses that restrict the conversion efficiency in the SHOCKLEY-QUEISSER-limit. However, this idea has not been realized yet. In a related and further developed concept, aimed on harvesting solar photons, we demonstrate a solar cell structure that consists of an InP pin-junction, a single PIA iteration of InGaAs/InAlAs/InAs and an InAlAs absorber. The device was grown with gas source molecular beam epitaxy (GSMBE) at the *Humboldt University Berlin*.

6.2.1 Design

General band schematics of the desired design are shown in Fig. 6.4(a) for dark conditions. On the left hand side there is a conventional pin-junction, with the n-type layer being heavily doped, so that the FERMI level lies above the conduction band minimum (CBM). The section on the right hand side in the n-type region, marked with a blue circle, shows a simplified diagram of the incorporated PIA. The two conduction bands represent the lowest two miniband levels with a gradient in energy according to the stepwise aligned states as indicated *e.g.* in Fig. 6.3(a) and Fig. 6.5(a). Due to the shape of the upper lying CB (CB2), photogenerated electrons are driven towards the n-contact on the right-hand side. The corresponding holes generated in the lower lying CB (CB1) — in the following referred to as "quasi-holes" to distinguish them from the valence band (VB) holes — are driven to the pin-junction. Here, they recombine with electrons that were photogenerated via interband optical transitions. The charge separation in the PIA leads to the splitting of the quasi-FERMI-levels of CB1 and CB2 and thus increases the provided voltage of the device as shown in Fig. 6.4(b), where the schematics are sketched for an illuminated cell.

To ensure that photogenerated holes are driven to the p-contact (left hand side in Fig. 6.4(a,b)), it is necessary that the band gap of the layer between the PIA and the n contact (right hand side in Fig. 6.4(a,b)) is larger than the band gap to the left of the PIA. Charge carriers, which are generated in this high-bandgap part by the absorption of high energy photons will also be separated in the PIA and contribute to the photocurrent (if recombination in the heavily n-doped sections is suppressed successfully). In this case, the hole quasi-FERMI-level is split off from the electron quasi-FERMI-levels throughout the whole structure as indicated with the green dashed

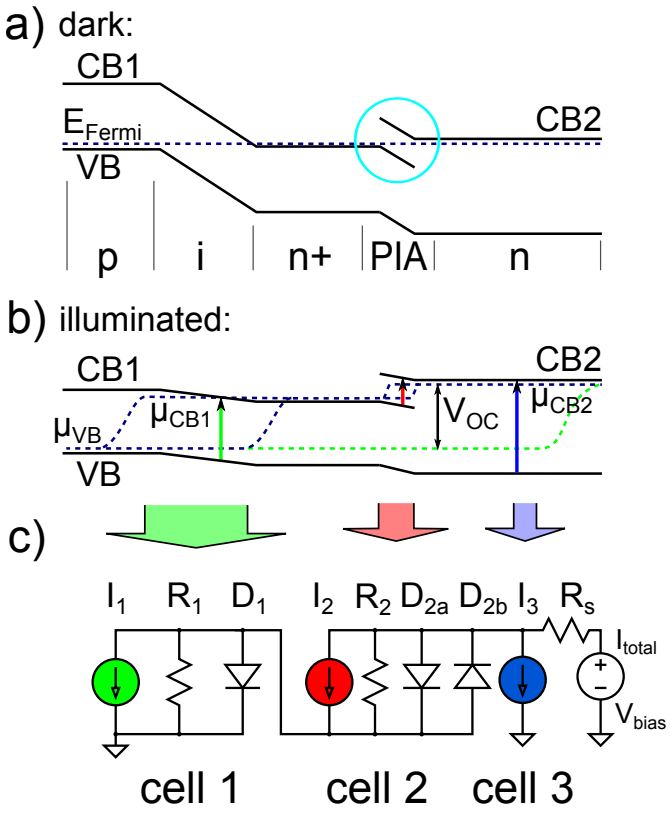

Figure 6.4: Principle of the proposed tandem cell: (a) under dark conditions with the blue circle marking the PIA, which can be realized e.g. with the design shown in in Fig. 6.5(a); (b) under illumination, with the arrows representing dipole transitions with different photon energies. μ_{VB}, μ_{CB1} and μ_{CB2} indicate the quasi-FERMI-levels for the corresponding bands. (c) Equivalent circuit design for the tandem cell.

line in Fig. 6.4(b). For photoexcitation of only the pin-junction and the PIA, the hole quasi-FERMI-level is represented by the lower blue dashed line in the pin-junction.

Similar to conventional multijunction (tandem) solar cells, this device requires current matching between charge carriers, which are generated in the PIA and those generated in the pin-section. This is illustrated in Fig. 6.4(c), where the structure is represented by an equivalent circuit model consisting of three solar cells. Each cell is represented by a current source, a diode and a resistor that are connected in parallel, following the single-diode equivalent circuit model. Cell 1 (InP-pin junction) and cell 2 (PIA) are connected in series and if only one of these two cells is illuminated, the diode of the respective other cell is driven in reverse direction and the photocurrent thus limited. Photoexcitation in the high-bandgap part should lead to a photocurrent, independent of the pin and PIA parts, and is thus represented as a third solar cell (cell 3), connected parallel with cells 1 and 2. For cell 3, the corresponding resistor and diode result from $R_{1,2}$ and $D_{1,2}$; the resistors and diodes of cells 1 and 2.

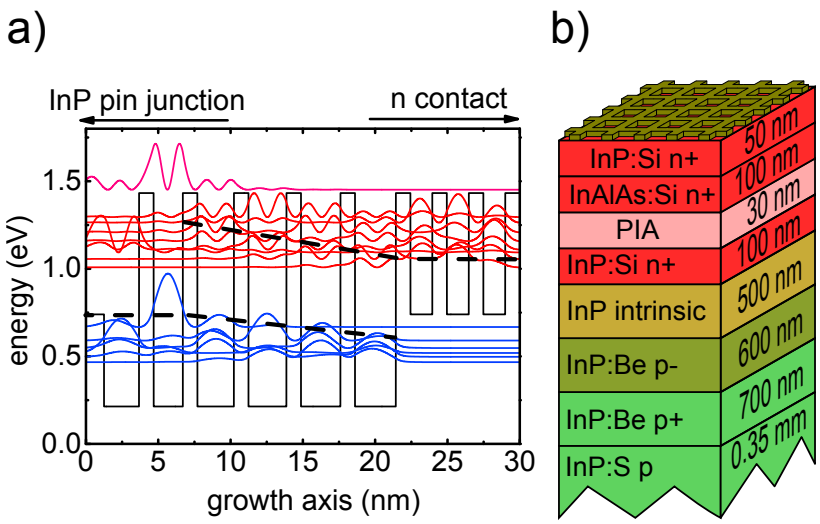

Figure 6.5: Cell design. (a) PIA part of the cell based on an asymmetric series of InGaAs/AlAs and InAlAs/AlAs quantum wells. The black solid line represents the barrier/well CBMs, and the red and blue curves represent the wavefunctions of the two lowest minibands. The dashed black lines are a guide for the eyes to illustrate the gradient in the upper CB that causes charge separation in this layer, as shown in Fig. 6.4(a) in the blue circle. (b) Schematic of the different layers of the actual investigated tandem sample, grown from bottom to top with GSMBE.

The design shown in Fig. 6.4 has some notable similarities with the concept of the intermediate band solar cell proposed by LUQUE and MARTÍ [4, 215] that was shown in Fig. 6.1. For the tandem concept proposed here, there are in principle also three different bands involved: the valence band and two conduction bands CB1 and CB2 (see Fig. 6.4(a)). Similar to the IBSC, also transitions between all three bands contribute to the photocurrent: VB $\rightarrow$ CB1 in the pin-junction, CB1 $\rightarrow$ CB2 in the PIA and VB $\rightarrow$ CB2 near the n-contact. Thus, the CB1 has a similar function as the IB. However, in contrast to the IBSC the transitions take place in spatially separated parts of the cell and charge carrier separation occurs directly inside the areas considered for the intersubband absorption and interband absorption. This could allow to reduce recombination losses, compared to the IBSC concept.

6.2.2 Two-beam photocurrent measurements

GSMBE was employed by the *HU* group to grow a layered structure on a p-type InP substrate. This structure contains a InP pin-junction and a PIA and follows the design that was presented in Fig. 6.4. A schematic of the different layers is shown in Fig. 6.5(b). The n-type section of the pin-junction is heavily doped with $n = 5 \times 10^{18}\,\mathrm{cm}^{-2}$, so that the FERMI level exceeds the CBM and the CB states are

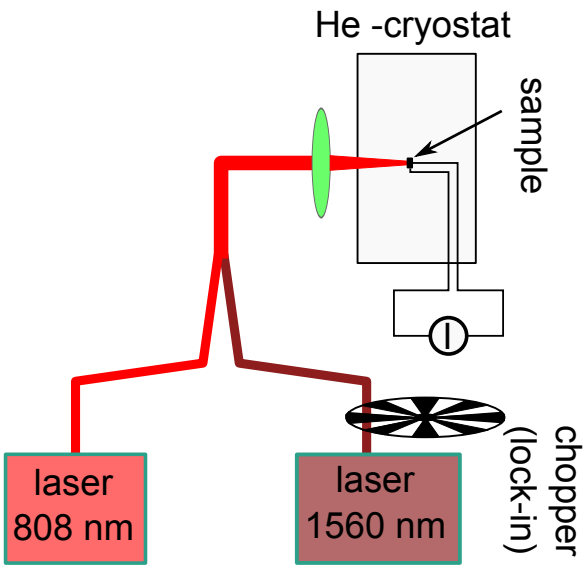

Figure 6.6: Experimental setup. The colored lines represent optical fibers. The 1560 nm laser could be chopped to allow for the use of lock-in detection.

partly filled with electrons. The implemented PIA consists of an asymmetrical stack of InGaAs/InAlAs/AlAs layers, as shown in Fig. 6.5(a) and is based on the design shown in Fig. 6.3. The energy of the corresponding confined states decreases towards the right hand edge of the PIA, as indicated with the black dashed lines, allowing for charge separation. The high bandgap section between the PIA and the n-contact is made of InAlAs, which has a higher band gap than InP to achieve an offset in the VB as in Fig. 6.4. We note that the VB of the PIA was not optimized, and thus might constrict the transport of holes to the p-contact.

Figure 6.6 shows the setup that we used to investigate the characteristics of the tandem sample under illumination. A continuous wave (cw) laser with central wavelength $\lambda = 808\,\text{nm}$ was used to pump the transition in the pin-junction (VB $\rightarrow$ CB1) and a second cw laser with $\lambda = 1560\,\text{nm}$ was used to pump the ISTs in the PIA[1] (CB1 $\rightarrow$ CB2). For the sake of simplicity, we omitted excitation of the high bandgap InAlAs section (VB $\rightarrow$ CB2). The tandem sample was mounted in a helium-cryostat and all of the measurements shown here have been conducted for a sample temperature of 20 K. Figure 6.7(a) shows the photocurrent for zero bias voltage as a function of the power of both lasers. For clarity, we subtracted the photocurrent, generated only by the $\lambda = 808\,\text{nm}$ laser. If the $\lambda = 808\,\text{nm}$ laser is turned off the $\lambda = 1560\,\text{nm}$ laser does not generate any photocurrent as the pin-junction is driven in reverse direction.

[1] We note that the laser wavelength of $\lambda = 1560\,\text{nm}$ is not optimal, as it does not match the maximum response (see Fig. 6.3(b)). At 1560 nm the response is $\approx 10\%$. In the following, this is compensated for by using high laser powers.

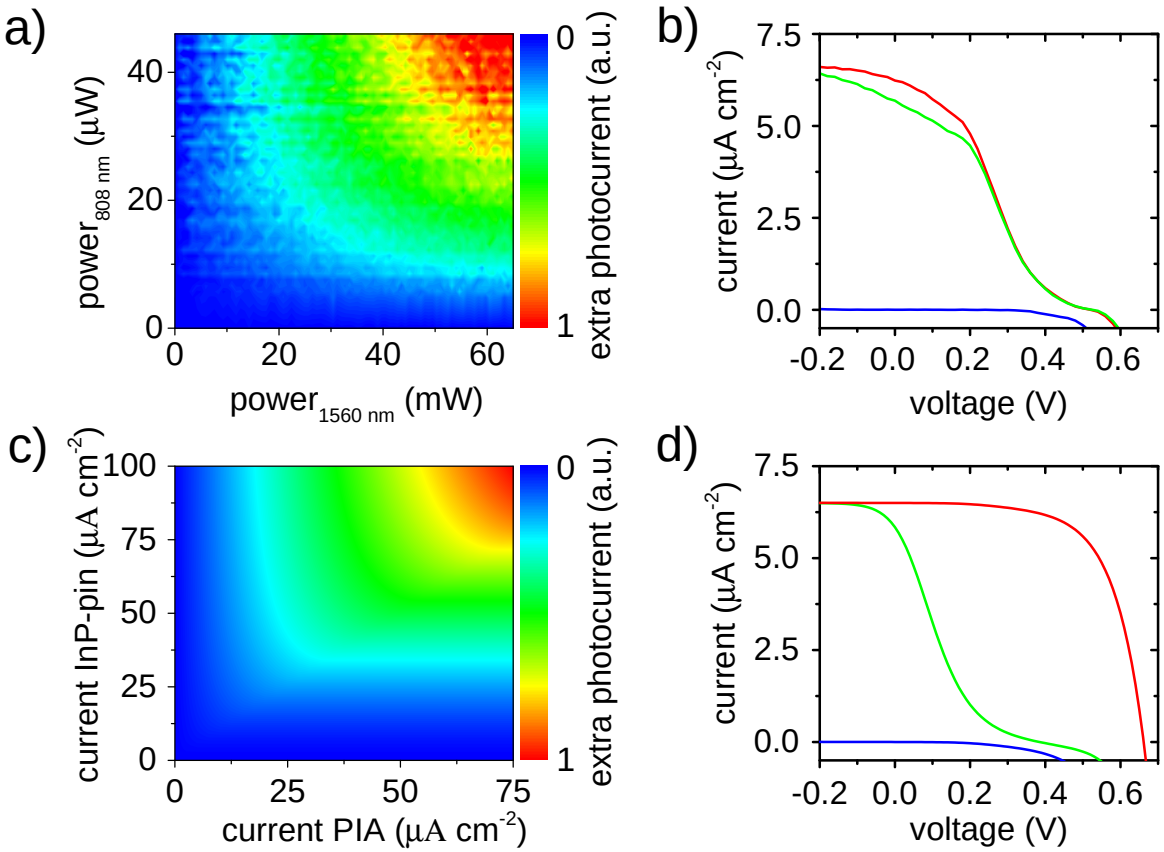

Figure 6.7: Photocurrent under different illumination conditions. (a) Photocurrent induced by the 1560 nm beam, plotted vs. the power of both lasers. (b) Measured IV-curves; blue: dark conditions; green: illumination with only the 808 nm laser (3.15 μW); red: with 808 nm laser (3.15 μW) and 1560 nm laser (70.2 mW). (c) as (a) but simulated curves. (d) as (b) but simulated curves.

However, if the $\lambda = 808$ nm laser is switched on, the pin-junction is filled with carriers and the quasi-holes, generated in CB1 in the PIA section can recombine with the electrons generated in the pin-junction. This leads to a photocurrent, induced by the $\lambda = 1560$ nm beam that depends on the intensity of both lasers and thus proves the tandem operation of both sub-cells.

In Fig. 6.7(b), IV-curves for different illumination conditions of the sample are shown. The curve recorded with only 1560 nm excitation has been omitted as it almost completely resembles the measurement under dark conditions (blue curve). The green curve represents the measurement under illumination of the sample with the 808 nm laser and shows a rather complex behavior: For $V < 0$ V we measure a photocurrent of $\approx 6.3\,\mu\mathrm{A\,cm^{-2}}$ with low voltage dependence. When applying a positive bias this photocurrent drops first linearly and for $V > 0.2$ V exponentially. For $V > 0.5$ V the photocurrent becomes negative, and again follows typical diode

characteristics. Additional illumination with the 1560 nm beam increases the current for $0.2\,\mathrm{V} < V < 0.2\,\mathrm{V}$, but has no effect for $V > 0.2\,\mathrm{V}$.

To investigate the anomalous IV-curve characteristics, we have simulated the IV-curves corresponding to the equivalent circuit model shown in Fig. 6.4(c) using the software *LTspice*. The characteristics of a classical tandem cell can be reproduced by implementing the diodes of cells 1 and 2 with the SHOCKLEY diode model [230]. This attempt, however, cannot describe the measured curve for illumination of the pin-section only (green). A far better agreement between model and measurement is achieved, if we allow for a current breakthrough that sets in at a certain voltage applied to the PIA. Due to the PIA's structure, we assume that such a current breakthrough is possible already at low voltages, which can be easily generated in the pin-section under illumination. This was implemented in the model by adding another parallel diode for the PIA in reverse direction and the results are shown in Fig. 6.7(d) for parameters, chosen to achieve best agreement with the measured data for dark conditions and illumination with the 808 nm laser.[2] The simulated curve for illumination of the pin-section only (green) now suddenly drops if the external bias exceeds a threshold value and compensates the voltage, generated in the pin-section. This is in agreement with the measured data. The exact curve shape in the region near the breakthrough thereby strongly depends on the particular breakthrough mechanism or even different competing breakthrough mechanisms, *e.g.* resonant and off-resonant tunneling, which our model fails to describe, leading to the significant discrepancy between data and model for $0\,\mathrm{V} < V < 0.5\,\mathrm{V}$.

The red curve in Fig. 6.7(d) shows the simulation for illumination of both sub cells. We see that for $V = 0\,\mathrm{V}$, only a slight increase in total photocurrent can be achieved by additionally pumping the PIA, in agreement with our experiments that show a similar result for zero external bias. Analogue to the measurement in Fig. 6.7(a), we plotted the calculated extra current in Fig. 6.7(c) for $V = 0\,\mathrm{V}$ as a function of current generated in the pin-section and the PIA and observe a similar trend as in our measurements. The principle appearance of this plot is that of any tandem cell device that requires current matching. This demonstrates that close to zero bias voltage the PIA structure shows the aimed-for charge-separating behavior.

However, the red curve in Fig. 6.7(d) shows a significant photovoltage enhancement due to illumination of the PIA up to $V \approx 0.6\,\mathrm{V}$, while in our measurements the additional photocurrent drops to zero for $V > 0.2\,\mathrm{V}$. We ascribe this to the miniband electronic structure that was optimized for conditions without bias. A volt-

[2] The parameters used here were: $R_s = 10\,\mathrm{k\Omega}$; $R_1 = 4\,\mathrm{G\Omega}$; $R_2 = 40\,\mathrm{k\Omega}$; D_1:($I_S = 3 \times 10^{-10}\,\mathrm{A\,cm^{-2}}$; $n = 6$); D_{2a}:($I_S = 4 \times 10^{-9}\,\mathrm{A\,cm^{-2}}$; $n = 6$); D_{2b}: ($I_S = 5 \times 10^{-8}\,\mathrm{A\,cm^{-2}}$; $n = 10$), with I_S and n being the saturation current and the ideality factor of the particular SHOCKLEY diode, respectively (compare Fig. 6.4(c)).

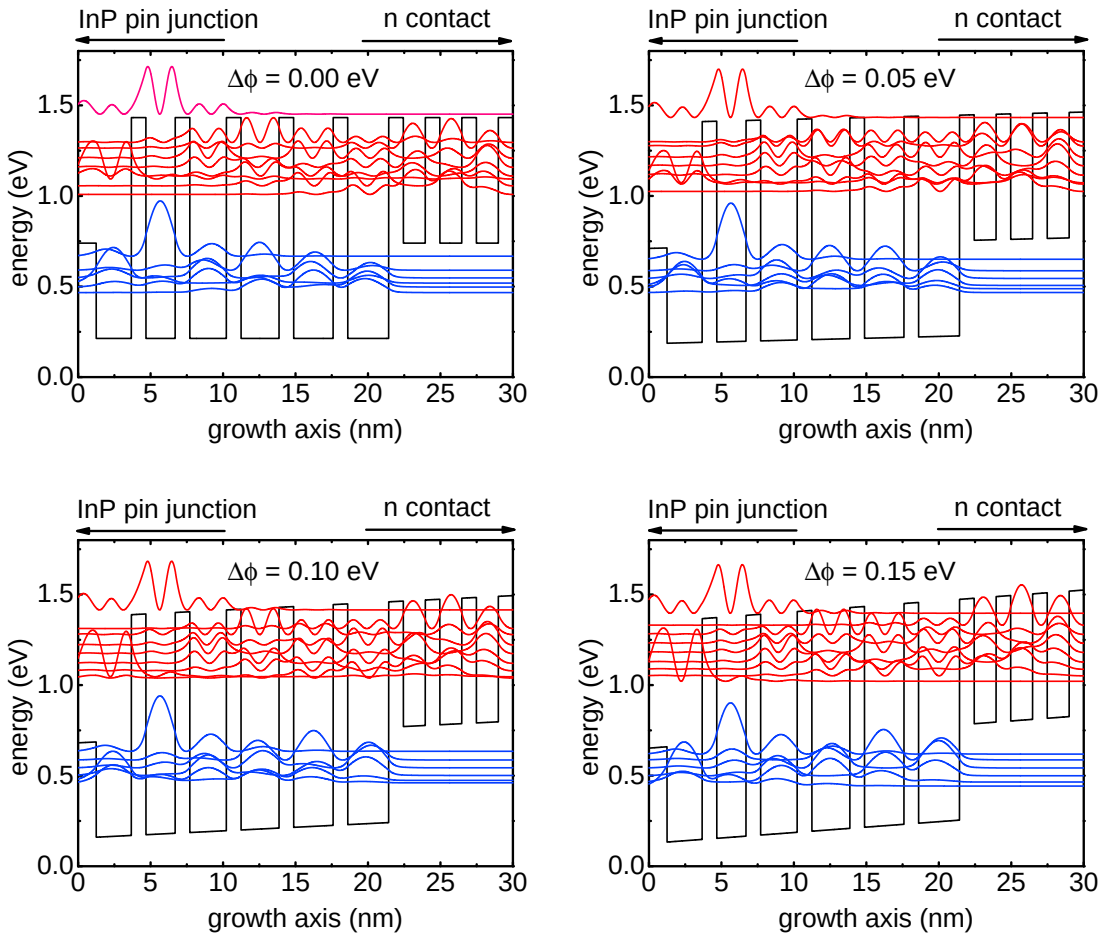

Figure 6.8: PIA part of the cell as in Fig. 6.5(a) but for different drops of potential between the edges of the PIA, assuming a constant electric field.

age drop between both sides of the PIA leads to a bending of the bands and thus changes the alignment of the miniband levels until the charge separating mechanism (cf. Fig. 6.5(a)) vanishes. The miniband alignment has been modeled for different drops in electric potential between the PIA edges, thus simulating the operation of the device with applied positive bias. This is shown in Fig. 6.8, where the solutions of the SCHRÖDINGER equation are shown, assuming a constant electric field over the structure. One clearly sees, that the energy downwards-staircase towards the n-contact vanishes. Electrons, which are photoexcited from CB1 to CB2, are not driven towards the n-contact by resonant phonon scattering, but rather relax down, back to CB1 by fast emission of phonons. Consequently, no photocurrent is generated in the PIA, which just acts as a diode that is driven in reverse direction and blocks the photocurrent of the InP cell. For a more efficient solar cell, the QW alignment therefore needs an improved adjustment, so that the minibands have the best charge separating properties at the desired working point.

6.2.3 Limitations of this approach

While providing proof-of-principal, the performance of the device is yet very limited and beyond any practical improvement of solar cell efficiency. This is not unexpected and was never intended with this first sample. Instead the particular design includes a variety of trade-offs between the experimental possibilities available on the time scale of the conducted research. This includes the pool of materials that could be grown by the team of the *HU* group and the processing of the solar cells but also the available wavelengths in the experimental setup used to measure the photocurrent under different illumination conditions. The most prominent limitations of the cell are addressed in the following paragraphs:

Efficient carrier separation in the PIA The shift of the minibands for an applied positive bias voltage and the arising problems have already been explained above. Also under ideal assumptions, efficient charge separation in a PIA is an issue. According to GIORGETTA *et al.* this is mostly determined by the relation of relaxation time τ_{rel} of electrons in the upper miniband and the escape time τ_{esc} to the "safe" side, facing the n-contact [224]. The escape probability then is $p_e \approx \frac{\tau_{rel}}{\tau_{rel}+\tau_{esc}}$ and for optimal performance $\tau_{rel} \gg \tau_{esc}$ is required. This again enhances the importance of long lifetimes of hot electrons as investigated in the previous chapters. According to our results, τ_{rel} will be mostly determined by the bulk band structure and difficult to optimize if not by switching to a different material class such as *e.g.* quantum dots. However, τ_{esc} could potentially be reduced by careful alignment of the miniband steps to match the LO-phonon energy. For a similar material system as used here (strain compensated InGaAs/InAlAs), escape probabilities as high as 30% have been reported [224, 231].

Light absorption and current matching For efficient carrier escape, the active absorber region of the PIA must be thin (typical QCPDs range from 5 nm to 20 nm, depending on the peak absorption wavelength [224]). This in turn reduces the capability to absorb light unless adequate light trapping is employed. Light management is also an issue due to the POYNTING-vector limitations. Gratings — as employed here — are one solution for this problem and could also be applied to the backside of the sample with theoretical efficiencies of 90% for a single QW [232]. Most of the studies performed on QCPDs employ a prism-like architecture (which is rather inapplicable for solar cells) and found single pass absorption values $< 3\%$. This and the off-resonant excitation (cf. Fig. 6.3(b)) can easily explain the low measured extra current despite of the high laser power used for the measurements in Fig. 6.7(b). This shows that either the grating design needs to be maxed-out or that a fundamentally different approach is required.

One option could be to incorporate the PIA as a radial core/multishell structure on vertical nanowires. This leads to a much higher volume of the PIA material compared to the interband absorber and thus a higher absorption. Furthermore, the POYNTING vector is parallel to the nanowires and the quantum well plane in this scenario. This would also solve the problem resulting from the dipole selection rules. In any case, the concept for absorbing infrared light with a PIA will be especially interesting in combination with conventional multijunction solar cells, since here the general current is lower and current matching will be thus easier to achieve.

Carrier recombination The third major limitation arises due to non-radiative recombination. The growth of multiple quantum wells also includes the preparation of several interfaces. Switching between different materials is likely to introduce roughness and defect states at the interfaces, which in turn can act as recombination centers and drastically reduce the carrier lifetime. Heavy doping of the materials further facilitates recombination. Measurements with time-resolved single photon counting and time-resolved terahertz spectroscopy have been performed to study the charge carrier lifetimes in InGaAs/InAlAs quantum wells. Samples with well thicknesses between 5 nm and 20 nm were provided by the *HU* group. Our measurements at room temperature reveal lifetimes that start from 30 ps and reach 1 ns, increasing with excitation density and thickness. The data can be well explained with SHOCKLEY-READ-HALL recombination via deep trap states, so that electrons and holes decay with the same time constants [233, 234]. At low excitation densities, as in the measurements at the solar cell, the deduced surface recombination velocity is $(\approx 2800 \pm 500)\,\frac{\mathrm{cm}}{\mathrm{s}}$. At $T = 20\,\mathrm{K}$, where the photocurrent measurements presented were preformed, the lifetimes exceed $> 1\,\mathrm{ns}$ but at room temperature, recombination will be problematic. Since the recombination is related to the interface, significant improvement might be achieved by careful interface preparation. This emphasizes the requirement of short diffusion lengths and again points out the advantages of this design compared to the IBSC. There light absorption takes places exclusively in a heavily doped region, where the recombination is most pronounced. In the tandem architecture, it will only effect the holes generated inside or to the right hand side of the PIA.

6.3 Discussion

The performed experiments verify the principle operation of a novel tandem-like solar cell consisting of a photovoltaic intersubband absorber (PIA) and a pin-junction that was previously suggested in a related form but not realized [226]. The ideal design could potentially exceed the efficiencies of conventional tandem solar cells as the absorption in the high bandgap front contact operates as a third, additional high-bandgap cell, connected parallel to a two-terminal tandem cell. Presently, this concept is much in its infancy and while there is clearly a contribution to the total photocurrent by the photovoltaic intersubband absorber, no contribution to the photovoltage could be measured. This is attributed to the design of the photovoltaic intersubband absorber for optimal performance at zero bias. For open circuit conditions or near the theoretically desired working point, the operation of the PIA breaks down, because the minibands shift with respect to each other if there is a drop in electrical potential between both sides of the PIA. This problem can be overcome with an improved adjustment of the PIA minibands to shift them into the charge separating operation mode at the working point of the solar cell. Other problems that will need to be addressed include current matching, efficient charge separation, absorption and non-radiative recombination. The results serve as a proof-of-principle and it shall be noted that the basic concept to separate interband absorber and intermediate band absorber spatially is not restricted to a design based on quantum well structures. It can be extended to most of the concepts that have previously been proposed for intermediate band solar cells, *e.g.* quantum dot arrangements [216]. However, it is necessary to implement an intrinsic charge separating mechanism in the intersubband absorber, which for quantum dots has also been shown just recently [235].

7 Conclusion

In this work, the electronic structure and its influence on the cooling of hot electrons in semiconductors was studied for a variety of materials. This was done with a focus on the role of the semiconductor's geometry and its surface and in view of potential photovoltaic concepts that employ hot carriers. Finally, a design for a solar cell was presented that implements fast charge carrier separation to compensate for the short hot-carrier lifetimes. Measurements with time-resolved two-photon photoemission spectroscopy (tr-2PPE) on CdSe nanostructures showed that manipulation of the sample geometry substantially effects electron-phonon scattering and can be used to slow down the electron relaxation. This is mostly related to the electron confinement effects that occur in low-dimensional semiconductors and that modify the electronic structure. For 0D CdSe quantum dots it was shown that electron-phonon scattering via conduction band states is not the dominant pathway for the loss of electron energy. Instead, the strong overlap between electron and hole promotes an AUGER-like mechanism, where the electron transfers its excess energy to the hole within $200 - 300\,\mathrm{fs}$. If this mechanism is suppressed with hole scavenging ligands, the relaxation is significantly slower, but still happens on a time scale of a few picoseconds with evidence for relaxation via intermediate states between the discrete conduction band states. Most plausibly, these relate to the surrounding ligands or Cd dangling bonds that are known to act as electron traps. In contrast, 2D nanoplatelets revealed very fast relaxation rates that lead to the loss of most of the energy within less than $500\,\mathrm{fs}$. This result is also found irrespective of different thicknesses, hole-scavenging ligands or a CdS shell surrounding the platelets. It is thus concluded that the dominant energy loss mechanism is not surface- or ligand-related, nor does it involve the photogenerated holes. Instead, the energy loss rate and its dependence on the electron temperature seem to be determined by LO phonon scattering in parabolic bands, characteristic for 2D semiconductors. This is emphasized by the good agreement between the experimental data and a theoretical model for this mechanism.

Following this, the importance of surface states on the relaxation of bulk electrons was studied exemplarily with 2PPE on III-V semiconductor surfaces prepared by metal organic vapor phase epitaxy. The electronic structure of the (100)-surface was investigated for GaP and InP and the scattering of electrons between 3D bulk and the 2D surface states was studied. It was shown for GaP(100) that the surface reconstruction has a significant impact on the surface electronic structure: The Ga-rich (2×4) mixed-dimer (100) reconstruction has two different unoccupied surface states near the conduction band minimum that are extremely sensitive to oxygen exposure.

For the P-rich $(2 \times 2)/c(4 \times 2)$ surface reconstruction no unoccupied surface states could be detected at all. An occupied surface state near the valence band maximum was found for both surfaces. These results were compared to reflection anisotropy spectroscopy (RAS) measurements and prominent features in the RA spectra could be explained with the surface states that were identified in 2PPE. The cooling of hot electrons in the vicinity of surface states was investigated with time-resolved 2PPE at the In-rich (2×4)-reconstructed InP(100) surface that is similar to the analogously reconstructed GaP(100) surface. In these measurements the scattering — back and forth — between bulk conduction band states and a particular surface state (C2) could be clearly identified. Comparison of data before and after oxygen exposure allowed to deduce a time constant of 20 fs for the scattering from C2 to isoenergetic bulk states, which is on the same time scale as bulk LO-phonon scattering. Simultaneously, these measurements revealed that the cooling of hot bulk carriers is not notably altered due to the presence of C2. This complements the findings on CdSe nanostructures: If the energy loss via conduction band states is significantly slowed down — as in quantum dots — scattering via the surface can be a fast alternative relaxation path. This pathway is still slower than bulk LO-phonon scattering in 3D or 2D semiconductors. As a result, quantum dots are the more promising candidates for photovoltaics based on hot carriers [117, 215, 218]. However, elaborate surface passivation, *e.g.* via core/shell structures [10], will be required to reduce the influence of alternative relaxation channels, as highlighted by the measurements on quantum dots. Also, transport and cell design are still an issue that would be easier to solve with 2D quantum wells that are grown epitaxially. However, no long hot carrier lifetimes are to be expected here due to the continuous density of states, as shown in the experiments.

In the last part of this thesis, an approach was shown to circumvent the energy loss related to short hot-carrier lifetimes by fast extraction of the hot carriers. This was done in form of a tandem solar cell design by combining an InP pin-junction with a photovoltaic intersubband absorber (PIA), consisting of InGaAs/InAlAs/InAs quantum wells. Charge separation in the PIA is achieved via an asymmetrical, step-like alignment of the electronic states. The operation of this concept, in principle, was confirmed experimentally and its basic characteristics could be explained with an equivalent circuit design. While this device is far from achieving reasonable efficiencies, possibilities for improvement were shown and the concept itself might provide inspiration for similar approaches. All in all, the results indicate that the realization of photovoltaic concepts based on hot carriers will remain a challenge, due to the fast carrier relaxation. However, the implementation of nanostructured devices that pursue a very fast collection of the hot carriers' extra energy could represent a promising pathway towards this goal.

Appendices

A Tr-2PPE signal for reversed pump-probe order

An additional influence on the 2PPE spectra is the "backward process" occurring at lower kinetic energy regions around $\Delta t = 0$ in which the roles of the laser pulses are exchanged. Hence, in this process, the probe pulse pumps and the pump pulse probes. Since the probe pulse is in the UV energy range, higher QD or ligand states can be excited. This process can be seen as the reverse process of "normal" 2PPE and thus a corresponding decay is seen at negative time delays when the probe pulse comes before the pump pulse. Figure A.1(a) shows the comparison of two transients at different kinetic energies for HDT capped QDs. The transient at lower kinetic energies decays at negative time delays which results from the reverse 2PPE process. The transient at higher kinetic energies shows the opposite behavior indicating a "normal" 2PPE process. To verify that the signal at negative time delays stems from a backwards process, we furthermore compare measurements with different pump photon energies but the same probe photon energy. For negative time delays this means that the electrons are pumped to the same intermediate state energy (by the probe), but are photoemitted with different kinetic energies. Figure A.1(b) shows transients recorded with $h\nu_{probe} = 4.59\,\text{eV}$ and either $h\nu_{pump} = 2.14\,\text{eV}$ or $h\nu_{pump} = 4.59\,\text{eV}$. Hereby, the transient with $h\nu_{probe} = 4.59\,\text{eV}$ shows electrons with a kinetic energy that is 2.45 eV higher than for the measurement with $h\nu_{pump} = 2.14\,\text{eV}$ so that both transients reflect the same intermediate state energy (cf. Sec. 2.4). The shape fo both transients is identical, which totally confirms our assumption.

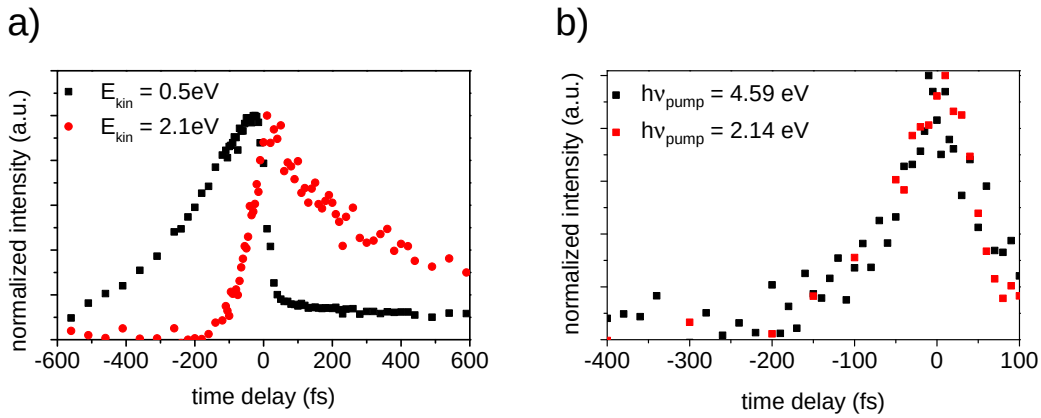

Figure A.1: (a) Signals for negative time delays for HDT capped QDs of 4.2 nm diameter at different kinetic energies. (b) Signals for negative time delays for OA capped QDs of 3.5 nm diameter for different pump photon energies (at negative times the probe pulse precedes the pump).

B Temperature dependent energy-loss-rate (ELR)

The energy dependent scattering rate $W_{\mathbf{k}}$ is a quantity that is very difficult to address directly with experimental methods, since in almost all know cases, ensembles of charge carriers are excited. As discussed in section 2.3, carrier-carrier scattering is typically faster or on the same time scale as carrier-phonon scattering. Thus, one usually measures the relaxation of the whole electron distribution, which is best characterized by an average energy loss rate per electron that depends on the temperature of the electron distribution, as well as on the occupation of phonon modes. Here, the average energy loss rate per electron is defined as:

$$\left\langle \frac{dE}{dt} \right\rangle = \frac{\int_0^\infty \rho(E) f(E) \frac{dE}{dt} dE}{\int_0^\infty \rho(E) f(E) dE} \tag{B.1}$$

with $\rho(E)$ being the electron density of states, $f(E)$ the electron distribution function, which for non-interacting carriers is given by the *Fermi-Dirac* distribution function

$$f(E) = \frac{1}{e^{\frac{E-E_F}{k_B T_e}} + 1} \tag{B.2}$$

where E_F is the chemical potential, although it will be referred to as *Fermi*-level in this work, which is a common nomenclature, although not totally correct as the *Fermi*-level is defined only for $T_e = 0\,\mathrm{K}$. $\frac{dE}{dt}$ is the energy loss rate of an electron with energy E, given by the absorption and emission rates:

$$\frac{dE}{dt} = \left.\frac{dE}{dt}\right|_{ab} + \left.\frac{dE}{dt}\right|_{em}. \tag{B.3}$$

For polar optical phonon scattering we can find a simple analytical expression by making a couple of assumptions. First, we assume that the energy of all LO-Phonons is $\hbar\omega_{LO}$ and that the scattering rate is independent of the electron energy. We also assume low excitation densities so that state filling can be neglected. Second, we assume that the emission and absorption rates are constant and described by a mean scattering time τ. Then

$$\left.\frac{dE}{dt}\right|_{ab} = n(\omega_{LO}) \frac{\hbar\omega_{LO}}{\tau}, \tag{B.4}$$

$$\left.\frac{dE}{dt}\right|_{em} = (n(\omega_{LO}) + 1) \frac{\hbar\omega_{LO}}{\tau} \Theta\left(E - \hbar\omega_{LO}\right) \tag{B.5}$$

The Θ - function makes sure, that only electrons with $E \geq \hbar\omega_{LO}$ can emit phonons.

Third, we assume a quantum will with infinite barriers. If all electrons are located

within in the lowest subband we can calculate with a constant density of states $\rho(E) = const.$

Forth, we assume that the electron distribution function can be approximated with the *Maxwell-Boltzmann* statistics which is valid for low electron densities in the conduction band. Hence $f(E) \propto e^{\frac{E}{k_B T_e}}$. Solving the integrals in Eq.B.1 with these assumptions we obtain

$$\left\langle -\frac{dE}{dt} \right\rangle = \frac{\hbar\omega_{LO}}{\tau} \exp\left(-\frac{\hbar\omega_{LO}}{k_B T_e}\right) \frac{\exp\left(\frac{\hbar\omega_{LO}}{k_B T_{lat}}\right) - \exp\left(\frac{\hbar\omega_{LO}}{k_B T_e}\right)}{\exp\left(\frac{\hbar\omega_{LO}}{k_B T_{lat}}\right) - 1}. \tag{B.6}$$

which becomes

$$\left\langle -\frac{dE}{dt} \right\rangle = \frac{\hbar\omega_{LO}}{\tau} e^{-\frac{\hbar\omega_{LO}}{k_B T_e}} \tag{B.7}$$

for $T_{lat} \to 0$, an expression, commonly used in literature [24, 236]. In a particular the second assumption needs to be carefully reviewed since especially for energies with high excess energy, the rates deviate considerably as shown in Fig. 2.10 and the ELR for electron distributions with high electron temperatures is thus overestimated with this approach, compared to a full numerical treatment of Eqs. 2.34 and 5.6.

C Background correction for tr-2PPE

Measurements with equal pump and probe photon energy For tr-2PPE measurements with equal pump and probe photon in the UV, there is always a background signal, related to electrons that are photoemitted by two-photon emission processes within the duration of the individual pulses. Basically these are the processes that were exploited Sec. 5.2 to study the electronic structure of GaP(100) and that were described in detail in Sec. 2.4. The resulting signal for an experiment with two beams can be described as

$$\begin{aligned} I_{total}(E_{kin}) &= A(E_{kin}) \cdot \left(I_{pump}^2 + I_{probe}^2\right) + B(E_{kin}, \Delta t) I_{pump} \cdot I_{probe} + \\ &+ C(E_{kin}) \cdot (I_{pump} + I_{probe}) , \end{aligned} \tag{C.1}$$

where $A(E_{kin})$ is the shape of the spectrum resulting from two-photon events within the duration of one single laser pulse and $C(E_{kin})$ corresponds to 1PPE events (see. e.g. Fig. 5.9(b)). $B(E_{kin}, \Delta t)$ finally, is the shape of the spectrum, resulting due to photoemission events involving one photon from the pump and one photon from the probe beam. In principle, this is the signal that we are interested in, when doing tr-2PPE experiments, while A and C are considered as background. Here the assumption was made, that the time-dependent signal does not depend on the intensities of pump or probe beam. As a first approach to gain access to $B(E_{kin}, \Delta t)$ one would consider to record one-beam 2PPE spectra with bot beam beams, separately, and afterwards subtract these spectra from the tr-2PPE signal. This would remove the $A(E_{kin})$ and $C(E_{kin})$ terms in Eq. C.1. However, thereby a problem was encountered resulting from the surface photovoltage that builds up with increasing laser intensities and shifts the spectrum to lower/higher energies for upward/downward bandbending at the surface (cf. Sec. 5.2.2). Thus, spectra recorded with two beams are shifted slightly compared to measurements recorded with only one beam and the tr-2PPE spectra corrected this way contain pronounced artifacts.

A solution of this problem is to subtract the spectrum recorded in the two-beam measurements when both beams overlap temporally *i.e.* $\Delta t = 0$, since $B(E_{kin}, 0) = A(E_{kin})$. To account for different beam intensities this spectrum was scaled down, to match the observed background for large Δt in the high energetic part of the spectrum as here $B(E_{kin}, \Delta t) = 0$. This approach results in a quite satisfying background correction but with the drawback that the linear term with $C(E_{kin})$ cannot be corrected leading to a remaining signal at low kinetic energies, where 1PPE is most pronounced. However, the signal that we are interested in lies typically at higher kinetic energies, so that this contribution can be neglected.

Measurements with VIS pump and UV probe This case is easier to treat than the case of equal pump and probe photon energies. The basic assumption is that for $\Delta t < 0$, *i.e.* when the probe pulse precedes the pump pulse, there is no photoinduced signal and $B(E_{kin}, \Delta t < 0) = 0$. Near$\Delta t = 0$ this is not always fulfilled, since also the probe can photoexcite electrons, which can be photoemitted subsequently by the pump (see *e.g.* Appendix A). However, for longer negative time delays this approximation is very reliable and subtraction of a spectrum recorded at $\Delta t = -10\,\mathrm{ps}$ yields a background-free tr-2PPE signal as the terms A and C in Eq. C.1 cancel completely.

Bibliography

[1] W. Shockley, H. J. Queisser: *Detailed Balance Limit of Efficiency of p-n Junction Solar Cells*, J. Appl. Phys. **32**, 510 (1961).

[2] F. Dimroth et al.: *Wafer bonded four-junction GaInP/GaAs//GaInAsP/GaInAs concentrator solar cells with 44.7% efficiency*, Prog. Photovolt: Res. Appl. **22**, 277 (2014).

[3] T. N. D. Tibbits et al.: "New Efficiency Frontiers with Wafer-Bonded Multi-Junction Solar Cells." in *29th European Photovoltaic Solar Energy Conference and Exhibition*, 1975, DOI: 10.4229/EUPVSEC20142014-4CP.2.1 (2014).

[4] A. Luque, A. Martí: *Increasing the Efficiency of Ideal Solar Cells by Photon Induced Transitions at Intermediate Levels*, Phys. Rev. Lett. **78**, 5014 (1997).

[5] R. T. Ross, A. J. Nozik: *Efficiency of hot-carrier solar energy converters*, J. Appl. Phys. **53**, 3813 (1982).

[6] P. T. Landsberg, H. Nussbaumer, G. Willeke: *Band-band impact ionization and solar cell efficiency*, J. Appl. Phys. **74**, 1451 (1993).

[7] R. Brendel, J. H. Werner, H. J. Queisser: *Thermodynamic efficiency limits for semiconductor solar cells with carrier multiplication*, Sol. Energy Mater. Sol. Cells **41–42**, 419 (1996).

[8] P. Würfel: *Solar energy conversion with hot electrons from impact ionisation*, Sol. Energy Mater. Sol. Cells **46**, 43 (1997).

[9] A. J. Nozik: *Spectroscopy and Hot Electron Relaxation Dynamics in Semiconductor Quantum Wells and Quantum Dots*, Annu. Rev. Phys. Chem. **52**, 193 (2001).

[10] A. Pandey, P. Guyot-Sionnest: *Slow Electron Cooling in Colloidal Quantum Dots*, Science **322**, 929 (2008).

[11] G. Czycholl, *Theoretische Festkörperphysik: Von den klassischen Modellen zu modernen Forschungsthemen*, 3rd ed., Berlin: Springer (2007).

[12] J. R. Chelikowsky, M. L. Cohen: *Nonlocal pseudopotential calculations for the electronic structure of eleven diamond and zinc-blende semiconductors*, Phys. Rev. B **14**, 556 (1976).

[13] B. K. Ridley, *Quantum Processes in Semiconductors*, 5th ed., Oxford: Oxford University Press (2013).

[14] T. Ihn, *Semiconductor Nanostructures: Quantum States and Electronic Transport*, Oxford: Oxford University Press (2009).

[15] P. Harrison, *Quantum Wells, Wires and Dots: Theoretical and Computational Physics of Semiconductor Nanostructures*, Chichester: John Wiley & Sons (2011).

[16] "II-VI and I-VII Compounds; Semimagnetic Compounds 41B", in: *Landolt-Börnstein - Group III Condensed Matter*, ed. by O. Madelung, U. Rössler, M. Schulz, Berlin/Heidelberg: Springer-Verlag, (1999).

[17] B. R. Nag, *Physics of Quantum Well Devices*, Luxembourg: Springer Science & Business Media (2001).

[18] Y. Fu, *Physical Models of Semiconductor Quantum Devices*, Luxembourg: Springer Science & Business Media (2013).

[19] L. Banyai, S. W. Koch, S. W. Koch, *Semiconductor Quantum Dots: Series on Atomic, Molecular and Optical Physics*, Singapore; River Edge, NJ: World Scientific Publishing Co Pte Ltd (1993).

[20] D. J. Norris, M. G. Bawendi: *Measurement and assignment of the size-dependent optical spectrum in CdSe quantum dots*, Phys. Rev. B **53**, 16338 (1996).

[21] A. I. Ekimov, F. Hache, M. C. Schanne-Klein, D. Ricard, C. Flytzanis, I. A. Kudryavtsev, T. V. Yazeva, A. V. Rodina, A. L. Efros: *Absorption and intensity-dependent photoluminescence measurements on CdSe quantum dots: assignment of the first electronic transitions*, J. Opt. Soc. Am. B **10**, 100 (1993).

[22] U. Woggon, S. V. Gaponenko: *Excitons in Quantum Dots*, phys. stat. sol. (b) **189**, 285 (1995).

[23] V. I. Klimov, *Nanocrystal Quantum Dots*, 2nd ed., Boca Raton (USA): CRC Press (2012).

[24] J. Shah, *Ultrafast spectroscopy of semiconductors and semiconductor nanostructures*, Berlin: Springer (1999).

[25] F. Sasaki, T. Mishina, Y. Masumoto, B. Fluegel, K. Meissner, N. Peyghambarian: *Non-equilibrium distribution of hot carriers in a CdSe thin film*, Semicond. Sci. Technol. **7**, B160 (1992).

[26] U. Hohenester, P. Supancic, P. Kocevar, X. Q. Zhou, W. Kütt, H. Kurz: *Subpicosecond thermalization and relaxation of highly photoexcited electrons and holes in intrinsic and p-type GaAs and InP*, Phys. Rev. B **47**, 13233 (1993).

[27] L. Rota, P. Lugli, T. Elsaesser, J. Shah: *Ultrafast thermalization of photoexcited carriers in polar semiconductors*, Phys. Rev. B **47**, 4226 (1993).

[28] H. Frohlich: *Theory of Electrical Breakdown in Ionic Crystals*, Proc. R. Soc. Lond. A **160**, 230 (1937).

[29] W. Cai, M. C. Marchetti, M. Lax: *Nonequilibrium electron-phonon scattering in semiconductor heterojunctions*, Phys. Rev. B **34**, 8573 (1986).

[30] J. Fritsch, P. Pavone, U. Schröder: *Ab initio calculation of the phonon dispersion in bulk InP and in the InP(110) surface*, Phys. Rev. B **52**, 11326 (1995).

[31] C. Jacoboni, *Theory of Electron Transport in Semiconductors: A Pathway from Elementary Physics to Nonequilibrium Green Functions*, Heidelberg: Springer (2010).

[32] "Group IV Elements, IV-IV and III-V Compounds. Part b - Electronic, Transport, Optical and Other Properties", in: *Landolt-Börnstein - Group III Condensed Matter*, ed. by O. Madelung, U. Rössler, M. Schulz, Berlin/Heidelberg: Springer, (2002).

[33] W. Fawcett, A. Boardman, S. Swain: *Monte Carlo determination of electron transport properties in gallium arsenide*, J. Phys. Chem. Solids **31**, 1963 (1970).

[34] B. K. Ridley: *The electron-phonon interaction in quasi-two-dimensional semiconductor quantum-well structures*, J. Phys. C: Solid State Phys. **15**, 5899 (1982).

[35] F. A. Riddoch, B. K. Ridley: *On the scattering of electrons by polar optical phonons in quasi-2D quantum wells*, J. Phys. C: Solid State Phys. **16**, 6971 (1983).

[36] B. K. Ridley: "II.1 - Electron–phonon interactions in 2D systems", in: *Hot Carriers in Semiconductor Nanostructures*, ed. by J. Shah, San Diego: Academic Press, (1992).

[37] T. Fauster: "VIII - Time-resolved two-photon-photemission", in: *Solid-state photoemission and related methods: theory and experiment*, ed. by W. Schattke, M. A. V. Hove, Weinheim: Wiley-VCH, (2003).

[38] H. Ueba, B. Gumhalter: *Theory of two-photon photoemission spectroscopy of surfaces*, Prog. Surf. Sci. **82**, 193 (2007).

[39] T. Hertel, E. Knoesel, M. Wolf, G. Ertl: *Ultrafast Electron Dynamics at Cu(111): Response of an Electron Gas to Optical Excitation*, Phys. Rev. Lett. **76**, 535 (1996).

[40] M. Göppert-Mayer: *Über Elementarakte mit zwei Quantensprüngen*, Ann. Phys. **401**, 273 (1931).

[41] R. Loudon, *The quantum theory of light*, Oxford: Oxford University Press (2000).

[42] R. Menzel, *Photonics: linear and nonlinear interactions of laser light and matter*, Berlin: Springer (2007).

[43] S. Hüfner, *Photoelectron Spectroscopy: Principles and Applications*, 3rd ed., Berlin: Springer (2003).

[44] M. P. Seah, W. A. Dench: *Quantitative electron spectroscopy of surfaces: A standard data base for electron inelastic mean free paths in solids*, Surf. Interface Anal. **1**, 2 (1979).

[45] W. A. Tisdale, M. Muntwiler, D. J. Norris, E. S. Aydil, X.-Y. Zhu: *Electron Dynamics at the ZnO* $(10\bar{1}0)$ *Surface*, J. Phys. Chem. C **112**, 14682 (2008).

[46] L. Gundlach, R. Ernstorfer, F. Willig: *Escape dynamics of photoexcited electrons at catechol:*TiO_2*(110)*, Phys. Rev. B **74**, 035324 (2006).

[47] D. E. Aspnes, A. A. Studna: *Dielectric functions and optical parameters of Si, Ge, GaP, GaAs, GaSb, InP, InAs, and InSb from 1.5 to 6.0 eV*, Phys. Rev. B **27**, 985 (1983).

[48] L. Gundlach, R. Ernstorfer, E. Riedle, R. Eichberger, F. Willig: *Femtosecond two-photon photoemission at 150 kHz utilizing two noncollinear optical parametric amplifiers for measuring ultrafast electron dynamics*, Appl. Phys. B **80**, 727 (2005).

[49] L. Gundlach, *Surface Electron Transfer Dynamics in the Presence of Organic Chromophores*, Berlin: FU Berlin (2005).

[50] L. Töben, *Untersuchungen zur Energetik und Dynamik von Elektronen an MOCVD-gewachsenen III-V Halbleiter Oberflächen*, Berlin: TU Berlin (2002).

[51] A. Hotzel, *Femtosekunden-Elektronendynamik der Adsorbat-bedeckten Cu(111)-Oberfläche*, Berlin: FU Berlin (1999).

[52] C. Gahl, *Elektronentransfer- und Solvatisierungsdynamik in Eis adsorbiert auf Metalloberflächen*, Berlin: FU Berlin (2004).

[53] K. Jakobi: "3.1.2.4 Work function data", in: *Electronic and Vibrational Properties*, ed. by G. Chiarotti, Berlin/Heidelberg: Springer, (1994).

[54] P. Weightman, D. S. Martin, R. J. Cole, T. Farrell: *Reflection anisotropy spectroscopy*, Rep. Prog. Phys. **68**, 1251 (2005).

[55] T. Hannappel, L. Töben, K. Möller, F. Willig: *In-situ monitoring of InP(100) and GaP(100) interfaces and characterization with RDS at 20 K*, J. Electron. Mater. **30**, 1425 (2001).

[56] H. Döscher, T. Hannappel, B. Kunert, A. Beyer, K. Volz, W. Stolz: *In situ verification of single-domain III-V on Si(100) growth via metal-organic vapor phase epitaxy*, Appl. Phys. Lett. **93**, 172110 (2008).

[57] O. Supplie, T. Hannappel, M. Pristovsek, H. Döscher: *In situ access to the dielectric anisotropy of buried III-V/Si(100) heterointerfaces*, Phys. Rev. B **86**, 035308 (2012).

[58] W. G. Schmidt, N. Esser, A. M. Frisch, P. Vogt, J. Bernholc, F. Bechstedt, M. Zorn, T. Hannappel, S. Visbeck, F. Willig, W. Richter: *Understanding reflectance anisotropy: Surface-state signatures and bulk-related features in the optical spectrum of InP(001)(2 x 4)*, Phys. Rev. B **61**, R16335 (2000).

[59] P. H. Hahn, W. G. Schmidt, F. Bechstedt, O. Pulci, R. Del Sole: *P-rich GaP(001)(2 x 1)/(2 x 2) surface: A hydrogen-adsorbate structure determined from first-principles calculations*, Phys. Rev. B **68**, 033311 (2003).

[60] P. Sippel, W. Albrecht, D. Mitoraj, R. Eichberger, T. Hannappel, D. Vanmaekelbergh: *Two-Photon Photoemission Study of Competing Auger and Surface-Mediated Relaxation of Hot Electrons in CdSe Quantum Dot Solids*, Nano Lett. **13**, 1655 (2013).

[61] P. Sippel, W. Albrecht, J. C. van der Bok, R. J. A. Van Dijk-Moes, T. Hannappel, R. Eichberger, D. Vanmaekelbergh: *Femtosecond Cooling of Hot Electrons in CdSe Quantum-Well Platelets*, Nano Lett. **15**, 2409 (2015).

[62] A. J. Nozik: *Quantum dot solar cells*, Physica E **14**, 115 (2002).

[63] A. L. Efros, V. Kharchenko, M. Rosen: *Breaking the phonon bottleneck in nanometer quantum dots: Role of Auger-like processes*, Solid State Commun. **93**, 281 (1995).

[64] E. Hendry, M. Koeberg, F. Wang, H. Zhang, C. de Mello Donegá, D. Vanmaekelbergh, M. Bonn: *Direct Observation of Electron-to-Hole Energy Transfer in CdSe Quantum Dots*, Phys. Rev. Lett. **96**, 057408 (2006).

[65] V. I. Klimov, A. A. Mikhailovsky, D. W. McBranch, C. A. Leatherdale, M. G. Bawendi: *Mechanisms for intraband energy relaxation in semiconductor quantum dots: The role of electron-hole interactions*, Phys. Rev. B **61**, R13349 (2000).

[66] R. Schaller, V. Klimov: *High Efficiency Carrier Multiplication in PbSe Nanocrystals*, Phys. Rev. Lett. **92**, 186601 (2004).

[67] R. D. Schaller, M. A. Petruska, V. I. Klimov: *Effect of electronic structure on carrier multiplication efficiency: Comparative study of PbSe and CdSe nanocrystals*, Appl. Phys. Lett. **87**, 253102 (2005).

[68] D. V. Talapin, J.-S. Lee, M. V. Kovalenko, E. V. Shevchenko: *Prospects of Colloidal Nanocrystals for Electronic and Optoelectronic Applications*, Chem. Rev. **110**, 389 (2010).

[69] D. Vanmaekelbergh, P. Liljeroth: *Electron-conducting quantum dot solids: novel materials based on colloidal semiconductor nanocrystals*, Chem. Soc. Rev. **34**, 299 (2005).

[70] R. Karel Capek, I. Moreels, K. Lambert, D. De Muynck, Q. Zhao, A. Van Tomme, F. Vanhaecke, Z. Hens: *Optical Properties of Zincblende Cadmium Selenide Quantum Dots*, J. Phys. Chem. C **114**, 6371 (2010).

[71] I. J. Kramer, E. H. Sargent: *The Architecture of Colloidal Quantum Dot Solar Cells: Materials to Devices*, Chem. Rev. **114**, 863 (2014).

[72] Z. Ning et al.: *Air-stable n-type colloidal quantum dot solids*, Nat. Mater. **13**, 822 (2014).

[73] C. B. Murray, D. J. Norris, M. G. Bawendi: *Synthesis and characterization of nearly monodisperse CdE (E = sulfur, selenium, tellurium) semiconductor nanocrystallites*, J. Am. Chem. Soc. **115**, 8706 (1993).

[74] L. Qu, Z. A. Peng, X. Peng: *Alternative Routes toward High Quality CdSe Nanocrystals*, Nano Lett. **1**, 333 (2001).

[75] C. de Mello Donegá, S. G. Hickey, S. F. Wuister, D. Vanmaekelbergh, A. Meijerink: *Single-Step Synthesis to Control the Photoluminescence Quantum Yield and Size Dispersion of CdSe Nanocrystals*, J. Phys. Chem. B **107**, 489 (2002).

[76] J. Joo, J. S. Son, S. G. Kwon, J. H. Yu, T. Hyeon: *Low-Temperature Solution-Phase Synthesis of Quantum Well Structured CdSe Nanoribbons*, J. Am. Chem. Soc. **128**, 5632 (2006).

[77] S. Ithurria, B. Dubertret: *Quasi 2D Colloidal CdSe Platelets with Thicknesses Controlled at the Atomic Level*, J. Am. Chem. Soc. **130**, 16504 (2008).

[78] C. Bouet, M. D. Tessier, S. Ithurria, B. Mahler, B. Nadal, B. Dubertret: *Flat Colloidal Semiconductor Nanoplatelets*, Chem. Mater. **25**, 1262 (2013).

[79] Z. Li, X. Peng: *Size/Shape-Controlled Synthesis of Colloidal CdSe Quantum Disks: Ligand and Temperature Effects*, J. Am. Chem. Soc. **133**, 6578 (2011).

[80] S. Ithurria, G. Bousquet, B. Dubertret: *Continuous Transition from 3D to 1D Confinement Observed during the Formation of CdSe Nanoplatelets*, J. Am. Chem. Soc. **133**, 3070 (2011).

[81] C. Bouet, B. Mahler, B. Nadal, B. Abecassis, M. D. Tessier, S. Ithurria, X. Xu, B. Dubertret: *Two-Dimensional Growth of CdSe Nanocrystals, from Nanoplatelets to Nanosheets*, Chem. Mater. **25**, 639 (2013).

[82] A. T. Dijksman, B. Dubertret: *Accurate energy-size dependence of excitonic transitions in semiconductor nanocrystals and nanoplatelets using a phase jump approach*, Phys. Status Solidi B **251**, 537 (2014).

[83] S. Ithurria, M. D. Tessier, B. Mahler, R. P. S. M. Lobo, B. Dubertret, A. L. Efros: *Colloidal nanoplatelets with two-dimensional electronic structure*, Nat. Mater. **10**, 936 (2011).

[84] R. Benchamekh, N. A. Gippius, J. Even, M. O. Nestoklon, J.-M. Jancu, S. Ithurria, B. Dubertret, A. L. Efros, P. Voisin: *Tight-binding calculations of image-charge effects in colloidal nanoscale platelets of CdSe*, Phys. Rev. B **89**, 035307 (2014).

[85] M. D. Tessier, C. Javaux, I. Maksimovic, V. Loriette, B. Dubertret: *Spectroscopy of Single CdSe Nanoplatelets*, ACS Nano **6**, 6751 (2012).

[86] M. D. Tessier, B. Mahler, B. Nadal, H. Heuclin, S. Pedetti, B. Dubertret: *Spectroscopy of Colloidal Semiconductor Core/Shell Nanoplatelets with High Quantum Yield*, Nano Lett. **13**, 3321 (2013).

[87] Z. Chen, B. Nadal, B. Mahler, H. Aubin, B. Dubertret: *Quasi-2D Colloidal Semiconductor Nanoplatelets for Narrow Electroluminescence*, Adv. Funct. Mater. **24**, 295 (2014).

[88] C. She, I. Fedin, D. S. Dolzhnikov, A. Demortière, R. D. Schaller, M. Pelton, D. V. Talapin: *Low-Threshold Stimulated Emission Using Colloidal Quantum Wells*, Nano Lett. **14**, 2772 (2014).

[89] B. Guzelturk, Y. Kelestemur, M. Olutas, S. Delikanli, H. V. Demir: *Amplified Spontaneous Emission and Lasing in Colloidal Nanoplatelets*, ACS Nano **8**, 6599 (2014).

[90] J. Q. Grim, S. Christodoulou, F. Di Stasio, R. Krahne, R. Cingolani, L. Manna, I. Moreels: *Continuous-wave biexciton lasing at room temperature using solution-processed quantum wells*, Nat. Nano **9**, 891 (2014).

[91] B. Mahler, B. Nadal, C. Bouet, G. Patriarche, B. Dubertret: *Core/Shell Colloidal Semiconductor Nanoplatelets*, J. Am. Chem. Soc. **134**, 18591 (2012).

[92] E. Zillner, S. Fengler, P. Niyamakom, F. Rauscher, K. Köhler, T. Dittrich: *Role of Ligand Exchange at CdSe Quantum Dot Layers for Charge Separation*, J. Phys. Chem. C **116**, 16747 (2012).

[93] D. F. Underwood, T. Kippeny, S. J. Rosenthal: *Ultrafast Carrier Dynamics in CdSe Nanocrystals Determined by Femtosecond Fluorescence Upconversion Spectroscopy*, J. Phys. Chem. B **105**, 436 (2000).

[94] P. Guyot-Sionnest, M. Shim, C. Matranga, M. Hines: *Intraband relaxation in CdSe quantum dots*, Phys. Rev. B **60**, R2181 (1999).

[95] S. F. Wuister, C. de Mello Donegá, A. Meijerink: *Influence of Thiol Capping on the Exciton Luminescence and Decay Kinetics of CdTe and CdSe Quantum Dots*, J. Phys. Chem. B **108**, 17393 (2004).

[96] Y. Liu, M. Gibbs, J. Puthussery, S. Gaik, R. Ihly, H. W. Hillhouse, M. Law: *Dependence of Carrier Mobility on Nanocrystal Size and Ligand Length in PbSe Nanocrystal Solids*, Nano Lett. **10**, 1960 (2010).

[97] X. Peng, M. C. Schlamp, A. V. Kadavanich, A. P. Alivisatos: *Epitaxial Growth of Highly Luminescent CdSe/CdS Core/Shell Nanocrystals with Photostability and Electronic Accessibility*, J. Am. Chem. Soc. **119**, 7019 (1997).

[98] M. P. Halsall, J. E. Nicholls, J. J. Davies, B. Cockayne, P. J. Wright, A. G. Cullis: *CdS/CdSe strained layer superlattices grown by MOCVD*, Semicond. Sci. Technol. **3**, 1126 (1988).

[99] N. J. Borys, M. J. Walter, J. Huang, D. V. Talapin, J. M. Lupton: *The Role of Particle Morphology in Interfacial Energy Transfer in CdSe/CdS Heterostructure Nanocrystals*, Science **330**, 1371 (2010).

[100] S.-H. Wei, S. B. Zhang, A. Zunger: *First-principles calculation of band offsets, optical bowings, and defects in CdS, CdSe, CdTe, and their alloys*, J. Appl. Phys. **87**, 1304 (2000).

[101] L. T. Kunneman, J. M. Schins, S. Pedetti, H. Heuclin, F. C. Grozema, A. J. Houtepen, B. Dubertret, L. D. A. Siebbeles: *Nature and Decay Pathways of Photoexcited States in CdSe and CdSe/CdS Nanoplatelets*, Nano Lett. **14**, 7039 (2014).

[102] U. Woggon, H. Giessen, F. Gindele, O. Wind, B. Fluegel, N. Peyghambarian: *Ultrafast energy relaxation in quantum dots*, Phys. Rev. B **54**, 17681 (1996).

[103] V. I. Klimov, D. W. McBranch, C. A. Leatherdale, M. G. Bawendi: *Electron and hole relaxation pathways in semiconductor quantum dots*, Phys. Rev. B **60**, 13740 (1999).

[104] P. Guyot-Sionnest, B. Wehrenberg, D. Yu: *Intraband relaxation in CdSe nanocrystals and the strong influence of the surface ligands*, J. Chem. Phys. **123**, 074709 (2005).

[105] L. Miaja-Avila, J. R. Tritsch, A. Wolcott, W.-L. Chan, C. A. Nelson, X.-Y. Zhu: *Direct Mapping of Hot-Electron Relaxation and Multiplication Dynamics in PbSe Quantum Dots*, Nano Lett. **12**, 1588 (2012).

[106] R. Koole, B. Luigjes, M. Tachiya, R. Pool, T. J. H. Vlugt, C. de Mello Donegá, A. Meijerink, D. Vanmaekelbergh: *Differences in Cross-Link Chemistry between Rigid and Flexible Dithiol Molecules Revealed by Optical Studies of CdTe Quantum Dots*, J. Phys. Chem. C **111**, 11208 (2007).

[107] M. T. Frederick, E. A. Weiss: *Relaxation of Exciton Confinement in CdSe Quantum Dots by Modification with a Conjugated Dithiocarbamate Ligand*, ACS Nano **4**, 3195 (2010).

[108] C. de Mello Donegá: *Formation of nanoscale spatially indirect excitons: Evolution of the type-II optical character of CdTe/CdSe heteronanocrystals*, Phys. Rev. B **81**, 165303 (2010).

[109] C. A. Leatherdale, W.-K. Woo, F. V. Mikulec, M. G. Bawendi: *On the Absorption Cross Section of CdSe Nanocrystal Quantum Dots*, J. Phys. Chem. B **106**, 7619 (2002).

[110] Z. Sun, I. Swart, C. Delerue, D. Vanmaekelbergh, P. Liljeroth: *Orbital and charge-resolved polaron states in CdSe dots and rods probed by scanning tunneling spectroscopy*, Phys. Rev. Lett. **102**, 196401 (2009).

[111] L. Töben, L. Gundlach, R. Ernstorfer, R. Eichberger, T. Hannappel, F. Willig, A. Zeiser, J. Förstner, A. Knorr, P. H. Hahn, W. G. Schmidt: *Femtosecond Transfer Dynamics of Photogenerated Electrons at a Surface Resonance of Reconstructed InP(100)*, Phys. Rev. Lett. **94**, 067601 (2005).

[112] L. Jdira, P. Liljeroth, E. Stoffels, D. Vanmaekelbergh, S. Speller: *Size-dependent single-particle energy levels and interparticle Coulomb interactions in CdSe quantum dots measured by scanning tunneling spectroscopy*, Phys. Rev. B **73**, 115305 (2006).

[113] A. M. Munro, B. Zacher, A. Graham, N. R. Armstrong: *Photoemission Spectroscopy of Tethered CdSe Nanocrystals: Shifts in Ionization Potential and Local Vacuum Level As a Function of Nanocrystal Capping Ligand*, ACS Appl. Mater. Interfaces **2**, 863 (2010).

[114] M. Soreni-Harari, N. Yaacobi-Gross, D. Steiner, A. Aharoni, U. Banin, O. Millo, N. Tessler: *Tuning Energetic Levels in Nanocrystal Quantum Dots through Surface Manipulations*, Nano Lett. **8**, 678 (2008).

[115] E. Talgorn, E. Moysidou, R. D. Abellon, T. J. Savenije, A. Goossens, A. J. Houtepen, L. D. A. Siebbeles: *Highly Photoconductive CdSe Quantum-Dot Films: Influence of Capping Molecules and Film Preparation Procedure*, J. Phys. Chem. C **114**, 3441 (2010).

[116] V. I. Klimov, D. W. McBranch: *Femtosecond 1P-to-1S Electron Relaxation in Strongly Confined Semiconductor Nanocrystals*, Phys. Rev. Lett. **80**, 4028 (1998).

[117] W. A. Tisdale, K. J. Williams, B. A. Timp, D. J. Norris, E. S. Aydil, X.-Y. Zhu: *Hot-Electron Transfer from Semiconductor Nanocrystals*, Science **328**, 1543 (2010).

[118] R. R. Cooney, S. L. Sewall, E. A. Dias, D. M. Sagar, K. E. H. Anderson, P. Kambhampati: *Unified picture of electron and hole relaxation pathways in semiconductor quantum dots*, Phys. Rev. B **75**, 245311 (2007).

[119] D. J. Trivedi, L. Wang, O. V. Prezhdo: *Auger-Mediated Electron Relaxation Is Robust to Deep Hole Traps: Time-Domain Ab Initio Study of CdSe Quantum Dots*, Nano Lett. **15**, 2086 (2015).

[120] P. C. Sercel: *Multiphonon-assisted tunneling through deep levels: A rapid energy-relaxation mechanism in nonideal quantum-dot heterostructures*, Phys. Rev. B **51**, 14532 (1995).

[121] D. F. Schroeter, D. J. Griffiths, P. C. Sercel: *Defect-assisted relaxation in quantum dots at low temperature*, Phys. Rev. B **54**, 1486 (1996).

[122] W. Wallauer, T. Fauster: *Two-photon excitation processes and linewidths of surface and image states on Cu(111)*, Surf. Sci. **374**, 44 (1997).

[123] C. Kentsch, M. Kutschera, M. Weinelt, T. Fauster, M. Rohlfing: *Electronic structure of Si(100) surfaces studied by two-photon photoemission*, Phys. Rev. B **65**, 035323 (2001).

[124] L. Töben, T. Hannappel, R. Eichberger, K. Möller, L. Gundlach, R. Ernstorfer, F. Willig: *Two-photon photoemission as a probe of unoccupied and occupied surface states of InP(100)*, J. Cryst. Growth **248**, 206 (2003).

[125] W. Zhao, W. Wei, J. White: *Two-photon photoemission spectroscopy: naphthalene on Cu(111)*, Surf. Sci. **547**, 374 (2003).

[126] L. Gundlach, J. Szarko, L. D. Socaciu-Siebert, A. Neubauer, R. Ernstorfer, F. Willig: *Different orientations of large rigid organic chromophores at the rutile TiO_2 surface controlled by different binding geometries of specific anchor groups*, Phys. Rev. B **75**, 125320 (2007).

[127] S. Pokrant, K. Whaley: *Tight-binding studies of surface effects on electronic structure of CdSe nanocrystals: the role of organic ligands, surface reconstruction, and inorganic capping shells*, EPJ B **6**, 255 (1999).

[128] V. I. Klimov, M. G. Bawendi: *Ultrafast Carrier Dynamics, Optical Amplification, and Lasing in Nanocrystal Quantum Dots*, MRS Bulletin **26**, 998 (2001).

[129] C. Javaux, B. Mahler, B. Dubertret, A. Shabaev, A. V. Rodina, A. L. Efros, D. R. Yakovlev, F. Liu, M. Bayer, G. Camps, L. Biadala, S. Buil, X. Quelin, J.-P. Hermier: *Thermal activation of non-radiative Auger recombination in charged colloidal nanocrystals*, Nat. Nano **8**, 206 (2013).

[130] E. Lhuillier, A. Robin, S. Ithurria, H. Aubin, B. Dubertret: *Electrolyte-Gated Colloidal Nanoplatelets-Based Phototransistor and Its Use for Bicolor Detection*, Nano Lett. **14**, 2715 (2014).

[131] L. Biadala, F. Liu, M. D. Tessier, D. R. Yakovlev, B. Dubertret, M. Bayer: *Recombination Dynamics of Band Edge Excitons in Quasi-Two-Dimensional CdSe Nanoplatelets*, Nano Lett. **14**, 1134 (2014).

[132] L. T. Kunneman, M. D. Tessier, H. Heuclin, B. Dubertret, Y. V. Aulin, F. C. Grozema, J. M. Schins, L. D. A. Siebbeles: *Bimolecular Auger Recombination of Electron–Hole Pairs in Two-Dimensional CdSe and CdSe/CdZnS Core/Shell Nanoplatelets*, J. Phys. Chem. Lett. **4**, 3574 (2013).

[133] M. Pelton, S. Ithurria, R. D. Schaller, D. S. Dolzhnikov, D. V. Talapin: *Carrier Cooling in Colloidal Quantum Wells*, Nano Lett. **12**, 6158 (2012).

[134] Y. Rosenwaks, M. C. Hanna, D. H. Levi, D. M. Szmyd, R. K. Ahrenkiel, A. J. Nozik: *Hot-carrier cooling in GaAs: Quantum wells versus bulk*, Phys. Rev. B **48**, 14675 (1993).

[135] A. S. Vengurlekar, S. S. Prabhu, S. K. Roy, J. Shah: *Large reduction in hot-carrier energy-loss rates in CdSe caused by nonequilibrium optical phonons*, Phys. Rev. B **50**, 15461 (1994).

[136] M. Pugnet, J. Collet, A. Cornet: *Cooling of hot electron-hole plasmas in the presence of screened electron-phonon interactions*, Solid State Commun. **38**, 531 (1981).

[137] A. Žukauskas: *Second nonequilibrium-phonon bottleneck for carrier cooling in highly excited polar semiconductors*, Phys. Rev. B **57**, 15337 (1998).

[138] H. Lobentanzer, W. Stolz, J. Nagle, K. Ploog: *Cooling of hot carriers in three- and two-dimensional Ga0.47In0.53As*, Phys. Rev. B **39**, 5234 (1989).

[139] C. H. Yang, J. M. Carlson-Swindle, S. A. Lyon, J. M. Worlock: *Hot-Electron Relaxation in GaAs Quantum Wells*, Phys. Rev. Lett. **55**, 2359 (1985).

[140] J. F. Ryan, R. A. Taylor, A. J. Turberfield, A. Maciel, J. M. Worlock, A. C. Gossard, W. Wiegmann: *Time-Resolved Photoluminescence of Two-Dimensional Hot Carriers in GaAs-AlGaAs Heterostructures*, Phys. Rev. Lett. **53**, 1841 (1984).

[141] P. A. Snow, D. J. Westland, J. F. Ryan, T. Kerr, H. Munekata, L. L. Chang: *Hot carrier cooling in GaSb: Bulk and quantum wells*, Superlattices Microstruct. **5**, 595 (1989).

[142] S. Ninomiya, S. Adachi: *Optical properties of cubic and hexagonal CdSe*, J. Appl. Phys. **78**, 4681 (1995).

[143] S. Ramakrishna, F. Willig, A. Knorr: *Time-resolved two-photon photoemission spectroscopy of semiconductor bulk states*, Appl. Phys. A **78**, 247 (2004).

[144] J. Even, L. Pedesseau, C. Katan: *Understanding Quantum Confinement of Charge Carriers in Layered 2D Hybrid Perovskites*, ChemPhysChem **15**, 3733 (2014).

[145] A. C. S. Algarte: *Cooling of hot carriers in highly photoexcited semiconductors*, Phys. Rev. B **38**, 2162 (1988).

[146] U. Bockelmann, G. Bastard: *Phonon scattering and energy relaxation in two-, one-, and zero-dimensional electron gases*, Phys. Rev. B **42**, 8947 (1990).

[147] P. Sippel, O. Supplie, M. M. May, R. Eichberger, T. Hannappel: *Electronic structures of GaP(100) surface reconstructions probed with two-photon photoemission spectroscopy*, Phys. Rev. B **89**, 165312 (2014).

[148] P. Sippel, J. M. Szarko, T. Hannappel, R. Eichberger: *Ultrafast electron scattering from surface to bulk states at the InP(100) surface*, Phys. Rev. B **91**, 115312 (2015).

[149] Y. Dan, K. Seo, K. Takei, J. H. Meza, A. Javey, K. B. Crozier: *Dramatic Reduction of Surface Recombination by in Situ Surface Passivation of Silicon Nanowires*, Nano Lett. **11**, 2527 (2011).

[150] M. Otto, M. Kroll, T. Käsebier, R. Salzer, A. Tünnermann, R. B. Wehrspohn: *Extremely low surface recombination velocities in black silicon passivated by atomic layer deposition*, Appl. Phys. Lett. **100**, 191603 (2012).

[151] I. Vurgaftman, J. R. Meyer, L. R. Ram-Mohan: *Band parameters for III–V compound semiconductors and their alloys*, J. Appl. Phys. **89**, 5815 (2001).

[152] P. Yu, M. Cardona, *Fundamentals of Semiconductors: Physics and Materials Properties*, 4th ed., Berlin: Springer (2010).

[153] H. Kalt, *Optical properties of III-V semiconductors: the influence of multivalley band structures*, Berlin: Springer (1996).

[154] A. E. Yunovich: *Strahlende Rekombination und optische Eigenschaften von GaP*, Fortschr. Phys. **23**, 317 (1975).

[155] P. Lawaetz: *Camel's back structure of the conduction band in GaP*, Solid State Commun. **16**, 65 (1975).

[156] H. Ibach, *Physics of Surfaces and Interfaces*, Berlin, New York: Springer (2006).

[157] K. Lüdge, P. Vogt, O. Pulci, N. Esser, F. Bechstedt, W. Richter: *Clarification of the GaP(001)(2 x 4) Ga-rich reconstruction by scanning tunneling microscopy and ab initio theory*, Phys. Rev. B **62**, 11046 (2000).

[158] L. Töben, T. Hannappel, K. Möller, H. J. Crawack, C. Pettenkofer, F. Willig: *RDS, LEED and STM of the P-rich and Ga-rich surfaces of GaP(100)*, Surf. Sci. **494**, L755 (2001).

[159] W. G. Schmidt, E. L. Briggs, J. Bernholc, F. Bechstedt: *Structural fingerprints in the reflectance anisotropy spectra of InP(001)*(2×4) *surfaces*, Phys. Rev. B **59**, 2234 (1999).

[160] P. Vogt, T. Hannappel, S. Visbeck, K. Knorr, N. Esser, W. Richter: *Atomic surface structure of the phosphorous-terminated InP(001) grown by MOVPE*, Phys. Rev. B **60**, R5117 (1999).

[161] T. Hannappel, S. Visbeck, K. Knorr, J. Mahrt, M. Zorn, F. Willig: *Preparation of P-rich InP surfaces via MOCVD and surface characterization in UHV*, Appl. Phys. A **69**, 427 (1999).

[162] W. G. Schmidt, F. Bechstedt: *Geometry and electronic structure of InP(001)*(2×4) *reconstructions*, Surf. Sci. **409**, 474 (1998).

[163] A. M. Frisch, W. G. Schmidt, J. Bernholc, M. Pristovsek, N. Esser, W. Richter: *(2 x 4) GaP(001) surface: Atomic structure and optical anisotropy*, Phys. Rev. B **60**, 2488 (1999).

[164] N. Esser, W. G. Schmidt, J. Bernholc, A. M. Frisch, P. Vogt, M. Zorn, M. Pristovsek, W. Richter, F. Bechstedt, T. Hannappel, S. Visbeck: *GaP(001) and InP(001): Reflectance anisotropy and surface geometry*, J. Vac. Sci. Technol. B **17**, 1691 (1999).

[165] O. Pulci, W. Schmidt, F. Bechstedt: *Structure and Energetics of P-rich GaP(001) Surfaces*, phys. stat. sol. (a) **184**, 105 (2001).

[166] W. G. Schmidt, J. Bernholc, F. Bechstedt: *(001) Surfaces of GaP and InP: structural motifs, electronic states and optical signatures*, Appl. Surf. Sci. **166**, 179 (2000).

[167] W. G. Schmidt, F. Bechstedt, J. Bernholc: *Understanding reflectance anisotropy: Surface-state signatures and bulk-related features*, J. Vac. Sci. Technol. B **18**, 2215 (2000).

[168] Y. Fukuda, M. Shimomura, N. Sanada, M. Nagoshi: *Spectroscopic evidence for reduction of unoccupied states in the band gap of GaP(001) by H2S passivation*, J. Appl. Phys. **76**, 3632 (1994).

[169] N. Kadotani, M. Shimomura, Y. Fukuda: *Surface structure of phosphorus-terminated GaP(001)-(2 x 1)*, Phys. Rev. B **70**, 165323 (2004).

[170] T. Hannappel, L. Töben, S. Visbeck, H. J. Crawack, C. Pettenkofer, F. Willig: *UPS and 20 K reflectance anisotropy spectroscopy of the P-rich and In-rich surfaces of InP(100)*, Surf. Sci. **470**, L1 (2000).

[171] W. G. Schmidt, P. H. Hahn, F. Bechstedt, N. Esser, P. Vogt, A. Wange, W. Richter: *InP(001)-(2×1) Surface: A Hydrogen Stabilized Structure*, Phys. Rev. Lett. **90**, 126101 (2003).

[172] T. Hannappel, S. Visbeck, L. Töben, F. Willig: *Apparatus for investigating metalorganic chemical vapor deposition-grown semiconductors with ultrahigh-vacuum based techniques*, Rev. Sci. Instrum. **75**, 1297 (2004).

[173] P. Kleinschmidt, H. Döscher, P. Vogt, T. Hannappel: *Direct observation of dimer flipping at the hydrogen-stabilized GaP(100) and InP(100) surfaces*, Phys. Rev. B **83**, 155316 (2011).

[174] A. Dobrich, P. Kleinschmidt, H. Döscher, T. Hannappel: *Quantitative investigation of hydrogen bonds on Si(100) surfaces prepared by vapor phase epitaxy*, J. Vac. Sci. Technol., B **29**, 04D114 (2011).

[175] H. Döscher, B. Kunert, A. Beyer, O. Supplie, K. Volz, W. Stolz, T. Hannappel: *In situ antiphase domain quantification applied on heteroepitaxial GaP growth on Si(100)*, J. Vac. Sci. Technol. B **28**, C5H1 (2010).

[176] H. Döscher, K. Möller, T. Hannappel: *GaP(100) and InP(100) surface structures during preparation in a nitrogen ambient*, J. Cryst. Growth **318**, 372 (2011).

[177] D. Li, K. Liu, H. Xiao, H. Dong, X. Zu: *First-principles study of GaP(001) surfaces*, J. Alloys Compd. **440**, 229 (2007).

[178] B. Kaiser, D. Fertig, J. r. Ziegler, J. Klett, S. Hoch, W. Jaegermann: *Solar Hydrogen Generation with Wide-Band-Gap Semiconductors: GaP(100) Photoelectrodes and Surface Modification*, ChemPhysChem **13**, 3053 (2012).

[179] S. Hu, C. Xiang, S. Haussener, A. D. Berger, N. S. Lewis: *An analysis of the optimal band gaps of light absorbers in integrated tandem photoelectrochemical water-splitting systems*, Energy Environ. Sci. **6**, 2984 (2013).

[180] J. F. Geisz, J. Olson, D. Friedman, K. Jones, R. Reedy, M. Romero: "Lattice-matched GaNPAs-on-silicon tandem solar cells", in *Conference Record of the Thirty-first IEEE Photovoltaic Specialists Conference, 2005*, DOI: 10.1109/PVSC.2005.1488226 (2005).

[181] H. Döscher, O. Supplie, M. M. May, P. Sippel, C. Heine, A. G. Muñoz, R. Eichberger, H.-J. Lewerenz, T. Hannappel: *Epitaxial III–V Films and Surfaces for Photoelectrocatalysis*, ChemPhysChem **13**, 2899 (2012).

[182] B. C. Wood, T. Ogitsu, E. Schwegler: *Local structural models of complex oxygen- and hydroxyl-rich GaP/InP(001) surfaces*, J. Chem. Phys. **136**, 064705 (2012).

[183] S. Jeon, H. Kim, W. A. Goddard, H. A. Atwater: *DFT Study of Water Adsorption and Decomposition on a Ga-Rich GaP(001)(2 × 4) Surface*, J. Phys. Chem. C **116**, 17604 (2012).

[184] M. M. May, O. Supplie, C. Höhn, R. v. d. Krol, H.-J. Lewerenz, T. Hannappel: *The interface of GaP(100) and H2O studied by photoemission and reflection anisotropy spectroscopy*, New J. Phys. **15**, 103003 (2013).

[185] S. Visbeck, T. Hannappel, M. Zorn, J.-T. Zettler, F. Willig: *Temperature dependence and origin of InP(100) reflectance anisotropy down to 20 K*, Phys. Rev. B **63**, 245303 (2001).

[186] X. Lu, S. Huang, M. Diaz, R. Opila, A. Barnett: "Wide band gap Gallium Phosphide solar cells for multi-junction solar cell system", in *2010 35th IEEE Photovoltaic Specialists Conference (PVSC)*, 002079, DOI: 10.1109/PVSC.2010.5616636 (2010).

[187] T. G. Deutsch, C. A. Koval, J. A. Turner: *III-V Nitride Epilayers for Photoelectrochemical Water Splitting: GaPN and GaAsPN*, J. Phys. Chem. B **110**, 25297 (2006).

[188] A. Okano, R. K. Thoma, G. P. Williams, R. T. Williams: *Two-photon photoelectron spectroscopy of GaP(110) after sputtering, annealing, and multishot laser damage*, Phys. Rev. B **52**, 14789 (1995).

[189] C. A. Schmuttenmaer, C. Cameron Miller, J. W. Herman, J. Cao, D. A. Mantell, Y. Gao, R. J. D. Miller: *Femtosecond time-resolved photoemission study of hot electron relaxation at the GaAs(100) surface*, Chemical Physics **205**, 91 (1996).

[190] S. J. Diol, C. C. Miller, C. A. Schmuttenmaer, J. Cao, Y. Gao, D. A. Mantell, R. J. D. Miller: *Photogenerated hot electron dynamics at GaAs (100) surfaces*, J. Phys. D: Appl. Phys. **30**, 1427 (1997).

[191] M. H. Hecht: *Time dependence of photovoltaic shifts in photoelectron spectroscopy of semiconductors*, Phys. Rev. B **43**, 12102 (1991).

[192] M. Alonso, R. Cimino, K. Horn: *Surface photovoltage effects in photoemission from metal-GaP(110) interfaces: Importance for band bending evaluation*, Phys. Rev. Lett. **64**, 1947 (1990).

[193] G. Hollinger, F. Himpsel: *Oxygen chemisorption and oxide formation on Si(111) and Si(100) surfaces*, J. Vac. Sci. Technol. A. **1**, 640 (1983).

[194] R. Ludeke, A. Koma: *Electronic surface states on clean and oxygen-exposed GaAs surfaces*, J. Vac. Sci. Technol. **13**, 241 (1976).

[195] G. Chen, S. B. Visbeck, D. C. Law, R. F. Hicks: *Structure-sensitive oxidation of the indium phosphide (001) surface*, J. Appl. Phys. **91**, 9362 (2002).

[196] N. Fraj, I. Saïdi, S. B. Radhia, K. Boujdaria: *Band structures of AlAs, GaP, and SiGe alloys: A 30 kp model*, J. Appl. Phys. **102**, 053703 (2007).

[197] C. Eickhoff, M. Teichmann, M. Weinelt: *Two-State Double-Continuum Fano Resonance at the Si(100) Surface*, Phys. Rev. Lett. **107**, 176804 (2011).

[198] S. Ramakrishna, F. Willig, A. Knorr: *Photoinduced bulk-surface dynamics: time resolved two photon photoemission signals at semiconductor surfaces*, Surf. Sci. **558**, 159 (2004).

[199] H. J. Lewerenz, C. Heine, K. Skorupska, N. Szabo, T. Hannappel, T. Vo-Dinh, S. A. Campbell, H. W. Klemm, A. G. Muñoz: *Photoelectrocatalysis: principles, nanoemitter applications and routes to bio-inspired systems*, Energy Environ. Sci. **3**, 748 (2010).

[200] R. Clady, M. J. Y. Tayebjee, P. Aliberti, D. König, N. J. Ekins-Daukes, G. J. Conibeer, T. W. Schmidt, M. A. Green: *Interplay between the hot phonon effect and intervalley scattering on the cooling rate of hot carriers in GaAs and InP*, Prog. Photovolt. **20**, 82 (2012).

[201] P. N. Saeta, J. F. Federici, B. I. Greene, D. R. Dykaar: *Intervalley scattering in GaAs and InP probed by pulsed far-infrared transmission spectroscopy*, Appl. Phys. Lett. **60**, 1477 (1992).

[202] M. Weinelt, M. Kutschera, R. Schmidt, C. Orth, T. Fauster, M. Rohlfing: *Electronic structure and electron dynamics at Si(100)*, Appl. Phys. A **80**, 995 (2005).

[203] J. R. Goldman, J. A. Prybyla: *Ultrafast dynamics of laser-excited electron distributions in silicon*, Phys. Rev. Lett. **72**, 1364 (1994).

[204] S. Jeong, H. Zacharias, J. Bokor: *Ultrafast carrier dynamics on the Si(100) (2 x 1) surface*, Phys. Rev. B **54**, R17300 (1996).

[205] T. Ichibayashi, K. Tanimura: *Ultrafast Carrier Relaxation in Si Studied by Time-Resolved Two-Photon Photoemission Spectroscopy: Intravalley Scattering and Energy Relaxation of Hot Electrons*, Phys. Rev. Lett. **102**, 087403 (2009).

[206] J. Azuma, K. Takahashi, M. Kamada: *Direct observation of the dispersion and relaxation of photoexcited electrons in InAs*, Phys. Rev. B **81**, 113203 (2010).

[207] M. Mauerer, I. L. Shumay, W. Berthold, U. Höfer: *Ultrafast carrier dynamics in Si(111)(7 x 7) dangling bonds probed by time-resolved second-harmonic generation and two-photon photoemission*, Phys. Rev. B **73**, 245305 (2006).

[208] L. Töben, L. Gundlach, T. Hannappel, R. Ernstorfer, R. Eichberger, F. Willig: *Dynamics of electron scattering between bulk states and the C1 surface state of InP(100)*, Appl. Phys. A **78**, 239 (2004).

[209] M. M. May, H.-J. Lewerenz, T. Hannappel: *Optical in Situ Study of InP(100) Surface Chemistry: Dissociative Adsorption of Water and Oxygen*, J. Phys. Chem. C **118**, 19032 (2014).

[210] S. Adachi: *Optical dispersion relations for GaP, GaAs, GaSb, InP, InAs, InSb, $Al_xGa_{1-x}As$, and $In_{1-x}Ga_xAs_yP_{1-y}$*, J. Appl. Phys. **66**, 6030 (1989).

[211] R. Haight: *Electron dynamics at surfaces*, Surf. Sci. Rep., **21**, 275 (1995).

[212] P. Sippel, S. Heitz, M. Elagin, M. Semtsiv, R. Eichberger, W. T. Masselink, T. Hannappel, K. Schwarzburg: *Concept and demonstration of an intermediate band tandem device for solar energy conversion*, Progress in Photovoltaics: Research and Applications , doi:10.1002/pip.2697 (2015).

[213] A. Luque, A. Martí: *A metallic intermediate band high efficiency solar cell*, Prog. Photovolt: Res. Appl. **9**, 73 (2001).

[214] A. D. Vos: *Detailed balance limit of the efficiency of tandem solar cells*, J. Phys. D: Appl. Phys. **13**, 839 (1980).

[215] A. Luque, A. Martí: *The Intermediate Band Solar Cell: Progress Toward the Realization of an Attractive Concept*, Adv. Mater. **22**, 160 (2010).

[216] A. Martí, E. Antolín, C. R. Stanley, C. D. Farmer, N. López, P. Díaz, E. Cánovas, P. G. Linares, A. Luque: *Production of Photocurrent due to Intermediate-to-Conduction-Band Transitions: A Demonstration of a Key Operating Principle of the Intermediate-Band Solar Cell*, Phys. Rev. Lett. **97**, 247701 (2006).

[217] P. G. Linares, A. Martí, E. Antolín, C. D. Farmer, i. Ramiro, C. R. Stanley, A. Luque: *Voltage recovery in intermediate band solar cells*, Sol. Energy Mater. Sol. Cells **98**, 240 (2012).

[218] A. Mellor, A. Luque, I. Tobías, A. Martí: *The feasibility of high-efficiency InAs/GaAs quantum dot intermediate band solar cells*, Sol. Energy Mater. Sol. Cells **130**, 225 (2014).

[219] E. Antolín, A. Martí, C. D. Farmer, P. G. Linares, E. Hernández, A. M. Sánchez, T. Ben, S. I. Molina, C. R. Stanley, A. Luque: *Reducing carrier escape in the InAs/GaAs quantum dot intermediate band solar cell*, J. Appl. Phys. **108**, 064513 (2010).

[220] M. Sugiyama, Y. Wang, K. Watanabe, T. Morioka, Y. Okada, Y. Nakano: "Photocurrent generation by two-step photon absorption with quantum-well superlattice cell", in *37th IEEE Photovoltaic Specialists Conference (PVSC)*, DOI: 10.1109/PVSC.2011.6186647 (2011).

[221] H. C. Liu, F. Capasso, *Intersubband transitions in quantum wells: Physics and device applications I*, San Diego: Academic Press (2000).

[222] X. Liu, S. G. Bishop, J. N. Baillargeon, K. Y. Cheng: *Band gap bowing in $GaP_{1-x}N_x$ alloys*, Appl. Phys. Lett. **63**, 208 (1993).

[223] L. Gendron, M. Carras, A. Huynh, V. Ortiz, C. Koeniguer, V. Berger: *Quantum cascade photodetector*, Appl. Phys. Lett. **85**, 2824 (2004).

[224] F. Giorgetta, E. Baumann, M. Graf, Q. Yang, C. Manz, K. Kohler, H. Beere, D. Ritchie, E. Linfield, A. Davies, Y. Fedoryshyn, H. Jackel, M. Fischer, J. Faist, D. Hofstetter: *Quantum Cascade Detectors*, IEEE Journal of Quantum Electronics **45**, 1039 (2009).

[225] J. Yin, R. Paiella: *Multiple-junction quantum cascade photodetectors for thermophotovoltaic energy conversion*, Opt. Express **18**, 1618 (2010).

[226] J. Yin, R. Paiella: *Limiting performance analysis of cascaded interband/intersubband thermophotovoltaic devices*, Appl. Phys. Lett. **98**, 041103 (2011).

[227] A. Rogalski: *Quantum well photoconductors in infrared detector technology*, J. Appl. Phys. **93**, 4355 (2003).

[228] C. Gmachl, F. Capasso, D. L. Sivco, A. Y. Cho: *Recent progress in quantum cascade lasers and applications*, Rep. Prog. Phys. **64**, 1533 (2001).

[229] M. Elagin, P. Schulz, M. Elagin, M. P. Semtsiv, H. Kirmse, A. Mogilatenko, W. T. Masselink: *Highly strained photovoltaic dual-channel intersubband photodetectors grown by gas-source MBE*, J. Cryst. Growth **378**, 607 (2013).

[230] W. Shockley, *Electrons and holes in semiconductors, with applications to transistor electronics*, Huntington, N.Y: R. E. Krieger Pub. Co (1976).

[231] F. R. Giorgetta, E. Baumann, R. Théron, M. L. Pellaton, D. Hofstetter, M. Fischer, J. Faist: *Short wavelength ($4\,\mu m$) quantum cascade detector based on strain compensated InGaAs/InAlAs*, Appl. Phys. Lett. **92**, 121101 (2008).

[232] K. W. Goossen, S. A. Lyon: *Grating enhanced quantum well detector*, Appl. Phys. Lett. **47**, 1257 (1985).

[233] W. Shockley, W. T. Read: *Statistics of the Recombinations of Holes and Electrons*, Phys. Rev. **87**, 835 (1952).

[234] R. N. Hall: *Electron-Hole Recombination in Germanium*, Phys. Rev. **87**, 387 (1952).

[235] X.-J. Wang, S.-Q. Zhai, N. Zhuo, J.-Q. Liu, F.-Q. Liu, S.-M. Liu, Z.-G. Wang: *Quantum dot quantum cascade infrared photodetector*, Appl. Phys. Lett. **104**, 171108 (2014).

[236] S. Das Sarma: "II.2 - Quantum Many-Body Aspects of Hot-Carrier Relaxation in Semiconductor Microstructures", in: *Hot Carriers in Semiconductor Nanostructures*, ed. by J. Shah, San Diego: Academic Press, (1992).

Acknowledgment

I would like to express my gratitude to all the people who helped me realize this thesis...

...Prof. Dr. Thomas Hannappel, for giving me the opportunity to write this thesis, for frequent motivation, for sharing his experience and lots of scientific inspiration.

...Prof. Dr. Daniël Vanmaekelbergh, for agreeing to be one of the assessors of this thesis, for providing me with a variety of fascinating materials and substantial scientific discussions.

...Prof. Dr. Jure Demsar, for agreeing to be one of the assessors of this thesis.

...Dr. Rainer Eichberger, for the technical supervision, for his help with the laser, for backing me up in all sorts of administration issues and for a great poster.

...Dr. Klaus Schwarzburg, for the introduction into the world of solar cells, semiconductors, detectors, for fixing every software issue and for tasty labsnacks.

...Oliver Supplie, Dr. Anja Dobrich, Dr. Matthias M. May, and all the other members of the former E-I5 group of the *HZB* (now known as the *Fachgebiet Photovoltaik* at the *TU Ilmenau*) for growing me lots of samples.

...Special thanks to OS and MMM for their contributions to the paper, that is reprinted in parts in Chap. 5 and for helping me with characterization of the samples.

...Christian Höhn for helping me with all kinds of UHV- and other technical issues.

...Wiebke Albrecht for fun 2PPE measurement sessions on the CdSe QDs, for helping me evaluating tons of data and for preparing and getting me the samples I needed.

...all members of the *Debye Institute for Nanomaterials Science* at the *University of Utrecht* who did most of the preparation and characterization of the CdSe samples and who contributed to the manuscripts that are in parts republished in Chapter 4.

...Dr. Mykhaylo Semtsiv, Simon Heitz and all other members of the *FeT* group at the *HU Berlin*, who prepared, processed and characterized the samples presented in Chap. 6 and contributed to the manuscript that in parts is republished in that chapter.

...Mario Borgwardt for an exciting time setting up the CPL and finally understanding what we were measuring. Heureka!

...Dr. Frank Milde and Prof. Dr. Andreas Knorr for theoretical input and discussions on ultrafast dynamics in quantum wells.

...Dr. Christian Strothkämper, Hannes Hempel, Dr. Robert Schütz, Söhnke Müller and all the current and former members of the group, now known as *Institute for Solar Fuels*, who helped making the time in the office and lab enjoyable.

...My girlfriend Jalda Kabierski, for enduring me and my lamentations in the last stage of my writing and for providing me with constant moral support.